Federation University Australia

Geotechnical and Hydrogeological Engineering Research Group

Faculty of Science, Engineering and Information Technology

RANDOM FINITE ELEMENT METHOD PREDICTION AND OPTIMISATION FOR OPEN PIT MINE SLOPE STABILITY ANALYSIS

A dissertation by

Ashley P. Dyson

Submitted in total fulfilment of the requirements

for the degree of

Doctor of Philosophy

September 2020

Abstract

Inherent soil variability can have significant effects on the stability of open-pit mine slopes. In practice, the spatial variability of materials is not commonly considered as a routine component of slope stability analysis. The process of quantifying spatially variable parameters, as well as the modelling of their behaviour is often a complex undertaking. Currently, there are no large-scale commercial software packages containing in-built methods for modelling spatial variability within the Finite Element environment. Furthermore, conventional Limit Equilibrium Methods (LEM) incorporating spatial variability are unable to consider the stress/strain characteristics of these materials.

The following research seeks to accurately model the slope mechanics of spatially variable soils, adopting The Random Finite Element Method (RFEM) developed by Griffiths and Fenton (2004) to determine slope failure mechanisms and safety factors. Techniques are developed to produce a set of optimised Random Finite Element Method simulations using the Monte Carlo Method. Additionally, random field analysis techniques are investigated to compare and categorise soil parameter fluctuation, providing a direct relationship between random field properties and slope failure surfaces. Optimisation and analysis techniques are implemented to examine the effects of cross-sectional geometries and input parameter distributions on failure mechanisms, safety factors and probabilities of failure.

Cross-sectional RFEM analysis is performed in the Finite Element Method (FEM) software package *Abaqus*, with the techniques of this research demonstrated for a large open-pit brown coal mine located in the state of Victoria, Australia. The outcome of this research is a comprehensive procedure for optimised RFEM simulation and analysis.

Statement of Authorship

This thesis contains no material for the acceptance of another award for any degree or diploma in any university or institution, nor does it contain published material extracted either in part or whole without acknowledgement and due reference. All research herein is the sole work of the author, except where explicit reference is made.

Ashley P. Dyson   **Professor Thomas Baumgartl**

Candidate   *Principal Supervisor*

Signed: Signed:

Dated: 09/03/2020   Dated: 01/04/2020

Acknowledgements

Table of Contents

List of Figures

List of Tables

1   Introduction

1.1   Rationale

Slope instability is a significant issue in geotechnical and mining engineering where landslides and slope failures pose a threat to life and damage to infrastructure, with considerable financial consequences. Slope soil profiles are seldom considered to be perfectly uniform or homogeneous due to the depositional and loading histories of the materials, rather, soils and their properties tend to vary from location to location [1]. The fluctuation of soil properties with respect to distance is known as spatial variability. Spatially variable soils can have profound impacts on both slope failure mechanisms and slope Factors of Safety (FoS) [2]. Griffiths and Fenton [2] stated that ignoring spatial variability can lead to unconservative, high safety factors, concluding that key parameters for random field slope stability include material cohesion (c) and friction angle (φ), unit weight (γ) and slope geometry.

In practice, slope stability analysis is commonly conducted using conventional limit equilibrium methods, while soil layers are often considered to be of uniform strength, with fixed homogenous material parameters as part of a deterministic framework. As such, best estimate soil parameters are frequently implemented to model individual soil layers. To account for spatial variation and material uncertainty, higher factors of safety are usually required. Direct analysis of spatially variable parameters is generally ignored, due to the complexities of modelling their behaviour, as well as the considerable computational requirements for their analysis. For these reasons, conventional slope stability analyses may provide poor estimates of the true strength of slopes containing significant spatially variable characteristics.

In recent years, Finite Element Method (FEM) slope stability analysis techniques have gained considerable attention due to their ability to explore stress-strain behaviour. The Random Finite Element Method (RFEM) allows spatially variable materials to be modelled by combining random field theory and Finite Element Method simulation, permitting engineers to assess the true safety,

reliability and failure mechanisms of a slope. Although RFEM provides a robust technique for considering spatially variable slopes, further attention to optimised simulation methods and the characterisation of underlying material variation is necessary to fully comprehend the impacts of spatially variable systems on the stability of slopes, excavations and embankments.

1.2   Research Objectives

The research detailed in this thesis aims to provide a set of procedures to assess the effects of soil variability on complex numerical slope stability models. In particular, the implementation of optimised methods of analysis is considered, coupled with prediction and categorisation techniques to directly determine the effects of soil variability on slope failure mechanisms. This research seeks to provide a greater understanding of the effects of soil variability on the stability of large slopes, allowing engineers and practitioners to quantify the impact of geotechnical strength parameters for various input distributions and two-dimensional slope geometries.

To achieve the objectives of this research, several specific goals are summarised below:

1. Define an optimised Strength Reduction Method (SRM) for Finite Element Method slope stability analysis, allowing slope safety factors to be efficiently calculated in Finite Element software packages that do not provide an in-built Strength Reduction Method. The method should be applicable to not only deterministic slope stability analysis, but also to probabilistic and spatially variable simulation methods where computational efficiency is an important factor.

2. Produce a set of prediction and classification techniques for the assessment of random fields, allowing spatially variable slope stability simulation results to be forecast based on the performance of similar random field structures. The investigation of random field similarity and comparison allows for further optimisation of probabilistic analyses, necessary in cases where large scale Monte Carlo analysis is confined by computational constraints such as system resources and excessive simulation times.

3. Develop random field categorisation techniques to associate spatially variable random field characteristics with slope failure mechanisms, slip surface locations and safety factors.

Commonly, RFEM slope stability analysis is used to determine Factors of Safety (FoS) and Probabilities of Failure (PoF). However, random field analysis techniques can be further developed to assess the impact of zones of containing strong and weak materials and the impacts on overall slope stability.

4. Develop methods of analysis to determine appropriate two-dimensional cross-sections, providing Factor of Safety distributions for evaluation of three-dimensional spatially variable slopes. When faced with complex strata, surface topologies and pore-water pressure distributions, the selection of an appropriate cross-section is often non-trivial. As such, the selection of unsuitable cross-sections can lead to overly optimistic Factor of Safety distributions and inaccurate levels of risk.

5. Compare various probabilistic Finite Element Method slope stability results with spatially variable RFEM slope stability simulations. Investigate the performance of the aforementioned techniques for a range of material input parameter distributions to determine the safety factor susceptibility to change, based on initial parameter distribution assumptions.

1.3   Scope of the Research

The research of this thesis is one of four PhD projects funded by the Victorian state government's Department of Jobs, Economic Development, Jobs, Transport and Resources (DEDJTR) as part of the "*Latrobe Valley Brown Coal Mine Batter Stability Research Project*", or simply the "*Batter Stability Project*". The purpose of the project is to address areas of geotechnical risk in response to the 2007 failure of a large slope at the Yallourn open-pit brown coal mine, located in Victoria, Australia. In particular, this PhD research project considers the spatial variability of Victorian Brown Coal (VBC) and associated Latrobe Valley geotechnical materials for the purpose of slope stability analysis.

The geotechnical parameters used for this research are the result of extensive prior research conducted by the State Electricity Commission of Victoria (SECV) – the state government-owned

body responsible for electricity generation and supply from 1918 to 1993, prior to privatisation. Computer Aided Design slope geometries and stratigraphies were generously provided by Energy Australia's Yallourn mine staff.

Due to the availability of university software licences, the slope stability analysis of this research is conducted with the Finite Element Method software package *Abaqus CAE 2018.*

1.4   Structure of the Thesis

This thesis is produced with the "thesis incorporating publication" approach, in accordance with the guidelines of Federation University Australia. Due to the nature of journal publication, the authors apologise for the necessary characteristic repetition and overlap within the background and introduction sections of each paper. The publications are presented in their preprint manuscript format to provide a cohesive, standardised structure throughout the thesis. Minor formatting modifications have been made to figure and table numbering, while all references have been collated and assembled into a single list at the conclusion of the thesis. The research structure of the thesis is shown in Fig. 1.1 with a brief overview of the chapters of the thesis provided below.

Chapter 2: A review of the current literature is presented. Numerical slope stability methods are outlined, including Limit Equilibrium Methods, Finite Element and Finite Difference methods, and design charts. Current probabilistic slope stability analysis methods are detailed, as well as techniques for modelling the effects of spatial variability, including random field generation and the Random Finite Element Method.

Chapter 3: An overview of the Latrobe Valley brown coal open-pit mines located in Victoria, Australia, is presented. Particular emphasis is given to the Yallourn mine slopes and Victorian Brown Coal (VBC). A brief history is provided, with site conditions, material specifications and spatially variable parameters for coal and associated materials.

Chapter 4: The Strength Reduction Method for Finite Element Method slope stability analysis is presented, with an optimised technique implemented in conjunction with the Finite Element package *Abaqus CAE*. The SRM is necessary to facilitate numerical slope stability analysis for the probabilistic, spatially variable simulations of the following chapters.

Chapter 5: A set of techniques are presented for the prediction of safety factors for slope stability models incorporating spatially variable material properties. The procedure minimises the computation required for complex slope stability models, where the simulation time for a large set of Finite Element Method instances is a limiting factor for obtaining results. The method is provided for several idealised examples, as well as cases of a two-dimensional cross-section of the Yallourn open-pit mine.

Chapter 6: The techniques implemented in *Chapters 4* and *5* are coupled with comparison and classification methods for spatially variable random field properties. These techniques allow for slope failure mechanisms to be associated with particular material zones within each random field, highlighting the locations of greatest impact on slope failure.

Chapter 7: A two-dimensional cross-sectional investigation is conducted using the aforementioned methods, to consider slope stability results with respect to changing slope geometry coupled with spatially variable shear strength parameters. The variation of weak material zones and the impact on failure mechanisms is considered for various slope cross-sections. This chapter provides a framework for assessing a range of slope cross-sections, to determine an appropriate slope geometry that will provide conservative slope safety factors.

Chapter 8: The performance of slope stability analyses incorporating spatially variable materials is compared with a range of probabilistic slope stability methods. Variation of the input shear strength distributions is considered to determine effects on slope safety factors and failure mechanisms.

Chapter 9: A summary of the research is presented with conclusions and recommendations for future research and development. The chapter provides an overview of the research and demonstrates the achievement of objectives established prior to commencement of the project.
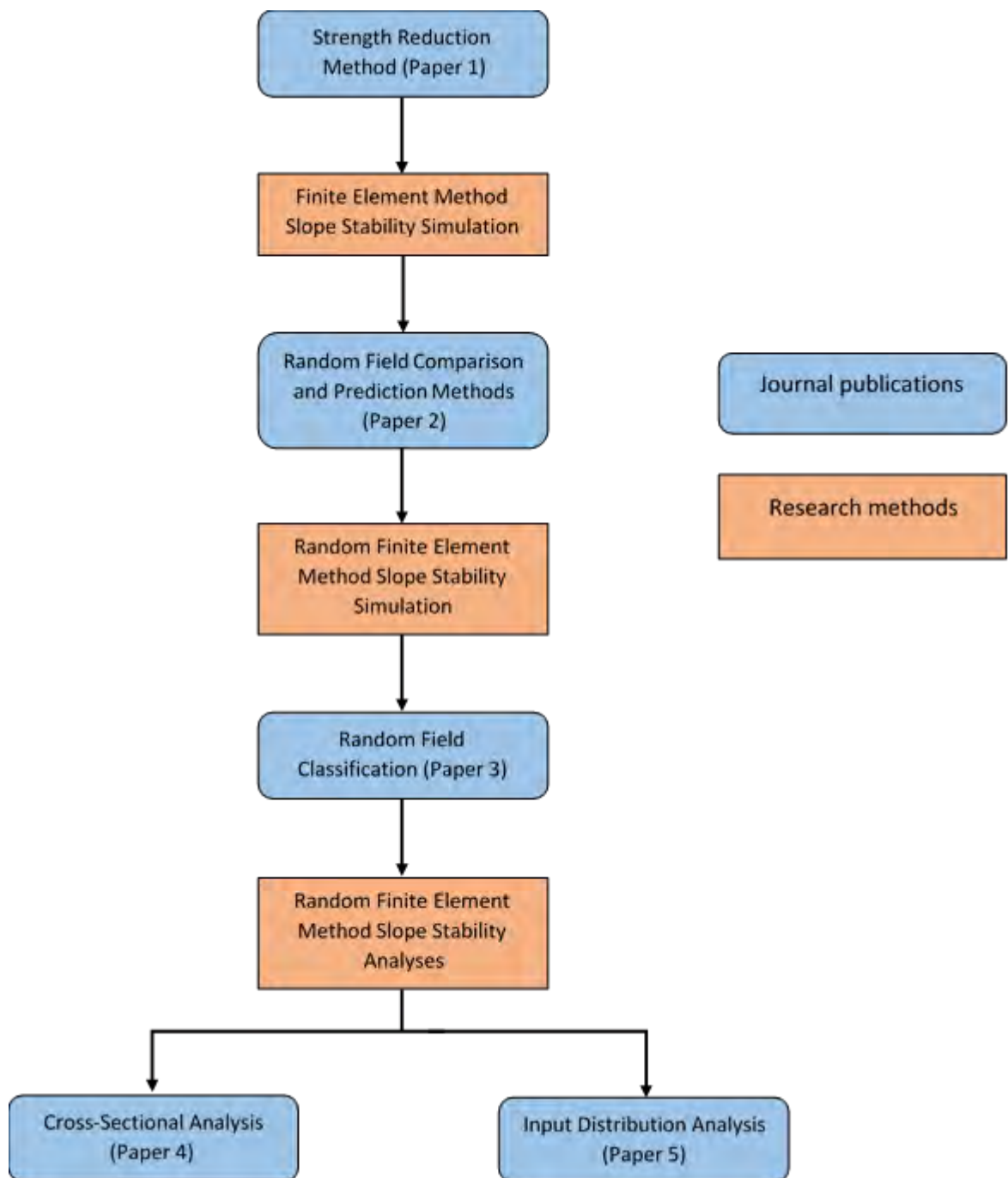
Fig. 1.1. Thesis structure

The papers presented in this thesis are as follows:

1. Paper 1 (Chapter 4)
   Dyson, AP. and Tolooiyan, A., 2018. Optimisation of strength reduction finite element method codes for slope stability analysis. *Innovative Infrastructure Solutions*.
   DOI: https://doi.org/10.1007/s41062-018-0148-1

2. Paper 2 (Chapter 5)
    Dyson, AP. and Tolooiyan, A., 2019. Prediction and classification for Finite Element slope stability analysis by random field comparison. *Computers and Geotechnics*.
    DOI: https://doi.org/10.1016/j.compgeo.2019.01.026

3. Paper 3 (Chapter 6)
    Dyson, AP. and Tolooiyan, A., 2019. Probabilistic investigation of RFEM topologies for slope stability analysis. *Computers and Geotechnics*.
    DOI: https://doi.org/10.1016/j.compgeo.2019.103129

4. Paper 4 (Chapter 7)
    Dyson, AP. and Tolooiyan, A., 2019. An investigation of cross-sectional spatial variation with Random Finite Element Method slope stability analysis.
    DOI: (Currently under journal review – Journal of Geotechnical and Geological Engineering)

5. Paper 5 (Chapter 8):
    Dyson, AP. and Tolooiyan, A., 2019. Comparative Approaches to Probabilistic Finite Element Methods for Slope Stability Analysis. *Simulation Modelling Practice and Theory*.
    DOI: https://doi.org/10.1016/j.simpat.2019.102061

Three additional published group research papers are provided as appendices (Appendix A, B and C). Although the objectives and conclusions of these articles do not directly relate to the numerical modelling untaken in this thesis, these group papers are intended to provide a further understanding of the site conditions, geotechnical parameters and material behaviour for the case study of this PhD research. Tables 1 – 3 provide details regarding the individual papers, as well as the author contribution.

The chapters listed within this thesis outline the necessary methods to perform numerical slope stability analyses when considering spatially variable materials. Methods for optimisation and prediction are implemented to simulate a sufficient number of probabilistic simulations, while comparison methods are considered to determine the impact of random field characteristics on slope safety factors and failure mechanisms. These methods are considered for a range of two-dimensional cross-sections to select appropriate analysis locations, while material input distributions are also varied to investigate the impact on stability results. Collectively, the research

of this thesis provides a structure for assessing the stability of large slopes exhibiting spatially

variable properties.

Table 1.1. Description of the journal article provided in Appendix A

Published article title	Application of Ground Penetrating Radar (GPR) to Detect Joints in Organic Soft Rock
Journal	ASTM Geotechnical Testing Journal
DOI	10.1520/GTJ20170279
Authors	A Tolooiyan, **A Dyson**, M Karami, T Shaghaghi and M Ghadrdan
Individual Contribution	20% - (Designed and performed the analysis, wrote the paper)

Table 1.2. Description of the journal article provided in Appendix B

Published article title	Investigation of an Australian Soft Rock Permeability Variation
Journal	Bulletin of Engineering Geology and the Environment
DOI	10.1007/s10064-019-01715-8
Authors	A Tolooiyan, **A Dyson**, M Karami, T Shaghaghi and M Ghadrdan
Individual Contribution	20% - (Designed and performed the analysis, wrote the paper)

Table 1.3. Description of the journal article provided in Appendix C

Published article title	Use of Stochastic XFEM in the Investigation of Heterogeneity Effects on the Tensile Strength of Intermediate Geotechnical Materials
Journal	Finite Elements in Analysis and Design
DOI	10.1016/j.finel.2018.03.003
Authors	**A Dyson**, Z Tang and A Tolooiyan
Individual Contribution	33% - (Designed and performed the analysis, wrote the paper)

The author of the thesis hereby acknowledges that the individual contributions detailed above are

an accurate representation of the work undertaken, as agreed on by all authors of the work.

2   Literature Review

2.1   Introduction

Probabilistic methods are an important aspect of risk assessment for slope stability analysis of open-pit mines. In many cases, probabilistic methods capture soil variability and uncertainty where deterministic methods cannot. Soils often exhibit inherently heterogeneous properties which can profoundly impact the soil mechanical behaviour of large geostructures such as open-pit mine slopes. In the following research, material heterogeneity and uncertainty are incorporated with the Finite Element Method to investigate and quantify the effects of spatially variable soils on slope stability. This chapter provides a review of the current literature for numerical slope stability analysis and soil variability, divided into the following sections:

2.1   A review of Limit Equilibrium and Finite Element Methods for slope stability analysis.

2.3.   Slope failure characteristics commonly observed in mine slopes and embankments.

2.4   Advanced methods for slope stability analysis, focusing on large deformation mechanics.

2.5   Probabilistic slope stability analysis.

2.6   Finite Element Method simulation optimisation techniques, improving computational efficiency.

The order of these sections is chosen to facilitate the understanding of traditional slope stability analysis, current day Finite Element Method slope stability analysis, probabilistic methods and optimisation techniques, as necessitated by the strong probabilistic and optimisation components of the chapters to follow.

2.2   Review of Numerical Methods for Slope Stability Analysis

Slope stability analysis is commonly performed to determine the safety of natural slopes, embankments, excavations, dams and landfills. Methods of analysis have evolved over the years from cumbersome manual calculations to advanced computer-driven commercial software packages. The following sections review the available methods for numerical slope stability analysis. The considered methods are detailed in Fig. 2.1.
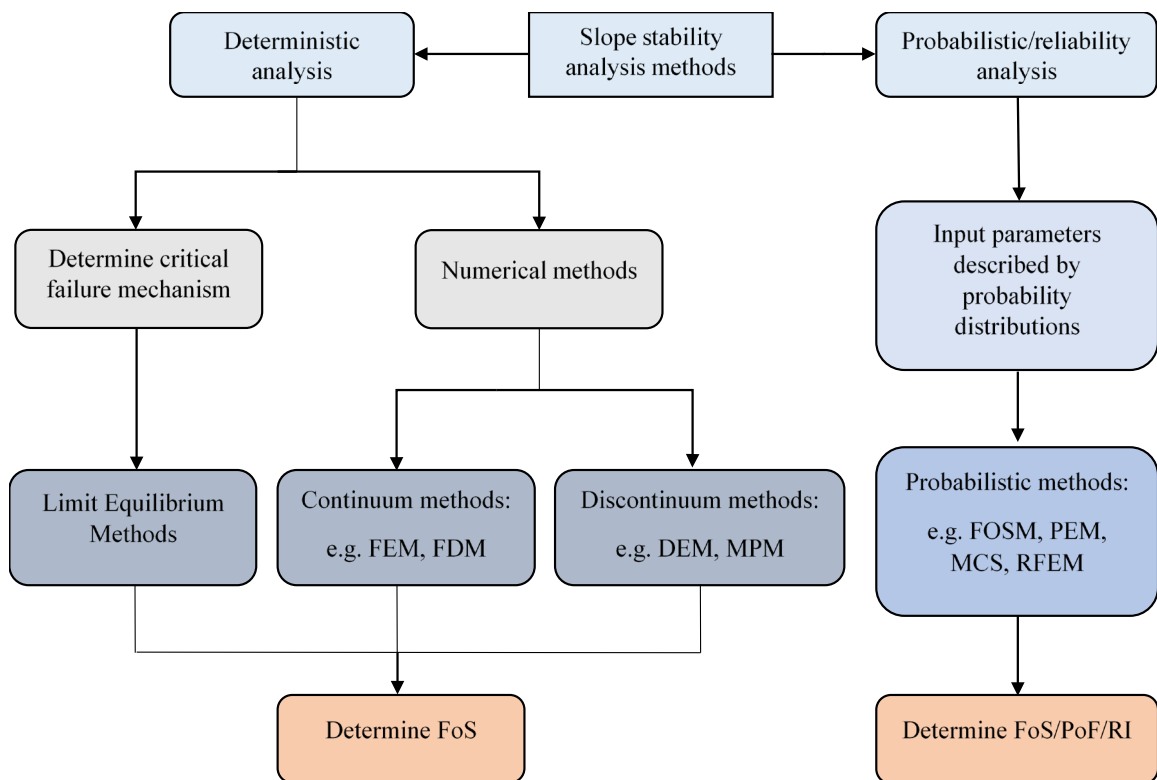
Fig. 2.1. Approaches to slope stability analysis

2.2.1   Limit Equilibrium Methods for Slope Stability Analysis

The most common method for assessing the stability of slopes is a class of techniques known as the Limit Equilibrium Methods (LEM). As the name suggests, the analysis is performed by assuming force and/or moment equilibrium. In the simplest form of LEM, only the force equilibrium is considered, where the sum of the forces driving slope failure are compared with the sum of resisting forces. The ratio of these two sums is defined as the Factor of Safety (FoS), as shown in Equation 2.1.

$$FoS = \frac{\sum resisting\ forces}{\sum driving\ forces} \qquad (2.1)$$

The methods of limit equilibrium consider a soil mass subdivided into (often vertical) slices. LEM uses representative geometries, materials, groundwater and loading/support constraints to determine slope Factors of Safety based on a set of simplified mechanical assumptions, as described in detail by Duncan et al. [3]. Numerous Limit Equilibrium Methods have been developed for the purpose of slope stability analysis, as briefly detailed below.

Ordinary Method of Slices (OMS)

The ordinary method of slices as introduced by Fellenius (also known as Fellenius' Ordinary Method of Slices) [4] is one of the simplest Limit Equilibrium Methods. The Limit Equilibrium Methods used to consider the stability of blocks, wedges and sliding planes are considered for a single free body and are not dependent on the effective normal stresses along the slip surface. The sliding soil mass above the failure surface is subdivided into *n* slices, with the inter-slice normal and shear forces neglected. The Ordinary method satisfies the moment equilibrium for a circular slip surface. Although the method can accommodate any candidate failure surface, the solution is indeterminate, with more unknowns than equations [5]. A particular advantage of the OMS is its simplicity in calculating the slope Factor of Safety, as the equation does not require an iterative process [6]. The Factor of Safety determined by the OMS is considered as a conservative estimate and can underestimate the true equilibrium FoS by as much as sixty percent [7]. The associated equations and unknowns for the method of slices are summarised in Table 2.1.

Bishop Simplified Method (BSM)

Bishop's simplified method [8] considers the inter-slice normal forces while neglecting the inter-slice shear forces [9]. The method also satisfies the vertical force equilibrium and the overall moment equilibrium, and is most applicable to circular slip surfaces. The Factor of Safety is determined by a summation of moments about the slip surface centre, and is not as such an explicit equation, requiring an iterative procedure.

Janbu's Simplified and Generalised Methods

Janbu's simplified method (JSM) [10] is based on a non-circular slip surface, with the FoS calculated by determining the horizontal force equilibrium. The method satisfies both force equilibria, however, it does not satisfy the moment equilibrium. The method is most commonly considered for composite non-circular shear surfaces. Both Janbu's simplified method and Bishops' simplified method assume zero inter-slice forces, reducing the number of equation unknowns to $(4n – 1)$ where n is the number of slices, leaving the solution overdetermined.

Janbu's Generalised Method (JGM) [11] considers a line of thrust to determine the relationship of inter-slice forces. The method satisfies both force and moment equilibria and is appropriate for complex geometries and multi-layered strata. For this reason, JGM is considered an advanced LEM. A comparison of various Limit Equilibrium Methods is shown in Table 2.2.

Table 2.1. Equations and unknowns for the method of slices [5]

Condition	Equations
Moment equilibrium for slice ($\sum M = 0$)	n
Horizontal and vertical equilibrium for slice ($\sum F_h$ & $\sum F_v = 0$)	$2n$
Mohr-Coulomb equation	n
Total number of equations	$4n$
Variable	***Unknowns***
Factor of Safety	*1*
Normal force (N)	*n*
Position of N on sliding plane	*n*
Shear force (τ)	*n*
Horizontal inter-slice forces	*n – 1*
Vertical inter-slice forces	*n – 1*
Line of thrust	*n – 1*
Total number of equations	*6n – 2*

Table 2.2. Summary of Limit Equilibrium Method features [12]

Method	Circular	Non-circular	Moment equilibrium	Force equilibrium
Ordinary	✓	✓	✓	-
Bishop simplified	✓	*	✓	**
Janbu simplified	*	✓	-	✓
Janbu generalised	✓	✓	***	✓
Lowe-Karafiath	-	✓	-	✓
Corps of Engineers	-	✓	-	✓
Sarma	✓	✓	✓	✓
Spencer	✓	*	✓	✓
Morganstern-Price	✓	✓	✓	✓

* Circular and non-circular failure surfaces accepted

** Satisfies vertical force equilibrium for base normal force

*** Satisfies moment equilibrium for intermediate thin slices.

Shear Strength

Slope stability analysis can be conducted considering either total or effective stress. Total stress analysis is pertinent for short-term analysis and multi-stage loading problems when rapid loading/unloading conditions are considered, while effective stress analysis is considered for excavation where long-term behaviour is critical [6]. When conducting total stress analysis, pore pressures are excluded from the analysis, and soil shear strength is described by the undrained shear strength. The drained shear strength of a soil for effective stress analysis with the Mohr-Coulomb failure criterion is described by:

$$\tau_f = c' + (\sigma_n - u) \tan \phi' \tag{2.2}$$

where, τ_f is the soil effective shear strength; c' is the soil effective cohesion; σ_n is the normal stress; u is the pore-water pressure; and ϕ' is the effective angle of internal friction. Equation (2.2) is applied in cases with fully saturated soils. The Mohr-Coulomb failure criterion can be modified for partially saturated and unsaturated soils as follows [13]:

$$\tau_f = c' + (\sigma_n - u_a)\tan\phi' + (u_a - u)\tan\phi^b \qquad (2.3)$$

where, u_a is the pore air pressure; ϕ^b is the soil internal friction angle with respect to the matric

suction $(u_a - u)$ [14] as $(\sigma_n - u_a)$ remains constant. All Limit Equilibrium Methods use the

Mohr-Coulomb failure criterion to determine shear strength along the failure surface. The most

common method for measuring the strength of a slope with LEM is the Factor of Safety. The FoS

of a slope can be defined in several ways, including:

1. The ratio of the shear strength of the soil with respect to the shear stress required for
   equilibrium;

2. The ratio of the current soil strength with respect to the minimum shear strength
   required to avert slope failure [8];

3. The ratio of the soil resisting forces with respect to the driving forces.

The mobilised shear stress τ is defined as

$$\tau = \frac{\tau_f}{FoS} = \frac{c' + \sigma_n \tan\phi'}{FoS} \qquad (2.4)$$

The available shear strength τ_f depends on the soil and the effective normal stress, with the

mobilised shear stress dependent on the forces external to the soil mass. Slip surfaces may be

planar, circular or non-circular in shape, with the slip surface required to be predetermined prior to

analysis for LEM. In most cases, LEM slope stability analysis is performed in a deterministic

setting with shear strength parameters, unit weights, permeabilities, etc. based on best estimate data.

Accordingly, LEM slope safety factors are dependent not only on the stability method of choice

and the assumed failure surface but also the accuracy of the input parameters. For these reasons,

coupled with soil uncertainty and variability, the analysis of FoS values often requires adjustment

by adopting a higher FoS to guarantee stability. Despite the modification, the practice has proven

to perform poorly when considering the effects of soil uncertainty and heterogeneity [15], leading

to the development in the 1970s of more sophisticated probabilistic tools of analysis [1, 16-18].

Three-Dimensional (3D) Limit Equilibrium Methods

Two-dimensional LEM software programs examine the stability of slopes with unit-width slices, ignoring the shear stresses on the sides of the slices. In certain cases, three-dimensional analyses are required to define slope geometries. Most 3D LEM analyses are based on the Method of Columns (or Prisms) - the three-dimensional analogue of the method of slices [19], however, numerous assumptions are required to satisfy the six static equilibrium equations, to produce a determinate solution. Duncan and Wright suggested 3D LEM be implemented cautiously, especially when used in cases where 2D analysis indicates unacceptably low Factor of Safety values [20].

2.2.2   Empirical Design Charts

Empirical design charts provide guidelines for a range of slope angles and heights based on the known performance of various historical slopes. Empirical charts can be traced back to Taylor's 1937 slope classifications [21], based on the total stress approach for dry, homogeneous slopes. More recently, Haines and Terbrugge [22] published a widely used set of charts based on the Laubscher Mining Rock Mass Rating (MRMR) System [23] (Fig. 2.2). Numerous slope stability charts have been developed based on the aforementioned methods [10, 21, 24-27] which are commonly used for initial estimations for the stability of a slope, although, in practice, stability analysis of slopes is most commonly performed with specialist geotechnical computer software. Stability charts require slopes to satisfy the following assumptions:

- Homogeneity of material, with uniform shear strength characteristics along the candidate failure surface;

- Shear strength characterised by the Mohr-Coulomb failure criterion;

- Circular or rotational failure surface, passing through the slope toe.

Design charts are inherently limited based on their historical nature, as acknowledged in the Haines and Terbrugge charts where a marginal zone suggests additional analyses are necessary to consider

stability. Despite this limitation, design charts are a useful tool for initial preliminary estimates at the conceptual stage of a project.
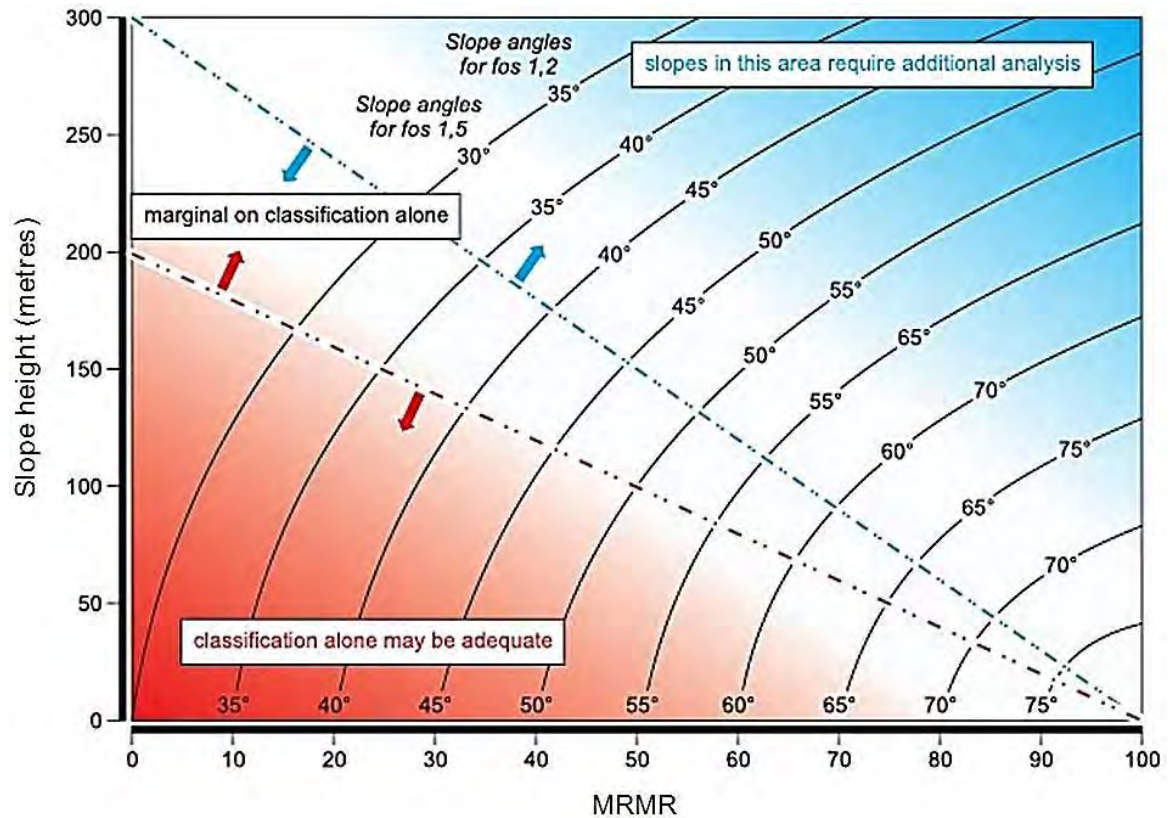
Fig. 2.2. Haines and Terbrugge chart for determining slope height and slope angle [22]

2.2.3 Finite Element Methods for Slope Stability Analysis

The Finite Element Method (FEM) is a powerful and increasingly prevalent method of analysis for slope stability. FEM was initially introduced by Courant [28] in the 1940s, however more recently, the method has been considered for geotechnical engineering applications [29-31]. Compared with the relatively less complicated Limit Equilibrium Methods which provide fast estimations of slope safety factors, FEM for slope stability often requires greater levels of complexity, input parameters and increased computational times. However, FEM has several advantages compared to the Limit Equilibrium Methods [32]:

1. FEM is capable of modelling the process of progressive failure up to the final shear failure.

2. Unlike LEM, pre-failure levels of deformation can be incorporated in the slope stability analysis.

3. A priori assumptions of the critical failure mechanisms, the slip surface shape and the failure location are not necessarily required. The slope failure process occurs naturally through elements whose applied shear stress is greater than the soil shear strength.

4. As the method does not require the subdivision of soils into slices, no assumptions are required regarding inter-slice forces and moments. FEM preserves global equilibrium until the slope failure is achieved.

Each Finite Element is assigned a material model and material properties. The simplest FEM material model is the linear-elastic model, using elastic properties (the elastic modulus E and Poisson's ratio v). Linear elastic/perfectly plastic stress-strain relationships are the most commonly used soil and rock mass material models. These models commonly use the Mohr-Coulomb failure criterion with no hardening component to limit the shear stress that an element can sustain, although more complex failure criteria exist, such as the Hoek-Brown failure criterion [33].

Early slope stability FEM models created by Smith and Hobbs [34] produced consistent results compared to Taylor's 1937 charts [21]. The development of elasto-plastic models extended the application of FEM in the field of geotechnics with Zienkiewicz et al. [35] implementing $c' - \phi'$ models, producing comparable results with Limit Equilibrium Methods. Since the 1980s, FEM slope stability has become a far more regularly used numerical technique for slope analysis [30, 32, 36, 37]. Potts et al. [38] used FEM to consider the failure mechanisms for a delayed collapse of a cut slope in stiff clays. Troncone [39] incorporated strain-softening behaviour in the elasto-plastic model, observing that strain-softening can play an important role in slope failure. Furthermore, Chai and Carter [40] observed large deformations when clay strain-softening behaviour was incorporated in FEM analysis.

Two-dimensional FEM analysis has since been conducted in a wide range of stability scenarios including earth dams, railway embankments and mine slopes under a wide range of conditions

including seismic disturbance [41-44]. The FEM is one of the few methods used to study complicated stability problems incorporating rain infiltration and transient unsaturated seepage analysis [45, 46].

Smith and Griffiths [47] published the first available two-dimensional finite element method slope stability analysis software in 1988. Since then, further updates have also incorporated three-dimensional elasto-plastic functionality [48] with comprehensive validation compared with LEM conducted by Griffiths and Lane [32]. Lane and Griffiths [37] estimated slope Factors of Safety under drawdown conditions and compared results from LEM, as determined by Morgenstern [49]. Lechman and Griffiths considered progressive earth slope failure under a range of loading strategies [50], while Griffiths and Marquez [36] made comparisons with three-dimensional Limit Equilibrium Methods. Based on FEM analysis, de Buhan et al. [51] observed that the final slope stability factors of safety may be influenced by scale-effects in rock masses.

FEM slope analysis is conducted by applying a gravity load to the weight of the soils and monitoring the stresses at each Gauss point. The process generates normal and shear stresses at these points within the FEM mesh, which are initially considered as elastic. The stresses can then be compared with the Mohr-Coulomb failure criterion, which can be defined in terms of the principal stresses as follows:

$$F = \frac{\sigma_1 + \sigma_3}{2} \sin \phi \quad - \frac{\sigma_1 - \sigma_3}{2} - c \cos \phi \qquad (2.5)$$

where σ_1 and σ_3 are the major and minor principal stresses, respectively; c and ϕ are the soil cohesion and internal friction angle parameters, respectively; and F is the failure function which can be interpreted as:

- F < 0 elastic (stresses inside the failure envelope)

- F = 0 yielding (stresses are on the failure envelope)

- F > 0 yielding but must be redistributed (stresses outside the failure envelope)

Plastic stress redistribution is performed with an iterative algorithm [52] which continues until the Mohr-Coulomb failure criterion and global equilibrium are satisfied.

Finite Element Method Modelling Considerations

Element size

Determining a suitable mesh distribution is one of the most common issues for modelling with Finite Elements. The calculation of stress and strain gradients within the slope geometry requires an appropriately sized element discretisation. A finer mesh often produces results with greater accuracy, however, a trade-off between accuracy and computation time is often a necessary consideration. Sazzad et al. investigated various two-dimensional triangular and quadrilateral elements ranging in size from 0.3 m to 1 m in length, resulting in comparable Factors of Safety [53]. Element size is particularly important when considering spatially variable soil parameters exhibiting short spatial correlation lengths [54]. Huang and Griffiths noted that the mesh size should be at least half the correlation length to ensure that the correlation length is appropriately sampled by the mesh [55].

Boundary conditions

The configuration of boundary conditions can yield a wide range of slope failure mechanisms. For continuum-based solutions for slope stability, model boundaries must extend well past the location where slope failure is likely to occur [56]. Common two-dimensional model boundary conditions are configured as follows:

a) No displacement in the x-direction at the ends of the slope model. These boundaries must be placed far enough away from the likely slope failure region.

b) No displacement at the base of the slope model. Similarly, this boundary is placed far enough away from the slope failure location.

c) Plane strain in the y-direction, implying the "out of the plane" displacement and shear stresses on the y-faces are zero.

Ho [57] noted that the thickness of the slope foundations and the location of the boundary underneath a homogeneous slope can affect the failure mechanisms. For the purpose of comparison, the boundary conditions adopted in this research align with the studies of Li et al. [58].

The presence of water

Groundwater interaction is one of the key variables influencing slope stability and design. In particular, rainfall infiltration is often a factor inducing landslides in unsaturated slopes [59]. Changes in pore-water pressures can directly influence effective stresses which can alter the shear strength of a soil as well as the consolidation behaviour. There are two types of water flow: steady-state and transient flow. When considering steady-state flow, the pore-water pressure is constant, while pore-waters vary in transient flow, as the name suggests. Troncone et al. noted that an increase in pore pressures can induce deformation prior to large-scale slope failure [60], as was noted in the 2007 Yallourn slope failure where a build-up of pore water pressures within coal joints triggered minor cracking and deformation prior to the slope collapse [61]. As such, the selection of appropriate pore-water distributions is necessary to determine accurate failure mechanisms and safety factors. Cascini et al. [62] observed that excess pore pressures occurring in the lower section of a slope can trigger landslides in the soil layers above. To specify the distribution of pore pressures within a slope, a complete flow analysis can be performed, with the resultant pore pressures used in stability analysis. Alternatively, a phreatic surface can be specified.

Constitutive models

The selection of an appropriate constitutive soil model is an imperative consideration for Finite Element Method slope stability analysis [63]. One of the most commonly implemented constitutive models for slope analysis is the linear-elastic model with a perfectly plastic Mohr-Coulomb yield criterion, however, numerous alternative constitutive models exist such as the elastic strain hardening cam-clay model developed by Roscoe and Schofield [64]. Soil and rock slopes may contain bedding planes, joint networks and other geometric discontinuities contributing to complex soil behaviour, requiring specific constitutive models [65], as the presence of these weakened material states often significantly influence the stability of slopes [66, 67]. The Generalized Hoek-Brown model considers three sets of Coulomb weakness planes and is frequently used to consider weak planes. Generalised Hoek-Brown consists of eight yield functions, not all of which need be active simultaneously. The performance of various constitutive models for slope stability analysis has been the subject of numerous publications [68-72].

Strength Reduction Method for Finite Elements

Slope safety factors in FEM can be calculated with two different procedures: overloading of the slope [73], or the Strength Reduction Method (SRM) [74]. In the overloading method, the gravitational force applied to the slope is steadily increased until slope failure occurs, with the Factor of Safety defined as the ratio of the minimum gravitational force necessary to bring the slope to failure, with respect to the true physical gravitational force. The Strength Reduction Method (also known as the Shear Strength Reduction Method) is calculated by iteratively reducing the slope shear strength parameters until the slope is on the verge of failure. The SRM Factor of Safety is defined as the initial slope shear strength divided by the shear strength necessary to bring the slope to the point of failure [75]. In most cases, the shear strength parameters are reduced by an incremental parameter known as the Strength Reduction Factor (SRF). Although neither method provides significant differences in Factors of Safety, slip surfaces produced by the overloading

method tend to be shallower in depth, compared to the SRM [76]. In this research, the Strength Reduction Method is implemented in the Finite Element environment. A brief description of the method is provided in Section 2.2.4.

2.2.4   Strength Reduction Method

The Strength Reduction Method was implemented as early as 1975 by Zienkiewicz et al. [35] and has since been applied by many others [30, 77-80]. The shear strength parameters (cohesion and friction angle) are reduced until the critical slope failure occurs. Three common criteria are defined as the primary mechanisms for determining slope failure:

1. Development of plasticised elements along the slope failure surface (often from the toe to the head of the slope) [30].

2. Large scale slope deformation or bulging of the slope profile [81].

3. Non-convergence of the FEM solver, indicating that no stress distribution can be determined to satisfy both the Mohr-Coulomb failure criterion and global equilibrium [35]. Non-convergence is associated with a rapid increase in nodal displacements.

It should be noted that non-convergence is determined by out of balance forces and the incremental nodal displacements, which are user-defined. For this reason, non-convergence does not necessarily mean the slope has failed [82].

In most cases, large slope deformation in the slope crest is considered as the sign of failure. Several other methods have been proposed for identifying failure, e.g. limitation of the shear stresses along the potential failure surface [83, 84], failure visualisation [85, 86] and identification of incremental shear strain concentrations along the shear zone and/or plastic zones [72, 87]. With the reduction in shear strength parameters, the resisting forces and moments are reduced such that they become equal to the driving forces and moments, at which point, slope failure commences.

The SRM procedure iteratively reduces shear strength parameters as follows:

$$c = \frac{c_0}{SRF} \tag{2.6}$$

$$\phi = \tan^{-1}\frac{\tan\phi_0}{SRF} \tag{2.7}$$

where, c_0 and ϕ_0 are the initial material cohesion and friction angle parameters, respectively; c and ϕ are the reduced parameters; and SRF is the iterative Strength Reduction Factor. Once the shear strength parameters are reduced to precipitate the onset of slope failure, the FoS is defined as the ratio of the initial shear strength parameters with respect to the final shear strength parameters by:

$$FoS = \frac{c_0}{c_f} = \frac{\tan\phi_0}{\tan\phi_f} \tag{2.8}$$

where, c_f and ϕ_f are the shear strength parameters required to bring the slope to the verge of failure. The FoS is defined as the ratio of the shear strength of the soil to the shear stress required for equilibrium [6]. The SRM technique can be applied to any elasto-plastic or non-linear elastic model to initiate slope failure with FEM simulation. Based on the SRM, Manzari and Nour [88] investigated the effects of soil dilatancy on slope stability, with the effect becoming increasingly relevant as the friction angle increases. Although the SRM is briefly described within this chapter for the purposes of the initial literature review, further detail is provided in Chapter 5 - Optimisation of Strength Reduction Finite Element Method Codes for Slope Stability Analysis.

2.3   Slope Failure Characteristics

Collapse of a slope or embankment can be the result of a number of different failure mechanisms. Due to the geological structure and stress state of soils and rock masses, certain failure modes occur with greater frequency than others. Many classification systems for slope failure mechanisms do not distinguish between slope failure, detachment or run out. Cruden and Varnes [89] divided slope failure classifications into categories of falls, topples, slides, spreads and blows. Poisel et al. [90] listed 14 different slope failure mechanisms (Fig. 2.3), defined as follows:

a) Falling;

b) Translational sliding on discontinuities;

c)   Sliding on a polygonal sliding plane;

d)   Slumping;

e)   Rotational failure;

f)   Hard on soft;

g)   Torsional failure;

h)   Buckling;

i)   Flexural toppling;

j)   Block toppling;

k)   Slope creep;

l)   Kink band slumping;

m)   Translational sliding parallel to the slope surface;

n)   Mudslide.

A brief description of the most frequent slope failure mechanisms is provided below.

2.3.1   Circular Failure

Circular failure, sometimes called rotational failure [91], is the failure of a slope in a circular arc. Circular failure generally occurs by rotation along a slip surface, commonly in homogenous soils [90]. Circular failure can occur in three ways (Fig. 2.4):

a)   Face failure or slope failure – when the soil above the toe contains weak zones, causing the failure plane to intersect the slope above the toe.

b)   Toe failure – the most frequent form of failure, where the slip surface passes through the toe of the slope.

c)   Base failure – when a weak soil strata under the toe causes the failure plane to pass through the base of the slope.

The LEM Ordinary Method of Slices satisfies the moment equilibrium for a circular slip surface.

2.3.2   Wedge Failure

Wedge failure may occur when two or more weak planes intersect each other, forming a wedge. Wedge failures may range in size from several cubic metres, to large landslides. The slope stability of soil and rock wedges is typically considered by assessing the orientations of intersecting pairs of planes, commonly determined by stereographic projection techniques [92]. Hoek and Bray claimed the wedge failure mechanism to be the most likely form of slope failure [91].

2.3.3   Planar Failure

Planar failure commonly occurs when structural discontinuities such as dipping joint planes form a well-defined weak zone. Planar failure leads to a sliding motion along the failure plane, commonly due to the presence of a single discontinuity. The dip angle of the failure plane should be less than the dip angle of the associated slope, known as the daylight condition. Failure frequently occurs in hard or soft materials with well-defined joints or discontinuities, e.g. layered sedimentary rock, block-jointed granite and volcanic rock flows.

2.3.4   Toppling Failure

Slope toppling failure occurs when a set of well-developed discontinuities dip steeply into a slope, producing the failure of a number of blocks or layers, characteristic of a successive breakdown of the slope. Toppling refers to columns of rock overturning, due to steeply dipping joints or discontinuities. The toppling failure may be initiated by crushing of the toe of the slope, known as secondary toppling. Bobet [93] considered analytical solutions for toppling failure based on a LEM approach, while Adhikary et al. [94] investigated the mechanisms of flexural toppling.
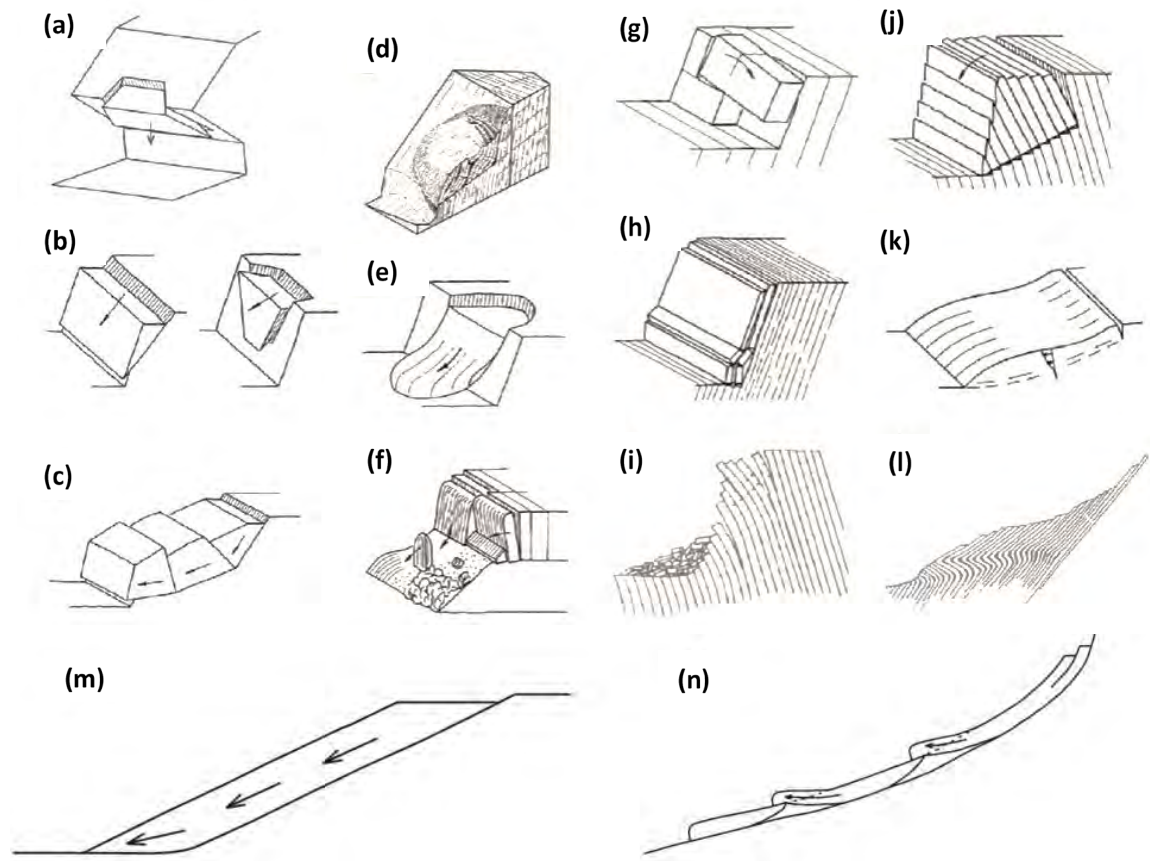
Fig. 2.3. Slope failure mechanisms [90]
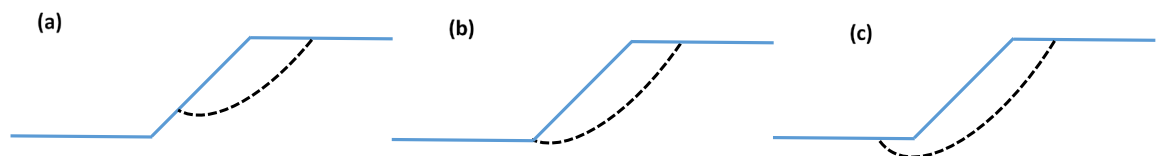
Fig. 2.4. Circular slope failure mechanisms. (a) face failure (b) toe failure (c) base failure

2.4 Alternative Advanced Numerical Slope Stability Methods

Although slope stability analysis is most commonly performed with Limit Equilibrium or Finite Element methods, several alternative techniques exist, including the Discrete Element Method (DEM), and the Material Point Method (MPM).

2.4.1 Discrete Element Method

The Discrete Element Method developed by Cundall et al. [95] is based on the mechanics of granular materials and can be applied to slopes considered granular in nature [96]. DEM follows the principles of Newton's second law of motion, using the relationship between particle forces and displacements. Masses are represented as a group of points (known as grains), with each point associated with an individual particle. Relationships between particles are modelled using springs and dashpots for the normal and shear directions, respectively. The method has been adapted to consider slope failure and rock fall, due to the method's applicability for moving boundaries [97]. Wang et al. [98] produced a DEM model to consider jointing of an excavated slope, using micro-particle parameters to create an assembly exhibiting the same deformational behaviour as an intact rock mass. Guan et al. [99] outlined a method to calculate the progressive slope failure of cohesive-frictional granular materials, using graph theory techniques to determine the Factor of Safety. Elmo et al. modelled a large open-cut mine in two and three dimensions using finite element/discrete element codes [84], while Xu et al. developed a coupled LEM-DEM method to transform the slice model in LEM into a DEM model, obtaining the sliding and resistance forces to calculate slope safety factors [100]. Compared with the Limit Equilibrium Method, the dynamic process is evaluated with an iterative method that does not require assumptions regarding force distributions [101]. Although DEM has the advantage of simulating the mesoscopic properties of granular materials, the method is known to be especially computationally intensive, and thus unsuitable for probabilistic analysis [102].

2.4.2 Material Point Method

The Material Point Method initially developed by Harlow [103], originated as a particle-in-cell method for computational fluid dynamics, and can be considered as a combination of FEM and mesh-free methods. MPM is particularly amenable to the analysis of large deformation/large strain analysis, such as slope failure and landslide run-out [104]. MPM discretises soils and updates mechanical behaviour as Lagrangian particles, while a fixed background mesh is used at each incremental calculation step. Dong et al. implemented MPM to investigate the impact forces on pipelines by submarine landslides [105]. Liu et al. [106] considered spatially variable soils, combining LEM and MPM to investigate large deformation failure mechanisms, determining that failure evolution was highly dependent on the spatial distribution of the soil shear strength parameters. Recently, a number of studies have incorporated MPM with a wide range of slope properties (e.g. rainfall infiltration) to investigate progressive slope failure mechanisms [107-111]. Vardon et al. [112] modelled various slope failure modes with MPM, while Coelho et al. [113] simulated the large deformation of dykes subject to flooding.

2.5   Methods of Probabilistic Slope Stability Analysis

Deterministic methods for slope stability analysis can be inadequate in accounting for soil variability and heterogeneity. For this reason, probabilistic methods are increasingly prevalent in a range of numerical analyses for geotechnical applications. As well as considering the slope FoS, probabilistic methods allow for the analysis of other slope safety measures such as the Probability of Failure (PoF) metric or Reliability Index (β) [114, 115]. Numerous probabilistic approaches to slope stability analysis exist, the most common including: (1) the First Order Second Moment (FOSM) method; (2) the Monte Carlo Method (MCM); (3) the Point Estimate Method (PEM); (4) the Random Finite Element Method, as described below.

2.5.1 First Order Second Moment

The First Order Second Moment (FOSM) method is one of the more simple techniques for accounting for parameter variability, with respect to a performance function (in the case of slope stability, commonly the Factor of Safety). The performance function is defined as the FoS equation for a chosen Limit Equilibrium Method (such as Bishop's simplified method of slices, Spencer's method, etc.) and is based on a Taylor series expansion, truncated after the first order (linear) term, as the name suggests. The mean and standard deviation input parameters (distribution first and second moments) are used to approximate the first and second moments of the performance function [116] as follows:

$$E[FoS] = \mu_{FOS} \approx g(E[X_1], E[X_2], \ldots, E[X_n]) \tag{2.9}$$

$$Var[FOS] = \sigma_{FOS}^2 \approx \sum_{i=1}^{n}\left[\left(\frac{\partial FOS}{\partial X_i}\right)^2 Var[X_i]\right] + 2\sum_{i=1}^{n}\sum_{j=1}^{n}\left[\left(\frac{\partial FOS}{\partial X_i}\frac{\partial FOS}{\partial X_j}\right)Cov[X_i, X_j]\right] \tag{2.10}$$

where, $E[FoS]$ is the mean Factor of Safety; $Var[FOS]$ is the Factor of Safety variance; $Cov[X_i, X_j]$ is the covariance between the random variables X_i and X_j; and n is the number of random variables. Numerous studies of FOSM applications have been described [16, 117-119]. Although the implementation of FOSM requires minimal setup, the limited overhead has several drawbacks. As the non-linearity of the FoS performance function increases due to the truncation of the Taylor series to solely the first order linear term, the FOSM method reduces in accuracy. Furthermore, most of the Limit Equilibrium Methods are inherently non-linear. Additionally, the evaluation of the non-linear partial derivatives of Equation 2.10 provides an added layer of complexity. FOSM does not provide any details of the output FoS Probability Density Function (PDF), which is required to determine the Probability of Failure parameter [120]. The method is primarily applied when no correlation exists between input variables. FOSM can be modified to handle multivariate correlations, although the alterations are particularly cumbersome. Duzgan and Bahsin [121] implemented FOSM for probabilistic modelling of a Norwegian rock slope while Hassan and Wolf [122] developed a reliability based index for mean value FOSM. Duncan [15] demonstrated that the method can be applied to a wide range of geotechnical applications, including slope stability, as

evidenced by numerous investigations [16-18, 118, 123]. Although FOSM is commonly implemented, the method suffers from several shortcomings [124], including :

- The performance function is linearly extrapolated for mean values solely for basic variables, therefore the approximation is dependent on how the given limit states are defined. In practice, these assumptions are seldom valid [125].

- The method is highly sensitive to the definition on each random variable, as the method does not accommodate for correlated variables or non-Gaussian cases.

- There is no possibility for error estimates to be determined unless the limit state surface is either fully convex or concave with respect to the origin.

2.5.2 First Order Reliability Method

The First Order Reliability Method (FORM) is a popular alternative to the First Order Second Moment method. The technique is widely considered to be more accurate than FOSM, as it does not suffer from several shortcoming listed in Section 2.4.1. The method has become standard practice in structural engineering and has recently gained acceptance in geotechnical engineering applications [126-128]. Developed by Hasofer and Lind, FORM proposes a different definition of the reliability index compared with FOSM, leading to a geometric interpretation. FORM determines the shortest path to the limit state surface as shown in Figure 2.5. The reliability index is defined by

$$\beta = \min(M) \sqrt{\left(\frac{x-E[x]}{\sigma_X}\right)^T C^{-1} \left(\frac{x-E[x]}{\sigma_X}\right)} \tag{2.11}$$

where β is the reliability index, M is the limit state surface, x is the vector of standard deviations from the mean for each random variable, and C is the correlation matrix. The limit state surface, also known as the failure surface is the difference between the load and resistence of the system, as defined by

$$M = R - L \tag{2.12}$$

where, R is the resistance and L is the load. The reliability index defined in Equation 2.11 is used

to measure the distance from the limit state surface, with the probability that M is less than zero

defining the probability of failure, given by

$$p_f = 1 - \phi(\beta) \tag{2.13}$$

where, p_f is the probability of failure and $\phi(\beta)$ is the normal standard distribution of the reliability

index. A detailed description of FORM for slope stability analysis procedure is given by Baecher

and Christian [125].
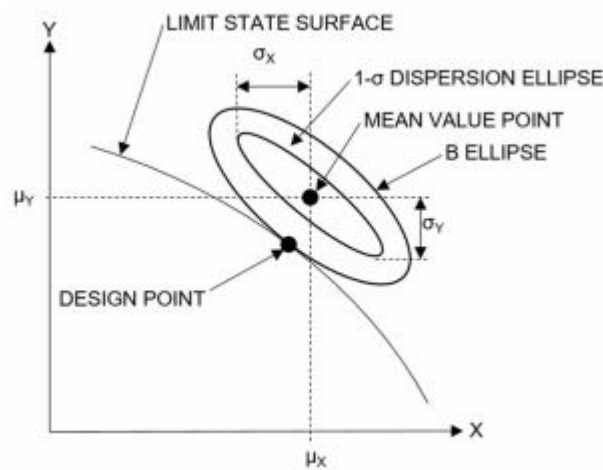
Figure 2.5. Illustration of FORM in relation to the limit state surface and reliability index [129].

2.5.3 Point Estimate Method

The Point Estimate Method (PEM) developed by Rosenblueth [130, 131] is a multivariate technique

for estimating the expected value of a performance function (often the Factor of Safety when

considering slope stability analysis). The method replaces continuous Probability Density Function

(PDF) input variables with sets of discrete point masses by evaluating PDF locations, as determined

by the distribution standard deviation and coefficient of skewness. Thus a two-point Probability

Mass Function (PMF) is created. The discrete point masses are multiplied by weighted factors to

calculate the first two moments (mean and standard deviation) of the performance function. Given

a performance function y of n variables (Equation 2.11), each variable is evaluated at two points x_{i+} and x_{i-} (Equation 2.12):

$$y = f(\boldsymbol{x}) = f(x_1, x_2, \dots, x_n) \tag{2.11}$$

$$x_{i+} = \bar{x}_i + \xi_{xi+} \cdot \sigma_{xi}, \, x_{i-} = \bar{x}_i + \xi_{xi-}\sigma_{xi} \tag{2.12}$$

where, $\bar{x}_i$ is the mean of the distribution of x_i; σ_{xi} the standard deviation; and ξ_{xi+} and ξ_{xi-} are the the standard deviation units, derived from the Pearson skewness coefficient ν_{xi}, as given in Equation 2.13. When symmetric distributions are considered, both ξ_{xi+} and ξ_{xi-} are equal to unity. When considering a single random variable, the weights (named probability concentrations) are determined for each point estimate by Equation 2.14. Conversely, uncorrelated variable weights i and j are given by Equation 2.15. When a random variable distribution is symmetric, both weights are equal to 0.5. The Factor of Safety performance function mean and standard deviation can be evaluated by Equations 2.15 and 2.16, respectively.

$$\xi_{xi+} = \frac{\nu_{xi}}{2} + \left[1 + \left(\frac{\nu_{xi}}{2}\right)^2\right]^2, \, \xi_{xi-} = \xi_{xi+} - \nu_{xi} \tag{2.13}$$

$$P_{x+} = \frac{\xi_{xi-}}{\xi_{xi+} + \xi_{xi-}}, \, P_{x-} = 1 - P_{x+} \tag{2.14}$$

$$P_{i,j} = P_{xi} \cdot P_{xj} \tag{2.15}$$

$$FoS_\mu = \sum_{i=1}^{2^n} P_i FoS_i \tag{2.16}$$

$$FoS_\sigma = \sqrt{\sum_{i=1}^{2^n} P_i (FoS_i - FoS_\mu)^2} \tag{2.17}$$

where, P_{xi} and P_{xj} are evaluated as the weights of a single random variable.

Two points are evaluated for each variable such that y is evaluated for a total number of 2^n combinations. Miller et al. [132] used PEM to investigate the stability of plane shear and rock wedge failures, while Park et al. [133] presented results of rock wedge failure based on random variable distributions with an incorporated safety margin. Valerio et al. [134] used PEM in conjunction with LEM to evaluate factors of safety for an open-pit diamond mine. Although the

PEM is a simple procedure, the number of required computations grows exponentially with the number of input variables, often beyond what is reasonable for practical purposes. For this reason, PEM is often less popular for slope stability analysis due to the excessive computational requirements, becoming tedious when numerous random variables are considered. However, a number of studies have considered probabilistic slope stability with PEM [135-137]. It should be noted that the Point Estimate Method is frequently used as an intitial test prior to more robust probabilistic analysis. The method is often considered with caution due to the limited number of probabilistic realisations that are used for slope stability simulation.

2.5.4   Monte Carlo Simulation

Monte Carlo Simulation (also known as the Monte Carlo Method) is an increasingly popular method of probabilistic analysis. Input parameters are sampled from PDFs, and the performance function is evaluated for a large set of instances. The process of stability evaluation is repeated with hundreds (often thousands) of realisations consisting of randomly sampled combinations of input parameters, until the performance function distribution attains convergence. The general iterative procedure of a Monte Carlo method for Finite Element Method slope stability is detailed in the four steps described below:

1)   Estimate the probability distribution for each input parameter for a given soil layer/region;

2)   Generate random values for each parameter;

3)   Finite Element Method simulation using parameters from step 2);

4)   Repeat the process N times (N > 100) to determine the converged statistical properties of interest.

One of the main advantages of Monte Carlo Simulation is the simplicity and lack of mathematical knowledge required compared with both FOSM and PEM. However, the method requires extensive

computation, thus the method is infrequently used in practice [120]. Monte Carlo Simulation coupled with Limit Equilibrium Methods for slope stability analysis has been used to incorporate soil heterogeneity and soil uncertainty [136, 138]. The method has gained attention when coupled with the Finite Element Method due to recent improvements and developments in computational performance.

2.5.5   Spatial Variation and the Random Finite Element Method

Classical statistics

The aforementioned probabilistic methods for slope stability analysis estimate the Factor of Safety of a slope by evaluating input parameters as random variables, and do not consider spatial variability. Soils are inherently variable from location to location, mainly due to the natural complexity of geological deposition and material loading history. When spatial variability is neglected, significant overestimation (or in some cases, underestimation) of failure probabilities, safety factors and the reliability index (RI) may occur, depending on the variation of the soil or rock mass properties [2, 118, 119, 139]. One of the main limitations of Limit Equilibrium Methods with probabilistic analysis is the spatial correlation of soil and rock properties. With LEM, spatial variability cannot be explicitly accounted for, however, some research has been performed to consider it implicitly, as soil properties are assumed as uniform within each soil layer. In many cases, the critical slip surface obtained with spatially variable shear strength parameters is distinct from the slip surface obtained from deterministic analyses [140], and may not always produce a circular or wedge shaped failure found with homogenous soils. Rather, failure often propagates from regions of low shear strength or zones of weakness. For this reason, critical slip surfaces may exhibit a wide range of failure shapes. Vanmarcke identified three primary sources of uncertainty soil parameters – inherent soil variability, statistical uncertainty (due to limited sampling data) and measurement uncertainty (arising from methods of laboratory and field testing equipment and procedures) [1]. Additionally, transformation model uncertainty arises when laboratory and field data are considered when designing soil models [141].

Classical soil variability and uncertainty considers soil and rock properties as random variables (often denoted as uppercase variables, e.g. *X* and *Y*) with each soil property sampled from a range of values from a Probability Density Function. Several classical statistical measures based on random variables are defined as follows.

Random variable mean

When considering a random variable *X*, with a PDF given by the function *f(x)*, the mean μ, or the expected value E[*X*] is defined as

$$\mu = E[X] = \int_{-\infty}^{\infty} x f(x)\, dx \qquad (2.18)$$

when considering continuous functions, and

$$\mu = E[X] = \frac{1}{n}\sum_{i=1}^{n} x_i \qquad (2.19)$$

for discrete functions, where *n* is the number of data points within the set *x.*

Random variable standard deviation and variance

The dispersion or spread of a distribution is often quantified by either the standard deviation (*s)* or variance (*s²* or Var[*X*]), measured about the mean value by

$$s^2 = Var[X] = E[(X - \mu)^2] = \int_{-\infty}^{\infty} (x - \mu)^2 f(x)\, dx \qquad (2.20)$$

for continuous functions, and

$$s^2 = Var[X] = \frac{1}{n-1}\sum_{i=1}^{n}(x_i - \mu)^2 \qquad (2.21)$$

for discrete functions.

Although the standard deviation and variance are commonly denoted by the symbol σ, the symbol *s* has been chosen in this research to avoid confusion with the symbol for stress.

The standard deviation is defined as the square root of the variance.

$$s = \sqrt{Var[X]} \tag{2.22}$$

Coefficient of Variation

The variability of soil distributions is often expressed by the dimensionless parameter denoted as Coefficient of Variation (CoV), defined as the ratio of the standard deviation with respect to the mean:

$$COV = \frac{s}{\mu} \tag{2.23}$$

Table 2.3 lists CoV values for different soil parameters, as considered by Queiroz [142].

Table 2.3 Typical Coefficient of Variation parameters observed after Queiroz [142]

Soil parameter	Coefficient of Variation (%)
Specific weight	3
Cohesion (undrained)	30
Effective friction angle	10
Effective cohesion	40
Elastic modulus	30
Permeability	300
Void ratio	25

Probability Density Function

The Probability Density Function for geotechnical applications most often characterises the variability of a soil/rock mass parameter. PDFs in geotechnical engineering often obey a Gaussian (normal) distribution or a lognormal distribution. Lumb [143] considered the chi-square test (χ^2) to consider vane shear tests as well as Unconfined Compression Tests (UCT) to investigate undrained shear strength (s_u), observing data followed a normal distributions, with similar results observed by Hooper and Butler [144], and Chiasson et al. [145]. Lumb also noted that other soil

properties were amenable to consideration with Gaussian distributions, including effective cohesion and friction angle. Other studies have suggested the use of lognormal distributions rather than normal distributions for shear strength parameters due to their strictly non-negative properties [2, 146]. Fenton noted that cone tip resistance for Conical Penetration Tests (CPT) are best represented by a lognormal distribution [147]. Although many parameters can be modelled by Gaussian and lognormal distributions, a number of other distributions (e.g. beta, gamma, triangular and Weibull distributions) are also pertinent for considering a range of geotechnical parameters [125].

The PDF for a Gaussian (normal) distribution is defined by

$$f(x) = \frac{1}{s\sqrt{2\pi}} \exp\left[-\frac{1}{2}\frac{(x-\mu)^2}{s}\right] \tag{2.24}$$

Although a normal distribution takes input values from $\pm\infty$, 99.7% of values are found within ± 3 standard deviations of the distribution mean. A Gaussian distribution with a mean of 100 and a standard deviation of 25 (Cov = 0.25) is given in Fig. 2.3.

Unlike the normal distribution, the lognormal distribution consists of strictly non-negative values, ranging from 0 to $+\infty$, and is frequently used to model non-negative geotechnical parameters (e.g. cohesion, friction angle, unit weight, etc.). For a lognormally distributed random variable X, with mean μ_X and standard deviation s_X, $\ln(X)$ follows a Gaussian distribution. The mean and standard deviation of $\ln(X)$ are defined in Equations 2.25 and 2.26, respectively.

$$\mu_{\ln(X)} = \ln\mu_X - \frac{1}{2}s^2_{\ln(X)} \tag{2.25}$$

$$s_{\ln(X)} = \sqrt{\ln(1 + Cov_X^2)} \tag{2.26}$$

Equations 2.25 and 2.26 can be rearranged to give the mean μ_X and standard deviation s_X, respectively:

$$\mu_X = \exp\left(\mu_{\ln(X)} + \frac{1}{2}s^2_{\ln(X)}\right) \tag{2.27}$$

$$s_X = \mu_X\sqrt{\exp\left(s^2_{\ln(X)} - 1\right)} \tag{2.28}$$
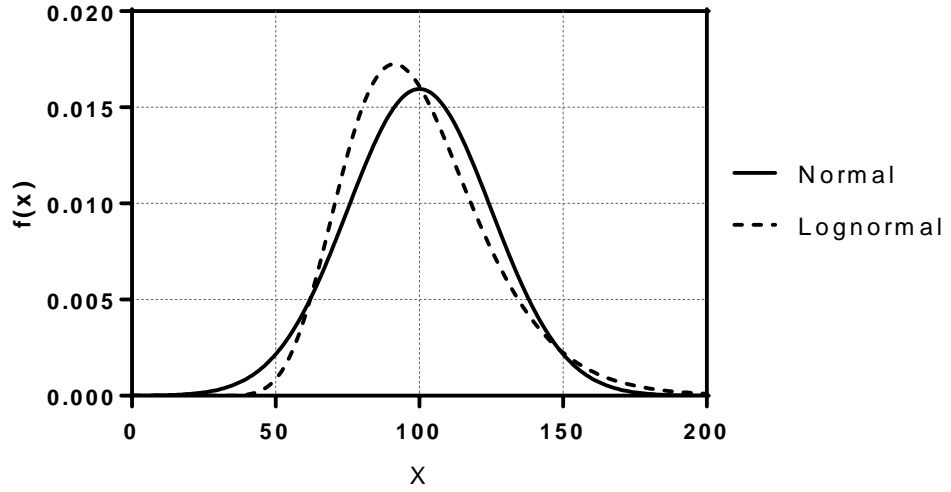
Fig. 2.3. Normal and lognormal probability density functions, with a mean of 100 and a standard

deviation of 25 (Cov = 0.25).

Random Variable Correlation

Often when given a pair of random variables for soil parameters *X* and *Y,* an interdependence can

be observed. Correlated variables are measured by the covariance function Cov[*X,Y*], not to be

confused with the Coefficient of Variation (CoV). The covariance of two variables for continuous

functions is defined as

$$Cov[X,Y] = E[(X - \mu_X)(Y - \mu_Y)]$$
(2.29)

where, μ_X and μ_Y are the mean values of *X* and *Y*, respectively.

For discrete functions, the covariance is given by

$$Cov[X,Y] = \frac{1}{n}\sum_{i=1}^{n}(x_i - \mu_X)(y_i - \mu_Y)$$
(2.30)

The coefficient of correlation (ρ_{XY}) is determined by the normalised covariance, with respect to the

X and *Y* standard deviations

$$\rho_{XY} = \frac{Cov[X,Y]}{s_X s_Y}$$
(2.31)

The correlation coefficient is bounded by ± 1, with $\rho_{XY} = \pm 1$ indicating a perfect (positive or negative) correlation between variables, while $\rho_{XY} = 0$ indicates completely linearly independent random variables.

A number of studies have considered the correlation of soil shear strength parameters for a range of materials [115, 148-150]. Cherubini noted cohesion/friction angle correlations of -0.24 to -0.7, indicating a weak negative relationship. Correlation coefficients for shear strength random variables (cohesion c and friction angle ϕ) can be implemented in slope stability analysis using the covariance decomposition matrix method described by Fenton [151], summarised below:

1. Specify the cross-correlation coefficient $\rho_{c\phi}$ such that $\left(-1 \le \rho_{c\phi} \le 1\right)$;

2. Produce a correlation matrix ρ;

$$\rho = \begin{bmatrix} 1 & \rho_{c\phi} \\ \rho_{c\phi} & 1 \end{bmatrix} \tag{2.32}$$

3. Perform the Cholesky factorisation of ρ, determining the lower triangular matrix *L*, whereby $LL^T = \rho$;

4. Generate two independent standard Gaussian random fields $G_1(x)$ and $G_2(x)$, each with a scale of fluctuation Θ;

5. For each point spatial location *x*, produce the point-wise correlated random fields as follows

$$\begin{Bmatrix} G_{\ln c}(x_i) \\ G_{\ln \phi}(x_i) \end{Bmatrix} = \begin{bmatrix} L_{11} & 0 \\ L_{21} & L_{22} \end{bmatrix} \begin{Bmatrix} G_1(x) \\ G_2(x) \end{Bmatrix} \tag{2.33}$$

6. Transform the Gaussian random field

$$X_i = \exp\left[\mu_{\ln(X)} + s_{\ln(X)} G(x_i)\right] \tag{2.34}$$

Random Fields for Spatially Variable Soil Properties

The random field techniques developed by Vanmarcke can be adopted to consider the spatial variability of slope parameters [1]. Soil variability is often comprised of two components: a

deterministic (often depth-dependent) trend component, and a fluctuation component [141] as shown below.

$$\xi(\boldsymbol{x}) = t(\boldsymbol{x}) + w(\boldsymbol{x}) \tag{2.35}$$

where, $\xi(\boldsymbol{x})$ is the geotechnical parameter to be modelled, $t(\boldsymbol{x})$ is the trend component and $w(\boldsymbol{x})$ is the fluctuation component, commonly named the "off the trend" variation. The fluctuation term $w(\boldsymbol{x})$ is most commonly described by the statistical distribution mean μ, standard deviation *s*, and scale of fluctuation (SoF) Θ [152]. The SoF is defined as the distance up to which random variables are strongly correlated, where little correlation is observed beyond. When Θ is small, parameters exhibit rapid fluctuations over small distances. As Θ increases, fluctuations decrease, producing smoothly varying random fields.

A random field is termed stationary if it is characterised by a probability distribution that is invariant throughout the parameter space, where the mean, variance and cumulative distribution are identical at all locations of the random field. Furthermore, the covariance Cov[*X, Y*] of any two random variables *X* and *Y*, are dependent solely on the separation distance, independent of their individual locations within the parameter space. The fluctuation term $w(\boldsymbol{x})$ is often modelled as a stationary random field. A random field is considered stationary if [152]:

- The distribution mean is non-varying with location or distance;

- The distribution variance is constant with location or distance (known as homoscedasticity).

Autocorrelation Function

An important property of random field characterisation is the Auto-Correlation Function (ACF), providing a measure of spatial correlation between properties, as a function of distance. When considering a two-dimensional isotropic random field, the ACF is often considered based on the absolute distance between points, rather than the orientation relative to each other. However, numerous autocorrelation functions exist for various scenarios [153, 154].

Spatial correlation can be considered by an ACF ρ, or an autocovariance c_k, measured at lag distance k. The autocovariance is defined as

$$c_k = Cov[X_i, X_{i+k}] = E[(X_i - \bar{X})(X_{i+k} - \bar{X})] \tag{2.36}$$

The autocorrelation coefficient ρ_k at lag distance k is defined as the ratio of c_k with respect to c_0, the autocovariance at lag distance 0. At a lag distance of $k = 0$, the autocovariance reduces to the variance Var[X]. As such ρ_k is defined by Equation 2.38.

$$\rho_k = \frac{c_k}{c_0} \tag{2.37}$$

$$\rho_k = \frac{Cov[X_i, X_{i+k}]}{Var[X]} = \frac{E[(X_i - \bar{X})(X_{i+k} - \bar{X})]}{Var[X]} \tag{2.38}$$

Two of the most common ACFs include the Markovian decaying exponential and the Gaussian squared exponential, as given by Equations 2.39 and 2.40, respectively.

$$\rho(k) = \exp\left(-\frac{2|k|}{k_0}\right) \tag{2.39}$$

$$\rho(k) = \exp\left(-\left[\frac{k}{k_0}\right]^2\right) \tag{2.40}$$

where, $\rho(k)$ is the autocorrelation function; k is the separation (lag) distance; and k_0 the "autocorrelation distance", defined as the distance where the ACF decays from 1 to $\frac{1}{e}$ [155]. In the case of both the Markovian decaying exponential, the SoF (θ) is equal to $2k_0$ and $\sqrt{\pi}k_0$, repsectively [152].

Spatial Averaging and Random Field Generation

Spatial variation is frequently considered for geotechnical investigation through spatial averaging (or local averaging) [1]. Frequently, geomechanical behaviour is considered to be controlled by average soil properties rather than the properties of point statistics at discrete positions. Hence, local averaging over a domain is often preferential to point-to-point statistics within a random field.

Spatial averaging often results in a reduction of variance, as soil parameters tend to cancel each-other out with an averaging process, suggesting that the variance of an average is often less than the variance of a set of discrete points. A variance function $\Gamma^2(T)$ as defined by Vanmarcke [1] measures the variance reduction at a point T, by local averaging, given by

$$\Gamma^2(T) = \frac{s_T^2}{s^2} \tag{2.41}$$

where, s_T^2 is the averaged soil parameter variance over the domain T; and s^2 is the point statistic variance. For large values of T, the variance function reduces to

$$\Gamma^2(T) = \frac{\theta}{s^2} \tag{2.42}$$

where, θ is the soil parameter scale of fluctuation. Hence, the SoF can be considered in the form detailed in Equation 2.43.

$$\theta = \Gamma^2(T)T \tag{2.43}$$

Vanmarcke [1] suggested that the variance function could be approximated with by Equation 2.44, whereby no reduction occurs when the averaging domain is less than or equation to the scale of fluctuation.

$$\Gamma^2(T) = \begin{cases} 1, T \leq \theta \\ \frac{\theta}{T}, T > \theta \end{cases} \tag{2.44}$$

Generation of random fields for shear strength parameters (i.e. cohesion c and friction angle ϕ) are frequently implemented with the Local Average Subdivision (LAS) method, as defined by Fenton and Vanmarcke [156], whereby local averages are generated based on spatial correlation functions. The LAS methodology described by Fenton [147], and Fenton and Vanmarcke [156] produces random fields by a recursive process where parent cells are subdivided into subsequent stages, satisfying the following four criteria:

1. Each subdivision must satisfy the correct variance defined by the initial random field statistics;

2. Each subdivision must be properly correlated with each other;

3. The subdivision variance is equal to the parent cell value;

4. Parent cells are properly correlated with the new cell subdivision.

When performing LAS in two dimensions, parent cells are divided into four equal sub-regions with each successive iteration.

Input parameters including the mean, standard deviation and the scale of fluctuation are initially defined at the point level, prior to LAS. Variance reduction is a function of both the domain size as well as the scale of fluctuation of the parameter of interest [157]. The variance reduction function for a Markovian exponentially decaying ACF is defined as

$$\Gamma^2(T) = 8\left(\frac{\theta}{T}\right)^2 \left(\frac{2T}{\theta} - 1 + \exp\left[-\frac{2T}{\theta}\right]\right) \tag{2.45}$$

Griffiths and Fenton [2] determined that the variance function for a square element in *x-y* space with side lengths of $\alpha\theta$ is equal to

$$\Gamma^2 = \frac{4}{\alpha\theta} \int_0^{\alpha\theta} \int_0^{\alpha\theta} \exp\left(-\frac{2}{\theta}\sqrt{x^2 + y^2}\right)(\alpha\theta - x)(\alpha\theta - y)dxdy \tag{2.46}$$

Small scales of fluctuation (i.e. $\alpha \to 0$) produce very little variance reduction factors (i.e. $\Gamma^2 \to 1$). Conversely, large scales of fluctuation produce significant variance reduction factors (i.e. $\Gamma^2 \to 0$). Hence, for elements of constant size, larger SoF values produce smaller reductions compared to smaller SoF values. Griffiths and Fenton [2] noted that Gaussian point distributions combined with LAS produced distributions of reduced variance without affecting the mean value, however, when considering lognormal distributions, both the mean and variance of the underlying Gaussian distribution were affected. When considering the impact of local averaging on Equations 2.27 and 2.28, lognormal sample mean and standard deviation parameters can be rewritten as:

$$\hat{\mu}_X = \exp\left(\mu_{\ln(X)} + \frac{1}{2}\Gamma^2 s_{\ln(X)}^2\right) \tag{2.47}$$

$$\hat{s}_X = \hat{\mu}_X \sqrt{\exp(\Gamma^2 s_{\ln(X)}^2) - 1} \tag{2.48}$$

Hence, $\hat{\mu}_X \to \exp\left(\mu_{\ln(X)}\right)$ and $\hat{s}_X \to 0$ as $\Gamma^2 \to 0$.

2.5.6   Random Finite Element Method

The Random Finite Element Method (RFEM) couples Random Field Theory and the Finite Element Method by mapping random fields to a Finite Element structure. Griffiths and Fenton [158] initially proposed the approach to consider a spatially variable approach to Monte Carlo FEM simulation. Apart from slope stability, RFEM has been applied to a range of geotechnical problems including bearing capacity of shallow foundations [159, 160], settlement of shallow foundations [161-163], retaining walls [164], and tunnelling [165, 166].

Using RFEM slope stability analysis, Griffiths et al. [167] reported that 2000 Monte Carlo simulations were sufficient to achieve convergence in Factor of Safety distribution for an scenario involving a 2-1 clay slope, with the number of simulations required dependent on the convergence of both the Factor of Safety and Probability of Failure. Zhu et al. [168] investigated worst-case spatial correlation lengths and their impact on slope stability, concluding that worst-case correlation lengths produced the highest observed Probability of Failure. In several papers, Hicks et al. considered the impacts of RFEM slope stability in a three-dimensional environment [169-171], noting that two-dimensional RFEM does not always produce conservative safety factors compared to three-dimensional analysis. Griffiths and Marquez [36] proposed that the most pessimistic 2D cross-section of a 3D model produces a considerably lower Factor of Safety compared to 3D simulation, as the slopes derive no support from the adjacent soil in the third dimension.

Critical slip surfaces observed through RFEM analysis can be wide ranging in shape and location, and often display considerably different failure mechanisms compared to deterministic analysis [126]. Huang et al. used RFEM to consider reliability analysis for slope, extending the analysis to include a risk assessment. Zhu et al. [172] investigated undrained clay slopes with RFEM for a wide range of slope angles, noting that for steep slopes, greater variability in the undrained shear strength displayed a significant range of slope failure mechanisms. Furthermore, a significant

number of deeper slip surfaces were observed when weaker soils were found in the slope foundation layers. In the case of RFEM, zones containing weakened shear strength parameters allow slopes to fail at lower Factors of Safety, as noted by Griffiths and Fenton [2]. Yang et al. [173] presented results of random fields conditioned on specific deterministic site data, stressing the need for numerical results to incorporate site-specific material data, as further noted by Chiles and Defliner [174]. Although many potential slip surfaces can be observed through RFEM analysis, failure probabilities are often governed by a much smaller subset of critical slip surfaces known as representative slip surfaces (RSS) [175].

Despite the advantages of RFEM for slope stability analysis, considerable computational requirements are necessary to attain distribution convergence [176]. Furthermore, Shen and Abbas [177] noted that often there is insufficient input data from laboratory and in situ field tests to adequately implement RFEM for slope stability.

2.6 Random Finite Element Method Efficiency and Optimisation

The Random Finite Element Method comes at a significant computational cost compared to deterministic Finite Element Method simulation. For this reason, a range of RFEM prediction and optimisation methods have been developed to improve computational efficiency. Recently, Artificial Neural Networks (ANN) have been coupled withn RFEM analysis for a range of geotechnical applications including slope stability and bearing capacity problems [178-180]. For RFEM slope stability analysis, Artificial Neural Networks implement a computational method based on training algorithms. As an output, networks estimate slope Factors of Safety as a function approximation model. ANNs can significantly reduce the number of random field instances required for simulation. Sakellariou and Ferentinou [178] used training sets consisting of 46 random fields, allowing Factor of Safety distributions to reach convergence without full Finite Element Method simulation.

Another popular method for improving the computational efficiency of RFEM analysis is the Subset Simulation Method (SSM), which can be used to evaluate slope reliability while also identifying key contributions of slope failure to be quantified [181]. Using generalised Subset Simulation (GSS), common failure events known as Representative Failure Events (RFEs) can be identified along with their probabilities of failure and the reliability index. Compared with traditional Monte Carlo Simulation using RFEM, the approach significantly improves computational efficiency in cases where failure events exhibit small probabilities. As such, RFEM simulations fall into two distinct categories: (1) methods targeting the reduction of the required number of Monte Carlo Simulation instances [182] and Subset Simulation [128, 183, 184].

Another recent optimisation method that is gaining popularity is the Response Surface Method (SRM). Based on reliability analysis, the method describes performance functions for possible failure modes, reducing the number of necessary RFEM simulation instances [176].

Although the aforementioned methods can increase the computational efficiency of RFEM simulation, significant effort is required to couple these methods with Finite Element Method slope stability analysis. In many cases, the performance of each method is highly dependent on the slope geometry, geology and material behaviour. More recently, methods such as "the parallel squeezing method" have focused on simplified techniques which are seamlessly integrated into Finite Element Method and Finite Difference Method packages [185].

2.7   Summary

The relevant literature contained within this chapter indicates that soil variability and uncertainty are infrequently considered for typical slope stability analyses compared to conventional Limit Equilibrium Methods, despite, the effects of soil variability on slope stability being well recognised.

Due to the complicated nature of implementing spatial variability in the Finite Element Method framework, the requirement of additional statistical parameters and data, and the excessive

computational cost of analysis, spatial variability with Finite Element Methods have yet to become common practice or incorporated in major commercial software packages. Fig. 2.6 presents a schematic overview of the aforementioned deterministic and probabilistic slope stability analysis methods.

When considering spatially variable shear strength parameters coupled with Finite Element Methods, the Random Finite Element Method, allows failure mechanisms to occur naturally, rather than prior to simulation, as with LEM. With the increase in computational power, RFEM is emerging as a powerful tool capable of incorporating spatially variable shear strength properties for probabilistic Finite Element Method slope stability analysis. The method provides a mechanism for investigating the impacts of spatially heterogeneous soils on slope geomechanics, and is discussed in the forthcoming chapters.

The literature within this section is provided to highlight the gaps in knowledge necessary to perform spatially variable slope stability analysis. A summary of each literature subsection and the importance in the context of the thesis is provided below:

- Section 2.2 describes Limit Equilibrium Methods and empirical design charts which remain common within industry, however, these methods are incapable of simulating the stress-strain behaviour of materials which are required for complex constitutive models. Additionally, the critical failure surface in LEM is specificed prior to simulation. Models including spatially variable shear strength parameters are often too complex to readily determine the appropriate failure mechanism, prior to failure. For this reason, spatially variable Limit Equilibrium Methods pose several disadvantages for large scale spatially variable slope stability analysis.

- Section 2.3 describes a range of slope stability failure characteristics common to open-pit mine failure events. In particular, circular and wedge failure methods are considered as primary failure modes for the mines of the Latrobe Valley.

- Section 2.4 describes several alternative methods for slope stability analysis. Currently these methods are seldom combined with spatially variable slope stability analysis and are

also require significant computational requirements, frequently including High Performance Computing facilities.

- Section 2.5 describes the a range of probabilistic methods of analysis, including the Random Finite Element Method. The method combines Monta Carlo simulation, random fields and the Finite Element Method. Although the method often requires numerous simulation instances to be computed, it is one of the most widely applicable methods.

- Section 2.6 describes currently implemented optimisation and computational efficiency methods for Random Finite Element Method slope stability analysis. Although a number of these methods provide techniques capable of reducing the number of simulation instances required to achieve Factor of Safety convergence, the methods are often extremely complex and are not regularly implemented within commercially available Finite Element Method packages.
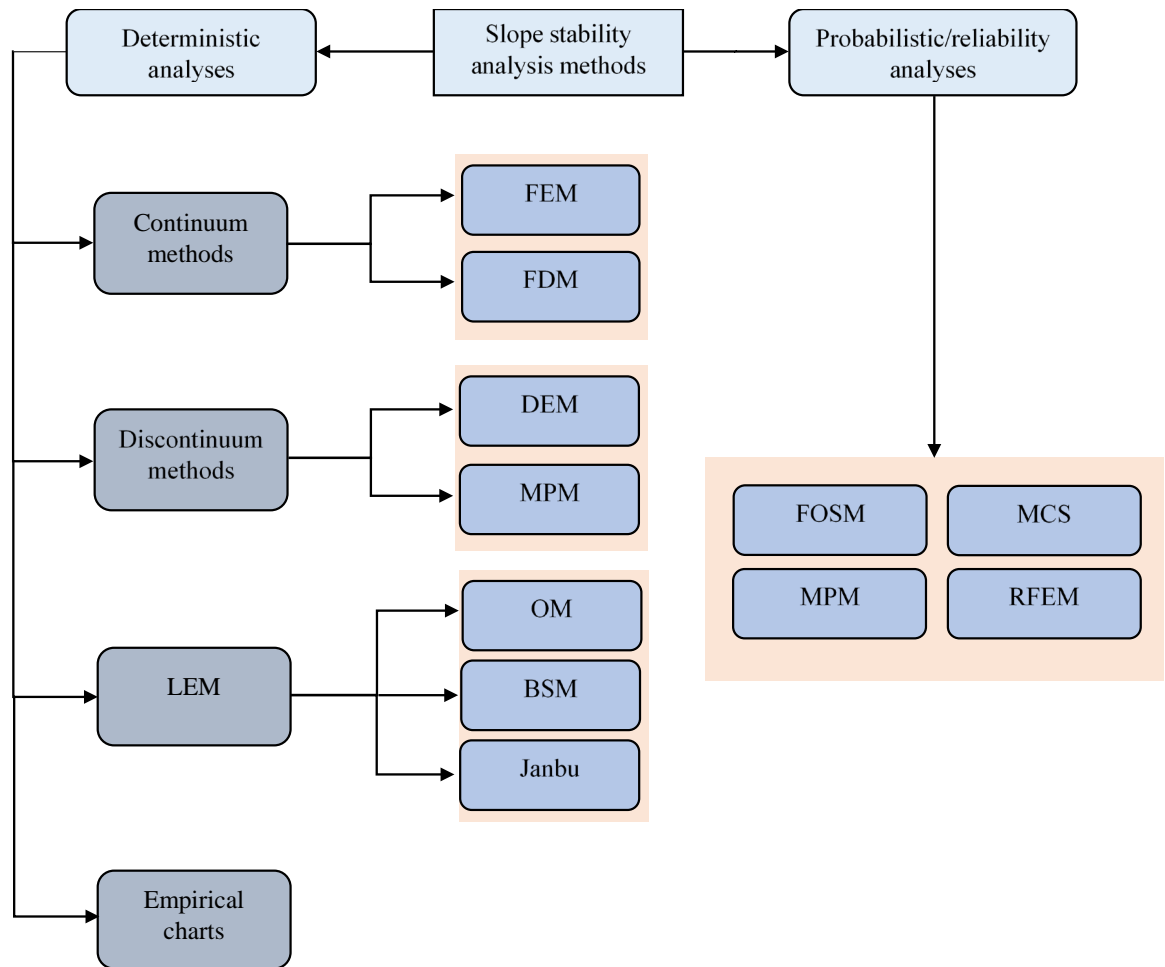
Fig. 2.6. Considered approaches to slope stability analysis

3   Yallourn Open-Pit Brown Coal Mine

3.1   Introduction

The techniques proposed in this thesis are presented in partnership with an overview of an operational open-pit brown coal mine located in Victoria, Australia. A review of the mining within the region, coupled with a set of geotechnical parameters obtained from the site is presented to provide the necessary background knowledge for the slope stability analyses in the following chapters.

3.2   Latrobe Valley

The Latrobe Valley Depression (LVD) is an extension of the Gippsland Sedimentary Basin (GSB) in the state of Victoria, Australia, covering an area of approximately 800km^2 [186]. The Gippsland basin contains some of the thickest continuous brown coal seams in the world [187], encompassing an estimated 65 billion tonnes of brown coal. Greater than 80 percent of Victoria's brown coal resources are located within the Latrobe Valley, approximately 150 km east of the state capital Melbourne (Fig. 3.1). Three large lignite mines in the region (Yallourn, Hazelwood and Loy Yang) supply the power stations responsible for the majority of Victoria's electricity production (Fig. 3.2). The coal seam thickness is typically greater than 50 metres at each of the mine site locations.

The Victorian Brown Coal (VBC) of the Latrobe Valley was deposited during the Eocene and late Miocene periods, and consists of three primary coal stratigraphic units – the Traralgon, Morwell and Yallourn formations, in ascending order, known as the Latrobe Valley group (Fig. 3.3). These seams accumulated in locations predominantly south of the present-day Latrobe River and west of a marine interface with the Gippsland Limestone [187]. The structures of the LVD have been described in detail by Thomas and Baragwanath [188], Gloe [186, 189] and Barton et al. [187]. The interseam materials between coal layers are low strength and highly variable in thickness, containing both clayey and silty deposits. Overburden thicknesses at the mine sites are typically less than 20 metres.
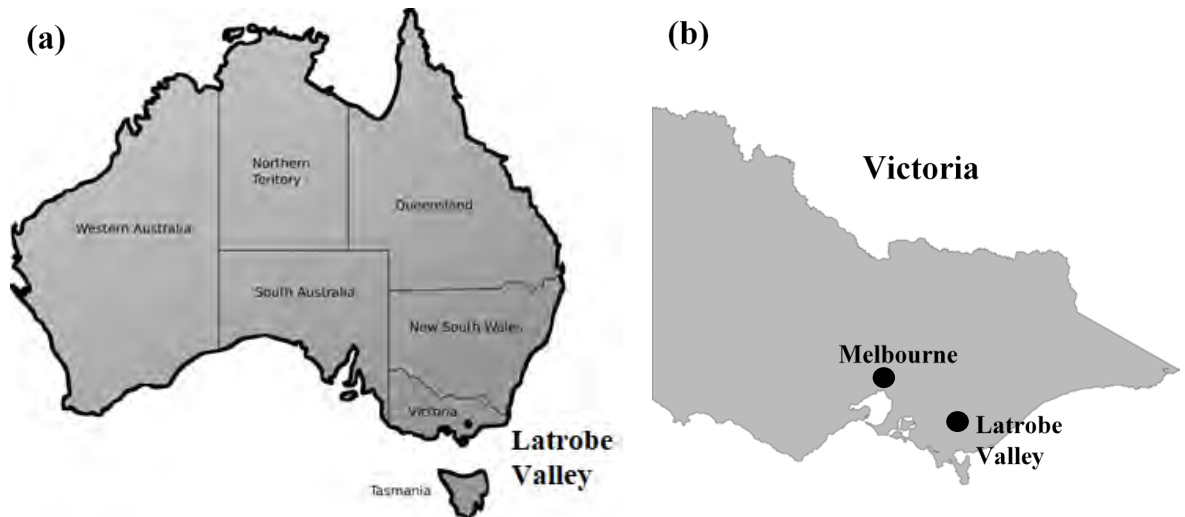
Fig. 3.1. Latrobe Valley location (a) map of Australia (b) map of Victoria
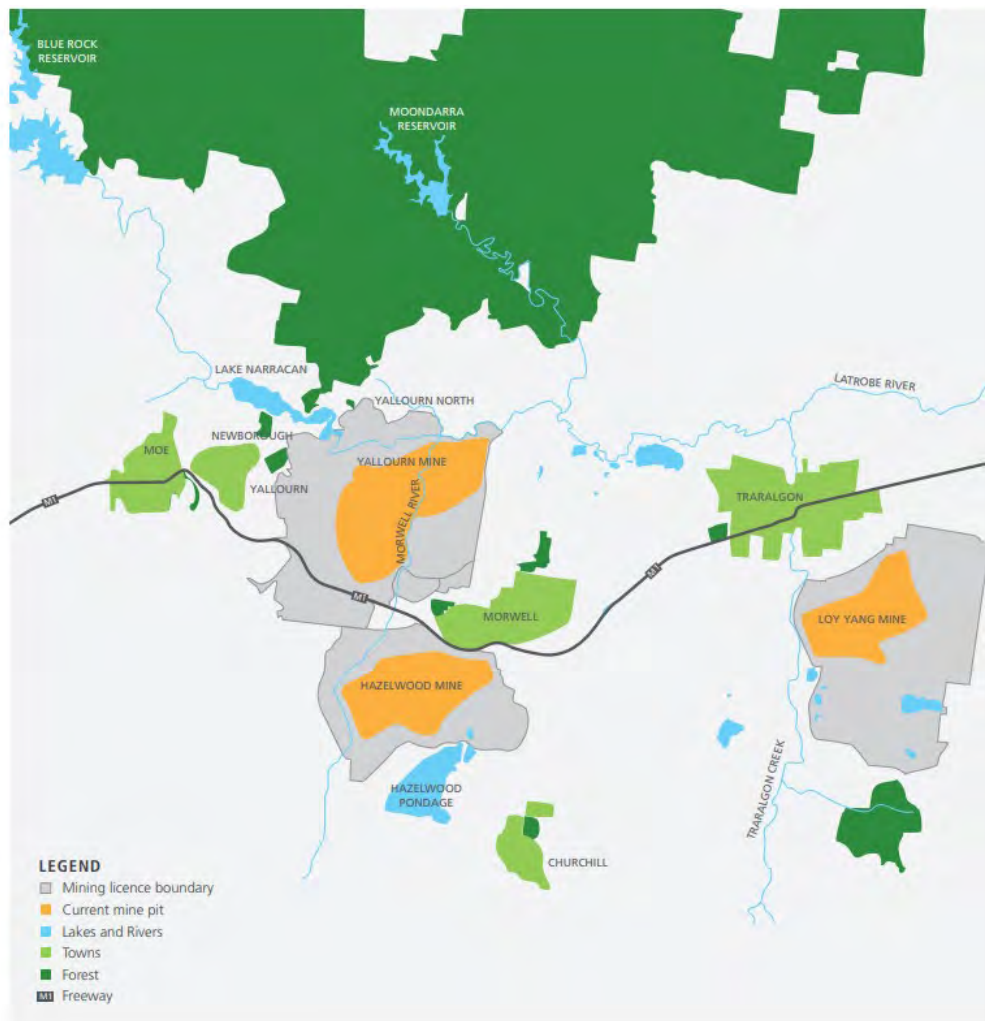
Fig. 3.2. Latrobe Valley open-cut mine regional map [190]
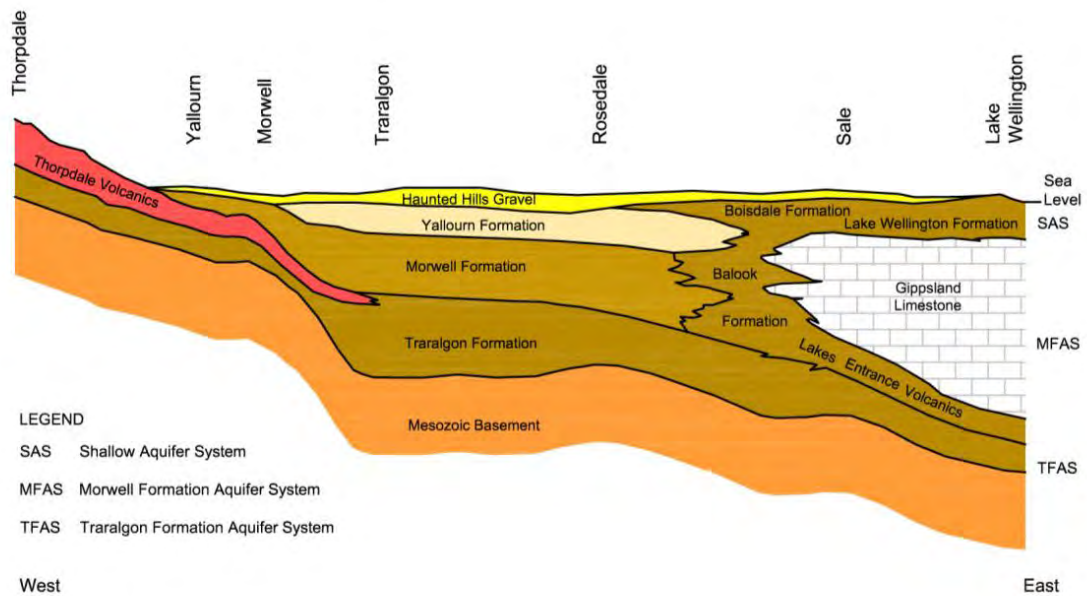
Fig. 3.3 Latrobe Valley stratigraphy [191]

Victorian Brown Coal is a soft, low-rank coal and can be considered as Lignite B, as classified by the American Society for Testing and Materials [192]. VBC is relatively light with a specific gravity around 1.1 gr/cm [193] and a water content above 60% by volume [194]. The permeability of VBC was observed by Tolooiyan et al. through in-situ Lugeon testing to be 7.6e-3 m/day [195]. Rosengren noted permeability values as low as 6.64e-4 m/day (4.22e-9 m/sec), declaring that fractures have a significant influence on permeability, such that field measurement may be the only reliable testing regime for estimating VBC permeabilities [196]. Victorian Brown Coal is mainly organic, with very little mineral content (typically less than 2% by weight [197]). The material can be highly variable both laterally and vertically within the formations, with increasing sizes of woody material within the upper sections of the formations. Odometer test results [198] indicate consolidation responses similar to undisturbed clays with well-defined pre-consolidation stresses and low elasticity. Trollope et al. [198] conducted both drained and undrained triaxial tests on brown coal, noting that failure was brittle in nature with definite observable shear surfaces. Woody

fragments within the coal affected the tensile strength of the material, but did not affect the compressive strength.

Brown coal production dates back to the 1800s when disruptions to Melbourne's black coal supplies prompted mining of Latrobe Valley coal. The State Electricity Commission of Victoria (SECV), was formed in 1919 with initial power generation commencing in 1924 [199]. Commencing in the 1950s, the SECV conducted a comprehensive exploration drilling program, consisting of approximately 15,000 boreholes, with a wide range of geotechnical parameters identified from both laboratory and in-situ tests on material samples. During the 1990s, the Victorian electricity industry and open-pit brown coal mines were privatised. Prior to privatisation, numerous SECV slope stability analyses of Latrobe Valley mine structures were conducted [200-203]. However, recent research has diminished, with current assumptions often made based on research prior to SECV privatisation. Although many of these findings continue to be relevant in the current day mining landscape, significant gaps remain in the knowledge of Latrobe Valley slope stability.

Recently, Latrobe Valley mine stability issues have occurred with increasing frequency, often with significant impacts on coal production, environment infrastructure and the local community. Since 2007, three major failures have occurred:

- **Yallourn East Field North East Batter Failure** (November 2007)

  The major collapse of a Yallourn batter, adjacent to the Latrobe River resulted in uncontrolled river flow into the Yallourn mine, causing significant damage and impacting coal production operations (Fig. 3.4). The event forced the Yallourn power station to operate at a decreased capacity, incurring significant costs and remediation measures ($160 million AUD).

- **Hazelwood Northern Batter Movement** (February 2011)

  Following significant rainfall, a sinkhole developed in the Morwell Main Drain, with cracking observed on the adjacent Princes Highway as well as ground surrounding the

Morwell township. The event caused the closure of the Princes Highway for eight months, requiring stabilisation of Hazelwood mine batters and surrounding infrastructure.

- **Morwell River Diversion Failure** (June 2012)

  The collapse of a Yallourn embankment conveyor tunnel resulted in the uncontrolled release of water from the Morwell River Diversion (MRD) into the surrounding Yallourn mine (Fig. 3.5), damaging mine infrastructure at a cost of approximately $100 million AUD.

Additionally, a major fire in Hazelwood mine (2014) heightened community and industry concern regarding the safety of mining operations in the region, as well as the potential impacts on the surrounding community.

Fig. 3.4. Yallourn batter collapse (2007) [204]

Fig. 3.5. Morwell River Diversion Failure (2012) [205]

f3.3   Yallourn Open-Pit Mine

The Yallourn open-pit mine North-East batter (Fig. 3.6) consists of several stratigraphic layers including overburden, coal and interseam materials (Fig. 3.7). Yallourn brown coal properties, as detailed by Perera et al. [206] are presented in Table 3.1. A 10 – 48 metre overburden layer covers the 40 – 88 metre thick Yallourn seam. Beneath the Yallourn seam, exists an 80 – 100 metre thick non-coal interseam layer consisting of clayey and silty materials, as well as localised minor coal splits much weaker in strength [207]. Below the interseam lies the Morwell seam, which is over 100 metres thick in some locations [208]. Due to the difference in strengths of the coal and interseam materials, block-sliding along the low frictional interseam is a likely failure mechanism [209].

0m   500m   1000m   1500m   2000m

Fig. 3.6. Yallourn mine North-East batter (2015)
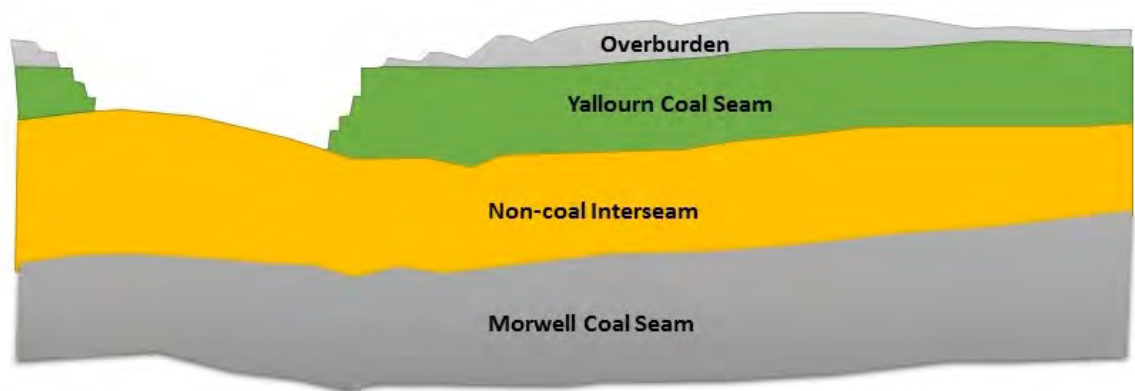
Fig. 3.7.   Yallourn open-pit mine stratigraphy [208]

Table 3.1. Yallourn brown coal properties [206]

Property	Value
Rank	ASTM lignite B
Moisture content (% wb)	58.0
Ash yield (% db)	1.7
Volatile matter content (% bd)	50.3
Fixed carbon (% db)	48.0
Sulphur content (% db)	0.28
Gross dry specific energy (MJ/kg)	26.1
Net wet specific energy (MJ/kg)	6.9

The geotechnical shear strength parameters used for the research in this thesis were attained from SECV databases and laboratory tests from Federation University Australia's Geotechnical and Hydrogeological Engineering Research Group (GHERG). Fig. 3.8 shows the locations of borehole data from Yallourn's North-East batter. Although numerous bores have been drilled for logging variations in lithology, a somewhat smaller set of material samples were collected from these bores for geotechnical testing.   Geotechnical parameters attained from material testing of the aformentioned boreholes is provided in Table 3.2, with shear strength parameters given in Table 3.3. The permeability of lignite and interseam materials was determined through in-situ Lugeon tests performed on-site, coupled with laboratory permeameter tests, as described by Tolooiyan et al. [210]. Previous SECV investigations have recorded Yallourn seam coal permeability values ranging from 7×10^{-7} m/s to 3.8×10^{-6} m/s with constant head permeability testing methods, and laboratory test permeabilities of 8.2×10^{-9} m/s [191]. Coal permeabilities observed with Lugeon tests were considerably higher in magnitude compared with laboratory permeabilities due to the presence of large-scale discontinuities commonly found within the mine. For this reason, in-situ permeabilities are preferred as modelling parameters for this study, as they are representative of the large-scale field conditions. A summary of VBC permeabilities can be found in "Investigation of an Australian soft rock permeability variation" in the appendix.

Shear strength parameters were derived from GHERG and SECV laboratory experiments using triaxial and Consolidated Undrained (CU), Unconsolidated Undrained (UU) tests. A total of 1236 laboratory tests were performed (predominantly due to a large number of tests performed by the SECV prior to dissolution) and used to calibrate the spatially variable parameters of this research.

As such, the number of tests performed per layer on material numbered in the hundreds for each layer. Laboratory tests used for model calibration were limited to the full region shown in Figure 3.8, with tests performed from the overburden on the surface to a maximum depth of 240 metres below the mine crest. GHERG laboratory test results and procedures are detailed by Karami and Tolooiyan [211]. Shear strength correlation lengths (Table 3.4) and correlations with respect to sample depth (Table 3.5) provide the necessary data for generation of the random fields necessary for the following research. Correlation lengths given in Table 3.4 were determined by fitting shear strength parameter data to a three-dimensional exponentially decaying Markovian function

$$\rho\left(\tau_x, \tau_y, \tau_z\right) = \exp\left(-\frac{2|\tau_x|}{\theta_x} - \frac{2|\tau_y|}{\theta_y}\right) \tag{3.1}$$

where, $\rho\left(\tau_x, \tau_y\right)$ is the correlation coefficient between random field values at lag distances τ_x and τ_y, in *x* and *y* directions, respectively. Similarly, θ_x and θ_y are defined as the scales of fluctuation in the *x* and *y*, respectively. The *x* and *y* directions correspond to the North/East and depth directions within the Yallourn mine, respectively.

It should be noted that the "across-the-bore" scale of fluctuation is particularly smooth, indicating a high correlation in samples for lateral lag distances up to several hundred metres. This is likely attributed to the depositional nature of materials within the mine. Laboratory tests performed on samples from a range of bores conducted at similar depths were analysed to confirm the correlation lengths of each shear strength parameter. Additional details of parameter distributions, including distribution graphs can be found in Chapter 6.
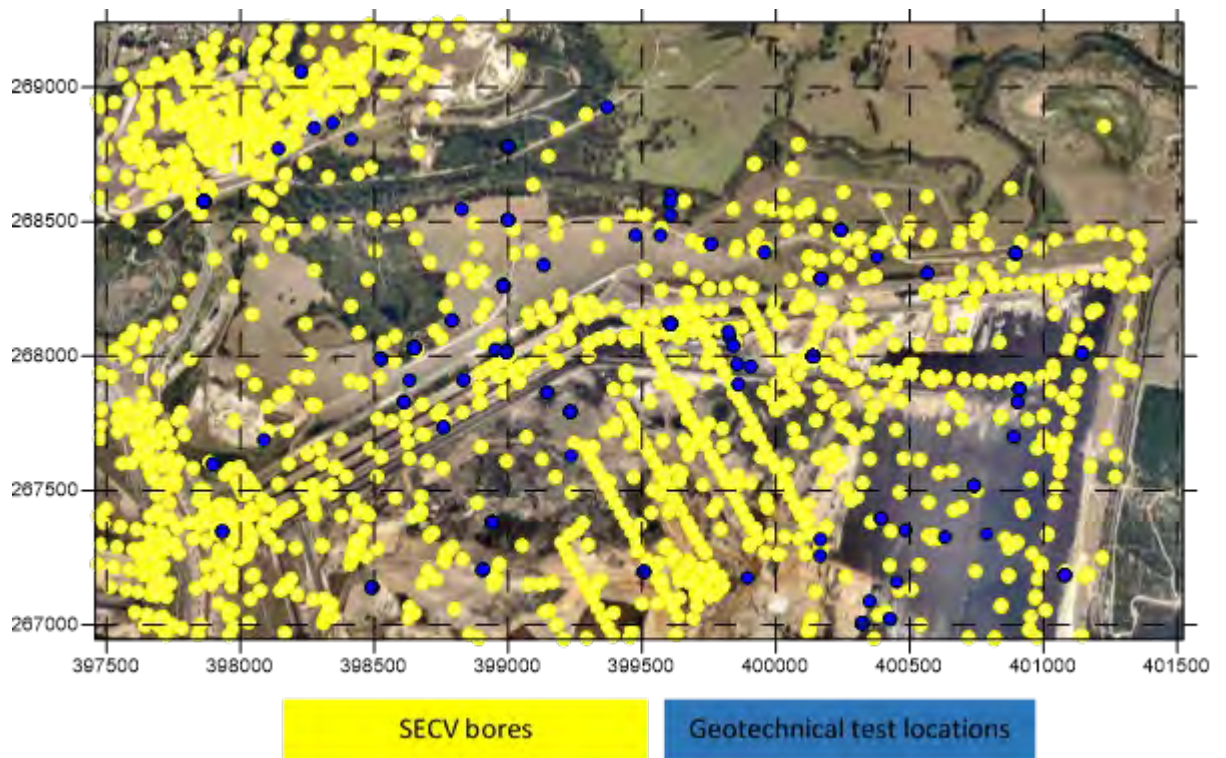
Fig. 3.8. Location of drilled bores and geotechnical test samples

Table 3.2. Geotechnical parameters for coal and non-coal materials

Material	Unsaturated unit weight γ_{unsat} (kN/m³)	Saturated unit weight γ_{sat} (kN/m³)	Elastic modulus E (MPa)	Poisson's ratio ν	Permeability k (m/day)
Coal	11.4	11.5	40	0.3	7.6e-3
Non-coal	20.15	20.2	52	0.3	4.7e-2

Table 3.3. Shear strength parameter statistics

Parameter	Coal		Non-coal	
	Cohesion c (kPa)	Friction angle ϕ (°)	Cohesion c (kPa)	Friction angle ϕ (°)
Mean (μ)	150.72	27.28	31.81	23.67
Standard Deviation (s)	69.78	4.91	5.00	4.51
COV	0.46	0.18	0.16	0.19

Table 3.4. Shear strength length scales

Scale of Fluctuation (m)	Coal		Non-coal	
	c	ϕ	c	ϕ
θ_x	320.3	772.4	812	627.8
θ_y	23.1	8.7	35	13.1

Table 3.5. Shear strength correlations with depth

	Coal		Non-coal	
	c	ϕ	c	ϕ
Correlation	0.129	-0.260	-0.027	-0.060
$r_{c,\phi}$	0.046		-0.003	

3.4   Summary

The information presented in this chapter provides a brief outline of the history of Latrobe Valley brown coal open-pit mining, in particular the Yallourn mine. Due to recent failure events, the analysis of mine slope stability in the region is deemed to be of particular importance to the region and the state of Victoria. Geotechnical parameters are presented from prior SECV and GHERG research. These parameters are implemented throughout this thesis and are largely based on extensive SECV data collection. As such, their validity is assumed, with further inquiry into their authenticity deemed beyond the scope of this research. Further information for all following slope stability analyses is provided specific to the associated chapters.

4 Optimisation of Strength Reduction Finite Element Method Codes for Slope Stability Analysis

The following journal paper introduces an optimised strength reduction method for slope stability analysis using the Finite Element software package Abaqus. The method defined in this chapter is used throughout the remainder of the research detailed in the thesis to conduct probabilistic numerical slope stability analysis. This journal paper is an accurate representation of the published version, with minor alterations to table and figure numbers for the purposes of continuity.

Abstract

One of the modern methods for estimating the Factor of Safety for the stability of slopes is the Strength Reduction Method. In recent times, computer codes have utilised the Strength Reduction Method in conjunction with Finite Element Analysis. This paper explores the implementation of a Strength Reduction Finite Element Method with FORTRAN and Python codes in conjunction with the computer aided engineering package Abaqus, incorporating a modified strength reduction definition, allowing for a refinement of the Factor of Safety search space. The computational efficiency of the modified method is compared with the traditional technique, for both 2D and 3D analysis. The algorithm results are compared for contrasting FEM element types and geometries, and benchmarked against proprietary geotechnical finite element solvers.

Keywords

Strength reduction method; Finite element method; Slope stability; Factor of safety; Abaqus FEM

4.1   Introduction and Background

Computational slope stability methods in geotechnical engineering have received considerable attention in recent times with the particular aim of prevention of serious subsidence events in embankments, mine batters and wide-ranging geostructures. Fundamental to the assessment of slope stability by Finite Element Methods (FEM) is the Strength Reduction Finite Element Method (SRFEM), sometimes referred to as SRFEA [78]. The SRFEM approach calculates a Factor of Safety (FoS) by defining the ratio of current soil strength to the minimum shear strength necessary to avert structural failure [212]. Alternatively, when considering the Mohr Coulomb failure criteria, the Factor of Safety can be considered as the minimum factor the soil strength must be reduced by to produce imminent failure [75].

Developments in computational capability have permitted the implementation of Strength Reduction for desktop computing with both Finite Element and Finite Difference algorithms. Since the initial development by [35], SRFEM has been extensively applied to slope stability by [32, 79, 213-216] and others, as well as in diverse fields such as anti-slide piling [80, 217]. The technique is often preferred to Limit Equilibrium Methods (LEM), as a result of several advantages [218, 219]. SRFEM does not require critical failure mechanisms or slip surfaces to be specified prior to simulation, and furthermore, no assumptions of inter-slice forces are required [77]. SRFEM can also be implemented to simulate the failure of soils with heterogeneous material strength properties. [37, 74].

Although a definition for determining the Factor of Safety exists, techniques for optimising the safety reduction procedure are less clear. EM Dawson, WH Roth and A Drescher [74] proposed a method of FoS calculation by successive bracketing and bisection, while Haibin Xue, Faning Dang, Xiaotao Yin, Weihua Ding and Chao Yang [220] integrated non-proportional internal friction angle and cohesion relationships for safety factor reduction. Hong Zheng, Guanhua Sun and Defu Liu [221] determined practical procedures for assessing critical slip surfaces using SRFEM.

The research detailed in this paper proposes SRFEM search strategies to minimise Factor of Safety calculation times. The methods are investigated with the computer-aided engineering package Abaqus 2017, (which does not implement predefined Strength Reduction Method codes) for the purpose of calculating slope safety factors and failure patterns with high computational efficiency. Algorithms are designed to be utilised with the Mohr-Coulomb failure criterion, while also allowing users to specify individual parts of the model to be subjected to strength reduction analysis rather than the whole model.

4.2   Objectives

As no predefined Strength Reduction Method exists within the Finite Element software Abaqus, this research implements in-house Python and FORTRAN codes in conjunction with Abaqus for the Strength Reduction of FEM slope stability simulations. The codes are developed to be used in cases with complex Finite Element geometries incorporating multiple soil layers and heterogeneous strength parameters. This paper explores techniques to further optimise the Strength Reduction Method for slopes with low friction angles which are often necessary for simulating large geometries with fine meshes. The results of these computer codes are examined for both 2D and 3D cases for a range of element types and geometries and validated against the inbuilt Strength Reduction Method of the geotechnical Finite Element package Plaxis [222].

4.3   Strength Reduction Finite Element Methodology

Final safety factors for slope stability with the Strength Reduction Finite Element Method can be interpreted in a number of different ways, depending on the definition of slope failure. In this research, three criteria are used as the primary mechanism for determining slope failure and the corresponding FoS:

1. Development of plastic zones from the toe to head of the slope [30].

2. Large deformation, often described by user-defined levels of tolerable nodal displacement, dependent on the specific problem being analysed.

3. Solution non-convergence, often symptomatic of failure in FEM slope subsidence simulations [35].

SRFEM is a valid technique for a range of material models including the Mohr-Coulomb yield criterion, and Drucker-Prager. Shear strength τ for the Mohr-Coulomb model is given by

$$\tau = c + \sigma_n \tan \phi \qquad (4.1)$$

with parameters cohesion (c) and friction angle (ϕ); and normal stress σ_n. For this reason, SRFEM is sometimes known as the phi-c reduction method. The Strength Reduction procedure is defined as follows (Equation 4.2 - 4.3):

$$c = \frac{c_0}{SRF} \qquad (4.2)$$

$$\phi = tan^{-1} \frac{\tan \phi_0}{SRF} \qquad (4.3)$$

where, c_0 and ϕ_0 are the original cohesion and friction angle parameters, respectively, and SRF is the trial Strength Reduction Factor leading to the final Factor of Safety (Equation 4.4).

$$FoS = \frac{c_0}{c_f} = \frac{\tan \phi_0}{\tan \phi_f} \qquad (4.4)$$

where, c_f and ϕ_f are the cohesion and friction angle at failure, respectively.

To calculate the FoS, a trial of Strength Reduction Factors is required, commencing with modest initial SRF values for the initial failure envelope based on c_0 and ϕ_0 (Fig. 4.1) that will not cause slope failure. The SRF is then iteratively increased at a constant user defined rate, thereby reducing cohesion and friction angle parameters until the failure envelope intercepts the final failure envelope which is defined by c_f and ϕ_f. When this happens, the final Factor of Safety is determined by the corresponding Strength Reduction Factor. The SRFEM presented in this paper considers materials with no dilatancy.
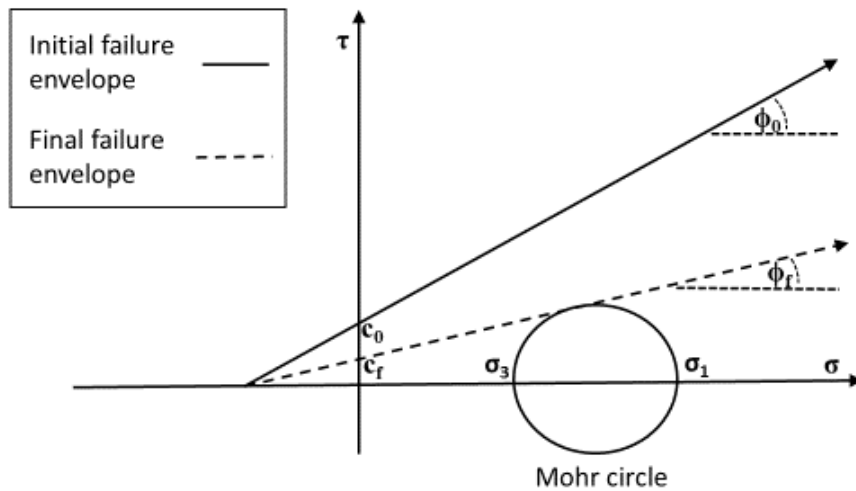
Fig. 4.1. Mohr-Coulomb failure envelope

SRFEM Code Procedure and Implementation

The finite element code of Abaqus 2017 [223] does not implement an inbuilt Strength Reduction Finite Element Method. To produce SRFEM models with Abaqus, in-house Python codes were designed to execute a set of Abaqus models sequentially, decrementing the SRF by a user-defined value until slope failure. The process detailed is in Fig. 4.2, where the Abaqus model is initially described by an Abaqus input file (a FORTRAN script that contains the model's geometry, initial material state parameters, loading stages, output settings, etc). Abaqus input files can be executed without the need for the Abaqus graphical user interface. Therefore the input files are well suited for repetitive procedural scripted code. Once the initial Abaqus simulation has completed execution, text files containing the maximum observed nodal slope deformation and solver increment information are generated for each Strength Reduction Factor stage. The Strength Reduction general failure criteria (1) - (3) are evaluated as termination conditions for each reduction step. Once the failure state is achieved the process stops and the Factor of Safety is established.
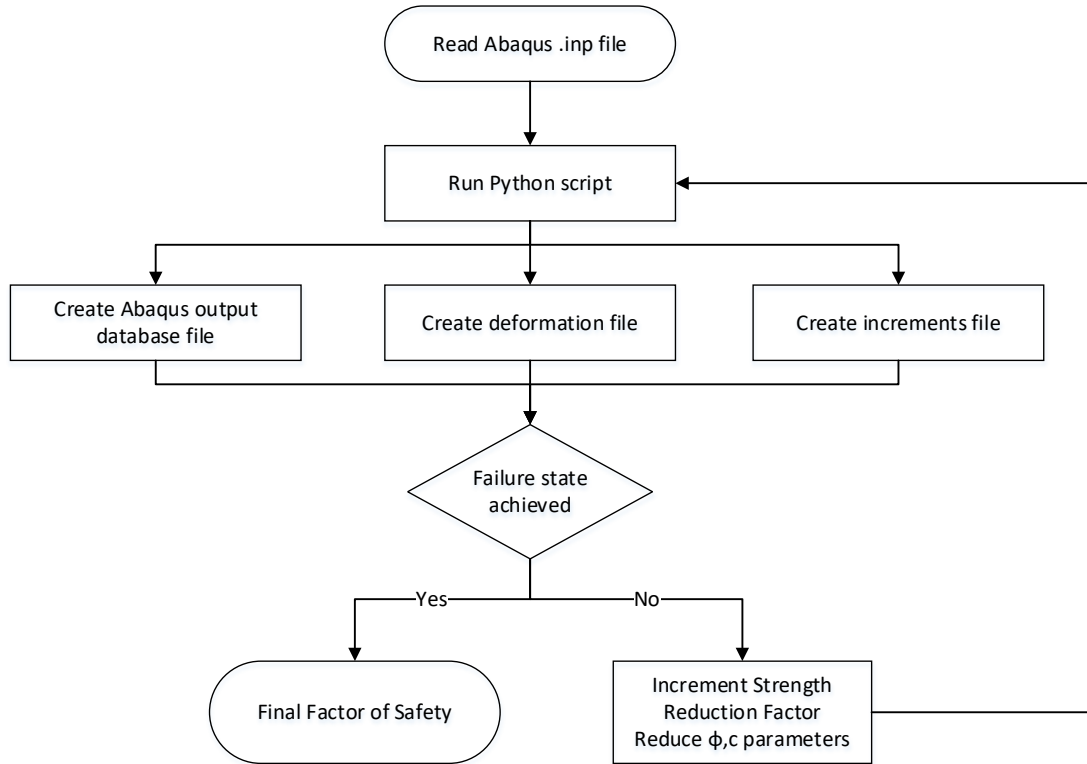
Fig. 4.2. SRFEM code flowchart

Alternative Definition of the SRFEM

The usual process of applying the SRFEM is to linearly increase in the Strength Reduction Factor

of (Equations. 4.2 and 4.3) until failure is reached.   As the reduction process commences, the

cohesion *c* decays at a greater rate of change than the friction angle ϕ. Fig. 4.3 shows the ϕ and *c*

gradients of a linear Strength Reduction Factor, with an initial cohesion of 20kPa and a friction

angle of 20 degrees. Both *c* and ϕ decrease at a rate of SRF^{-2} as shown in Equations. 4.5 and 4.6.

However, it is evident that *c* decays at a greater rate.

$$\frac{dc}{dSRF} = -\frac{c_0}{SRF^2} \tag{4.5}$$

$$\frac{d\phi}{dSRF} = -\frac{\phi_0}{\phi_0{}^2 + SRF^2} \tag{4.6}$$

When considering slope stability models with small friction angles such as soft clays, the traditional technique can be improved by introducing a reduction method where the initial ϕ gradient is steeper than c, reducing the number of Strength Reduction steps to achieve a Factor of Safety. Hence a modified Strength Reduction Finite Element Method, named MSRFEM is suggested for cases involving small friction angles (less than 30 degrees) (Equations. 4.7 and 4.8). In the MSRFEM, the rate of change of ϕ and c are equal to the rates of change of the SRFEM c and ϕ, respectively.

$$\phi = \frac{\phi_0}{SRF} \tag{4.7}$$

$$c = tan\left(tan^{-1}\frac{c_0}{SRF}\right) \tag{4.8}$$

As the Arctangent function is defined only on the domain $(-\frac{\pi}{2}, \frac{\pi}{2})$, Equation 4.6 is redefined by the tangential function of Equation 4.9. Thus the SRFEM Factor of Safety can be defined by Equation 4.10.

$$c = \frac{c_0}{tan\,\phi_0}tan\frac{\phi_0}{SRF} \tag{4.9}$$

$$FoS = \frac{tan\,\phi_0}{tan\,\phi_f} \tag{4.10}$$

Comparison of SRFEM and MSRFEM in Fig. 4.4 shows the number of reduction steps required to arrive at a friction angle of 14°, from a starting value of 20°. In this particular case, the MSRFEM has a 6% decrease in the number of reduction steps compared to the traditional SRFEM, a substantial increase when considering large simulations with fine mesh distributions.
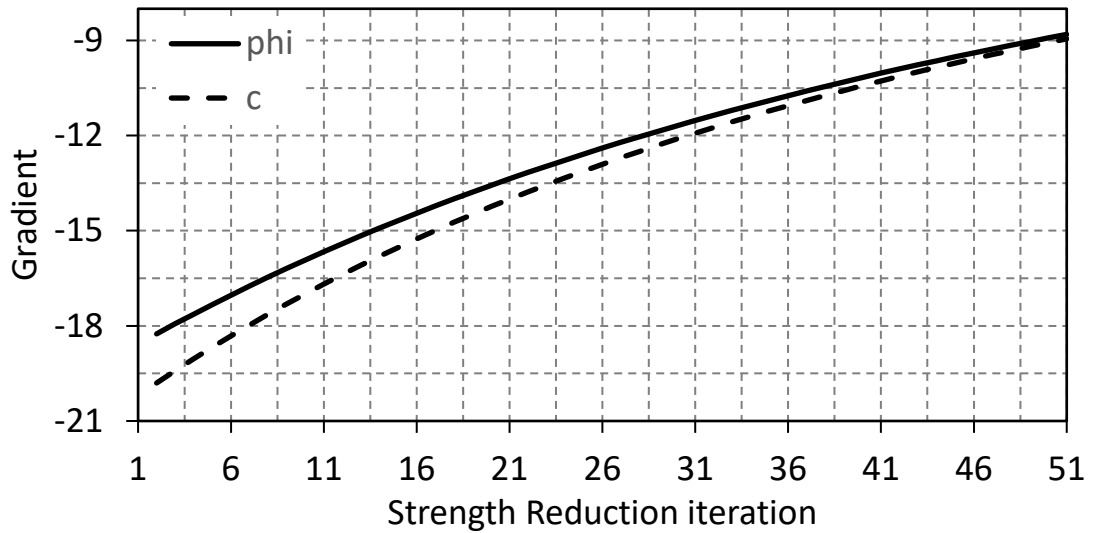
Fig. 4.3. Friction angle (phi) and cohesion (c) gradients
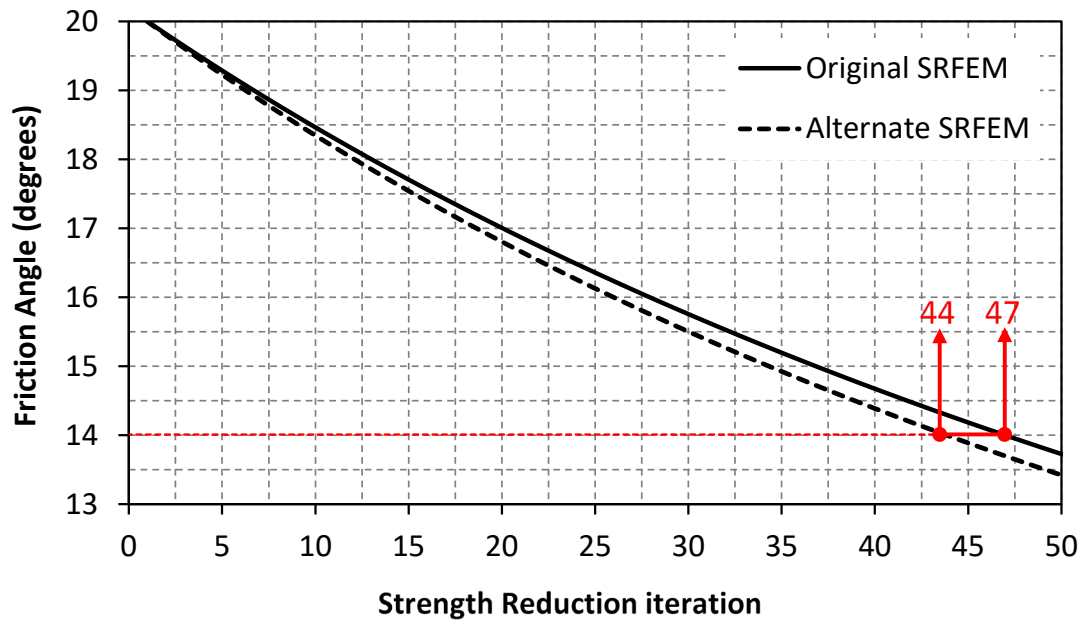
Fig. 4.4. SRFEM/MSRFEM friction angle step comparison

Nonlinear Decrements in the Strength Reduction Factor

The Strength Reduction Factors detailed in the above methods have been linearly reduced from a predefined initial value. This reduction technique can be improved by the introduction of information relating to slope deformation. As the deformation of each reduction step is stored in output files, the extent of Strength Reduction may be modified based on the size of the deformation

from the immediately preceding step. The selected process of decrementing the SRF based on maximum nodal slope deformation is given by Equation 4.11.

$$SRF_{n+1} = \begin{cases} SRF_n + \frac{\bar{U}-U_n}{\bar{U}^2}, U_n < \bar{U} \\ \bar{U}, U_n \geq \bar{U} \end{cases}$$

(4.11)

where, SRF$_n$ is the nth reduction of the SRF, $\bar{U}$ is the predefined maximum permissible nodal dimensionless deformation, and U_n is the maximum nodal dimensionless deformation of nth reduction step. The maximum observed nodal dimensionless deformation U is defined as shown by Equation 12.

$$U = \frac{E|x|}{\gamma A}$$

(4.12)

where, *E* is Young's modulus, |*x*| is the absolute maximum observed nodal deformation, γ is the bulk density of the material, and *A* is the material surface area for 2D cases. For 3D cases, *A* is defined as the maximum x-y plane cross sectional area. This paper considers four search strategies by combining SRFEM and MSRFEM with constant, and deformation dependent SRF processes (Table 4.1). Although several non-sequential search methods were considered such as bracketing methods including the bisection method, sequential methods were deemed preferential for the capture of slope deformation changes as the SRF approaches failure.

Table 4.1. Strength Reduction search strategies

Method	SRFEM	MSRFEM	Constant SRF	Deformation dependent SRF
1	X		X	
2		X	X	
3	X			X
4		X		X

4.4   Finite Element Modelling and Results

The numerical accuracy and computational efficiency of the methods detailed in Table 4.1 are
examined through 5 forms of analysis:

1. Investigation of SRFEM and MSRFEM for 2D and 3D cases with constant and deformation
   dependent SRF. Factors of Safety, maximum nodal dimensionless deformation, computational
   time and SRF iterations are compared.

2. Performance of Abaqus reduction code with 2D triangular and quadrilateral, and 3D hexahedral
   and tetrahedral finite elements.

3. Slope analysis of a layered geometry formed by combining slope instances previously
   examined with similar factors of safety.

4. Strength Reduction comparison with the commercial finite element codes Plaxis 2D and 3D.

5. Strength Reduction analysis with explicit Abaqus Finite Element Methods.

Slope geometry and soil properties

Table 4.2 shows material parameters common to the theoretical slope instances constructed for the
purpose of this research. Abaqus calculation requires non-zero dilation angles, thus ψ was set to a
nominal value of 0.1. Initially, four slope geometries (Fig. 4.5) were produced, two each for 2D and
3D analysis, with varying soil cohesion, friction angle, and soil density (Table 4.3), selected as the
MSRFEM is most widely applicable to slopes with low friction angles. Boundaries for each of the
instances were prescribed far away from the slope gradients to ensure no interaction between slope
stresses and boundary conditions during loading and failure. Displacement boundaries were fixed
for nodes along the slope base, with horizontal displacements fixed for nodes along the left and
right boundaries (with front and back boundaries also normally fixed for 3D instances), allowing
slope slip surfaces to deform freely with gravity loading applied to the whole geometry.   All
simulation of soils were modelled using plane strain model of linear elastic elements with the Mohr-
Coulomb failure criterion. Using the soils described in Table 4.3, a slope instance consisting of

multiple layers (Fig. 4.6) was created by placing Slope 1(b) on top of Slope 1(a). A finer mesh was

considered to produce a more accurate slip surface at the toe of Slope 1(b).

Table 4.2. Soil parameters

Poisson's ratio	Elastic modulus (MPa)	Dilation angle
0.35	50	0.1
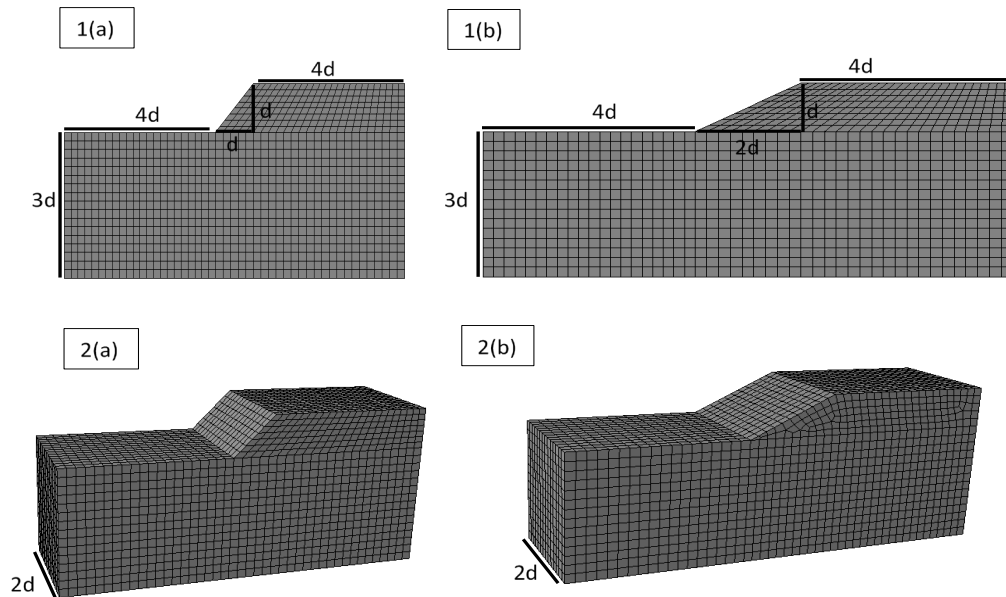
Fig 4.5. Slope instance geometries

Table 4.3. Slope physical and mechanical soil parameters

Slope	ϕ (°)	c (kPa)	Soil density (kg/m³)	Elements	Abaqus Element Type
1(a)	20	22	1800	999	CPE4R (Quadrilateral)
1(b)	21	7	1700	911	CPE4R (Quadrilateral)
2(a)	20	22	1800	12090	C3D8R (Hexahedral)
2(b)	21	7	1700	11564	C3D8R (Hexahedral)
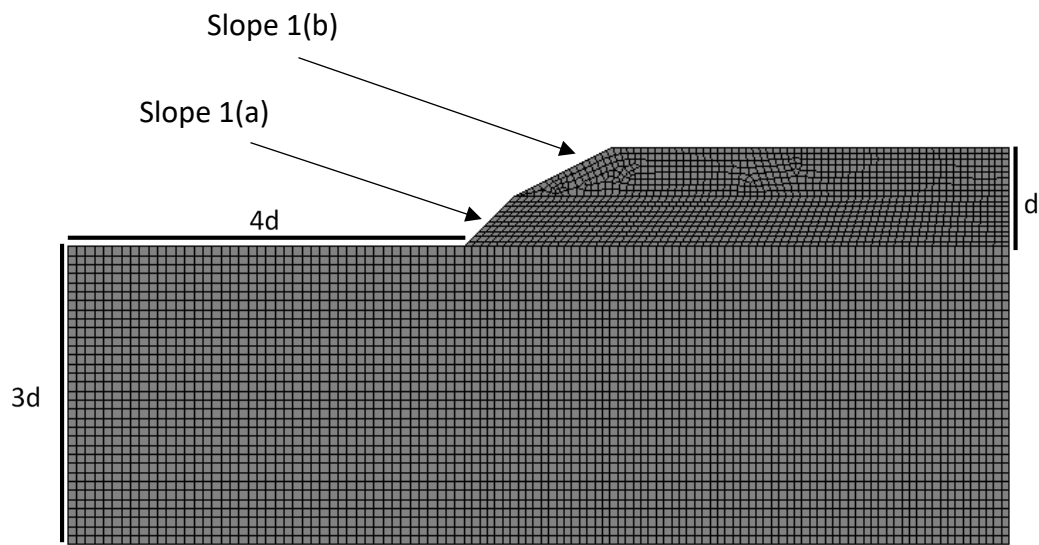
Fig 4.6. Layered slope instance

4.5   Simulation Results and Discussion

One of the main concerns with the Strength Reduction Finite Element Method is the judgement

process for considering when the final slope deformation failure state is attained. With the criteria

of (1) formation of plastic zones, (2) user-defined excessive deformation cut-offs (Fig. 4.7) and (3)

non-convergence, Factors of Safety were calculated for Slopes 1(a), (b), 2(a) and (b), as shown in

Table 4.4.   Methods 2 and 4, which employed the MSRFEM, surpassed the SRFEM in

computational efficiency for both runtime and solver iterations, in each of the four test cases. The

computation times for both 3D cases containing meshes with a large number of elements is vastly

improved. In each instance, final Factor of Safety values were consistent, with minimal observed

variation. It is as expected that the MSRFEM with deformation determined Reduction Factor

(method 4) performed most efficiently of the four methods, due to the technique's ability to increase

the SRF when far away from the final Factor of Safety. Final slip surfaces for each of the four

methods shown in Fig. 4.8 are indicated by the plastic zones, through the Abaqus parameter

PEMAG (magnitude of equivalent plastic strain), while the progression of the slip surface formed

in Case 1a is shown in Fig. 4.9, culminating with the formation of the full slip shape at a FoS of

1.48.

Table 4.4. SRFEM/MSFREM model results

Case 1a (2D)				
Method	FoS	Iterations	Time (mins)	Dimensionless deformation
1	1.48	49	5:36	2.085
2	1.483	46	5:00	2.135
3	1.507	24	4:50	2.5
4	1.476	21	4:17	1.91
Case 1b (2D)				
Method	FoS	Iterations	Time (mins)	Dimensionless deformation
1	1.37	38	4:54	1.943
2	1.368	35	4:21	1.897
3	1.372	17	3:46	1.994
4	1.3767	15	3:34	2.104
Case 2a (3D)				
Method	FoS	Iterations	Time (mins)	Dimensionless deformation
1	1.49	50	35:30	2.07
2	1.493	47	32:50	1.944
3	1.528	25	9:20	2.527
4	1.486	23	8:10	1.932
Case 2b (3D)				
Method	FoS	Iterations	Time (mins)	Dimensionless deformation
1	1.38	39	11:10	2.027
2	1.379	36	7:50	1.962
3	1.396	17	6:40	2.091
4	1.402	16	6:00	2.177
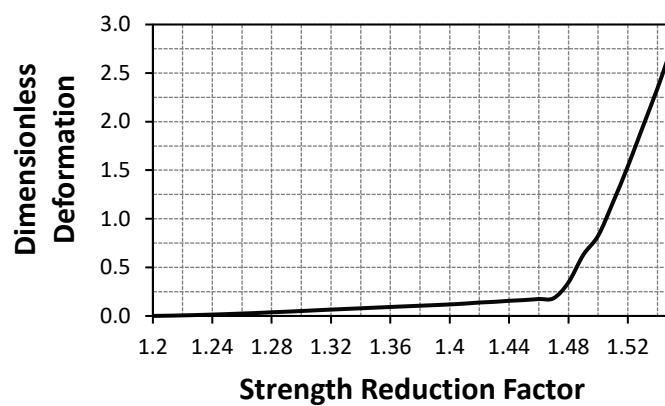
Fig. 4.7. Deformation profile similarities for Slope 1(a) with Strength Reduction Method 2
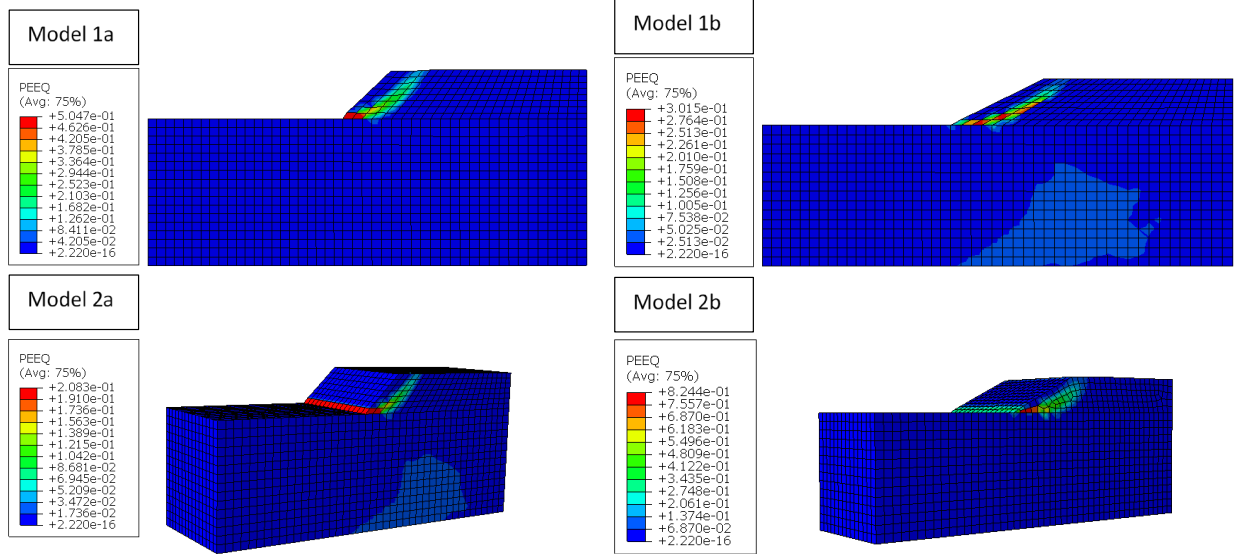
Fig 4.8. Final slip surface profiles
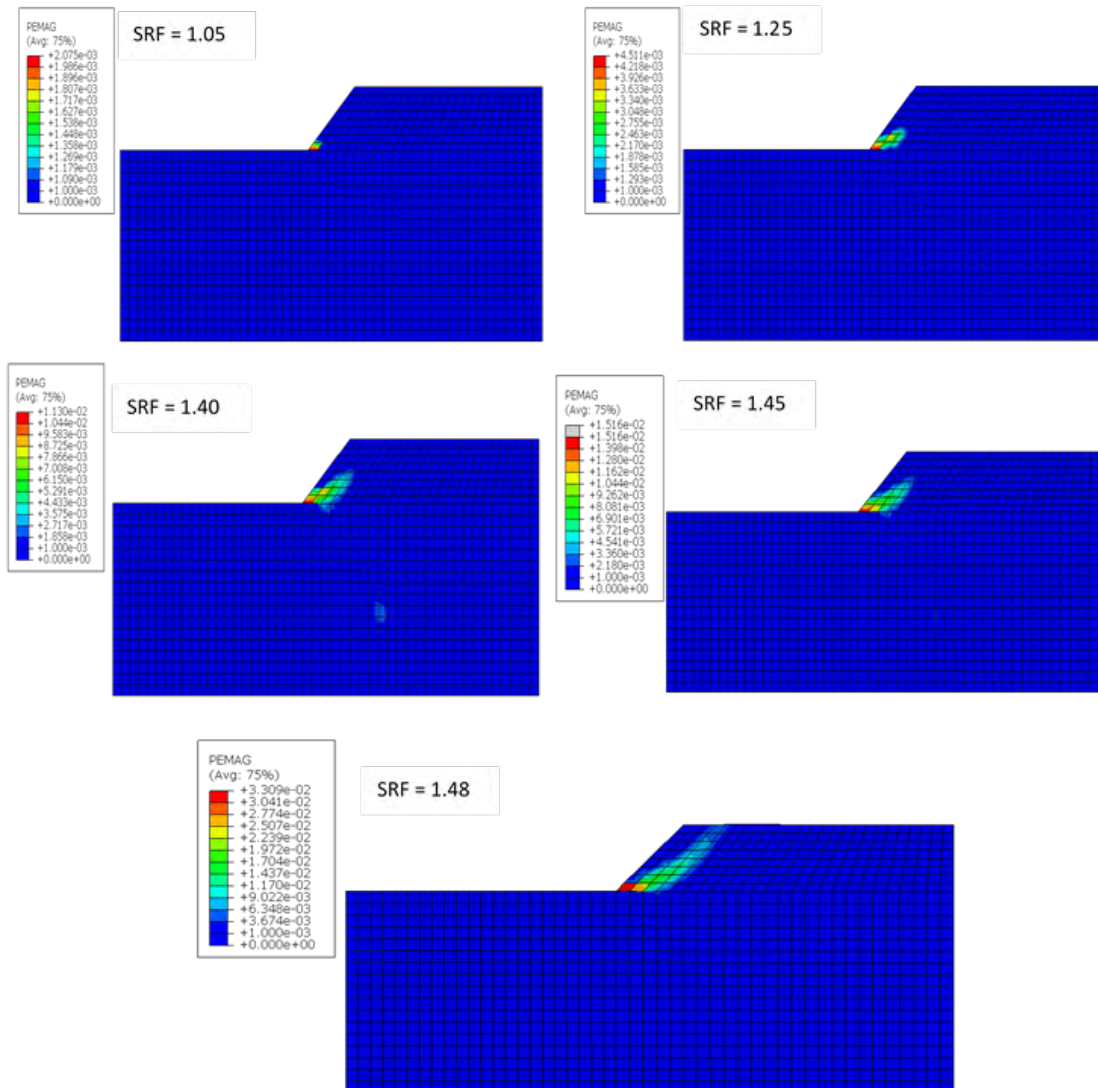
Fig 4.9. Strength Reduction plastic zone formation

Comparison of finite element types

To further examine the performance of the Strength Reduction algorithms, meshes with triangular
(in 2D) and tetrahedral (in 3D) elements were constructed, with mesh sizes comparable to the
previous quadrilateral and hexahedral models (Table 4.5). The resulting Factors of Safety were
not affected by element geometry (Table 4.6), with similar observed computation times.

Table 4.5. Number of finite elements per slope instance

	Finite Elements			
Model	Triangular	Quadrilateral	Hexahedral	Tetrahedral
Case 1a (2D)	1524	999		
Case 1b (2D)	1790	911		
Case 2a (3D)			12090	21655
Case 2b (3D)			11564	19464

Table 4.6. Comparison of finite element type FoS performance

Case 1a (2D)				
Method	FoS	Iterations	time (mins)	Deformation
1	1.48	49	5:36	2.085
2	1.483	46	5:00	2.135
3	1.507	24	4:50	2.5
4 (Quad elements)	1.477	21	4:17	1.91
4 (Tri elements)	1.477	21	4:30	1.895
Case 1b (2D)				
Method	FoS	Iterations	time (mins)	Deformation
1	1.37	38	4:54	1.943
2	1.368	35	4:21	1.897
3	1.372	17	3:46	1.994
4 (Quad elements)	1.3767	15	3:34	2.104
4 (Tri elements)	1.3767	15	3:10	1.944
Case 2a (3D)				
Method	FoS	Iterations	time (mins)	Deformation
1	1.49	50	35:30	2.07
2	1.493	47	32:50	1.944
3	1.528	25	9:20	2.527
4 (Hex elements)	1.486	23	8:10	1.932
4 (Tet elements)	1.486	23	7:56	1.929
Case 2b (3D)				
Method	FoS	Iterations	time (mins)	Deformation
1	1.38	39	11:10	2.027
2	1.379	36	7:50	1.962
3	1.396	17	6:40	2.091
4 (Hex elements)	1.402	16	6:00	2.177
4 (Tet elements)	1.402	16	6:21	2.138

Strength reduction of a layered slope

The layered slope of Fig. 4.6 (Case 3) was modelled using the same techniques for MSRFEM as

previous simulations, with both materials reduced by the same Strength Reduction Factor. As the

slope considered in Fig. 4.6 is a combination of the previously analysed slope cases 1(a) and (b),

the most computationally efficient method, (MSFREM with non-linear SRF) was selected to

demonstrate the code's ability to handle slopes containing multiple soil layers. Due to the added

weight of Slope 1(b) on top of Slope 1(a), the Factor of Safety (Table 4.7) for the combined slope

was found to be less than the FoS of Slopes 1(a) and (b) when considered separately. The slip

surface is observed in Fig. 4.10.
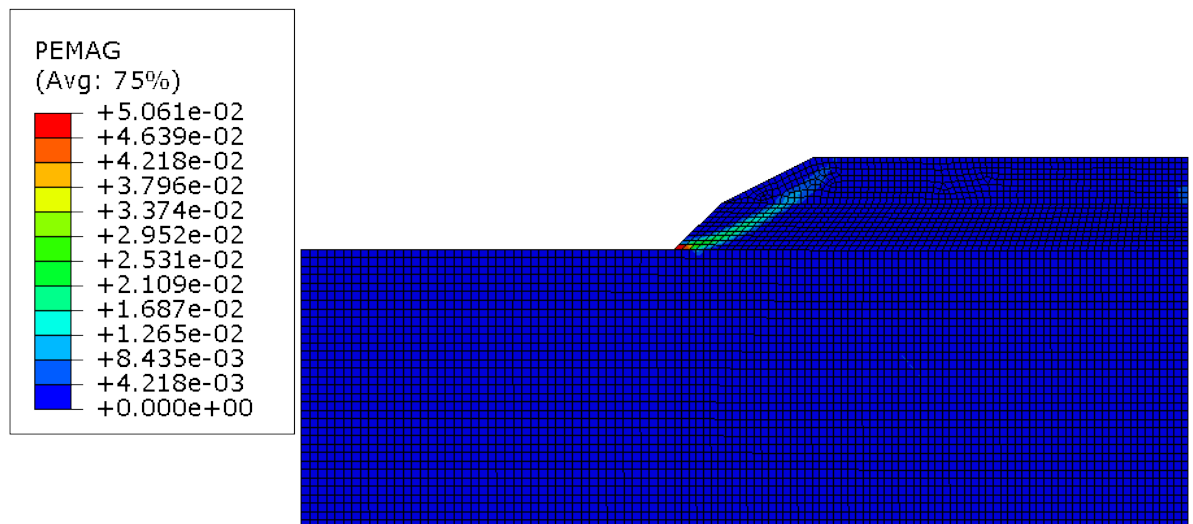
Fig 4.10. Layered slope slip surface

Table 4.7. Layered slope MSRFEM results

Layered slope (2D)				
Model	FoS	Iterations	time (mins)	Deformation
4	1.21	9	4.13	2.07

Comparison against Plaxis inbuilt Strength Reduction Method

To compare the Factor of Safety results of the SRFEM and MSRFEM algorithms coded with Python scripts in conjunction with Abaqus, Strength Reduction analyses were conducted on the same slope instances in the Plaxis Finite Element code which has its own inbuilt solver and algorithm for the Strength Reduction Method. Two Plaxis Strength Reduction Methods exist, a targeted SRFEM and an incremental multiplier SRFEM. The incremental multiplier SRFEM does not allow for the control of a maximum strength reduction iterations. Instead, the method will continue until the maximum number of allowable computation steps is reached. Therefore, this method is unsuitable for comparison to the number of iterations produced by the Abaqus MSRFEM. The Plaxis target SRFEM requires an initial approximation of the FoS as a lower bound, then the final SRF iteration is determined by a tolerance factor. For comparison with the Abaqus MSRFEM, Plaxis targeted SFREM was chosen, with an initial FoS given by the Abaqus MSRFEM. The Plaxis incremental multiplier SRFEM was also computed, to guarantee that given initial FoS approximations for the targeted SRFEM were below the necessary final targeted FoS value. As the number of SRF iterations for each Plaxis method does not allow for a SRF iteration ceiling, the Abaqus MSRFEM and Plaxis SRFEM were compared based on the final FoS and computation time.

Table 4.8 shows the comparison in FoS and computation times. When considering models with a limited number of elements, Plaxis outperformed the MSFREM Abaqus algorithms, however in the 3D instances with a large number of elements, the MSFREM codes executed in less time, producing similar FoS results. Although the Abaqus MSRFEM was outperformed in computational time for the smaller 2D models, the method has the added benefit of producing results for each Strength Reduction Factor iteration, providing further details for discerning the differences between the slope for each reduction factor.

Table 4.8. MSFREM comparison with Plaxis 2D and 3D

Model	Abaqus coded FoS			Plaxis FoS			Comparison (Abaqus – Plaxis)	
	Elements	FoS	time (mins)	Elements	FoS	time (mins)	Normalised FoS ratio (%)	Normalised time ratio (%)
Case 1a 2D	1524	1.477	4:30	1552	1.48	0:31	-0.202	+771
Case 1b 2D	1790	1.3767	3:10	1779	1.367	0:41	-0.049	+363
Case 2a 3D	21655	1.486	7:56	22854	1.508	9:06	1.459	-12.82
Case 2b 3D	19464	1.402	6:21	21499	1.378	8:04	1.711	-21.3

Abaqus Explicit Strength Reduction

The Abaqus/Explicit solver determines solutions without iteration by advancing the kinematic state from the previous time increment. For scenarios with significant computational cost, Abaqus/Explicit requires substantially less disk space and memory than the Abaqus/Standard methods. Table 4.9 shows the comparison of MSFREM using Abaqus/Explicit, with Abaqus/Standard. The FoS is agreeable with implicit methods, with a reduction in computation time.

Table 4.9. Comparison of Implicit and Explicit Strength Reduction

Case 1a (2D)				
Method	FoS	Iterations	time (mins)	Deformation
1	1.48	49	5:36	2.085
2	1.483	46	5:00	2.135
3	1.507	24	4:50	2.5
4	1.476	21	4:17	1.91
4 Explicit	1.491	-	3:30	2.326

3D layered case with a weak interseam

A final 3D geometry (Case 3) is presented in Fig. 4.11 (a) - (d), consisting of a clay slope sandwiching a weaker clay interseam (Table 4.10), which intersects the rearmost section of the slope toe. The Abaqus MSRFEM procedure was compared with the Plaxis Strength Reduction

Method, exhibiting a comparable FoS (Table 4.11), and significant improvement in computation time. The full Plaxis slip surface can be observed in Fig. 4.12 (a) and the MSRFEM Abaqus slip surface in Fig. 12 (b) where slip surface locations for both simulations are comparable. In both cases, the slip surface propagates through the week clay material at the slope toe. The final factor of safety for the MSRFEM is calculated to be 1.698, slightly lower than the Plaxis SRFEM of 1.701 (Table 4.11). Replacement of the weaker interseam clay with the slope's primary clay produces a considerably higher FoS of 1.982, highlighting the strong impact of the weak interseam clay on the instability of the slope.
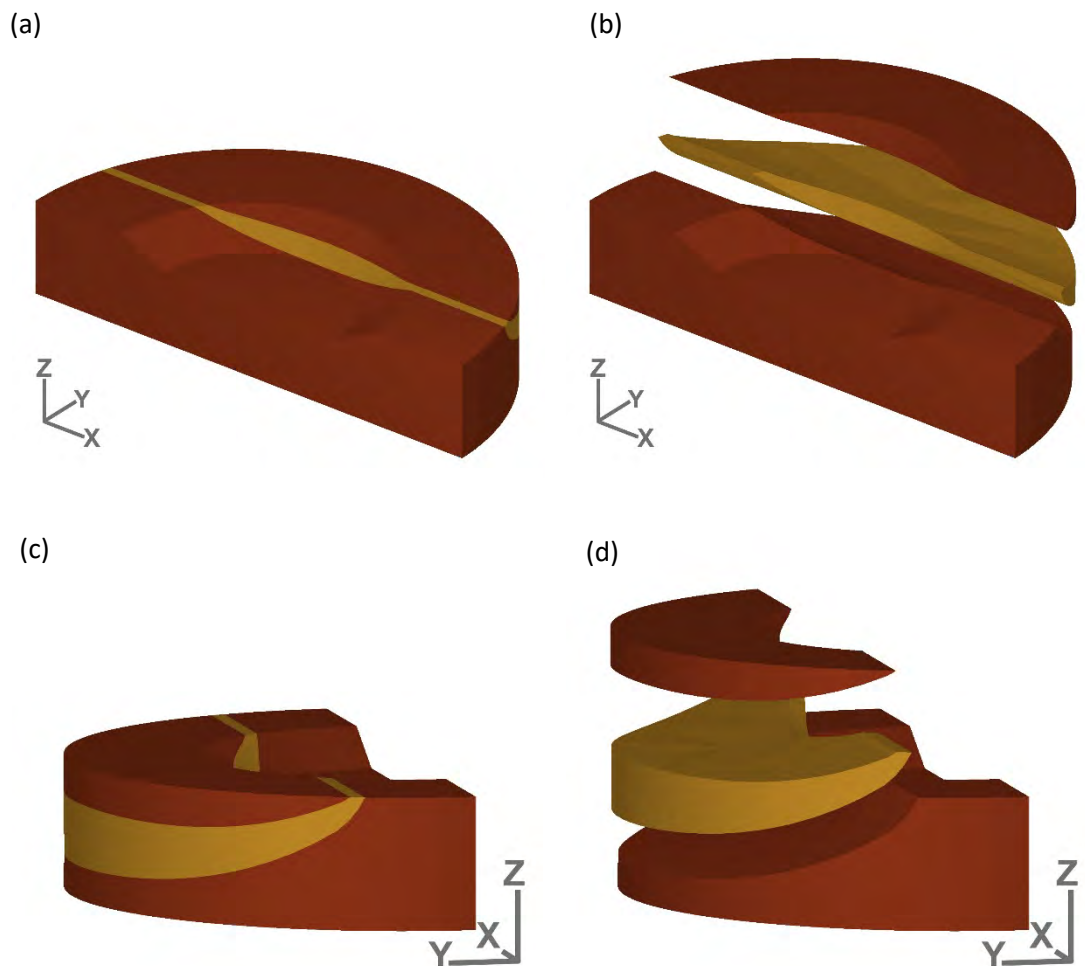
Fig. 4.11. Case 3 geometry. (a) front view (b) front view with separated layers (c) side view (d) side view with separated layers

Table 4.10. 3D slope material and numerical modelling parameters

Material	ϕ (°)	c (kPa)	Soil density (kg/m³)	E (kN/m²)	ν	Elements	Abaqus Element Type
Primary clay	15	21	18	20	0.35	26142	C3D10 (tet)
Interseam Clay	15	10	18	20	0.35	1286	C3D10 (tet)

Table 4.11. MSFREM comparison with Plaxis 3D

Abaqus coded FoS			Plaxis FoS			Comparison (Abaqus – Plaxis)	
FOS	time (mins)	Elements	FoS	time (mins)	Elements	Normalised FoS ratio (%)	Normalised time ratio(%)
1.698	8:13	27428	1.701	8:51	27698	0.177	7.156
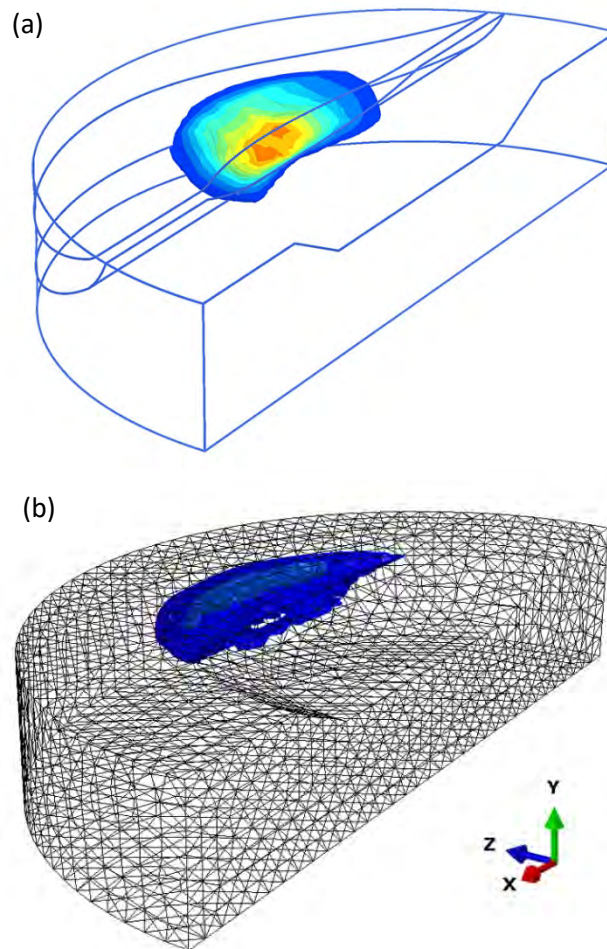
Fig. 4.12. Slip surfaces of Case 3. (a) Plaxis slip surface (b) Abaqus slip surface

4.6   Conclusion and Recommendations

The availability of desktop computers and access to Finite Element Method codes has made it possible to readily produce Strength Reduction Methods for the analysis of slope stability safety factors. The creation of Python scripts in conjunction with Abaqus FEM allowed for the creation of a Strength Reduction Finite Element Method and a modified technique for added computational efficiency, analysing slope deformation and slip surfaces for a range of Strength Reduction Factors. Analyses were performed on several of slope instances with distinct material parameters and slope geometries in both 2 and 3 dimensions, with safety factors verified by the Finite Element code Plaxis. The technique proves an effective tool for geometries consisting of a large number of finite elements, and can be implemented for simulations containing more than one soil layer, using either

implicit or explicit Finite Element codes. Due to the coded approach of reducing material strength, the method is appealing for investigations containing random finite elements, and heterogeneous material sections. This technique is suitable for probabilistic analysis, where the geometry is sectioned into small subsections, with individual strength parameters, then the MSRFEM is applied to all relevant subsections. Although several bounded search strategies may be used to decrease the computational cost of SFREM, the MSRFEM technique is an attractive approach for the sequential Strength Reduction slope stability analysis of large models requiring considerable computational resources, as it provides full simulation results of each optimised reduction stage, rather than only the final result.

5 Prediction and Classification for Finite Element Slope Stability Analysis by Random Field Comparison

The following journal paper introduces similarity based prediction and classification methods for Random Finite Element Method slope stability analysis, building on the Strength Reduction Method developed in the previous chapter. This chapter explores Random Field simulation to determine slope Factors of Safety without the need for large scale Monte Carlo simulation. This journal paper is an accurate representation of the published version, with minor alterations to table and figure numbers for the purposes of continuity.

Abstract

This paper considers probabilistic slope stability analysis using the Random Finite Element Method (RFEM) combined with processes to determine the level of similarity between random fields. A procedure is introduced to predict the Factor of Safety (FoS) of individual Monte Carlo Method (MCM) random field instances prior to finite element simulation, based on random field similarity measures. Previous studies of probabilistic slope stability analysis have required numerous MCM instances to reach FoS convergence. However, the methods provided in this research drastically reduce computational processing time, allowing simulations previously considered too computationally expensive for MCM analysis to be simulated without obstacle. In addition to computational efficiency, the comparison based procedure is combined with cluster analysis methods to locate random field characteristics contributing to slope failure. Comparison measures are presented for slope geometries of an Australian open pit mine to consider the impacts of associated factors such as groundwater on random field similarity predictors, while highlighting the capacity of the similarity procedure for prediction, classification and computational efficiency.

Keywords

Random field; slope stability; random finite element method; RFEM; probabilistic methods; clustering analysis.

5.1   Introduction

Numerical methods for slope stability analysis are of prime importance for the prevention of slope collapse within a wide range of geo-structures. Slope stability remains a challenging aspect of large open-pit mining projects due to the inherent complexities of geological structures. Furthermore, uncertainties within geological and geotechnical properties suggest that deterministic analysis can produce poor estimates of slope stability factors when soil layers exhibit non-uniform or heterogeneous characteristics [120]. Initial probabilistic slope stability research gained attention in the late 1970s [1, 16, 17, 30], with the field rising in prominence as computational power continues to increase [2, 115, 120, 153, 224].

Two techniques for probabilistic slope stability are commonly implemented – probabilistic Limit Equilibrium Methods (LEM), and the Random Finite Element Method (RFEM) [2, 32, 158]. The latter combines finite element analysis with random field simulation, explicitly modelling soil spatial correlation parameters without the requirement of the predefined critical failure shape and location. This technique is often preferred to Limit Equilibrium Methods due to several advantages, as prior assumptions regarding inter-slice forces are not required [218, 219]. Instead, slope failure occurs naturally when elements with applied shear stresses exceed the material shear strength, causing excessive distortion. Hicks et al. considered the influence of soil variation on the probability of failure (PoF) as well as the slip mass of three-dimensional slopes, with RFEM [169]. Liu et al. analysed the impacts of boundary stratigraphic uncertainty on layered slopes with variable soils [225].

Fenton and Vanmarke developed the Local Averaging Subdivision (LAS) technique to incorporate spatial correlation within geotechnical random field parameters such as soil weight, elastic modulus,

friction angle, cohesion etc. [156]. RFEM is commonly coupled with LAS to model spatially varying soils in geotechnical investigations such as bearing capacity of shallow foundations [160], seepage analysis [226], and slope stability [227].

This investigation considers the similarity of random fields of cohesive-frictional (c-φ) soils with spatially correlated shear strength parameters. Slope stability simulations are implemented with the FEM package Abaqus 2018. To calculate the Factor of Safety of each slope instance, the Strength Reduction Method (SRM) developed by Zienkiewicz [35] is implemented. The FoS is commonly defined as the ratio of the current soil strength compared to the minimum shear strength required to avert structural failure [78]. As there is no predefined strength reduction method implemented within Abaqus, algorithms produced in Fortran and Python were developed, as described by Dyson and Tolooiyan [228] and Dyson et al. [229].

This research considers a set of random fields which are generated and then compared with several devised similarity techniques and clustering methods. RFEM slope stability models are then simulated to determine the correlation between random field similarity and slope failure characteristics such as FoS and slip surface shape. Clustering analysis techniques are investigated to categorise probabilistic slope geometries based on random field similarity to predict the FoS without having to undertake the lengthy process of finite element method simulation. Due to the considerable computation time required to produce numerous RFEM instances by Monte Carlo simulation, the analysis of random field instances with similarity-based prediction provides an efficient framework for probabilistic slope stability analysis.

5.2   Probabilistic Slope Stability Description

Random fields for the Finite Element Method

When considering random fields for finite elements, soil variability is commonly divided into two components, a deterministic (often depth-dependent) trend component, and a fluctuation component [141]

$$\xi(\boldsymbol{x}) = t(\boldsymbol{x}) + w(\boldsymbol{x}) \tag{5.1}$$

where, $\xi(\boldsymbol{x})$ is the geotechnical parameter to be modelled, $t(\boldsymbol{x})$ is the trend component and $w(\boldsymbol{x})$ is the fluctuation component, commonly named the "off the trend" variation. The fluctuation term is generated based on random field theory, by three properties of statistical distribution: the mean μ, standard deviation s, and scale of fluctuation Θ [1, 152]. Geotechnical parameter variability can be represented by the dimensionless parameter known as the Coefficient Of Variation (COV) defined by the ratio of the standard deviation (s) with respect to the mean (μ).

$$COV = \frac{s}{\mu} \tag{5.2}$$

The scale of fluctuation Θ describes the spatial correlation of the geotechnical property, and is defined as the distance where strong correlation is observed within the random field [230]. When Θ is small, the geotechnical property exhibits a rapid fluctuation with respect to distance. As Θ increases, the rate of fluctuation decreases, producing a smoothly varying random field. The scale of fluctuation is commonly determined by an Auto-Correlation Function (ACF) that defines the average correlation between locations separated by lag distance τ [152]. A range of ACFs exist, as illustrated by Hilyati et al. [153], the most common being the Markovian spatial correlation function [231-233]. Li et al. considered the effects of five theoretical ACFs on slope stability, concluding that slope reliability is insensitive to the auto-correlation type [234]. However, various studies have noted significant effects on the FoS [235-237]. The two-dimensional Markovian spatial correlation function is defined as:

$$\rho(\tau_x, \tau_y) = \exp\left(-\frac{2|\tau_x|}{\theta_x} - \frac{2|\tau_y|}{\theta_y}\right) \tag{5.3}$$

where, $\rho(\tau_x, \tau_y)$ is the correlation coefficient between random field values at lag distances τ_x and τ_y in x and y directions, respectively. Similarly, θ_x and θ_y are defined as the scales of fluctuation in the x and y directions. Random fields with spatial correlation are often generated by

implementing the Local Average Subdivision method (LAS) defined by Fenton and Vanmarke [156].

Random fields most commonly considered for RFEM analysis include soil cohesion c, friction angle φ, dilation angle ψ, elastic modulus *E*, Poisson's ratio *v*, unit weight *γ*, and permeability *k*. Griffiths and Lane [238] noted the variation of parameters with the most significant impact on slope stability RFEM are the strength parameters *c* and φ, as well as the soil weight and slope geometry. Furthermore, variation of the unit weight has considerably less impact on the slope FoS compared with the previously described strength parameters [16].

Soil parameters are often characterised by a lognormal distribution (with mean μ_x and standard deviation s_x) when the parameter is strictly non-negative, e.g. cohesion and friction angle. A lognormal random field is produced from a standard Gaussian random field $G(x)$ through the transform

$$X_i = \exp\left[\mu_{\ln X} + s_{ln\,X} G(x_i)\right] \tag{5.4}$$

where X_i is the transformed soil property of the ith element, x_i is the coordinates of the centre point of the ith element, and $\mu_{\ln X}$ and $s_{ln\,X}$ are the mean and standard deviation of the underlying normal distribution ln (X), determined by Equations (5.5) and (5.6) as follows:

$$\mu_{\ln X} = \ln(\mu) - \frac{1}{2} s_{ln\,X}{}^2 \tag{5.5}$$

$$s_{ln\,X}{}^2 = \ln\left(1 + \frac{s^2}{\mu^2}\right) \tag{5.6}$$

Cross-correlation of random variables can be implemented by the covariance matrix decomposition method described by Fenton [151]. Cherubini [148] noted cross-correlations of c and φ between -0.24 to -0.7, suggesting a weak negative relationship, as confirmed in several additional studies [149, 150].

Monte Carlo simulation of probabilistic geotechnical problems can be conducted by generating a series of random fields from the aforementioned statistical properties. As the number of simulations increases, parameters such as the mean FoS and probability of failure begin to converge.

Finite Element Method for slope stability

In this study, we perform finite element method slope stability analysis with linear elastic model combined with the Mohr-Coulomb perfectly plastic failure criterion. The implementation of FEM for slope stability is comprehensively described by Griffiths and Lane [238]. Forces are generated by gravity loading of the soils, creating normal and shear stresses. The stresses are compared with the Mohr-Coulomb criterion defined as:

$$F = \frac{\sigma_1 + \sigma_3}{2} \sin \phi - \frac{\sigma_1 - \sigma_3}{2} - c \cos \phi \tag{5.7}$$

where, σ_1 and σ_3 are the major and minor principal stresses, respectively. When stresses at a point reach the Mohr-Coulomb failure envelope, the location is considered to be yielding. Stresses within the envelope are deemed to remain in an elastic state.

In this research, the finite element geometry is partitioned into distinct element sets, such that each element set within the domain is allocated material strength parameters based on an associated random field cell. The *Abaqus* element type CPE4P (a 4-node plane strain quadrilateral, bilinear displacement, bilinear pore pressure element) was implemented. A particularly fine mesh was constructed, consisting of 40,000 elements, due to the complexity of the geometry and layering, coupled with the number of elements required for the necessary spatial variation. The random field is initially developed as a point distribution, however, when considering a log-normal distribution, both the mean and standard deviation are diminished by the process of local averaging. This is due to the dependence of the log-normal distribution mean on both the mean and standard deviation of the underlying normal relationship (Equations 5.5 and 5.6). For this reason, the random field point statistics must be adjusted according to the FEM simulation element size. The random field is

mapped onto a mesh consisting of square finite elements. Henceforth, a variance reduction factor is applied due to the local averaging process. Further details of the procedure implemented in this study are extensively described by Griffiths and Fenton [2].

Strength reduction method

The Strength Reduction Method, sometimes referred as the Strength Reduction Finite Element Method (SRFEM) is a technique to calculate the slope FoS, defined as the ratio of current soil shear strength to the minimum shear strength necessary to avoid failure. Alternatively, FoS is considered as the minimum factor to reduce the soil strength to produce imminent failure [75]. In SRFEM, sometimes known as phi-c reduction, the soil cohesion and friction angle parameters are iteratively reduced until failure occurs.

The Strength Reduction procedure is commonly defined as follows:

$$c = \frac{c_0}{SRF} \tag{5.8}$$

$$\phi = \tan^{-1}\frac{\tan\phi_0}{SRF} \tag{5.9}$$

where, c_0 and ϕ_0 are the initial cohesion and friction angle parameters, respectively, and SRF is the trial strength reduction factor. The final factor of safety is given by:

$$FoS = \frac{c_0}{c_f} = \frac{\tan\phi_0}{\tan\phi_f} \tag{5.10}$$

where, c_f and ϕ_f are the cohesion and friction angle at failure, respectively. Initially, a modest trial strength reduction factor (SRF) is required, which does not cause slope failure. The SRF is then iteratively increased, reducing the cohesion and friction angle until slope failure occurs. There are several criteria for slope failure, the most common being:

1. Development of plastic zones from the head to the toe of the slope [30].

2. Large deformation, often defined by an acceptable level of nodal displacement.

3. Solution non-convergence, often occurring when slope failure produces excessive element distortion.

5.3 Random Field Similarity

Matrix norm comparisons of random fields

When considering a two-dimensional random field, the matrix $\mathbf{A}$ consists of elements a_{ij} where a represents the value of the parameter in the ith row and the jth column. In relation to the FEM slope stability simulation, the matrix indices correspond to lattice locations of the slope geometry. In this study, comparisons between random fields are formulated by computing matrix norms of the element-wise difference between random field matrices, by the following process:

1. Generate n random field instances for Monte Carlo simulation

2. Compute the difference between matrices $\mathbf{A}$ and $\mathbf{B}$ for all matrix pairs within the dataset of n random field simulations, producing $\frac{n(n-1)}{2}$ similarity comparisons. The matrix difference $\mathbf{D}$ is computed by $\boldsymbol{D} = \boldsymbol{A} - \boldsymbol{B}$.

3. Select a matrix norm to calculate the size of $\boldsymbol{A} - \boldsymbol{B}$. A matrix norm is a distance metric derived from inducing a vector norm on a matrix. The Frobenius norm calculates the square root of the sum of squares of the matrix entries (Equation 11) and is analogous to Euclidean distance. A range of matrix norms exist, including the $\|\boldsymbol{A}\|_1$ norm, which determines the maximum absolute row sum of a matrix, and $\|\boldsymbol{A}\|_\infty$, which calculates the maximum absolute column sum of a matrix. However, the Frobenius norm is a measure well suited to comparison of random fields with complex geometries, as each element within the field is included in the sum. When $\boldsymbol{A} = \boldsymbol{B},$ the Frobenius norm $\|\boldsymbol{D}\|_F$ (Equation 11) is equal to zero, indicating that the two random fields are identical. Small Frobenius norm values indicate the two random fields are similar. As $\|\boldsymbol{D}\|_F$ continues to increase, the random fields become increasingly disparate.

$$\|\boldsymbol{D}\|_F = \left(\sum_{i=1}^{m} \sum_{j=1}^{n} |a_{ij} - b_{ij}|^2\right)^{1/2} = \sqrt{trace[(\boldsymbol{A} - \boldsymbol{B})^T (\boldsymbol{A} - \boldsymbol{B})]}$$

(11)

4. Calculate the norms for both sets of geotechnical strength parameters (i.e. cohesion and friction angle).

5. Run all n Monte Carlo slope stability simulations and determine the FoS of each instance.

6. Calculate the absolute difference of the FoS between all possible pairs of Monte Carlo simulations.

7. Plot the absolute difference in FoS of each pair versus the associated Frobenius norm similarity measure. The correlation between FoS and similarity can be calculated to determine the relationship between slope stability and random field similarly.

This method is further described in Fig. 5.1, detailing the required stages for both RFEM prediction leading to convergence in the FoS, as well as the classification of RFEM instances based on the observed safety factor.

The potential exists for random fields to be compared with correlation techniques rather than matrix norms. However, due to the speed of calculating the matrix trace given in Equation 5.11, the formerly specified matrix norm comparison method is preferred within this study.
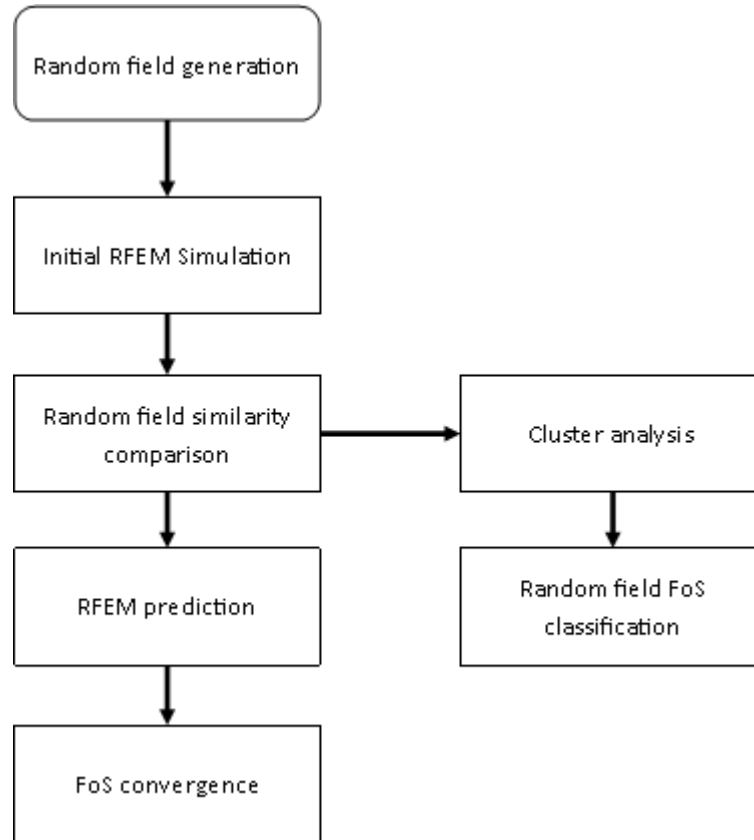
Figure 5.1. Random field similarity flowchart methodology

RFEM similarity of a single-layered slope under undrained conditions ($\phi_u = 0$)

A single-layered 2-1 generalised slope, initially detailed by Cho [231] (Fig. 5.2) is presented to provide an elementary example of the random field similarity method. The range of the resulting simulation slip surfaces is displayed. The material properties for the slope are given by Table 5.1, with a normally distributed undrained shear strength c_u. A Markovian exponential autocorrelation structure is defined with $\theta_x = 20m$ and $\theta_y = 2m$. Initially, 50 random field instances where generated, producing 1275 random field similarity comparisons. The mean factor of safety associated with the critical failure surface was found to be 1.38, with a distribution shown in Fig. 5.3. As with the factors of safety, the random field similarities exhibit a distinct Gaussian distribution (Fig. 5.4). The relationship between normalised random field similarity and the absolute difference in FoS is evident in Fig. 5.5, whereby similar random fields produce comparable

factors of safety. As the random field comparisons become increasingly dissimilar, the range of values of the observed safety factor broadens. Fig. 5.6 indicates the normalised similarity levels required to observe an absolute difference in safety factors within a given tolerance. In this case, approximately 5% of all random field similarity comparisons are less than the normalised similarity value of 0.12 necessary to observe FoS differences less than a value of 0.1.

The random field similarity comparison method can be implemented as a predictive measure. After the generation of an arbitrary number of random field instances, similarity comparisons can be made to predict the FoS of individual instances based on their similarity to previously simulated realisations. Fig. 5.7 compares the cumulative FoS of the predictive model with the observed values from full Monte Carlo simulation. Each model was given a set of 950 further random field instances, with both cases converging to the same FoS after 1000 realisations. Both models converged to a lower FoS than observed after the initial 50 instances, suggesting a true mean FoS of 1.35.
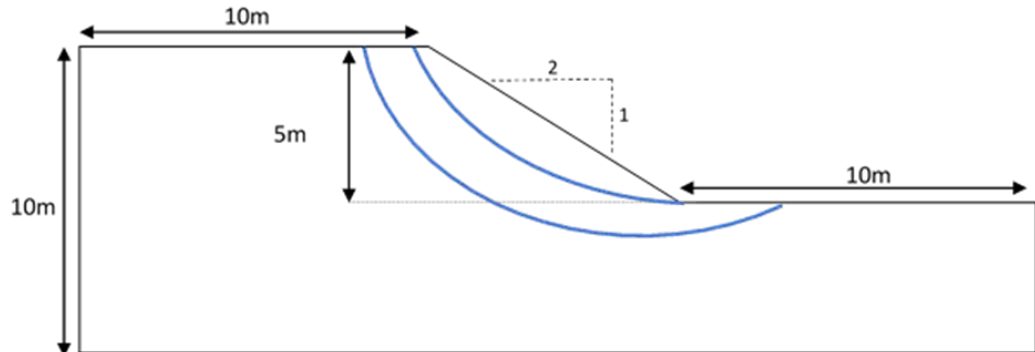
Figure 5.2. 2-1 single layered slope displaying various slip failure mechanisms

Table 5.1.   Statistical properties of soil parameters

Parameter	Parameter mean	Coefficient of variation
Unit weight γ_{sat} (KN/m³)	20	0
Undrained shear strength c_u (kPa)	23	0.3
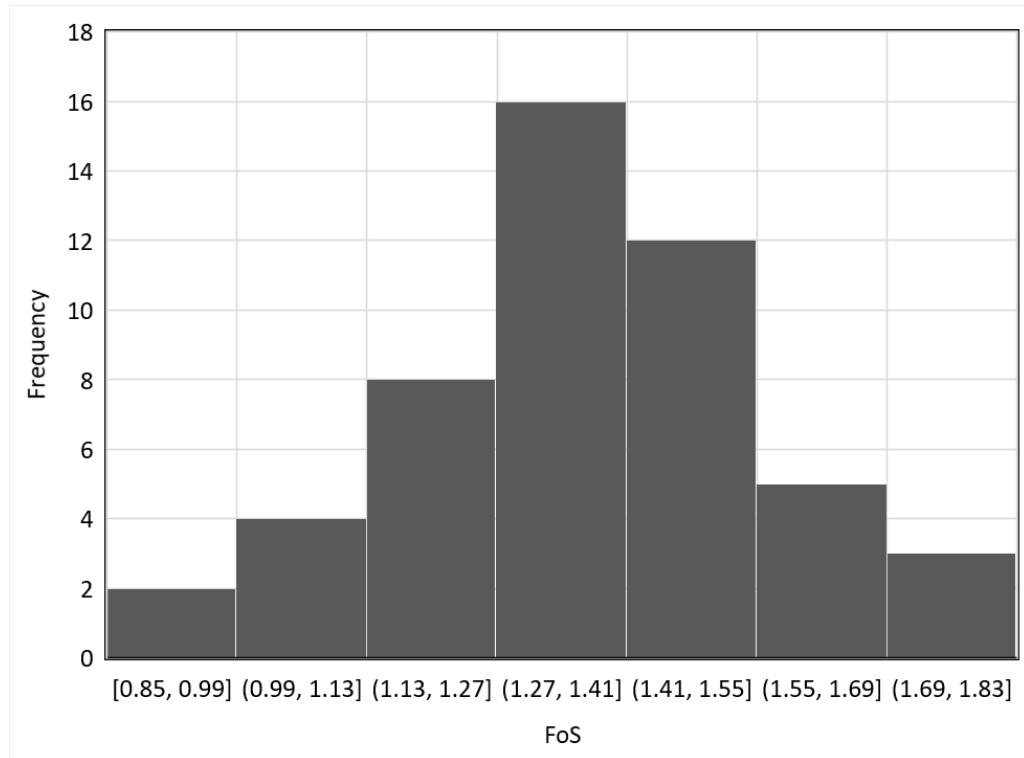
Figure 5.3. Histogram of the FoS distribution
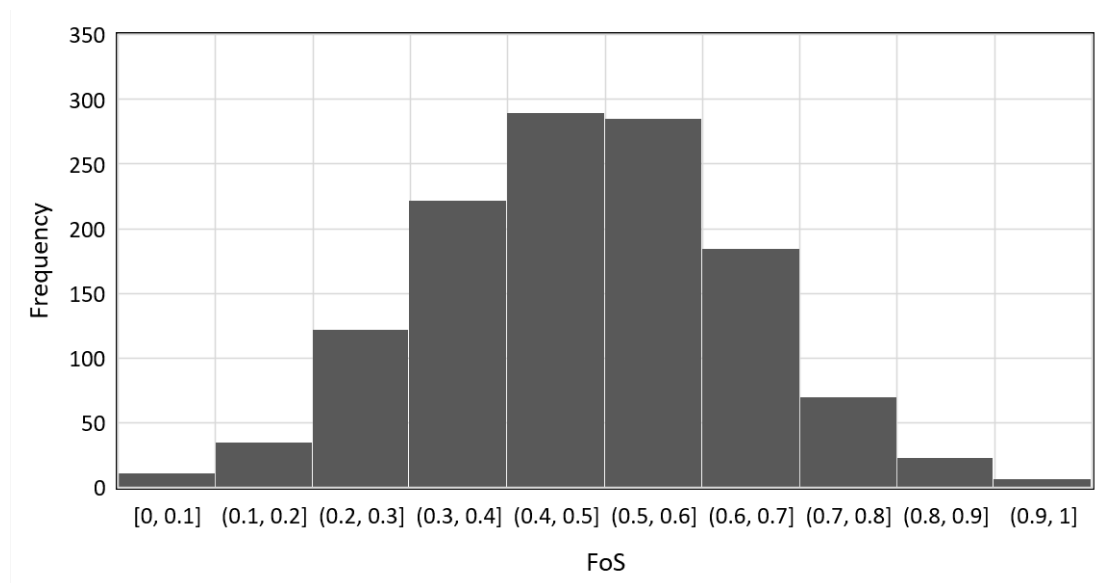
Figure 5.4. Random field similarity distribution
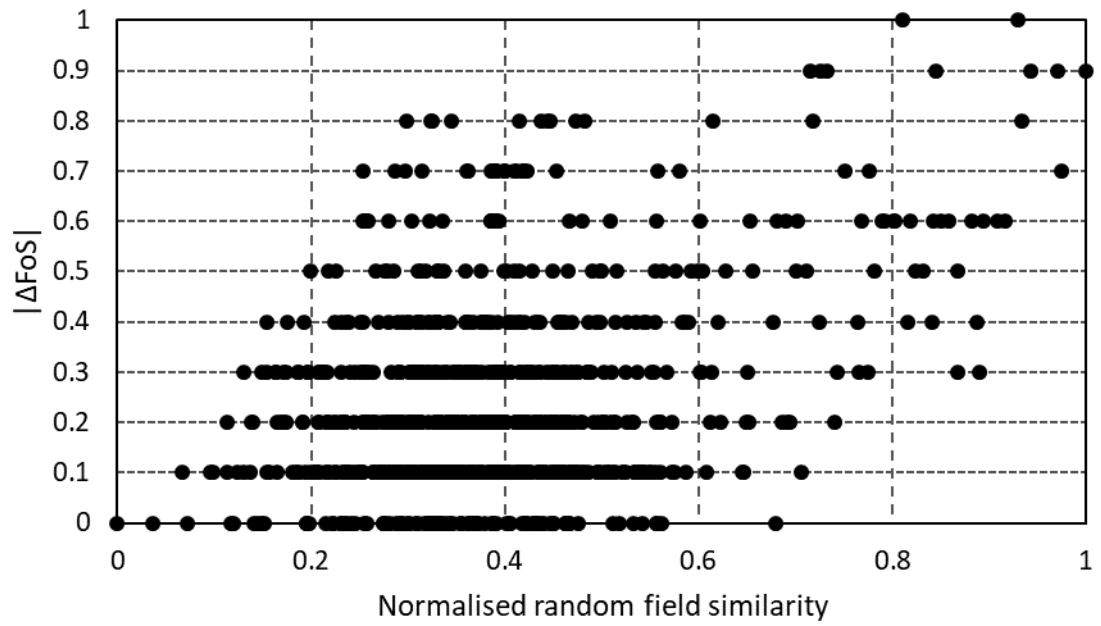
Figure 5.5. FoS absolute difference vs. normalised random field similarity data points
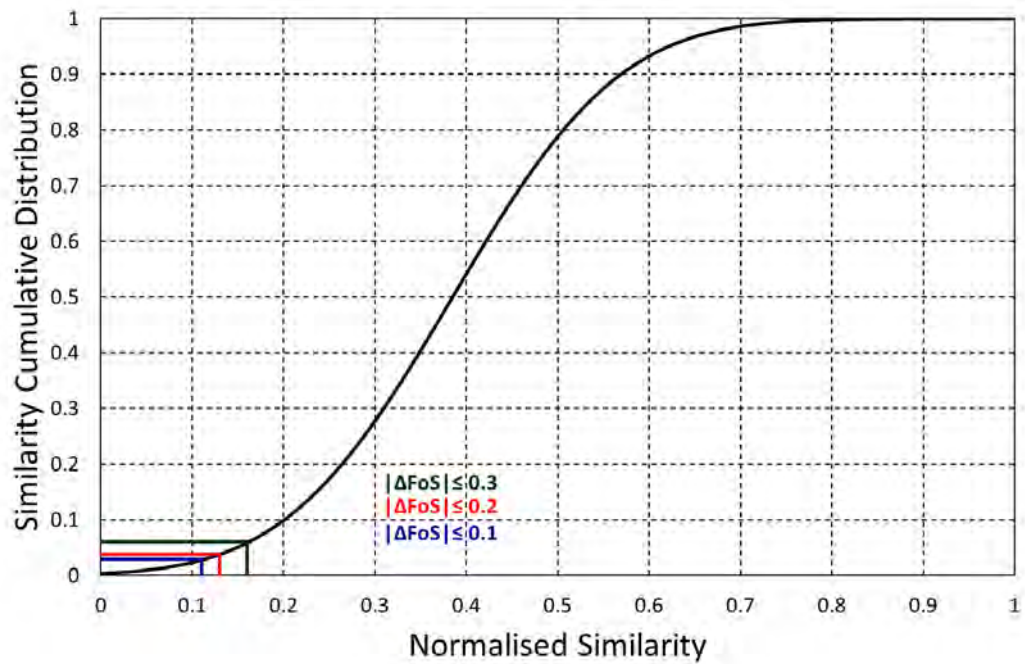
Figure 5.6. Normalised similarity cumulative distribution function
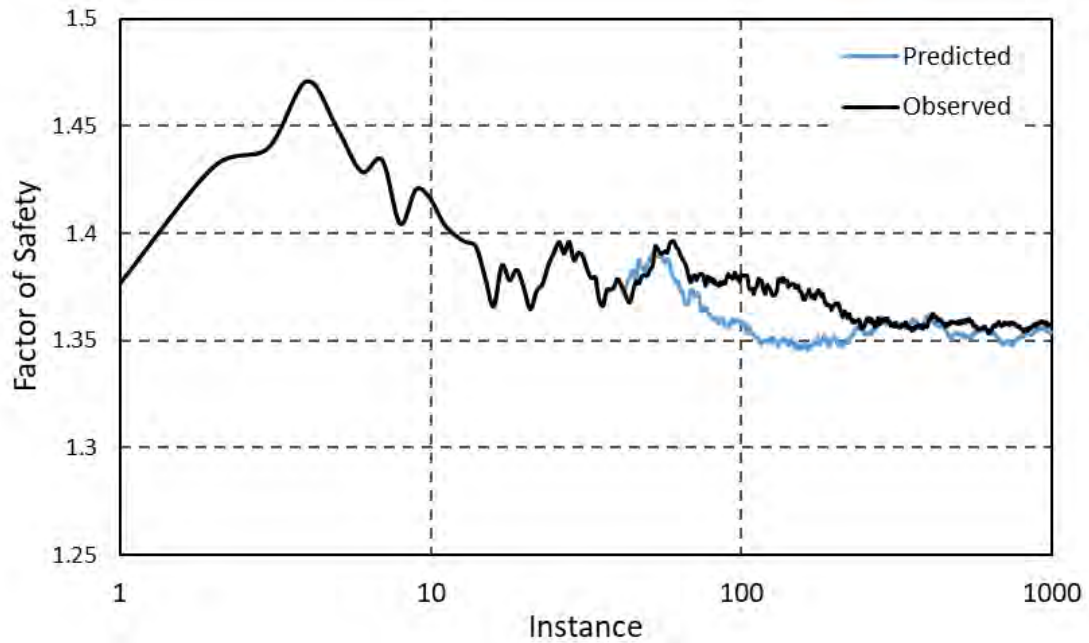
Figure 5.7. Observed and predicted cumulative FoS

Clustering

To further understand the effects of random field similarity, several clustering algorithms are investigated to determine whether random fields can be categorised based on characteristics determined by matrix norms. Once random fields are grouped into clusters, the effects of cluster characteristics on slope deformation and FoS are analysed. Numerous clustering methods are considered for statistical and probabilistic applications [239] with particular attention given to hierarchical clustering [240] and k-means clustering [241] in this research.

Hierarchical Clustering Analysis (HCA) is a method for hierarchically ordering clusters based on similarity.   Two hierarchical clustering subclasses exist: divisive clustering, whereby all observations are assigned to a single cluster, then observations are recursively partitioned until one observation per cluster remains; alternatively, agglomerative clustering (also known as bottom-up clustering) initially assigns each observation to its own individual cluster, then computes cluster similarities, allowing observations to be iteratively linked until a single cluster remains.

For comparison of random fields for slope stability, hierarchical clustering allows for the identification of the most similar random field pairs, as well as the level of similarity.

Fig. 5.8 shows a hierarchical cluster dendrogram (a tree diagram, used to visualise hierarchical clusters) of 40 random fields with the divisive clustering method. It is noted that in this example, random field numbers 12 and 23 are considered most similar, due to their depth along the dendrogram tree.
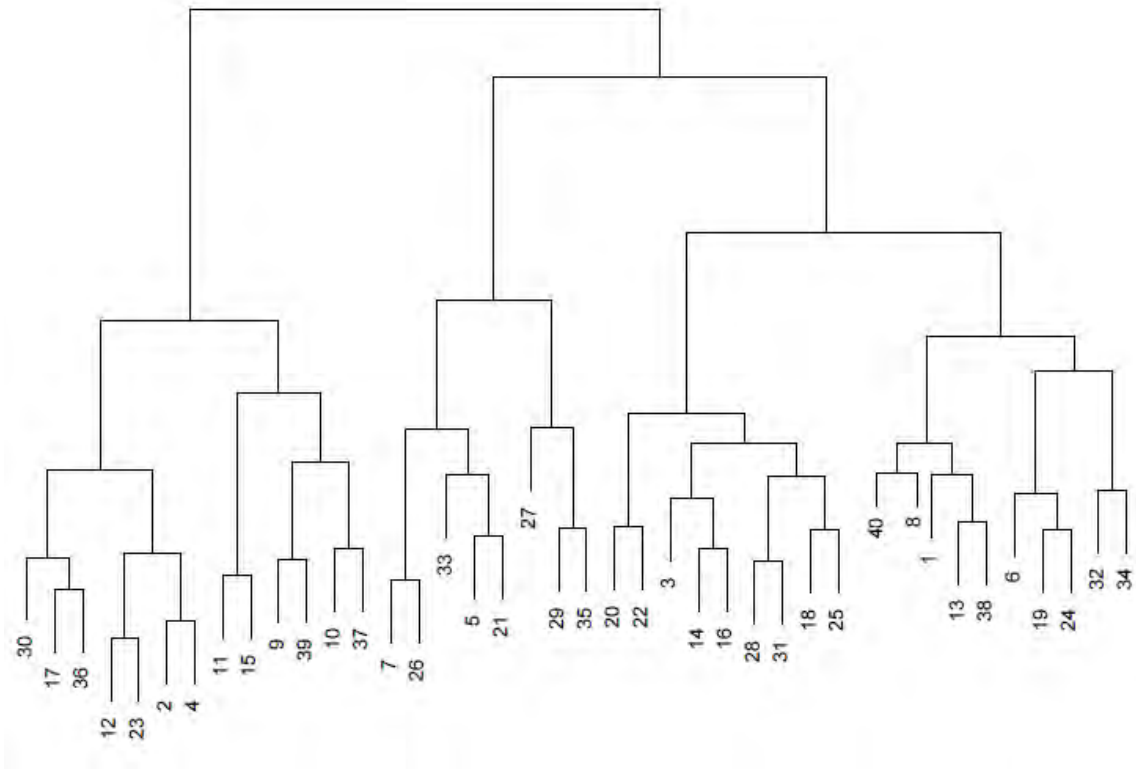
Figure 5.8. Hierarchical cluster dendrogram of 40 random fields

K-means clustering, also known as MacQueen clustering is a method that has received significant attention due to its simplicity and computational efficiency. The objective of the algorithm is the grouping of the data into K clusters, iteratively assigning each data point to one of the K groups based on the similarity of each cluster. The cluster centroid is determined for each cluster group. Each data point is associated with its nearest centroid, determined by squared Euclidean distance such that the distance from each cluster centroid is minimised (Equation 5.12).

$$\arg min_S \sum_{i=1}^{k} \sum_{x \in S_i} ||x - \mu_i||^2 \qquad (5.12)$$

Where arg min_S refers to the process of minimising the domain of input data values for a given

function, k is the number of clusters, x is the data points, S_i is the set of points in the ith cluster,

and $\boldsymbol{\mu}_i$ is the ith cluster centroid. Fig. 5.9 shows the cluster partitioning of the same 40 random

fields presented in Fig. 5.8, indicating how random fields can be categorised based on their

similarity. In this case, two clusters of random fields can be described without interaction effects

with other clusters. However, most of the random fields are described as exhibiting characteristics

from several clusters.
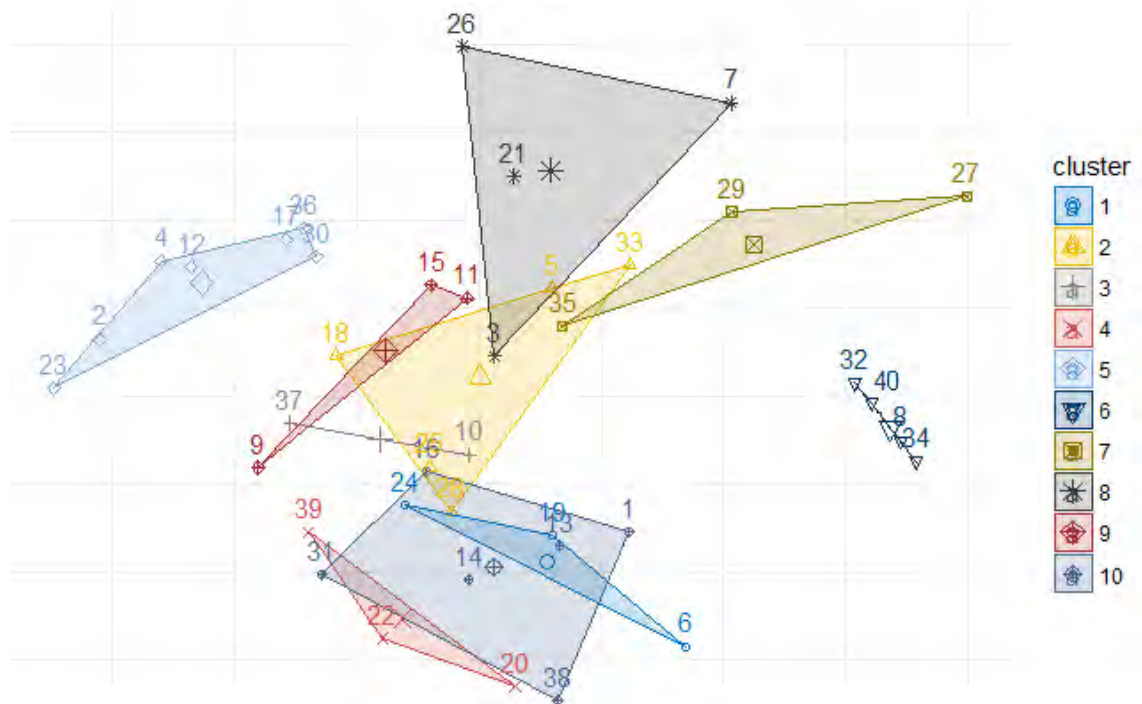
Figure 5.9. K-means cluster plot interpretation of 40 random fields given in Fig. 5.8

Prediction

The similarity measures and clustering techniques described above are presented with the

intention of detailing methods not only for characteristic analysis, but also as a predictive tool to

determine whether additional random fields need be simulated with full slope stability analysis.

Should an additional random field exhibit properties similar enough to previous random field

simulations, assumptions can be made about the results of the supplementary random field. If a

random field is considered similar enough to not warrant simulation, computation efficiency is

drastically increased. The performance of these methods are presented in detail in conjunction

with a case study of the Australian brown coal mines of the Latrobe Valley.

5.4   Case Study

Yallourn open cut coal mine

The Yallourn open cut brown coal mine, located in the Latrobe Valley, Victoria (Fig. 5.10) is

Australia's second largest open-cut mine. Situated 150 km east of Melbourne, the Latrobe Valley

coal formations contain some of the thickest continuous lignite seams in the world [187]. A two-

dimensional cross-section of the northeast batter is considered (Fig. 5.11), consisting of layers of

coal and clay. Fig. 5.12 shows the model geometry prior to and after excavation, with associated

deterministic geotechnical parameters presented in Table 5.1.

Figure 5.10. Yallourn mine location

Figure 5.11. Two dimensional cross section location
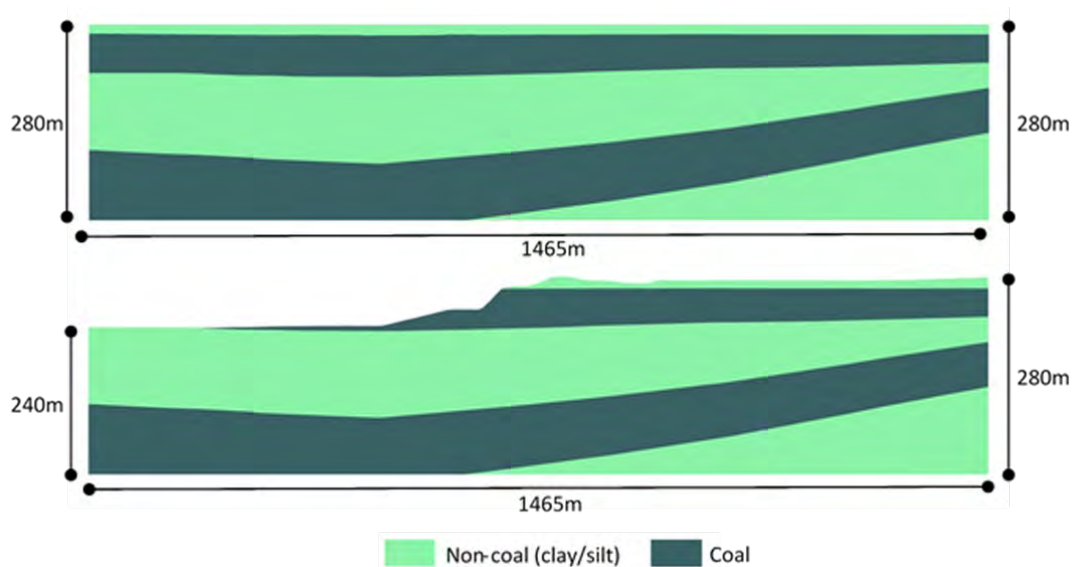
Figure 5.12. Model geometry prior to and post-excavation

The shear strength parameters cohesion (c) and friction angle (φ) determined from laboratory and

field investigations are presented in Table 5.2. The layers do not exhibit depth dependent trends,

and individual coal/non-coal layers arise from the statistical distributions that describe each

material. In each case, the parameters exhibited log-normal distributions, with scales of fluctuation

θ_x and θ_y (Table 5.3) characterising across the bore and down the bore fluctuations, respectively.

Visualisations of one probabilistic instance of shear strength parameters on the excavation geometry

is shown in Fig. 5.7, where strong anisotropy of both non-coal and coal for the friction angle and

cohesion parameters is evident. The authors wish to note that the jagged nature of the base coal

layer boundary is due to the partitioning of the layer in Abaqus. Due to the lengthy computation

time of RFEM for this large geometry, smoothing of the boundary layer was not considered

appropriate for this study. A limitation of the Abaqus Finite Element environment is that spatially

variable material parameters cannot be easily visualised without additional Python scripting. Even

with scripting, Abaqus employs a cap to the number of data points that can be visualised on a cross-

section. For this reason, the discretisation of the Random Fields shown in Figure 5.13 indictes

correlation structures which are artifacts of the visualisation process.

Table 5.1. Geotechnical parameters for coal and non-coal materials

Material	γ_{unsat} (kN/m^3)	γ_{sat} (kN/m^3)	E (MPa)	ν	k (m/day)
Coal	11.4	11.5	40	0.3	7.6e-3
Non-coal	20.15	20.2	52	0.3	4.7e-2

Table 5.2. Shear strength parameter statistics

	Coal		Non-coal	
Parameter	c (kPa)	φ (°)	c (kPa)	φ (°)
Mean (μ)	150.7	27.3	31.8	23.7
Standard Deviation (s)	69.8	4.9	5.0	4.5
COV	0.5	0.2	0.2	0.2

Table 5.3. Shear strength length scales

	Coal		Non-coal	
Scale of Fluctuation (m)	c	φ	c	φ
θ_x	320.3	772.4	812	627.8
θ_y	23.1	8.7	35	13.1

Figure 5.13. Cohesion (kPa) random field (above). Friction angle (degrees) random field (below).

Results presented herein use the aforementioned RFEM similarity methods instead of full Monte Carlo simulation. Full RFEM Monte Carlo simulation of the North-East batter requires significant computational capacity and high performance computing facilities. For this reason, it is seldom performed for large open-pit mine analysis. The simplest mine geometry and geology often requires in excess of 2000 simulation instances. As such, full RFEM Monte Carlo simulation of the Yallourn North-East batter is not conducted in this research. Instead, the simplified full Monte Carlo simulation case provided earlier in the Chapter has been used as a validation case.

5.4.1   Case 1 – Constant Friction Angle Model without Groundwater

To assess similarity based prediction methods, an initial case was selected without the presence of groundwater to consider the simplest slope stability case. As no groundwater is present within the

model, dry parameters were chosen, with a constant friction angle of 27.28 and 23.67 degrees for coal and non-coal. Although this initial scenario is not indicative of the case in reality at the Yallourn mine, several secnarios including the presence of groundwater are given after Case 1. The material cohesion varies in accordance with the shear strength statistics of Tables 5.2 and 5.3. The finite element model was developed in three stages – an initial geostatic stage, followed by an excavation step, and a strength reduction step to determine the final slope factor of safety. Thereafter, 40 RFEM slope instances were simulated, then analysed with the aforementioned random field similarity measures. Deterministic simulation of the slope yielded a factor of safety of 2.9 (Fig. 5.14). However, RFEM simulation produced normally distributed safety factors ranging between 2.3 and 3 (Fig. 5.15), with a reduced mean FoS of 2.6. As expected, the slip surface is observed in the deterministic analysis through the slope batter from head to toe, and is visualised with the Abaqus variable PEMAG – the magnitude of the plastic strain. Pairwise comparisons of the 40 individual random field instances produced 820 random field similarities. As with the distribution of safety factors, these random field similarities exhibit a distinct Gaussian distribution (Fig. 5.16).

The absolute difference in FoS for all pairs of cohesion random fields with respect to normalised similarity is presented in Fig. 5.17. Of particular interest are the random fields with normalised similarities below 0.2. When random fields exhibit similarities below this value (i.e., random fields with particularly similar characteristics), all observed FoS differences reduce to zero. This suggests when random fields are sufficiently similar, their safety factors converge. Furthermore, as the similarity measure increases above 0.2, the spread of FoS differences also increases, with the trend towards larger FoS differences for less-similar random fields. From Fig. 5.16 and Fig. 5.17, a similarity Cumulative Distribution Function (CDF) can be calculated to determine the likelihood of similarity pairs occurring, as well as the expected absolute difference in FoS (Fig. 5.18). In this case, a normalised similarity of 0.27 is required to produce an absolute difference of FoS of less than 0.1, occurring in 5% of all random field sample pairs. Similarly, an absolute FoS difference of less than 0.2 arises in 12% of random field pairs. With traditional Monte Carlo simulation,

several hundred to several thousand instances may be required to attain convergence in the mean FoS. However, the technique described suggests that after the 40 initial realisations, 5% of all similarity comparisons produced factors of safety with differences less than 0.1. When considering FoS prediction, approximately 5% of similarity comparisons from any further generated random field instances will produce normalised similarities less than the requisite value of 0.27 necessary to predict the FoS within a tolerance of 0.1. This 5% prediction value suggests at least 20 random field instances are required to produce at least one similarity pair for prediction. However, double the number of initial random field instances were simulated as a precautionary measure to ensure there are sufficient similarity pairs for prediction. Furthermore, it is necessary to be confident that convergence is reached at the 5% level. In this case, this percentage was observed after 25 instances, and remained constant thereafter. Thus, approximately 40 simulations are sufficient as a conservative estimate of the number of simulations required for execution for this case. Thereafter, numerous random fields can be generated, with each FoS instance value assumed, without the requirement of finite element method simulation. Whenever a random field instance did not produce the random field similarity comparison necessary for prediction, full FEM simulation was deemed for the instance in question. In this example, the simulation of 40 instances compared to potentially 1000 random fields required for traditional Monte Carlo simulation constitutes less than 5% of the necessary number of instances of the conventional method. Fig. 5.19 shows the observed FoS from 40 generated instances, as well the predicted FoS after 1000 instances, generated from similarity comparisons, converging at a FoS of 2.6.
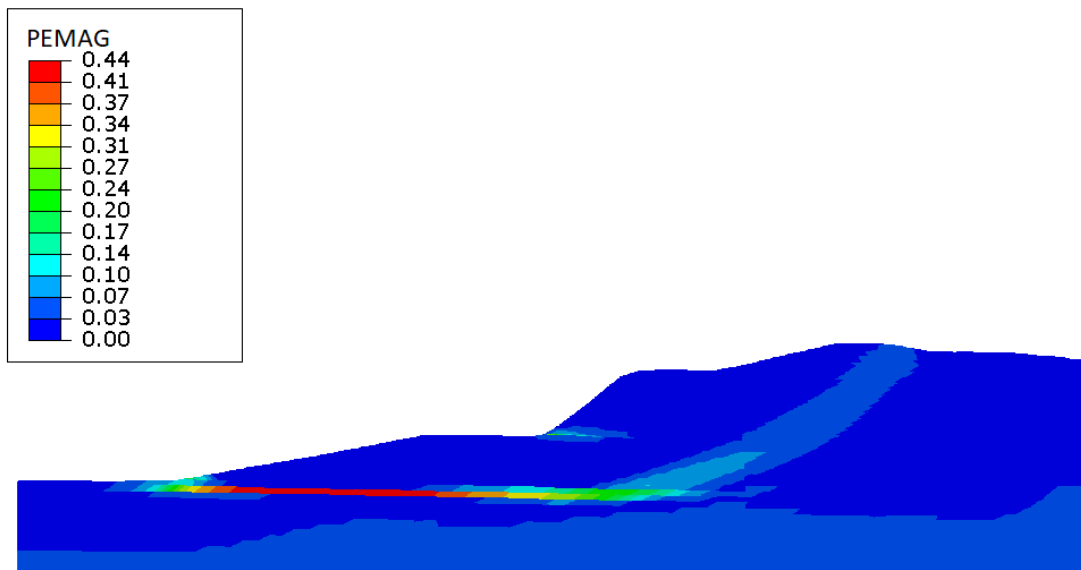
Figure 5.14. Deterministic simulation slip surface
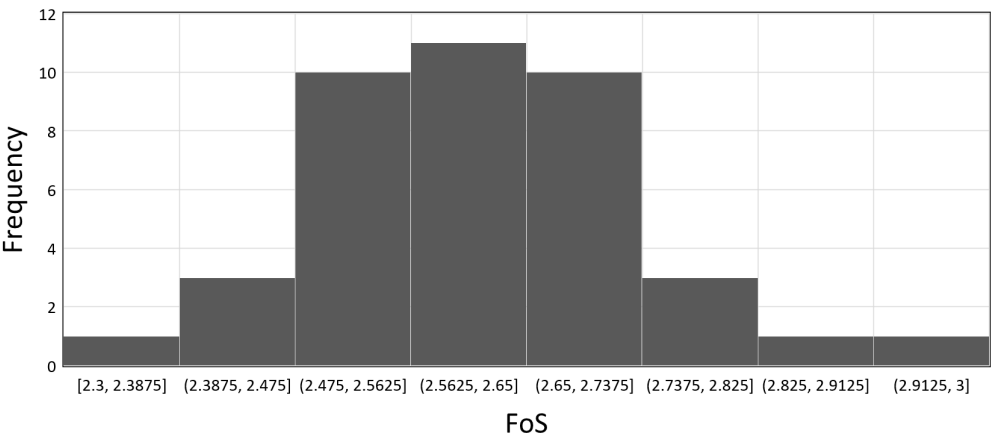
Figure 5.15. Histogram of the FoS distribution
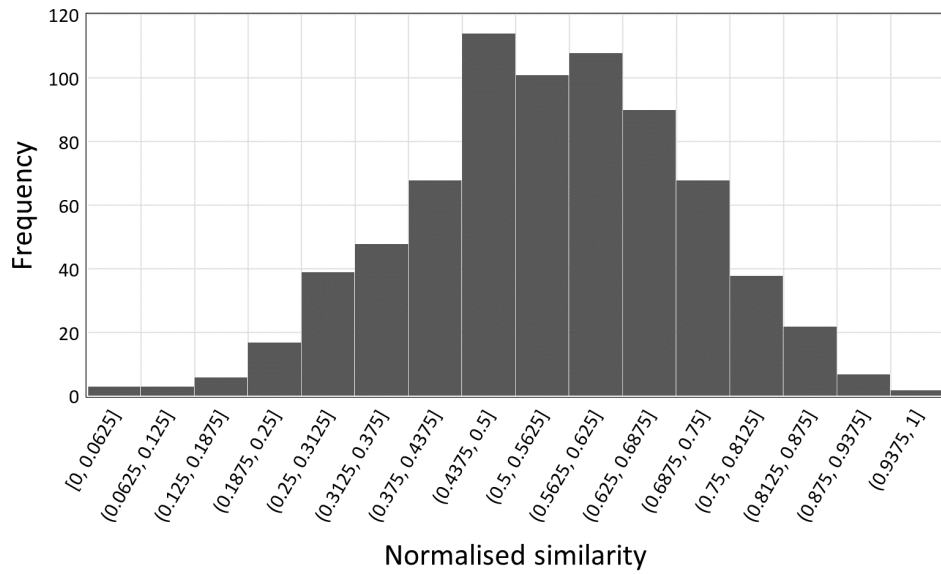
Figure 5.16. Random field similarity distribution
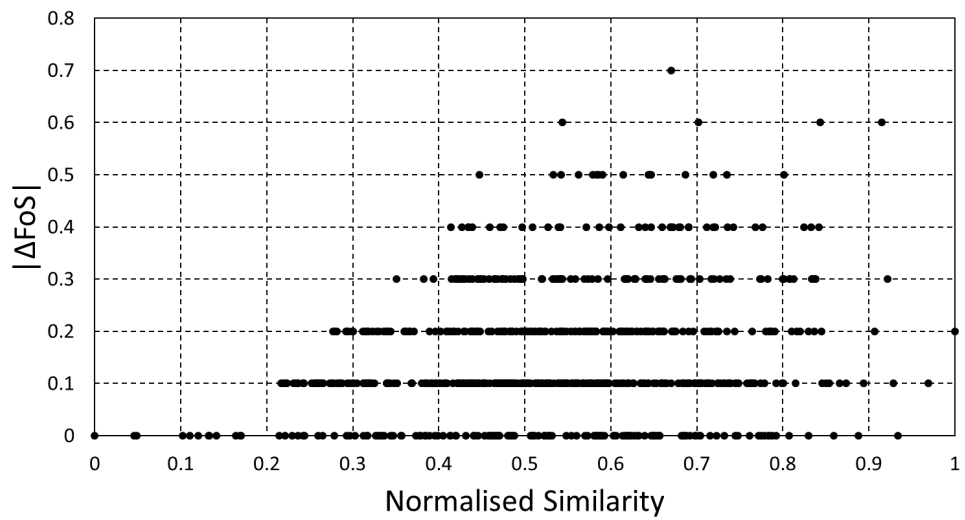
Figure 5.17. FoS absolute difference vs. normalised cohesion random field similarity data points
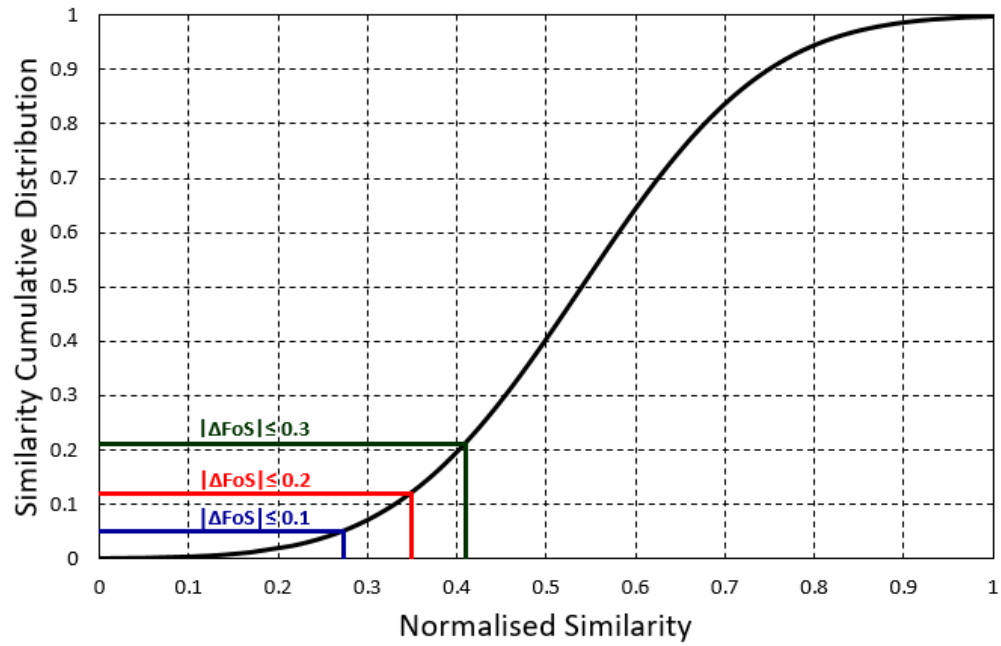
Figure 5.18. Normalised Similarity Cumulative Distribution Function
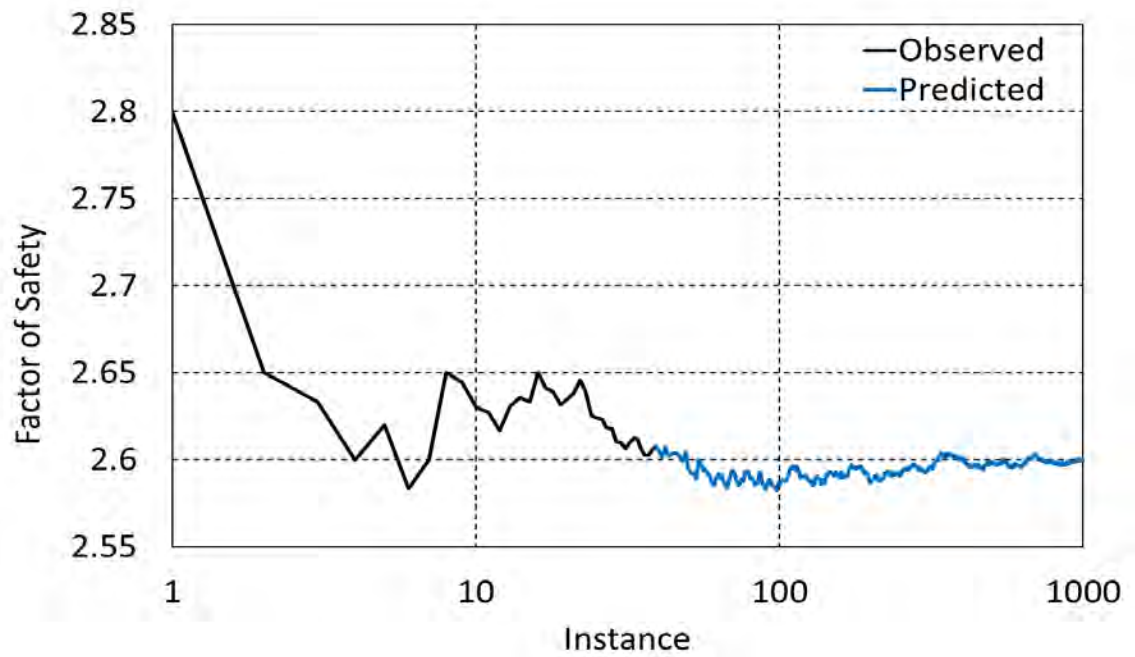
Figure 5.19. Observed and predicted cumulative FoS

K-means cluster analysis of these instances is presented in Fig. 5.9, with the associated hierarchical

cluster dendrogram in Fig. 5.8. It is observed that instances 2 and 4, and 12 and 23 exhibit strong

similarity, and reside within a single, non-overlapping cluster, with slip surfaces of this cluster

shown in Fig. 5.20. The slip surfaces extend from the head to the toe of the slope, with plasticity observed at the toe of the bench, located at the middle of the slope. Conversely, a range of slip surfaces are observed from instances outside the cluster (Fig. 5.21). Instance 5 shows a deep slip surface, extending through the clay layer, while instance 18 produces a slip surface without the plasticity observed within the cluster of Fig. 5.20. Finally instance 29 does not produce a slip surface throughout the entire slope, instead initiating at the base of the slope bench.

Once instances have been categorised into clusters, the dynamics of additionally generated instances can be predicted with the cluster analysis by associating the instance characteristics with a cluster exhibiting similar properties.
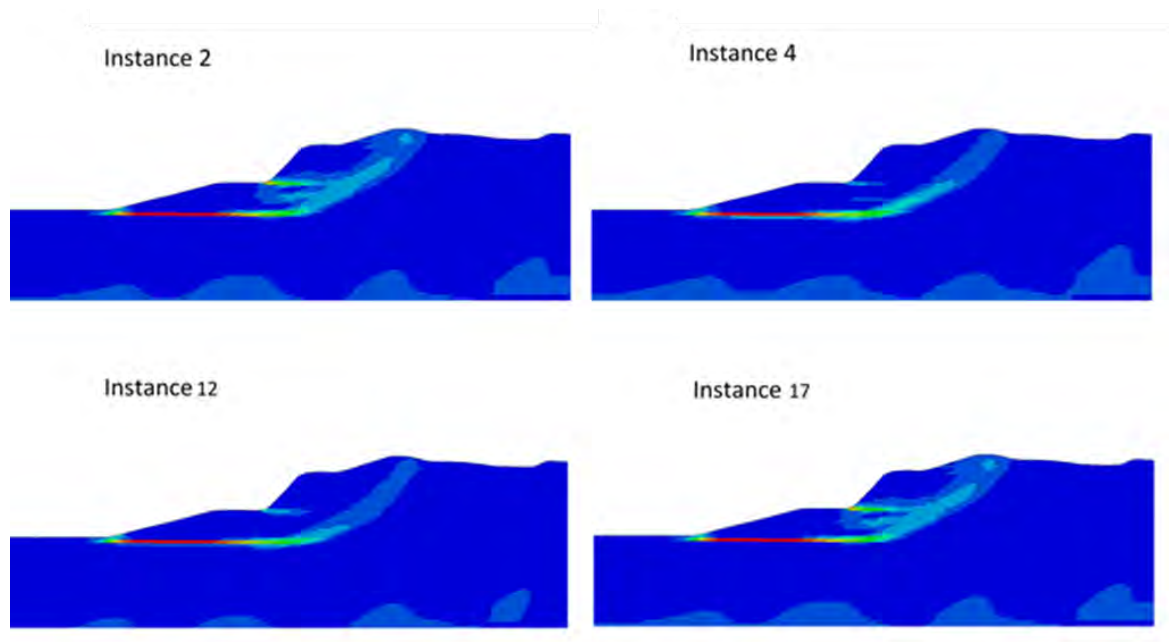
Figure 5.20. Slip surfaces of within-cluster instances
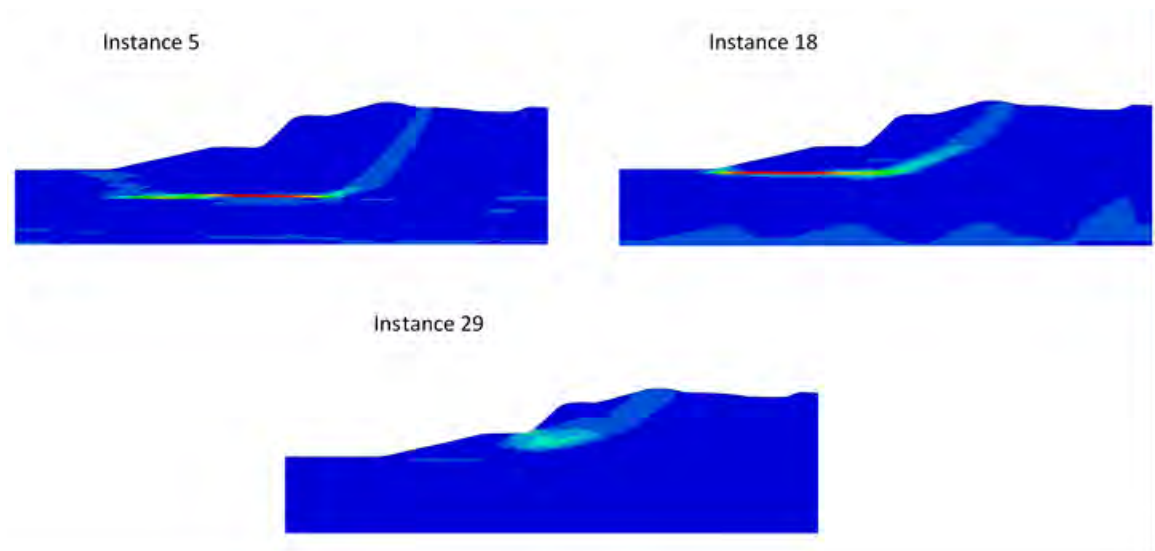
Figure 5.21. Additional slip surfaces

The mid-bench plasticity observed within Fig. 5.20 can be associated with the characteristics common to all instances within the cluster group. In this case, each random field exhibited a weak zone situated in the neighbourhood of the mid-bench, as visualised with random field instance number 2 in Fig. 5.22.
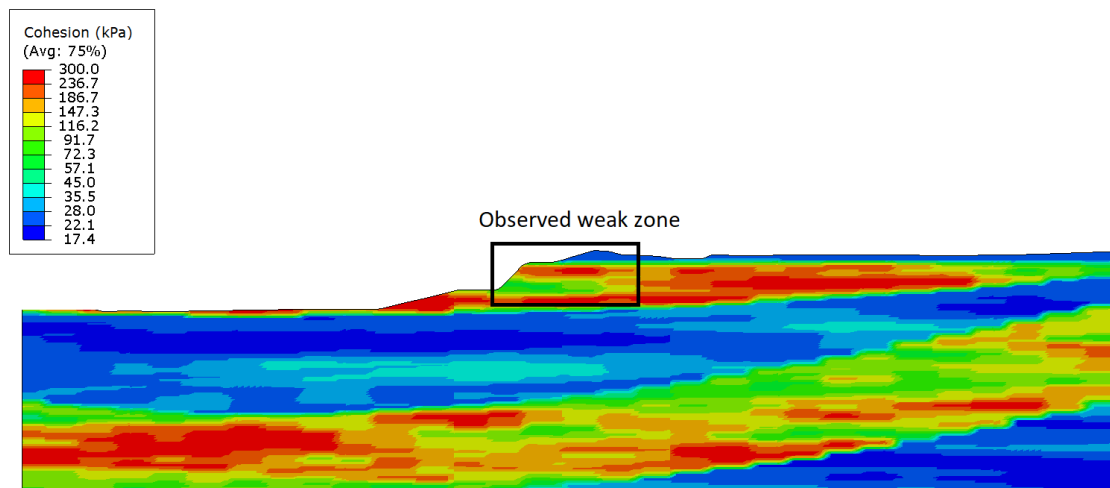
Figure 5.22. Zone of weakness of the cohesion random field instance number 2

5.4.2   Case 2 – Variable Cohesion and Friction Angle Model without Groundwater

When considering the variability of both cohesion and friction angle random fields, a considerable reduction in the FoS is observed compared to Monte Carlo simulation with a fixed friction angle (Fig. 5.23).   The relationship between normalised similarity of cohesion and friction angle compared to the absolute difference in FoS is shown in Fig. 5.24 and Fig. 5.25, respectively. Although a clear trend is evident in cohesion similarity to FoS, the relationship between friction angle and FoS is less evident for this particular model of soil spatial variation.   It is noted that friction angle similarity does play a role in FoS comparability. However, the influence of cohesion random field similarity is significantly larger.   A model consisting of a linear combination of cohesion and friction angle is presented in Fig. 5.26, with linear coefficients chosen to minimise the FoS trend error.   In this example, the ratio of the cohesion to friction angle coefficient was 0.95, indicating the cohesion similarity to be highly influential in determining the FoS.   Fig. 5.27 shows a reduced prevalence of the lower values of random field similarity required to determine an arbitrary absolute difference FoS, compared with Case 1, suggesting a greater number of Monte Carlo simulations are required for prediction.   Nevertheless, with 3% of all similarities producing an absolute difference FoS of less than or equal to 0.1, the number of simulation instances remains significantly less than the requisite instances for traditional Monte Carlo simulation.   Therefore, clustering analysis can be performed with the linear combination of random field similarities.   The incorporation of k-means clusters based on a linear combination of parameters increases the cluster overlap (Fig. 5.28), as slope instance characteristics are dependent on both cohesion and friction angle random field characteristics, reducing the likelihood of random field pairs exhibiting strong similarity.
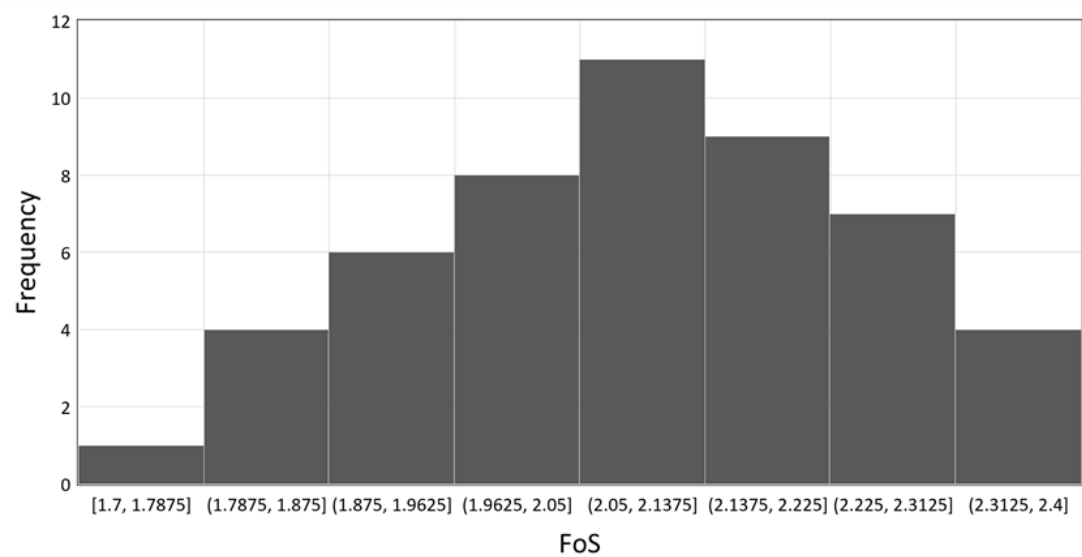
Figure 5.23. Histogram of the FoS distribution
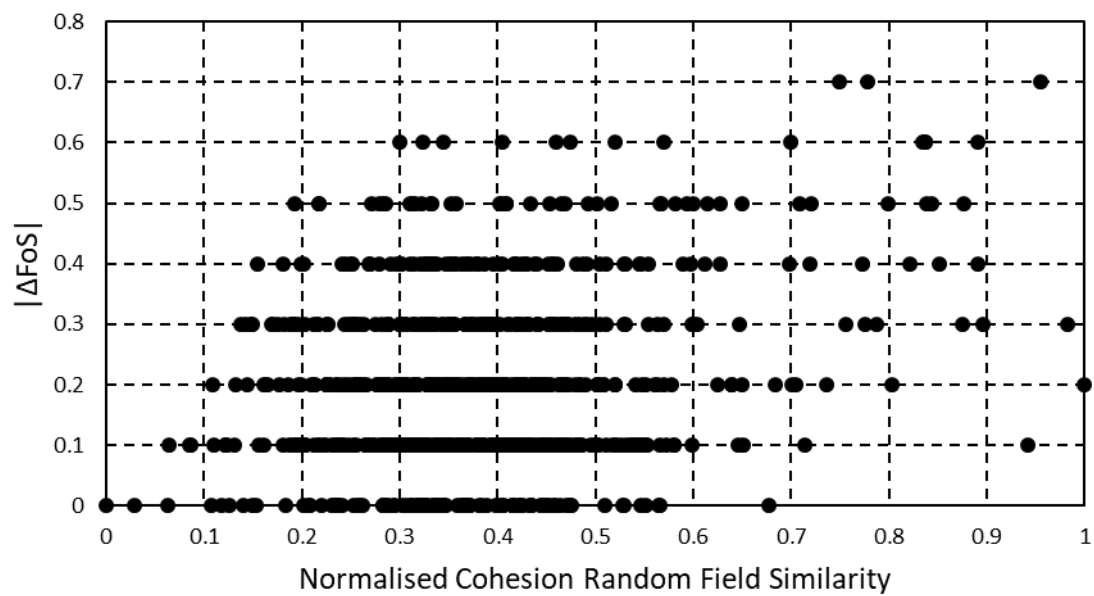
Figure 5.24. Normalised cohesion random field similarity vs. factor of safety absolute
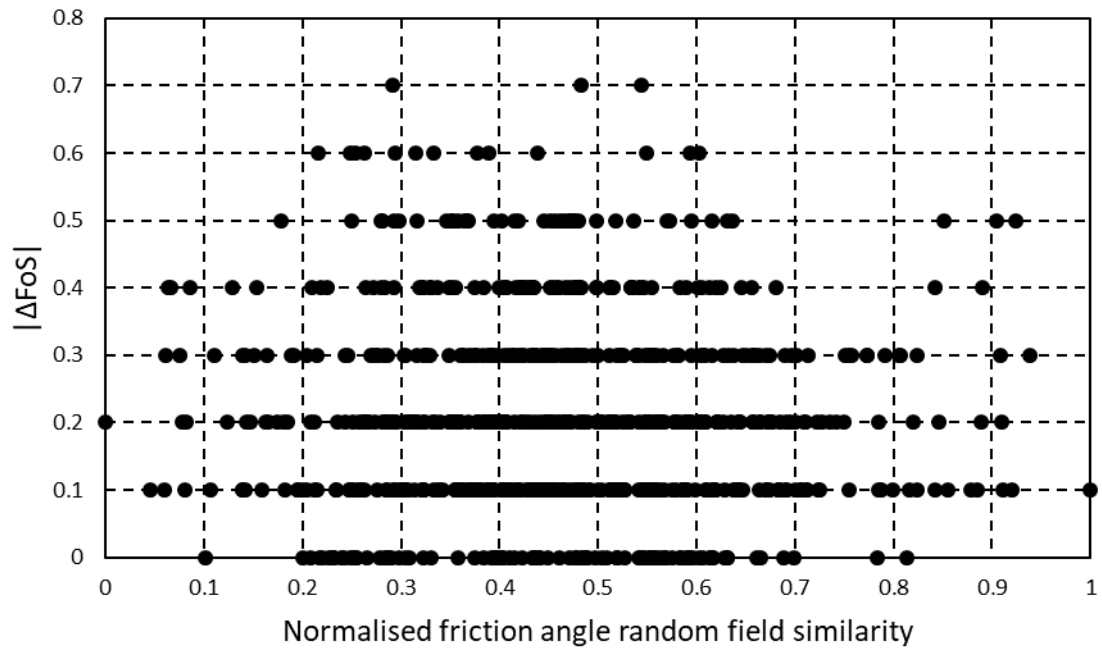
difference

Figure 5.25. Normalised friction angle random field similarity vs. factor of safety absolute
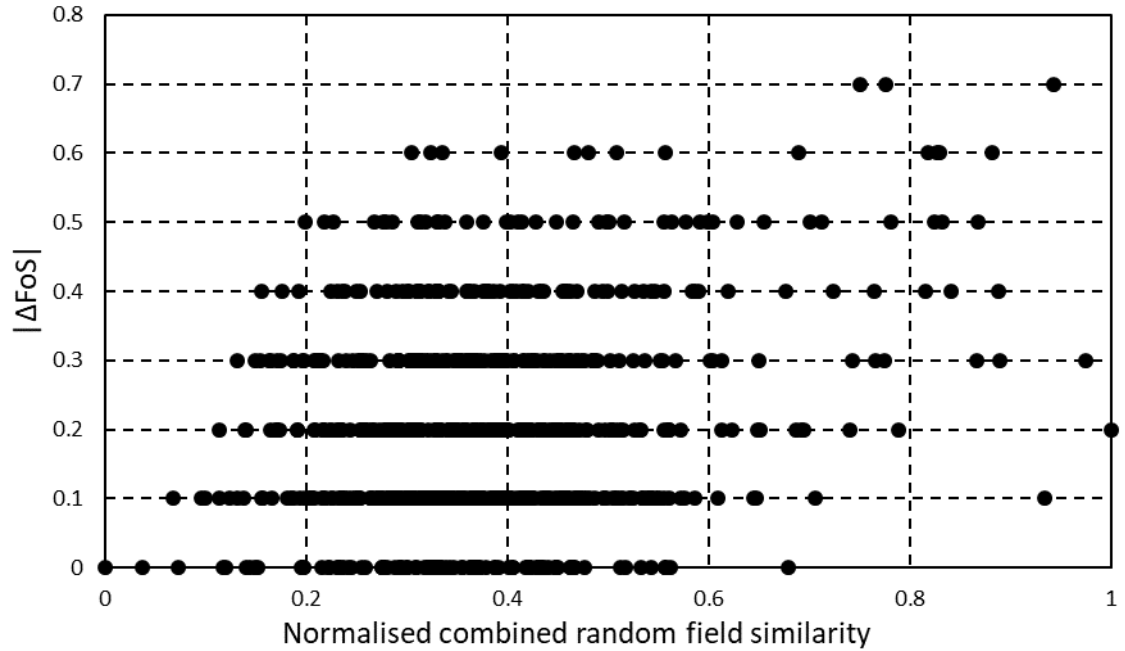
difference

Figure 5.26. Normalised combined random field similarity vs. factor of safety absolute difference
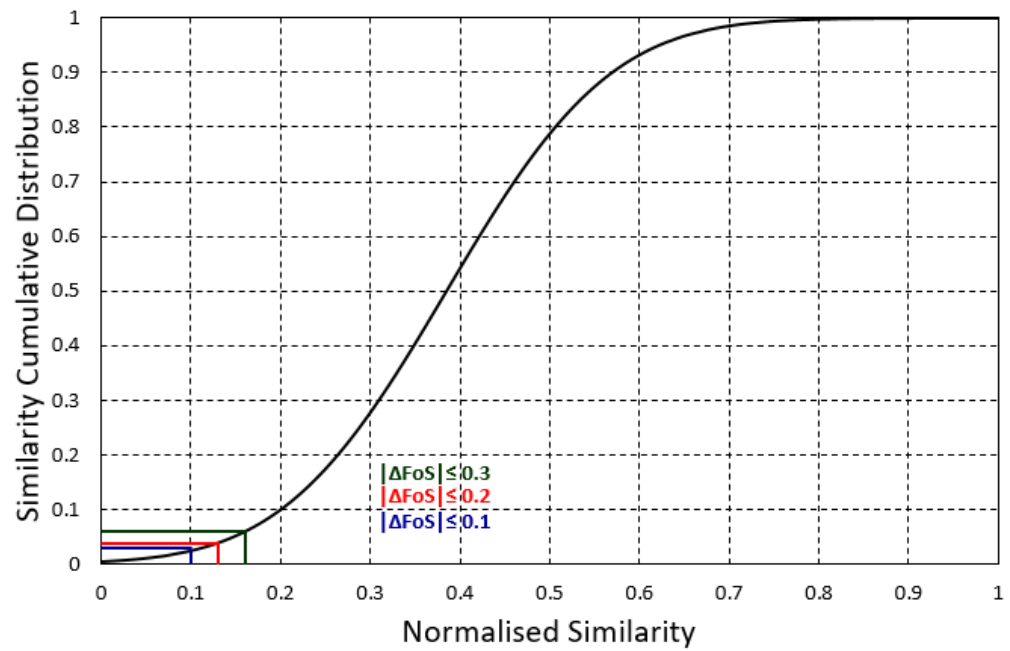
Figure 5.27. Case 2 - Normalised Similarity Cumulative Distribution Function
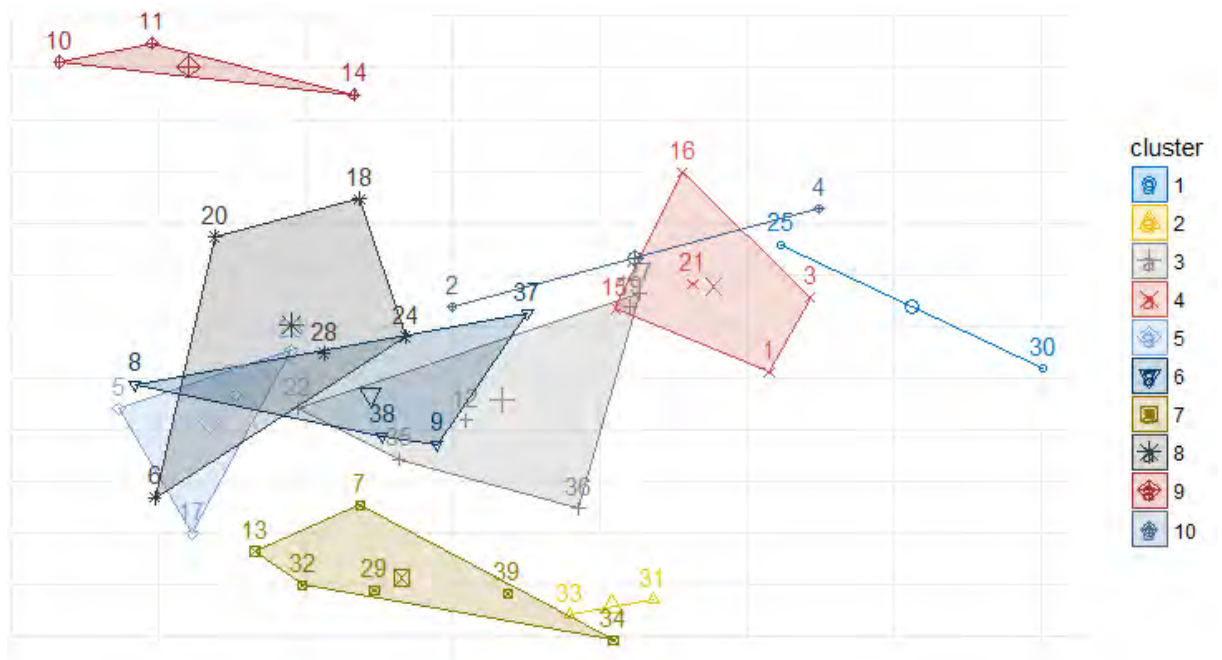
Figure 5.28. K-means clustering of cohesion and friction angle similarity linear combination

5.4.3   Case 3 – Variable Cohesion and Friction Angle Model with Groundwater

Finally, a fully coupled flow-deformation model is presented. Constant water inflow is introduced

into the system through a river located near to the top of batter (Fig. 5.29).
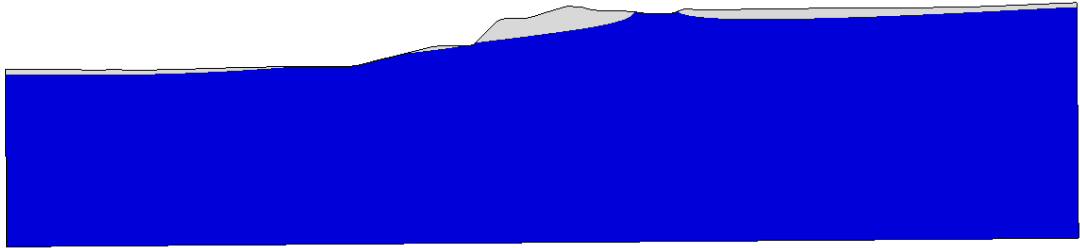
Figure 5.29. Phreatic level after 5 year excavation period

With the inclusion of water through a coupled flow-deformation model, the relationship between

random field similarity and absolute difference FoS remains apparent (Fig. 5.30). Although the

addition of water within the model does not affect the similarity of shear strength random field

similarities, the normalised similarity values required to detect an absolute difference FoS less

than a given value are subject to change (Fig. 5.31).
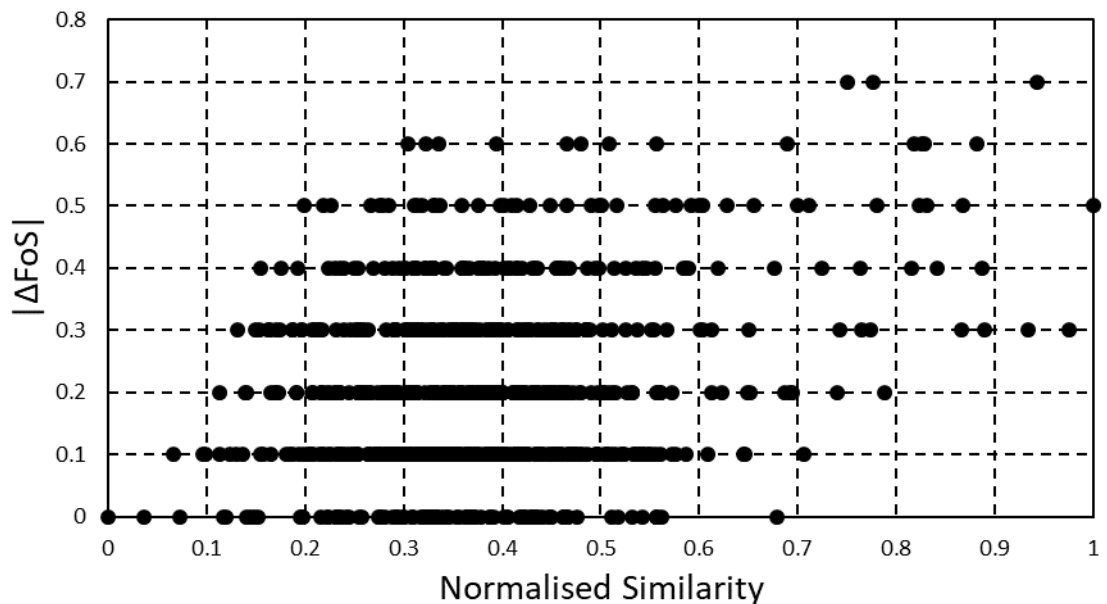
Figure 5.30. Case 3 - Normalised combined random field similarity vs. factor of safety absolute

difference
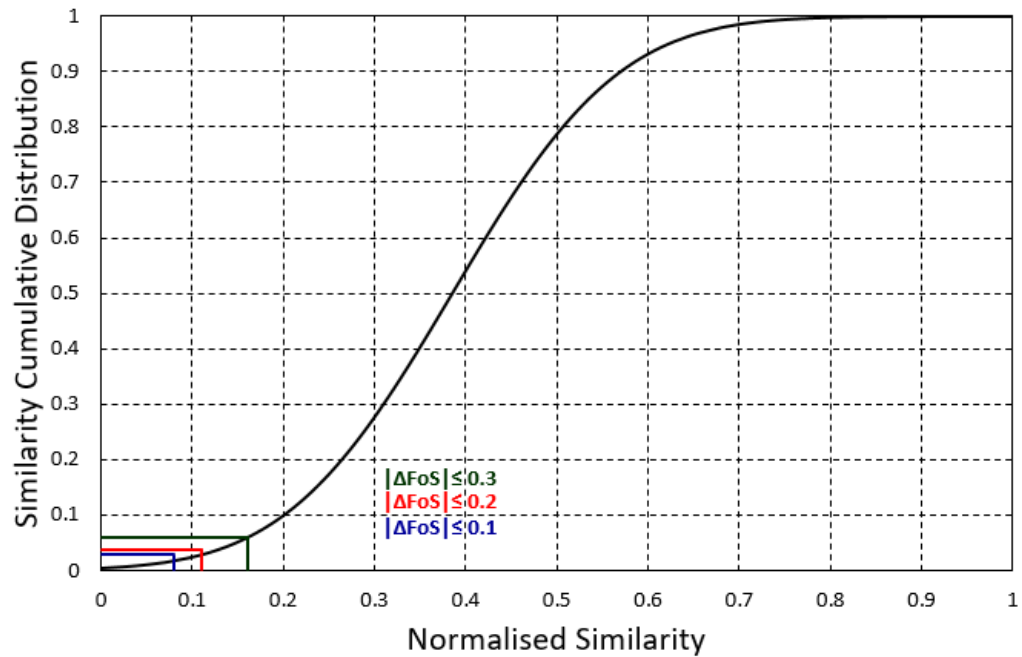
Figure 5.31. Case 3 - Normalised Similarity Cumulative Distribution Function

5.5   Discussion and Conclusion

A method of random field comparison and prediction for finite element slope stability has been
presented in the paper. Three case study simulations of a real open-pit brown coal mine were
provided: the first with constant friction angle without groundwater, the second also without
groundwater but with varying cohesion and friction angle, and the third with groundwater and
variable cohesion and friction angle. The observed Factor of Safety distributions for each case
produced a wide range of values, each encompassing the Factor of Safety of the deterministic case.
The results indicate that spatially variably shear strength parameters can severely impact design the
and risk assessment of real life open-pit mines. Although in each case, the probability of failure
was either low or equal to zero, the reduction of the Factor of Safety in numerous instances may
result in a cases whereby the slope does not conform to design stanrdards. The predictive Random
Field similarity methods detailed within the manuscript are particularly useful for RFEM simulation
of large open-pit mines where classical Monte Carlo simulation is infeasible due to excessive
computational costs.

Reliability analysis is a common method for the RFEM simulation technique, where the probability of failure is estimated by the ratio of stable slope instances to total simulation realisations. In the cases presented within this research, the probability of failure was observed to be either particularly small or equal to zero. For this reason, RFEM simulation combined with the Strength Reduction Method is preferred to reliability anaylsis. The authors agree that in alternative cases with a higher probability of failure, reliability analysis provides a mechanism for greatly reducing the computational cost of analysis, as Strength Reduction is the primary contributing factor to computational cost.

For each case study, the random field comparison technique successfully identified random field instances that contained similar characteristics and structure. Slope stability Monte Carlo simulation instances with high structural similarity exhibited comparative slip surfaces and safety factors. These instances were clustered based on Frobenius matrix norm similarity, allowing sets of instances with similar strength characteristics to be grouped. Further Monte Carlo instances can be compared to these categories, as a predictive tool to determine the likely failure mechanism and factor of safety of a random field that has yet to be simulated. Results of random field case study similarities found the number of random fields required for comparison to predict further simulation instances was exceedingly low compared to traditional Monte Carlo methods. This process substantially reduces the computational requirements of Monte Carlo simulation, with savings in the order of 90% of the necessary number of simulation instances. The technique presents a pathway to drastically increase the computational efficiency of complex random finite element simulations while also comparing and predicting random field characteristics, and their impact on slope failure mechanisms. Although two-dimensional numerical slope simulation has been considered in this case, further attention is required for three-dimensional random field models. It is expected with the inclusion of an additional dimension, the frequency of similar random field pairs decreases as the range of potential random field structures increases. An increase in the number of random field instances required for prediction is anticipated, compared with two-dimensional simulation. However, as the number of instances required for convergence with

conventional three-dimensional Monte Carlo simulation is also significantly larger than the two-dimensional analogue, the authors believe the random field similarity comparison and prediction method is suitable for both two and three-dimensional cases. The potential for in-depth analysis of individual random field characteristics exists, however further attention is required for investigation of the influence of locationally dependent random field characteristics and their individual effects on slope parameters such as slip surface shape and location.

Acknowledgements

6   Probabilistic   Investigation   of   RFEM Topologies for Slope Stability Analysis

The following journal paper explores the similarity based methods defined in the previous chapter to investigate and characterise weak and strong zones within random fields and their impact on slope stability. This journal paper is an accurate representation of the published version, with minor alterations to table and figure numbers for the purposes of continuity.

Abstract

The Random Finite Element Method (RFEM) is an increasingly popular tool in geotechnical engineering, especially for analysis of spatial variation and uncertainty in slope stability. Although the method has gained prominence in recent years, topological effects of strong and weak zones and the impact of their locations remain largely unknown. Although numerous potential slip surface realisations can be generated with RFEM, probabilistic failure statistics are often governed by several representative slip surfaces (RSS). In this research, random field similarity methods and clustering techniques are coupled with RFEM slope stability simulation to determine the impact of shear strength spatial patterns on slope failure mechanisms and safety factors. Regions of significance are highlighted within a case study of a Victorian open-cut brown coal mine, with particular attention given to the effects on the slope failure surface as well the factor of safety. Results are presented of Factor of Safety distributions when particular slip surfaces and clustering constraints are imposed, providing further understanding of the impacts of shear strength characteristics on probabilistic simulation results.

Keywords

Random field; slope stability; random finite element method; RFEM; probabilistic methods; failure surface; topology.

6.1   Introduction

Inherent soil variability and uncertainty are important considerations for geotechnical engineering applications including slope stability analysis. Material heterogeneity often affects localised soil mechanical behaviour as well as the overall response of large geotechnical structures [140]. The stability of slopes and embankments containing high levels of soil heterogeneity and anisotropy are often governed by zones containing weakened materials [242]. Material uncertainty stems from a range of sources including spatial variability, limited site investigation data and measurement errors [243] are key factors contributing to slope failure mechanics [141]. While homogeneous slopes often exhibit well-defined behaviour governing the failure mode and Factor of Safety (FoS), probabilistic simulations containing heterogeneous parameters often exhibit varying failure mechanisms and FoS distributions [244].

Probabilistic slope stability analysis has continued to gain attention [1, 16, 17], increasing with the prevalence of high-performance computing [115, 120, 153, 227]. A common method for heterogeneous slope stability analysis is the Random Finite Element Method (RFEM). RFEM combines random field generation with Finite Element Method (FEM) simulation to perform Monte Carlo Method (MCM) analysis, modelling soil spatial variation without a predefined critical failure surface as required for Limit Equilibrium Methods [2] FEM also allows for the simulation of the progressive failure of a slope until the the final slope failure surface is reached. The generation of random fields of geotechnical parameters can provide a description of soils exhibiting spatial correlation structures. Neglecting the spatial correlation of soil properties can significantly exaggerate the factor of safety and the probability of slope failure [118, 119].

Random field soil profiles for RFEM are often generated with the Local Average Subdivision (LAS) method developed by Fenton and Vanmarcke [156]. LAS produces local averages of soil properties based on the standard normal distribution and a spatial correlation function, the most common correlation function being the Markovian correlation function. RFEM has been implemented with LAS in many forms of research to consider the spatial variation of soils in such fields as seepage analysis [226], bearing capacity of foundations [160] and slope stability analysis [245].

The FoS and critical slip surface of individual RFEM simulation instances are dependent on the patterns and topologies that occur within each random field and are described by the random similarity and clustering methods of Dyson and Tolooiyan [246]. Although many potential slip surfaces can be observed through RFEM analysis, failure probabilities are often governed by a much smaller subset of critical slip surfaces known as representative slip surfaces [175]. This paper presents the results of locationally dependent strong and weak zones of random fields and their impact on the RFEM slope stability analysis. In particular, random fields are clustered into groups based on shear strength similarity, then used to determine the regions of greatest importance on slope failure mechanisms and factors of safety. The relationships between clusters, regions of interest, slip surface depths and safety factors are explored, with particular attention given to the change in Factor of Safety distributions when clusters are constrained or excluded from the analysis. A case study of the Yallourn open-cutbrown coal mine located in Victoria, Australia is presented with a focus on determining the areas of greatest influence on the FoS and slip surface geometry.

6.2   Probabilistic Slope Stability

Random field theory

Vanmarcke's random field theory [247] is a common tool for describing the spatial variability of geotechnical properties. Soils are inherently variable from location to location, mainly due to the natural complexity of geological deposition and material loading history. Soil variability is often

comprised of two components: a deterministic (often depth-dependent) trend component, and a fluctuation component [141]

$$\xi(\boldsymbol{x}) = t(\boldsymbol{x}) + w(\boldsymbol{x}) \tag{6.1}$$

where, $\xi(\boldsymbol{x})$ is the geotechnical parameter to be modelled, $t(\boldsymbol{x})$ is the trend component and $w(\boldsymbol{x})$ is the fluctuation component, commonly named the "off the trend" variation. The fluctuation term $w(\boldsymbol{x})$ is most commonly described by properties a statistical distribution mean μ, standard deviation s, and scale of fluctuation (SoF) Θ [152]. The SoF is defined as the distance up to which random variables are strongly correlated, where little correlation is observed beyond. When Θ is small, parameters exhibit rapid fluctuations over small distances. As Θ increases, fluctuations decrease, producing smoothly varying random fields. The dimensionless parameter known as the Coefficient of Variation (COV) is expressed as the ratio of the standard deviation (s) with respect to the mean value (μ) (Equation 6.2).

$$COV = \frac{s}{\mu} \tag{6.2}$$

A random field is termed stationary if it is characterised by a probability distribution that is invariant throughout the parameter space, where the mean, variance and cumulative distribution are identical at all locations of the random field. Furthermore, the covariance (Cov[X,Y]) of any two random variables X and Y, are dependent solely on the separation distance, independent of their individual locations within the parameter space.

Stationary random fields can be divided into two categories: isotropic, with a scale of fluctuation independent of direction; and anisotropic direction-dependent scales of fluctuation, commonly expressed with a major axis SoF θ_1 and minor axis SoF SoF θ_2. Spatial correlation models are fitted from experimental covariance functions or variograms of field data. The SoF is commonly described by an Auto-Correlation Function (ACF), specifying the average correlation between locations at a lag distance τ. A range of common correlation structures for geotechnical parameters have been categorised [153, 154], the most commonly used being the Markovian exponential and the Gaussian squared exponential ACFs given by Equations (6.3) and (6.4), respectively.

$$\rho(\tau) = \exp\left(-\frac{2|\tau|}{\theta}\right) \tag{6.3}$$

$$\rho(\tau) = \exp\left(-\left(\frac{\tau}{\theta}\right)^2\right) \tag{6.4}$$

where $\rho(\tau)$ is the autocorrelation function; τ is the separation distance; and θ is the scale of fluctuation. Zhu and Zhang [233] summarised a range of anisotropic ACFs characterising common patterns of anisotropy within geotechnical random fields, while various studies have observed significant changes to the FoS based on varying ACFs [235, 236]. The two-dimensional Markovian exponential ACF as implemented in this research is defined as:

$$\rho(\tau_x, \tau_y) = \exp\left(-\frac{2|\tau_x|}{\theta_x} - \frac{2|\tau_y|}{\theta_y}\right) \tag{6.5}$$

where, $\rho(\tau_x, \tau_y)$ is the correlation coefficient between values at lag distances τ_x and τ_y in the x and y directions, respectively. Similarly, θ_x and θ_y are defined as the SoFs in the x and y directions.

The Local Average Subdivision method divides global averages into subdivided regions such that local averages of the divisions preserve the overall global parent value. The method provides a guideline for generating the cell-to-cell variation required by the SoF structure discussed earlier.

Griffiths and Fenton [2] concluded that key parameters for random field slope stability include material cohesion (c) and friction angle (φ), unit weight (γ) and slope geometry. Previous studies have noted that the variation of material unit weight has significantly less impact on the slope FoS compared with material friction angle and cohesion [16]. Furthermore, due to the lack of available data regarding the spatial correlation lengths for the unit weight of Victorian Brown Coal and associated materials, this study focuses exclusively on the influences of cohesion and friction angle variation on slope stability.

Many soil parameters are characterised by a log-normal distribution (with a mean μ_x and standard deviation s_x), as the log-normal distribution consists of strictly non-negative values. Random fields generated by LAS, requiring a lognormal distribution must be transformed from the standard normal Gaussian with as follows:

$$X_i = \exp\left[\mu_{\ln X} + s_{\ln X} G(x_i)\right] \tag{6.6}$$

where X_i is the transformed soil property of the ith element; x_i is coordinates of the centre point of

the ith element; $G(x)$ is the standard normal random field; and $\mu_{\ln X}$ and $s_{\ln X}$ are the mean and

standard deviation of the underlying normal distribution $\ln (X)$, determined by Equations (6.7) and

(6.8) as follows:

$$\mu_{\ln X} = \ln(\mu) - \frac{1}{2} s_{\ln X}{}^2 \tag{6.7}$$

$$s_{\ln X}{}^2 = \ln\left(1 + \frac{s^2}{\mu^2}\right) \tag{6.8}$$

Finite Element Method (FEM) for Slope Stability

In this study, we conduct FEM slope stability analysis with two-dimensional plane strain conditions.

Linear elastic stress-strain conditions are implemented with the perfectly plastic Mohr-Coulomb

failure criterion. This method is comprehensively described by Smith, Griffiths and Margetts [248]

and Griffiths and Lane [32]. Forces are generated by the load of the soil under gravity, creating

normal and shear stresses. These stresses are compared with the Mohr-Coulomb failure criterion

as follows:

$$F = \frac{\sigma_1 + \sigma_3}{2} \sin\phi - \frac{\sigma_1 - \sigma_3}{2} - c\cos\phi \tag{6.9}$$

where, σ_1 and σ_3 are the major and minor principal stresses, respectively; c is the material cohesion;

ϕ is the material friction angle; and F is the failure function interpreted as follows:

F < 0   elastic (stresses inside the failure envelope)

F = 0   yielding (stresses are on the failure envelope)

F > 0   yielding but must be redistributed (stresses outside the failure envelope)

When point stresses reach the Mohr-Coulomb failure envelope, the material at the considered

location is determined to be yielding, while stresses within the envelope remain in an elastic state.

An arbitrary number of RFEM instances are simulated. Although each random field is defined by the same set of statistical distributions, the individual arrangement of strong and weak zones can produce wide-ranging simulation outcomes. For this reason, RFEM analysis requires numerous repeated simulations of random field realisations, as part of the Monte Carlo Method (MCM) framework. The probability of failure P_f is defined by

$$P_f = \frac{n_f}{n_t} \qquad (6.10)$$

where n_f is the number of simulation instances reaching slope failure; and n_t is the total number of simulation instances.

In general, the accuracy of the probability of failure increases with the number of simulations. Hahn and Shapiro [249] proposed an equation for the minimum number of probabilistic instances required for a desired confidence level:

$$n_{min} = m \left(\frac{100d}{\varepsilon}\right)^2 \frac{(1-P_f)}{P_f} \qquad (6.11)$$

where, n_{min} is the minimum number of Monte Carlo simulations; m is the number of random variables; d is the normal standard deviate dependent on the desired confidence level; and ε is the relative percentage error in estimating P_f; Griffiths and Fenton [2] determined that 1000 Monte Carlo simulation instances was sufficient for a 2:1 undrained clay slope, to achieve convergence in the probability of failure and factor of safety.

In this study, the finite element geometry was partitioned into numerous distinct element partitions, such that each element set was allocated material strength parameters based on the location of an associated random field cell. *Abaqus* elements of type CPE4P (4-node plane-strain quadrilaterals bilinear displacement, bilinear pore pressure) were implemented for all elements within the model. A fine mesh of 40,000 elements was composed (Fig. 6.1), due to the intricacy of the slope geometry and material layering, coupled with the element size stipulated by the underlying material parameter spatial distribution.

240m

280m

1465m

Excavated material   Post-excavation slope
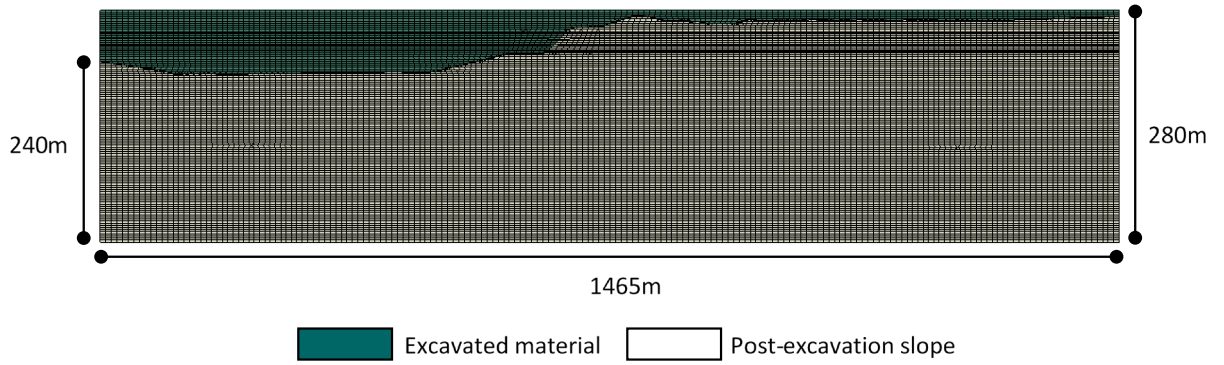
Figure 6.1. FEM model geometry and mesh distribution

When a random field is mapped to the finite element domain, the impact of the local averaging process must be considered. Log-normal mean and standard deviation parameters are affected by LAS, due to the dependence of the log-normal mean on the underlying Gaussian distribution mean and standard deviation (Equations 6.6 and 6.7). Hence, the random field must be adjusted when mapped to the finite element geometry, based on element size, with a variance reduction factor applied. The variance reduction procedure employed in this research is comprehensively detailed by Griffiths and Fenton [2].

Strength Reduction Method

The factor of safety of a slope is defined as the ratio of the original shear strength parameters to the values necessary to bring the slope to the point of failure. Alternatively, the FoS can be considered as the minimum factor required to bring the slope to failure [75]. The strength reduction method, commonly referred to as c/φ reduction is a procedure to iteratively reduce the shear strength parameters until slope failure is achieved. The strength reduction method equations are defined as follows:

$$c = \frac{c_0}{SRF} \qquad\qquad (6.12)$$

$$\phi = \tan^{-1}\frac{\tan\phi_0}{SRF} \qquad\qquad (6.13)$$

where, c_0 and ϕ_0 are the initial cohesion and friction angle parameters, respectively; and SRF is the

trial strength reduction factor. The FoS is given by:

$$FoS = \frac{c_0}{c_f} = \frac{\tan\phi_0}{\tan\phi_f} \qquad (6.14)$$

where, c_f and ϕ_f are the cohesion and friction angle at failure, respectively. Three common

mechanisms for determining slope failure and the corresponding factor of safety are:

1. Development of plastic zones forming a critical slip surface [30].

2. Considerable slope deformation.

3. Non-convergence of the FEM solution [35].

This study implements an optimised SRM, as described by Dyson and Tolooiyan [228] in the Finite

Element Method software package *Abaqus*, which has no predefined inbuilt SRM.

Random Field Similarity

The random field similarity methods comprehensively detailed by Dyson and Tolooiyan [246]

allow for characterisation and prediction of the slope stability FoS for individual random field

instances. Random field instances are compared by the locationally dependent element-wise

difference of geotechnical parameters, in conjunction with the Frobenius norm $||\boldsymbol{D}||_F$, defined as

$$||\boldsymbol{D}||_F = \left(\sum_{i=1}^{m}\sum_{j=1}^{n}|a_{ij} - b_{ij}|^2\right)^{1/2} = \sqrt{trace[(A-B)^T(A-B)]} \qquad (6.15)$$

where, A and B are two random field matrix instances for comparison of size m x n; and a_{ij} and

b_{ij} are their elementwise components, respectively. When $||\boldsymbol{D}||_F$ is small, the two random field

instances are similar, producing comparable FoS values. As $||\boldsymbol{D}||_F$ increases, the random fields

become dissimilar, meaning FoS comparison is no-longer possible. The Mantel test which

establishes the level of interrelation between two matrices [250] is implemented to determine the

likelihood of an associated structure between matrices of random field similarities and safety

factors. The test adopts a Monte Carlo method whereby the elements of the random field matrices

are randomly permuted and then compared, to determine the likelihood of the initial non-permuted random field structure occuring by natural variation. When the association of the initial matrices is located at the tail of the distribution of permuted matrices, the likelihood of occurance by natural variation is low. Once a structure suggesting a strong relationship between random field similarity and FoS is identified, the random field similarities can then be used as a prediction method to determine the slope FoS without undergoing the lengthy process of FEM simulation. Furthermore, these random field instances can be clustered into categories based on their similarity to highlight . Fig. 6.2a provides an example of 10 categories of random fields based on similarities, with the k-means clustering algorithm, while Fig. 6.2b shows pairs of the most similar random fields with a cluster dendogram.
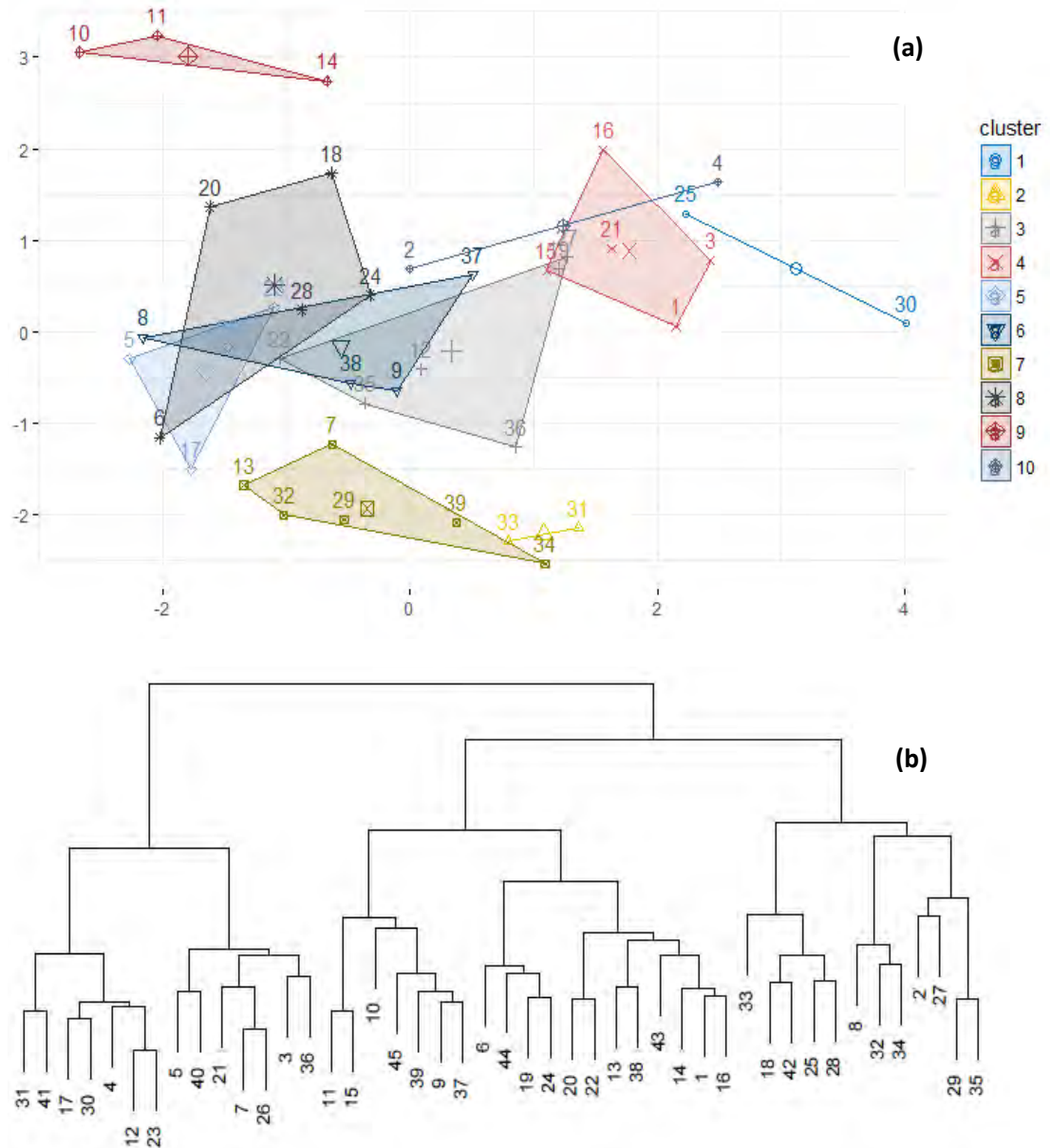
Figure 6.2. (a) K-means cluster of random field instances; (b) cluster dendrogram of random field

instances.

The process of random field generation, finite element method simulation and failure mechanism

classification is outlined in Fig. 6.3. Once weak zones are identified using random field similarity

techniques, spatially dependent failure mechanisms can be determined. These prediction

techniques are used to optimise the method of obtaining FoS convergence by limiting the number

of necessary FEM simulations.
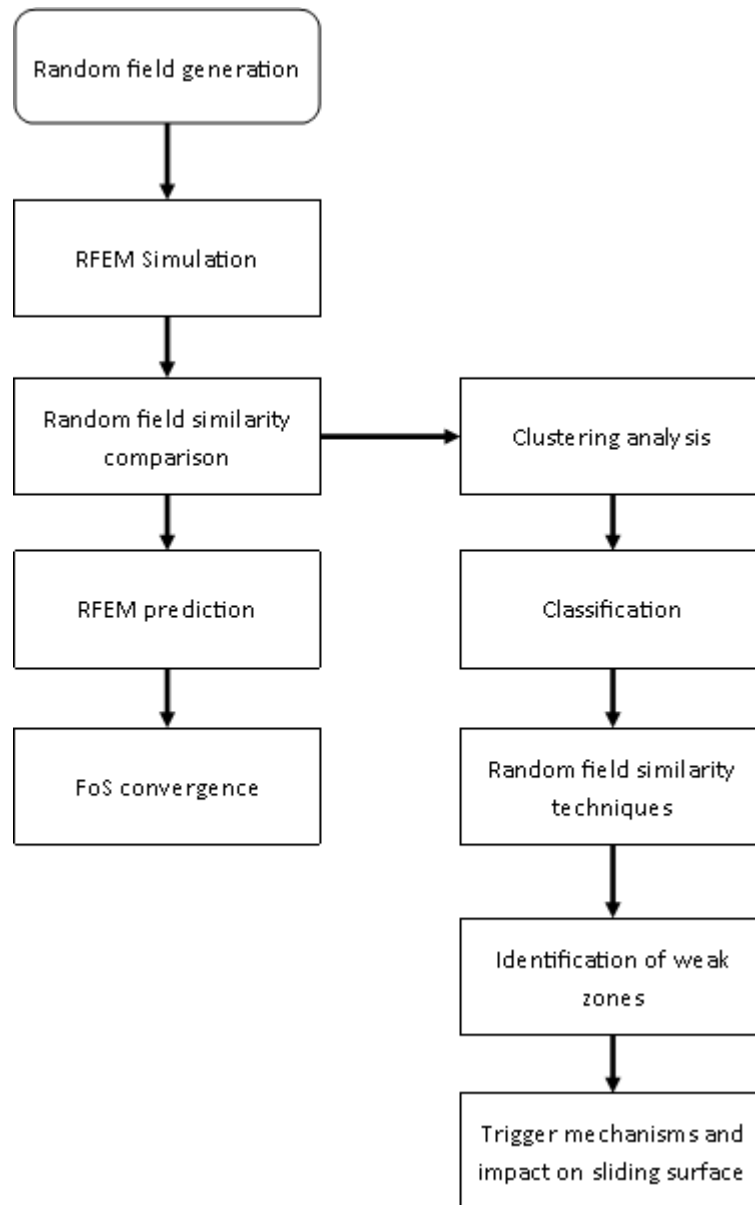
Figure 6.3. RFEM generation and analysis methodology.

6.3   Case Study Site Conditions

The Yallourn brown coal mine of the Latrobe Valley (Fig. 6.4a) is Australia's second largest open-cut mine. Due to a batter failure in the open-cut in 2007, the TRUenergy Yallourn power station lost roughly two-thirds of its power generation capacity for weeks, causing significant damage to the mine [204]. Below the coal seam at Yallourn lies a layer of interseam material, much weaker in strength [207]. The significant difference between coal and interseam shear strengths increases the likelihood of block-sliding failure mechanisms along the top of the interseam layer [209]. In

this research, a two-dimensional cross-section of the north-east batter of the Yallourn open-cut (Fig.

6.4b) is considered, with slope geometry before and after excavation described by Fig. 6.4c and Fig.

6.4d, respectively.
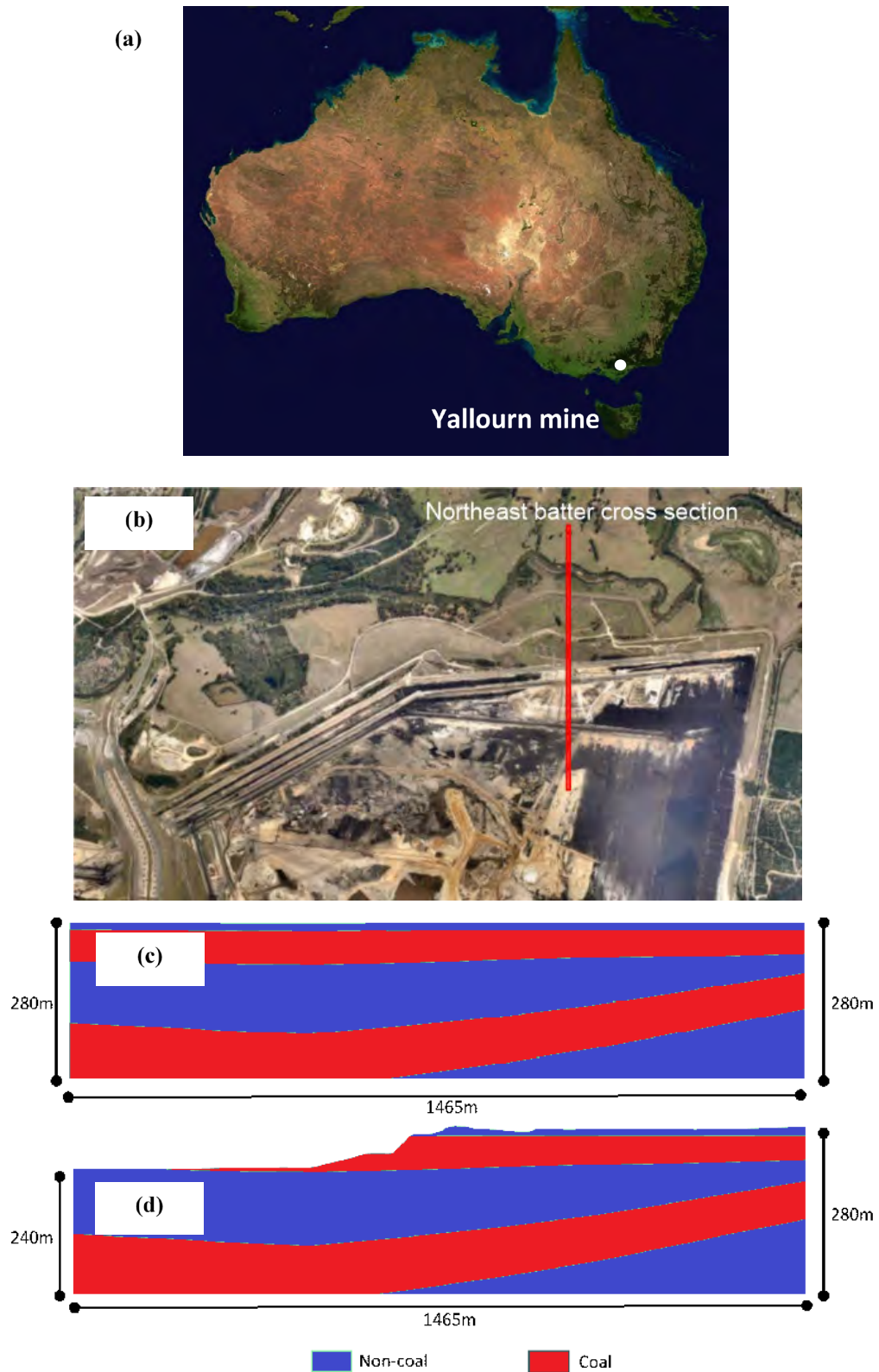
Figure 6.4. a) Location of the Yallourn mine in the Latrobe Valley b) two-dimensional cross-

section of the north-east batter at the Yallourn mine c) slope strata prior to excavation d)

excavation geometry

Table 6.1 lists the material parameters of both coal and the non-coal interseam, including saturated

and unsaturated unit weight γ, Elastic modulus E, Poisson's ratio v, and permeability k. Material

shear strength statistics and distributions are given by Table 6.2 and Fig. 6.5, respectively. In each

case, a log-normal distribution is fitted to the data such that all values are strictly non-negative. The

friction angle is often considered as a bounded function (as the angle is required to be between 0

and 90 degrees). However, the spread of friction angles (Fig. 6.5b and 6.d) is sufficiently narrow in

both cases to ensure that sampled values almost certainly remain less than the upper bound of 90

degrees. For this reason, the authors have implemented a lognormal distribution of the friction

angle, rather than the commonly used lognormal of the tangent of the friction angle. The lognormal

distribution is able to approximate normal distributions for given mean and standard deviation

parameters, hence the use of this particular distribution does not compromise the shape of the

function. Of particular note is the high coefficient of variation observed for the cohesion of coal.

This is attributed to the brittle nature of the material which commonly exhibits micro-fracture,

cracking and large scale jointing [251, 252].

Fig. 6.6 – 6.7 and Table 6.3 detail the spatial autocorrelation of coal and non-coal shear strengths.

The observed spatial correlation structures are fitted with Markov decaying exponential trends. It

is evident that the spatial variation in the down-the-bore direction τ_y varies more rapidly than the

across-the-bore direction τ_x, for both coal and non-coal shear strength parameters. This anisotropic

feature is common to soft-rock materials due to processes controlling their depositional creation

and consolidation. In particular, the friction angle of coal in the τ_y direction fluctuates over a matter

of metres, while all material parameters in the τ_x direction exhibit smoothly varying values over a

distance of hundreds of metres, producing a layer-cake description of shear strengths. Numerous

studies have been conducted to determine the relationship between shear strength variables for a

range of materials [148-150, 253]. The correlation coefficients of shear strength parameters with

respect to core specimen depth, as well as c/φ cross-correlation coefficients are presented in Table 6.4, with Pearson's r defined as:

$$r_{x,y} = \frac{\sum_{i=1}^{n}(x_i-\bar{x})(y_i-\bar{y})}{\sqrt{\sum_{i=1}^{n}(x_i-\bar{x})^2 \sum_{i=1}^{n}(y_i-\bar{y})^2}} \tag{6.16}$$

where, r is Pearson's correlation coefficient; n is the sample size; x_i and y_i are i^{th} indexed variable samples; and $\bar{x}$ and $\bar{y}$ are the sample means. Often shear strength parameters of materials exhibit a weak negative correlation, however, in this case, no discernible correlation exists between cohesion and friction angle, nor is any depth dependent shear strength trend present.

Table 6.1. Geotechnical parameters for coal and non-coal materials

Material	γ_{unsat} (kN/m³)	γ_{sat} (kN/m³)	E (MPa)	v	k (m/day)
Coal	11.4	11.5	40	0.3	7.6e-3
Non-coal	20.15	20.2	52	0.3	4.7e-2

Table 6.2. Shear strength parameter statistics

	Coal		Non-coal	
Parameter	c (kPa)	φ (°)	c (kPa)	φ (°)
Mean (μ)	150.7	27.3	31.8	23.7
Standard Deviation (s)	69.8	4.9	5.0	4.5
COV	0.5	0.2	0.2	0.2

Table 6.3. Shear strength length scales

	Coal		Non-coal	
Scale of Fluctuation (m)	c	φ	c	φ
θ_x	320.3	772.4	812	627.8
θ_y	23.1	8.7	35	13.1

Table 6.4. Shear strength correlations

	Coal		Non-coal	
	c	φ	c	φ
Correlation with depth	0.129	-0.260	-0.027	-0.060
$r_{c,\varphi}$	0.046		-0.003	
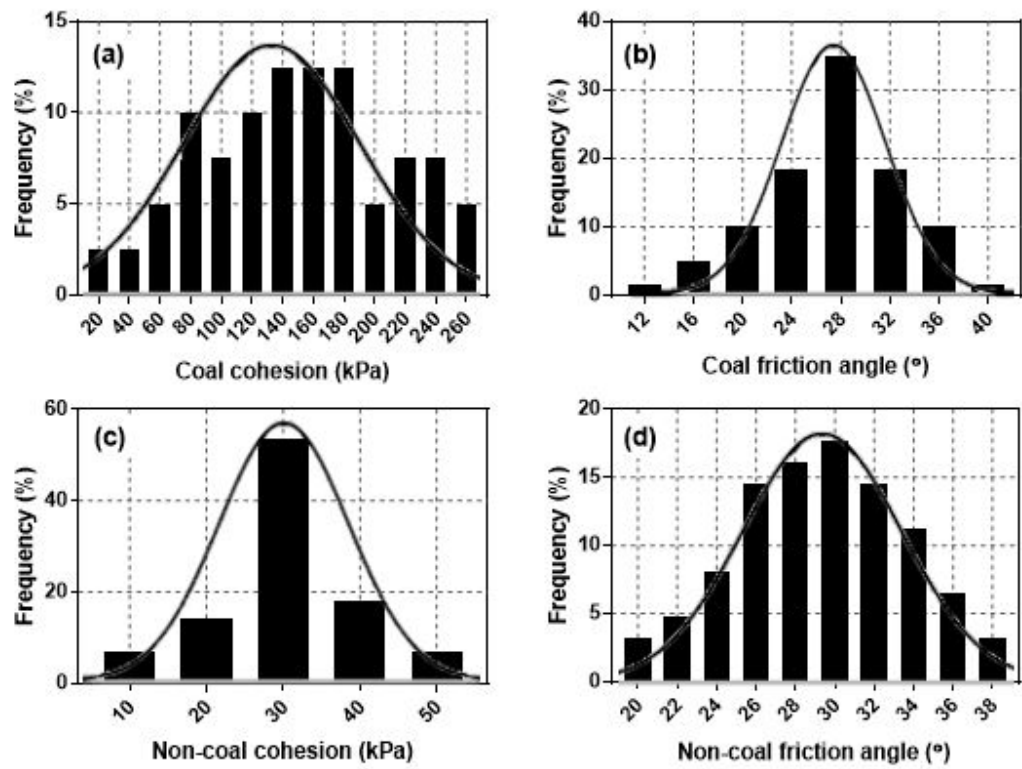
Figure 6.5. Geotechnical parameter probability density functions: a) coal cohesion b) coal

friction angle c) non-coal cohesion d) non-coal friction angle.[1]

[1]Minor modifications to this figure have been made after publication.
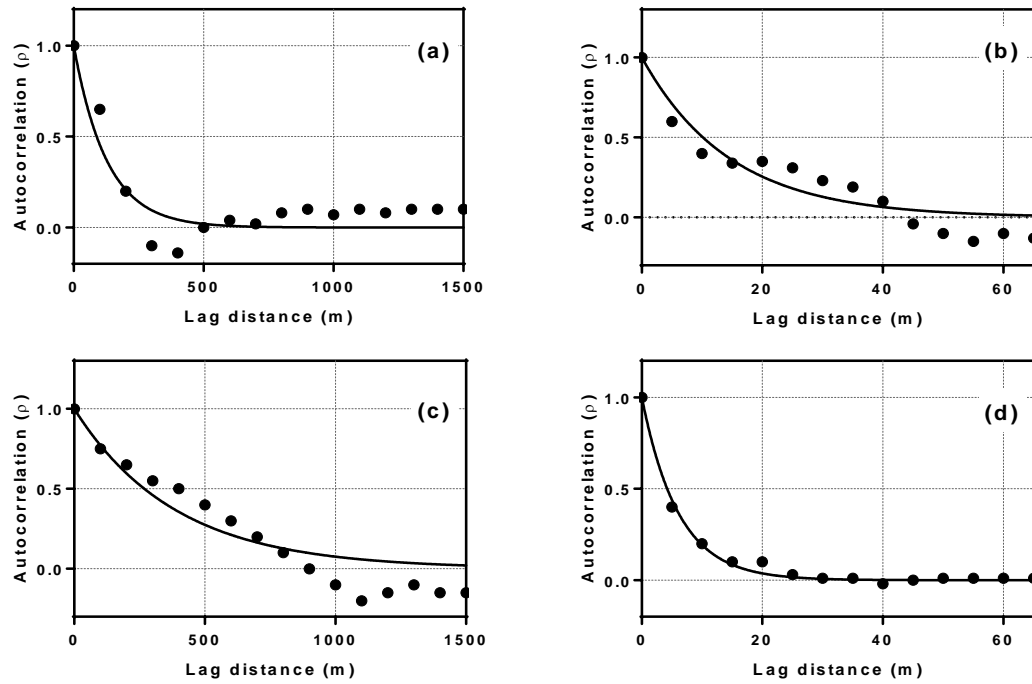
Figure 6.6. Coal shear strength fitted spatial autocorrelation functions: a) cohesion, horizontal plane b) cohesion, vertical plane c) friction angle, horizontal plane d) friction angle, vertical plane.
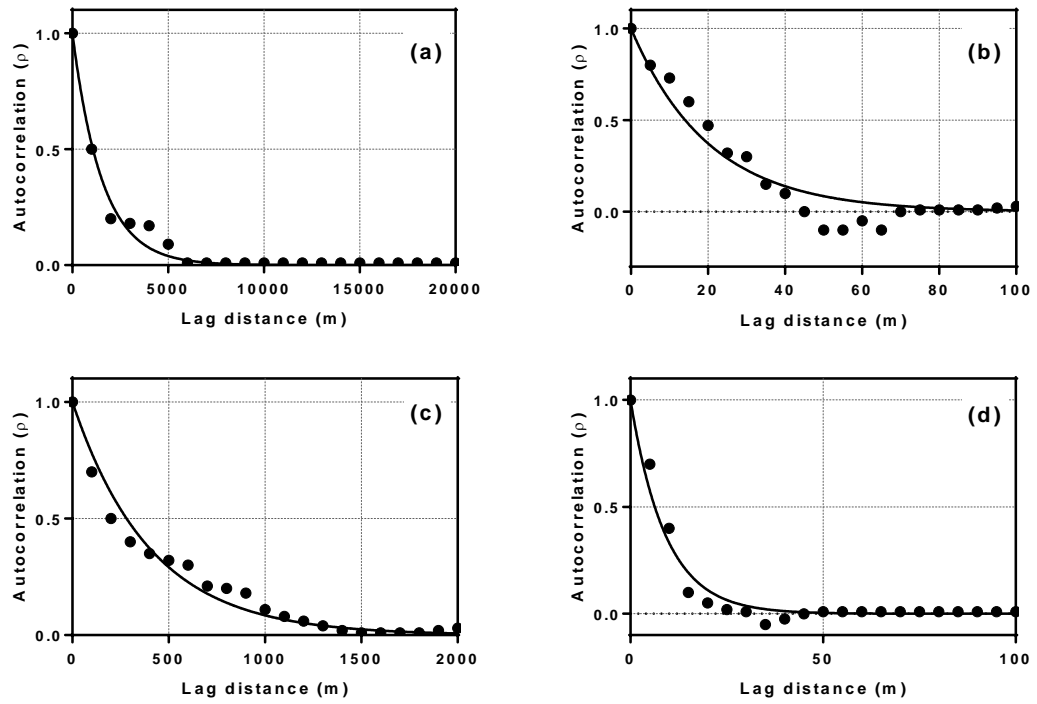
Figure 6.7. Clay shear strength fitted spatial autocorrelation functions: a) cohesion, horizontal

plane b) cohesion, vertical plane c) friction angle, horizontal plane d) friction angle, vertical

plane.

6.4 Results

RFEM Slope Stability

Strength reduction of the deterministic slope yielded a FoS of 2.1, with a slip surface along the base

of the coal (Fig. 6.8). Initially, 40 random field instances were generated for RFEM Monte Carlo

simulation. After these initial random fields were simulated, the Mantel test was implemented to

determine the correlation between random field similarity and FoS (Fig. 6.9a). The cohesion and

friction angle random field similarities vs FoS presented in Fig. 6.9b and 6.9c. The overall

correlation (r = 0.0212) determined from the Mantel test is weak. However, the test shows the

relationship between random field similarity and FoS is unlikely to occur purely by natural

variation. A p-value of 0.0139 indicates this correlation would only occur by chance 1.39% of the

time, for Monte Carlo simulation. Although the similarity vs FoS relationship is weak when

considering the full spectrum of similarity values, a strong relationship exists for small cohesion

similarity values (Fig. 9b). As the correlation structure is much weaker between friction angle

similarity and FoS (Fig. 9c), a linear combination of the two random fields is necessary for FoS

prediction. Fig. 9(d) indicates the likelihood of a FoS difference of 0.1 and 0.2 is 5% and 9% of all

random field similarity comparisons, respectively. Hence, approximately 5% of normalised

similarities from any further generated random field instances would be less than the value of 0.2

necessary to predict the FoS within a tolerance of 0.1. The prediction level of 5% suggests at least

20 random field realisations are necessary to produce at least one random field similarity

comparison pair (i.e. 5% of 20) for the purposes of FoS prediction. The number of pairwise

comparisons of a set of n objects is given by $\frac{n(n+1)}{2}$. As a precautionary measure to ensure a

sufficient number of similarity comparison pairs, double the number of initial random field

instances (40 realisations) were initially generated, producing $\frac{40 \times 41}{2} = 820$ similarity comparisons.

It is also necessary to be confident that the comparison rate has converged at the 5% level. For this

particular example, the 5% level stabilised after 25 random field realisations, and remained constant

thereafter. Hence, the initial 40 simulation realisations were deemed sufficient as a conservative

estimate of the number of realisations required for initial RFEM treatment. Thereafter, further random field realisations can be generated, with the FoS assumed without the requirement of finite element simulation. When the comparison with the initial 40 instances did not produce the similarity necessary for prediction, the random field realisation was deemed necessary for full FEM simulation.

The observed random field spatial variation is visible in Fig. 6.10. RFEM simulation yielded a FoS of 1.55, significantly lower than the value of 2.1 from deterministic simulation, highlighting the impact of weak zones on reducing the slope strength. The converged mean FoS obtained from random field similarity prediction after 1000 realisations is shown in Fig. 6.11a, with individual safety factors normally distributed, varying from 1.1 to 2.0 shown in Fig. 6.11b and Fig. 6.11c. A range of failure surface shear bands are observed, with depths varying from RL -41 to RL -99, a difference of nearly 60 metres (Fig. 6.12). The boundary between the coal base and the interseam layer sits at RL -41. The Monte Carlo simulation results illustrate that failure mechanisms of block sliding along the top of the interseam layer, as well as deeper circular failure through the interseam occur in different random field realsations. The most common failure depth occurs along the coal-interseam boundary (Fig. 6.13a). Although some random field realisations result in slip surfaces progressing below RL -41, slip surfaces with plasticised elements below RL -80 occur infrequently. Shear surfaces invariably plasticised from the toe of the slope along the lower bench to the crest of the slope, with little variation in the location of shear band endpoints. The shear band length varied between 340m and 460m (Fig. 6.13b), producing a total area of deformation between 14,000m^2 and 36,000m^2 (Fig. 6.13c). Of particular note is the correlation between slip length and mobilised area. As the plasticised region always materialises near the slope toe and slope crest, the failure area can be represented purely in terms of the slip length. Furthermore, Fig. 6.13d suggests a linear relationship between FoS and slip surface length (and additionally depth) indicating low factors of safety occur when the plasticised region does not penetrate the non-coal domain, allowing coal blocks to slide along the interseam layer. Although low factors of safety coincide with shorter, shallower failure surfaces and similarly, and higher FoS values with deeper slip surfaces, the

relationship between the FoS and slip surface is increasingly complex about the FoS mean (FoS =

1.55).
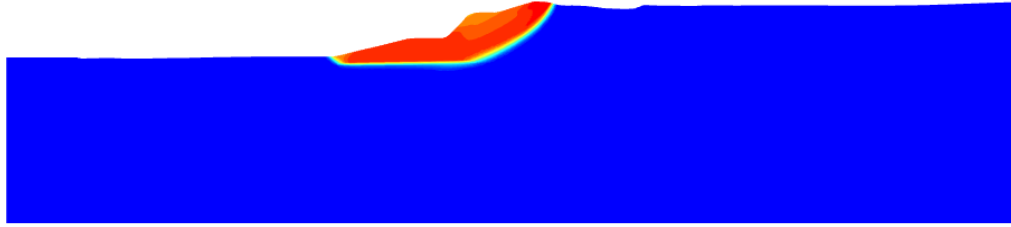
Figure 6.8. Deterministic slope failure surface.
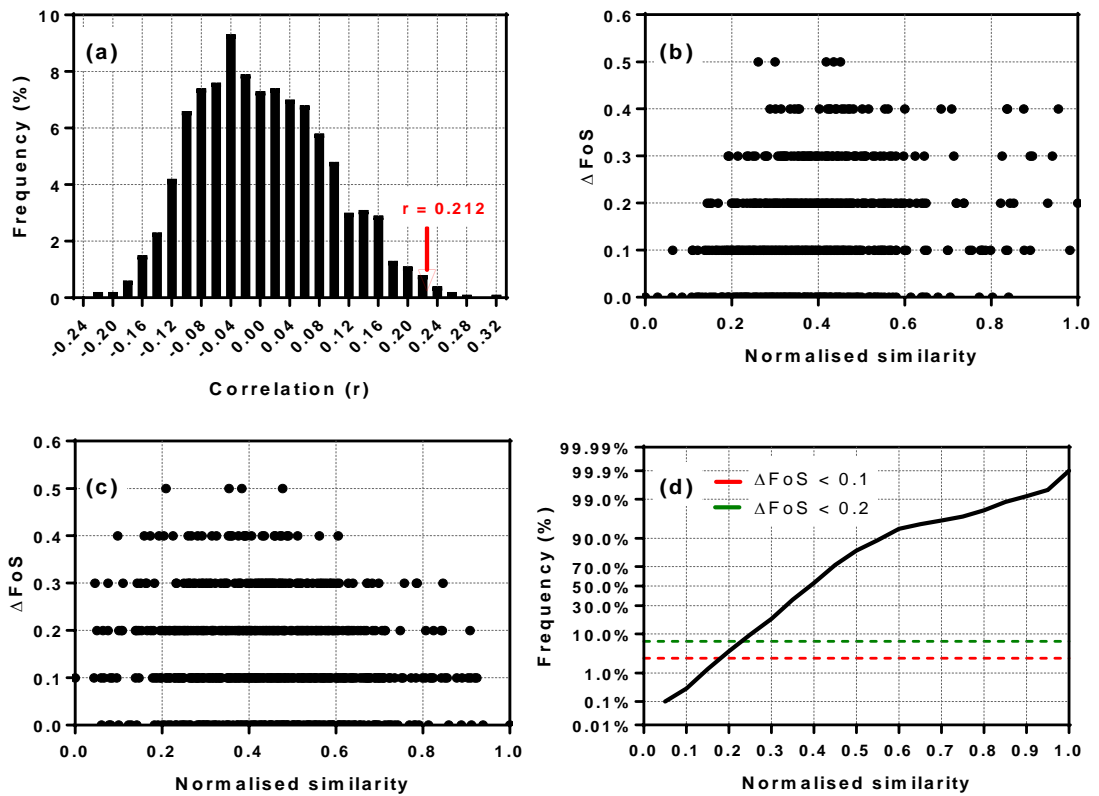
Figure 6.9. a) Mantel matrix similarity distribution b) normalised cohesion random field

similarity vs FoS c) normalised friction angle random field similarity vs FoS d) cumulative

frequency distribution of random field normalised similarity.
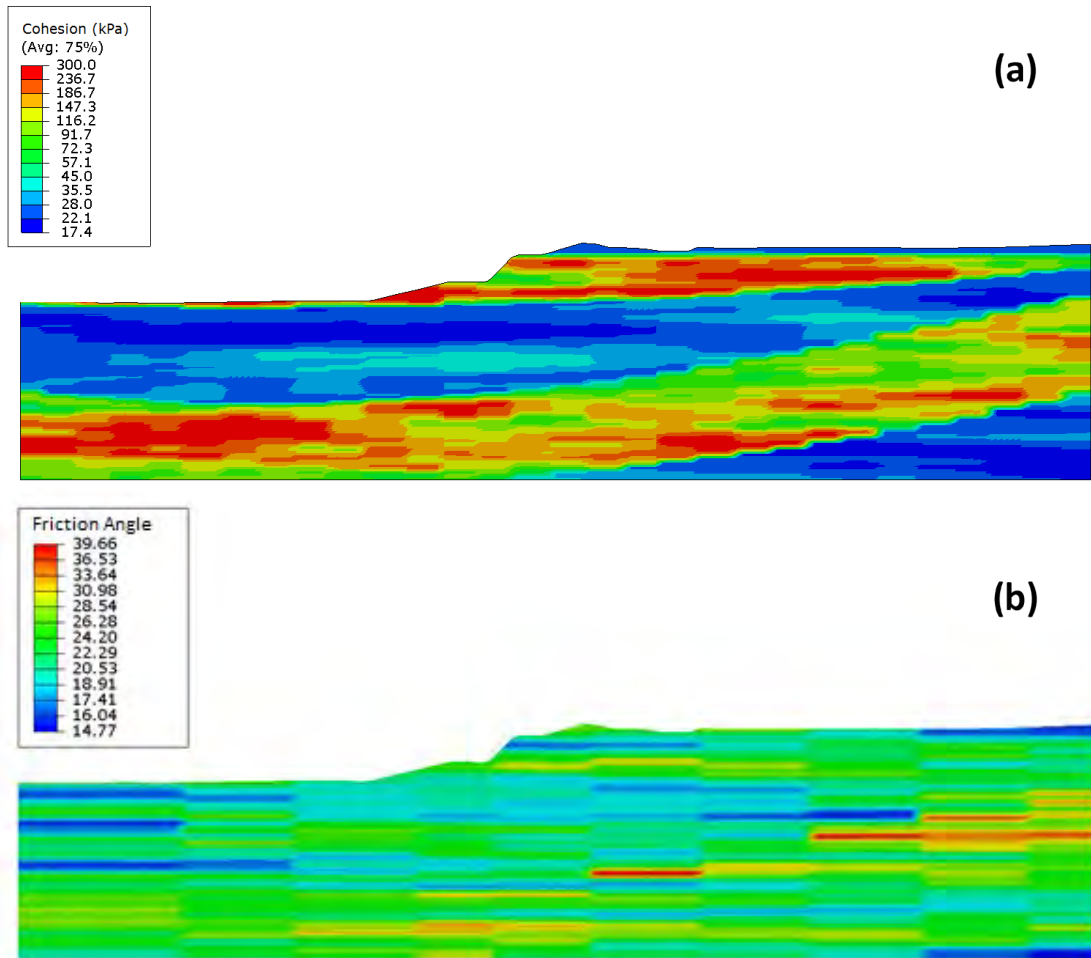
Figure 6.10. A random field realisation a) cohesion random field b) friction angle random field.
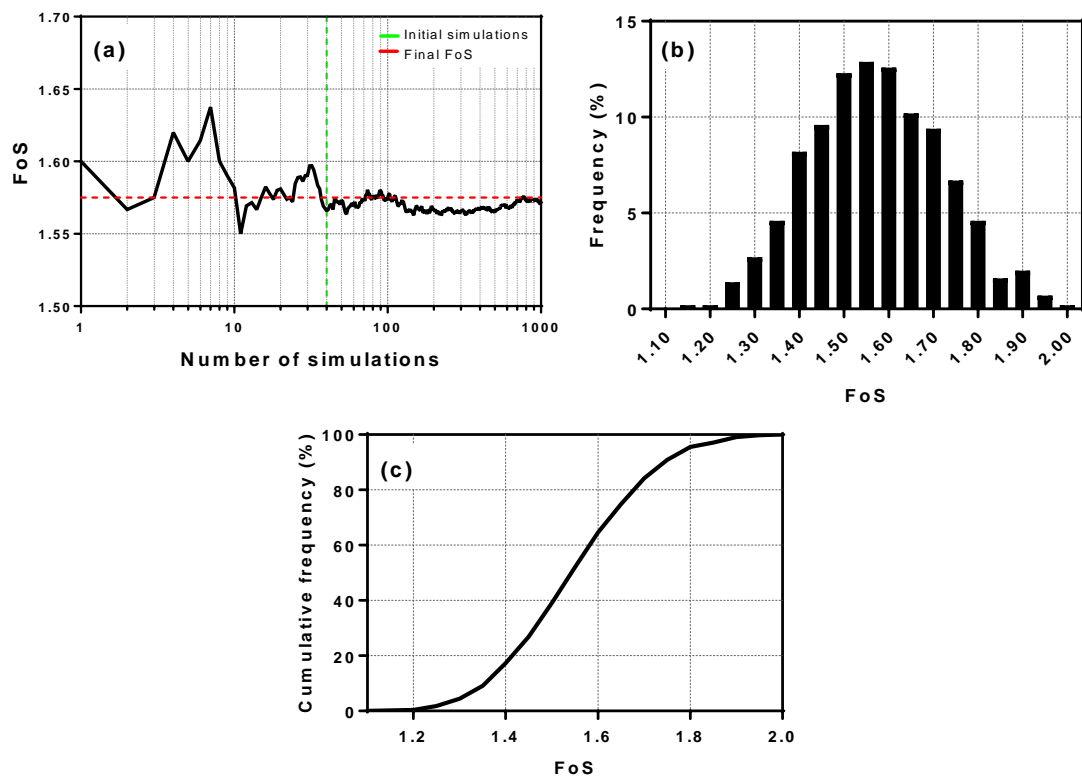
Figure 6.11. a) FoS convergence b) FoS probability distribution c) FoS cumulative distribution.
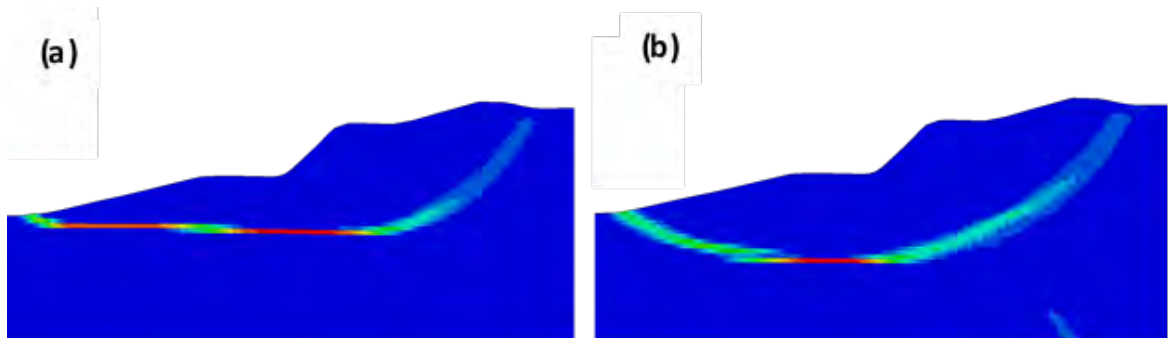
Figure 6.12. Two slip surface realisations: a) slip surface along the top of the interseam, depth:
RL -45 b) slip surface into the interseam layer, depth: RL -91.
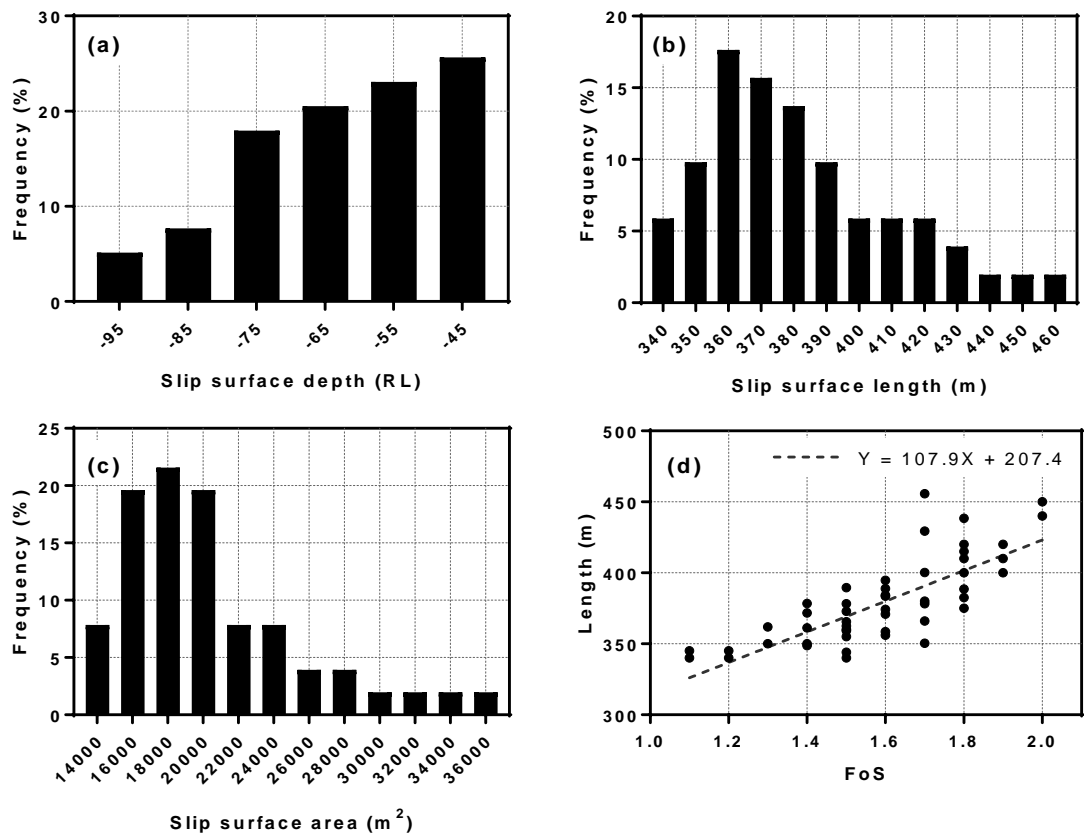
Figure 6.13. Slip surface histograms: a) slip surface depth b) slip surface length c) slip surface area d) slip length vs. factor of safety.

6.4.1   RFEM Topological Effects

Clustering of the initial realisations based on normalised random field similarity is presented in Fig. 6.14. It is noted that each individual representative slip surface cluster exhibits tight bounds on FoS differences. The maximum observed FoS of 2.0 is found in the cluster containing realisations 11 and 12, while the minimum FoS of 1.1 is found within the cluster containing realisations 5 and 6. This cluster has some overlap with other realisations of another cluster where the FoS ranges from 1.2 to 1.4. Fig. 6.15a details the normalised random field difference of two realisations within the same cluster, while Fig. 6.15b shows the normalised difference of two realisations located within disparate clusters. It is evident that the two random fields compared in Fig. 6.15a contain similar spatial structure within the non-coal interseam, however not within the coal layers. Conversely, Fig. 6.15b random field dissimilarity is noticeable in both the coal and non-coal bands. The random

field differences presented in Fig. 6.15a and Fig. 6.15b are determined by calculating the

elementwise absolute difference between the pairs of random fields.
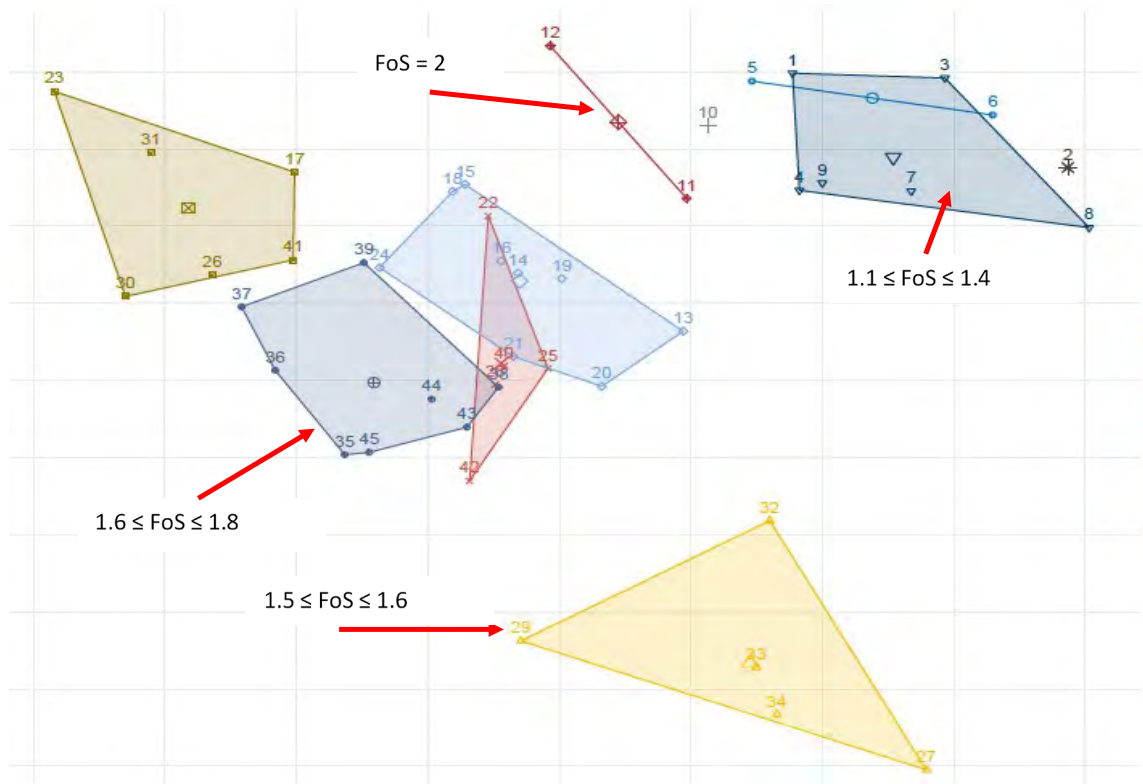
Figure 6.14. Cluster plot of random field realisations.
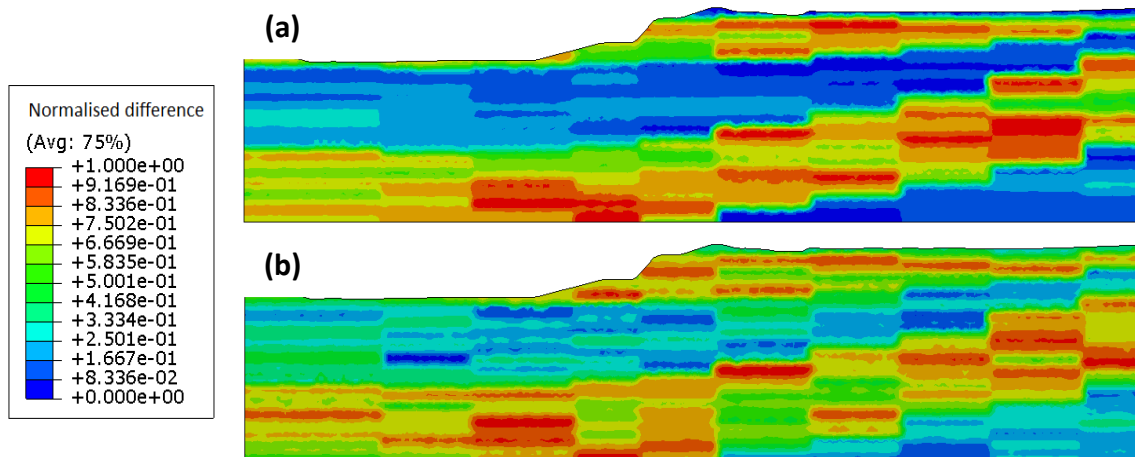
Figure 6.15. Random field similarity profile a) a realisation of within-cluster random field

similarity profile b) a realisation of cluster-to-cluster random field similarity.

The total pairwise absolute difference of each realisation within the cluster is determined for each

element within the random field using the equation:

$$C_k = \sum_{i \neq j \in K} \left| M_i - M_j \right| \qquad\qquad (6.17)$$

where, C_k is the overall similarity matrix C of the cluster K; and M_i and M_j are the ith and j^{th} random

fields of the cluster K. Elements within the matrix C_k with values approaching zero are locations

with parameters common to the random fields within the cluster. Once the locations of significance

within the cluster are identified, the individual random fields are analysed to determine the values

within the region of interest. Similarly, the process is repeated with clusters consisting of random

fields producing similar slip surfaces rather than clusters of similarities, to determine the

mechanisms behind shear bands located at various depths. The clusters deemed of greatest

importance are those with safety factors at the extremities of the FoS distribution, as well as those

with most shallow and deep slip surfaces. Fig. 6.16a shows the area of significance for the cluster

containing the lowest FoS values (realisations 5 and 6), which overlaps with realisations 1 and 3

within the surrounding cluster. The the interseam layer directly below the slope consists of a

material with a low cohesion (13 – 20kPa), located between RL -45 and RL -120. Considering the

mid range Factors of Safety (1.6 to 1.8), Fig. 16b shows the importance of a stronger layer, at an

increased height compared to Fig. 16a. Similarly, the cluster containing the highest FoS of 2.0

(realisations 10 and 11) contains a layer of highly cohesive coal directly behind the batter (Fig.

6.16c) from RL 16 to RL -38. Within the region, a particularly strong material zone exists (over

250kPa) at RL -18, running horizontally 150 metres behind the batter. Although similar patterns

are detected in random fields with associated realisations (Fig. 6.17a and b), the location, size and

magnitude of random field values of the region of interest are subject to variation. However, of

particular note is the location, region size and parameter magnitude of the random fields within the

clusters containing the highest and lowest safety factors. As the regions of interest diverge away

from these locations and random field values, the FoS regresses towards the mean FoS of 1.55. In

each of these cases, the material cohesion played a far greater role in the region of interest than the

friction angle.
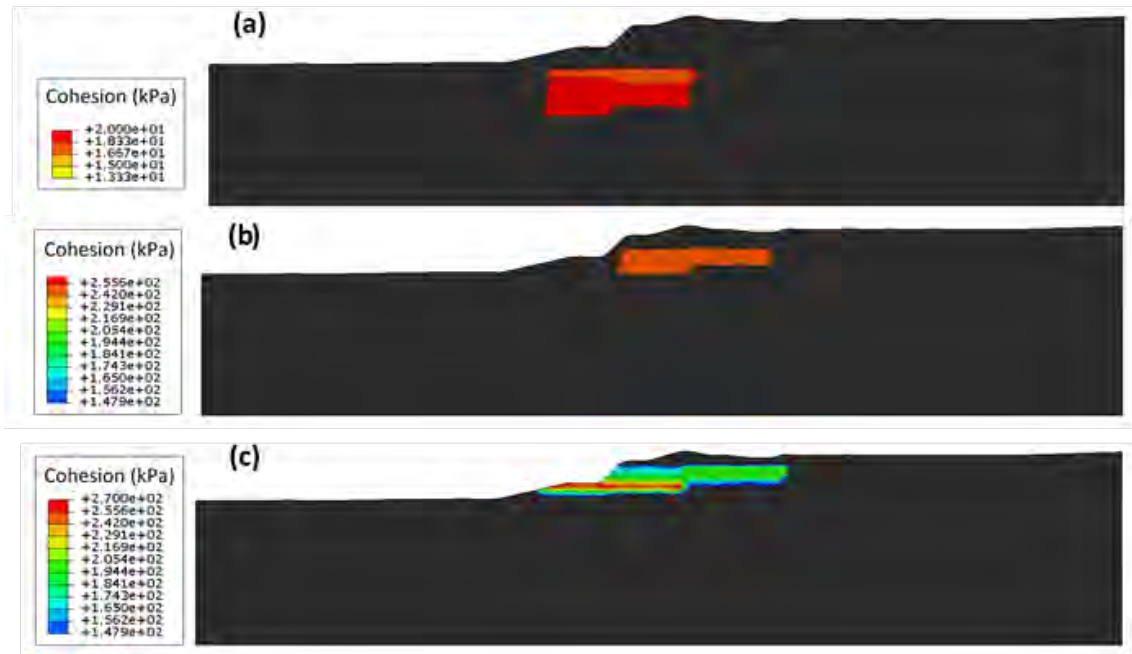
Figure 6.16. Regions of significance for random fields with FoS values of: (a) 1.1 – 1.4 (b) 1.6 –

1.8 (c) 1.8 – 2
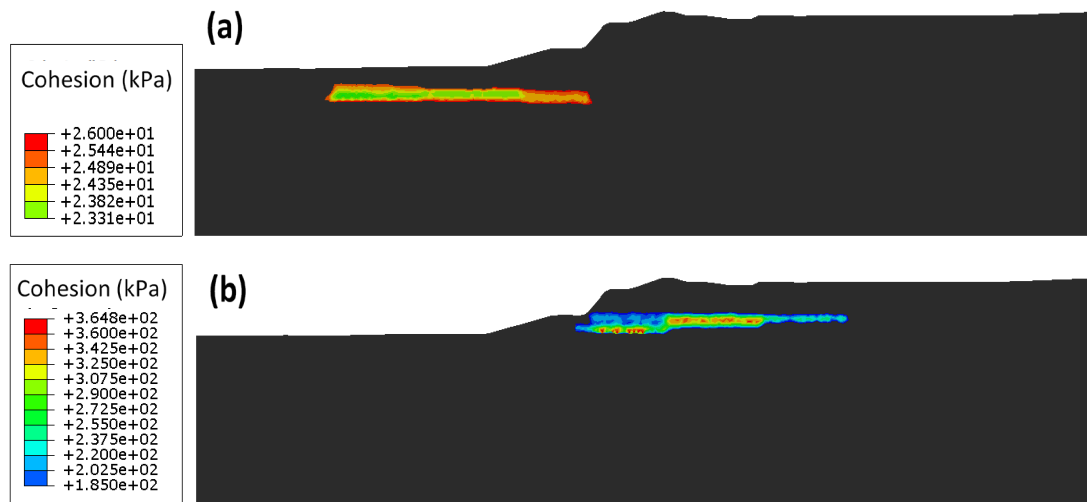
Figure 6.17. a) random field realisation 9; FoS = 1.3 b) random field realisation 15; FoS = 1.7

When considering regions of interest that impact on the shape of the slip surface, low valued friction

angle bands occur within the interseam layer, directly coincide with the basement of the slip surface

(Fig. 6.18a-c). As such, anisotropic bands of friction angles less than 20 degrees in this region are

a direct predictor of the slope failure shape.

Once the clusters of safety factors, slip surfaces and regions of interest common to each cluster are identified, the effects of each cluster on the overall distribution are considered. When conducting stochastic slope stability analyses with the objective of identifying random field characteristics, certain properties may be of greater interest than others. In particular, deeper slip surfaces consisting of larger sliding masses may be of greater concern than shallow failure surfaces. Similarly, further site exploration may indicate that certain strength parameters within regions of interest are practically infeasible. As such, a modified FoS distribution can be considered when particular clusters are removed from consideration. Conversely, certain circumstances warrant targeting particular characteristics while removing all other potential clusters. Table 5 presents modified FoS results when clusters are removed based on the slip surface depth. A FoS increase of over 10% is observed when shallow slip surfaces are removed, while a decrease of over 10% is observed when removed the deepest slip surfaces from consideration.
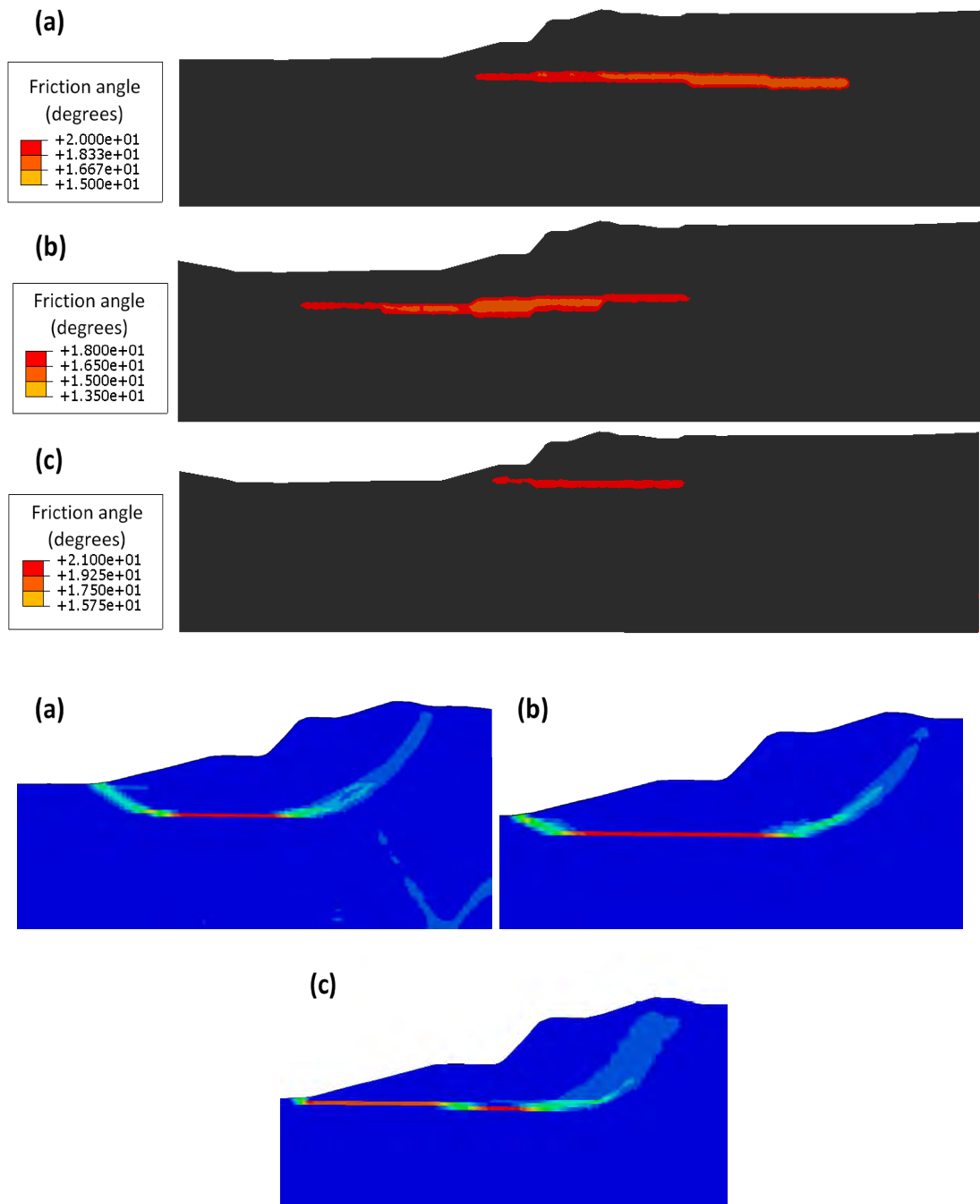
Figure 6.18. Friction angle impact on the slip surface: a) RL -55 b) RL -75 c) RL -45

Table 6.5. Impact of removing slip surface clusters on the FoS

Removed region (RL)	Probability of occurrence (%)	FoS	Change in FoS (%)
<= -45	25.65	1.73	11.61
[-45,-70]	46.23	1.47	-5.16
[-70,-95]	28.12	1.38	-10.97

6.5 Discussion and Conclusion

Spatial variation of shear strength characteristics can significantly impact the failure mechanisms of open-cutmines, and as such, great care is necessary when considering the shear strength properties. Historical data from a large number of conducted laboratory tests have been evaluated to determine spatial correlation lengths and parameter distributions for both coal and non-coal interseam materials. Numerical slope stability models with the Random Finite Element Method coupled with random field similarity and clustering techniques have drastically reduced the number of Monte Carlo RFEM simulations required for convergence of safety factors. Furthermore, random field similarity techniques were employed as a classification and comparison tool, determining spatial structures that significantly impact safety factors and slip surface shapes.

Two key regions of significance were identified for assessing the factor of safety: a highly cohesive band located in the coal batter, and a non-coal interseam band consisting of low cohesion values. The impact of friction angle variation within the regions of significance was negligible when considering the FoS. A direct correlation between low friction angle bands of interseam material and the failure slip shape was observed, a result that has significant implications for prediction of failure surfaces. Furthermore, results are presented for the removal of particular random field simulations, allowing for a targeted analysis based on slip surface shape and desired regions of interest locations. The authors believe that further research is required to determine the impacts of varying slope geometry, stratigraphic layering and material statistical distributions on the location, shape and magnitude of regions of significance and their role in slope stability analysis.

Acknowledgments

Page **150**

*Chapter 7. An Investigation of Cross-Sectional Spatial Variation
with Random Finite Element Method Slope Stability Analysis*

7 An Investigation of Cross-Sectional Spatial Variation with Random Finite Element Method Slope Stability Analysis

The following journal paper explores the variation of a set of two-dimensional cross-sections using the methods developed in the previous chapters to determine the impact of spatially variable shear strength parameters when applied to different slope geometries and layerings. This journal paper is an accurate representation of the published version, with minor alterations to table and figure numbers for the purposes of continuity.

Abstract

The selection of two-dimensional cross-sections for plane-strain slope stability analysis often requires a range of assumptions such that the most appropriate cross-section is considered. When faced with complex strata, surface topologies and pore-water pressure distributions, the selection of an appropriate cross-section is non-trivial. Circumstances are further complicated when considering spatially variable soils and heterogeneous strength parameters. In this study, the effects of spatially variable geotechnical parameters are examined for a range of two-dimensional Random Finite Element Method (RFEM) simulations of an open-cut mine. A distinct set of random field instances are provided to each cross-section to isolate the impact of geometry and strata variation when coupled with spatially variable soil characterisations. Particular attention is given to the regions providing the greatest impact on Factors of Safety (FoS) and Representative Slip Surfaces (RSS) for each slope geometry, evaluating the need for full three-dimensional RFEM simulation. Further statistical analyses are conducted to establish which random field slope stability cross-sections are significantly different from the underlying cross-section population, thereby identifying the best cross-section to represent the overall slope geometry.

Keywords

Random field; slope stability analysis; random finite element method; cross-section; spatial variability;

7.1   Introduction

Numerical slope stability analysis is an important consideration for geotechnical and mining engineering when slope failure can be irreversible, dangerous and costly. For slope stability simulation, two-dimensional (2D) plane strain simulation methods are often preferred over three-dimensional (3D) alternatives due to their simplicity and computational efficiency [254, 255]. Many previous studies have noted that the safety factors from 2D slope stability analyses are typically more conservative than 3D cases [56, 256-258]. Griffiths and Marquez [36] proposed that the most pessimistic 2D cross-section of a 3D model produces a considerably lower factor of safety (FoS) compared to 3D simulation, as the slopes derive no support from the adjacent soil in the third direction. Arellano & Stark [259] noted that the back analysis of a 2D slope will lead to an unconservative overestimation of soil shear strength, while Anagosti indicated that in some cases, the 3D FoS can be as much as 50% higher than the 2D [260]. Conversely, several studies observed that particular soil properties, groundwater conditions, complex dimensions and boundary conditions may produce lower 3D safety factors compared with 2D instances [261-265]. Wines [266] proposed that numerical geotechnical analyses fall into two distinct categories: problems where 3D analysis is not necessary, such as high walls with low curvature, the stability of tunnel sections some distance away from a working face, longwall panels, etc. and problems where 2D is unable to describe necessary 3D phenomena, such as areas near the entrance of tunnels and stopes, and mined slopes with irregular geometry or high curvature. Duncan observed differences between 2D and 3D with the curvature radius of a concave slope [6]. If the curvature radius is greater than the slope height, 2D and 3D results are agreeable [267]. Chen [268] observed that the effect of cohesive slopes is considerable compared to cohesionless instances.   When conducting

axisymmetric simulation, as the slope radius increases, the failure shape approaches that of the plane strain case [269].

When considering slope stability analysis in both 2D and 3D, the Random Finite Element Method (RFEM) is an increasingly prevalent method for modelling soils with spatially variable shear strengths [32]. Unlike Limit Equilibrium Methods (LEM), FEM allows failure mechanisms to develop naturally, without a priori specification. When combined with the strength reduction method (SRM) devised by Zienkiewicz [35], RFEM provides an effective method for analysing the strength of probabilistic slope stability cases. In this study, five two-dimensional slope cross sections are analysed with RFEM to investigate the effects of spatial heterogeneity when coupled with varying slope geometries and strata, with particular interest given to the effects on 2D slope failure mechanisms and safety factors of a 3D mine section. Random field similarity measures and clustering techniques [246] are employed to identify common random field characteristics and their effect on safety factors when combined with a variation of cross-sectional geometry. Monte Carlo simulation is performed to identify the distribution of Factors of Safety for each cross-section and to determine if cross-sectional FoS distributions are locationally dependent, or similar enough to be considered of a single distribution. Probabilistic slope stability analyses can produce a wide range of different slope failure surfaces. However, failure probabilities are often governed by a subset of critical slip surfaces known as Representative Slip Surfaces (RSS) [175]. In this paper, the frequencies of common RSS instances are considered for each 2D cross-section, as well as the regions of greatest importance (known as Regions of Significance) within each geometry that affect the overall slip surface shape. A case study of the Yallourn open-cut brown coal mine, located in Victoria, Australia is provided, with a focus on determining the impact of slope failure mechanisms on a range of two-dimensional cross-sections. The variation of groundwater conditions coupled with complex geometry and spatially variable shear strength parameters are considered to determine appropriate Factor of Safety distributions by selecting the most pessimistic of the 2D cross-sections considered.

Page **153**

Chapter 7. An Investigation of Cross-Sectional Spatial Variation with Random Finite Element Method Slope Stability Analysis

7.2   Probabilistic Slope Stability Description

Random field theory

Geotechnical parameters are inherently variable from location to location, mainly due to a range of naturally occurring complex processes related to geological deposition history and material loading. A common method for modelling spatially variable geotechnical properties is the random field theories initially developed by Vanmarcke [247]. Random fields are often compartmentalised into two independent parts – a deterministic trend component and an error component regularly known as the "off the trend" variation:

$$\xi(x) = t(x) + w(x) \tag{7.1}$$

in which, $\xi(x)$ is the spatially variable geotechnical property of interest; $t(x)$ is the deterministic trend component, and $w(x)$ is the off the trend fluctuating component [2]. The off the trend term is generally defined by three statistical properties – the distribution mean μ, standard deviation s and scale of fluctuation Θ [152, 270]. Often, the variability of a distribution is described by the ratio of the distribution standard deviation with respect to the mean, defined as the dimensionless property named the Coefficient of Variation (COV):

$$COV = \frac{s}{u} \tag{7.2}$$

Often, one must consider a number of random variables simultaneously, as individual variable behaviours may not be independent. The covariance function Cov[X,Y] describes the strength of the relationship between random variables X and Y, and is defined as

$$Cov[X, Y] = E[XY] - E[X]E[Y] = E[XY] - \mu_X \mu_Y \tag{7.3}$$

while the normalised non-dimensional Autocorrelation Coefficient (ACF) of X and Y is defined as

$$\rho_{XY} = \frac{Cov[X,Y]}{s_X s_Y} \tag{7.4}$$

A significant property of random field soil characterisation is the Scale of Fluctuation (SoF) [1], which is used to characterise the lag distances (τ) where strong correlations are observed.

Page **154**

Chapter 7. An Investigation of Cross-Sectional Spatial Variation with Random Finite Element Method Slope Stability Analysis

Generally, two points i and j within a random field are constrained such that when τ is small, geotechnical properties at these points exhibit a strong correlation, decreasing as τ increases in distance. The SoF is commonly defined by an autocorrelation function, which indicates the average correlation between locations separated by τ. Li et al. [271] investigated five theoretical ACFs for slope stability analysis and determined that the reliability of a slope was insensitive to the type of ACF [234]. Also, Hilyati et al. presented a range of the most commonly used ACFs [153], while the most common being the Markovian exponentially decaying AFC [235-237] defined as:

$$\rho\left(\tau_x, \tau_y\right) = \exp\left(-\frac{2|\tau_x|}{\theta_x} - \frac{2|\tau_y|}{\theta_y}\right) \tag{7.5}$$

where, $\rho\left(\tau_x, \tau_y\right)$ is the autocorrelation coefficient at lag distances τ_x and τ_y, in the x and y directions, respectively. Similarly, θ_x and θ_y are the SoFs for both x and y.

Random fields may be applied to a wide range of geotechnical parameters for RFEM analysis. Although they are most frequently applied to material strength parameters such as cohesion c, internal friction angle φ and dilation angle ψ, as well as the elastic modulus E, unit weight γ and permeability k. Griffiths and Lane [32] observed that variation of cohesion and friction angle parameters provided the greatest impact on slope stability RFEM safety factors, along with the slope geometry and material unit weight. Furthermore, Alonso [16] noted that variation of material strength parameters c and ϕ were a significant contributing factor in FoS distributions compared with soil unit weight variation.

Common distributions for geotechnical parameters include the Gaussian, lognormal and Weibull distributions [2]. Material properties are often described by a lognormal distribution (with mean μ_x and standard deviation s_x) when the parameters require strictly non-negative values e.g. cohesion, friction angle, unit weight etc. A lognormal random field X is transformed from a standard normal random field G(x) by:

$$X_i = \exp\left[\mu_{lnX} + s_{lnX}G(x_i)\right] \tag{7.6}$$

in which X_i is the transformed lognormal soil parameter for the ith random field element; x_i designates the centre point of the ith element; and μ_{lnX} and s_{lnX} are the mean and standard deviation of the normal distribution ln (X). The random variables μ_{lnX} and s_{lnX} are determined by:

$$\mu_{lnX} = \ln(\mu) - \frac{s_{lnX}^2}{2} \tag{7.7}$$

$$s_{lnX}^2 = ln(1 + \frac{s^2}{\mu^2}) \tag{7.8}$$

while the lognormal probability density function is characterised by:

$$f(X) = \frac{1}{X\, s_{\ln X}\, \sqrt{2\pi}} exp\left\{ -\frac{1}{2}\left(\frac{\ln X - \mu_{\ln X}}{s_{\ln X}}\right)^2 \right\} \tag{7.9}$$

The fluctuations of more than one random variable at a time may be considered, in cases where behaviour is determined to be linked or jointly influenced by another parameter (e.g. c and $\tan \phi$). However, there is a lack of observed correlations between these two random variables. Cherubini [148] noted weak negative c/φ cross-correlations ranging from -0.7 to -0.24, while Yucemen et al. [150] reported correlations between -0.49 and -0.24. A negative correlation between the two shear strength parameters suggests that low valued friction angles coincide with high values of cohesion and vice versa. Hence, the overall shear strength uncertainty is less than the total uncertainty of the two shear strength parameters, as the shear strength variation is reduced by c/φ combinations dictated by the negative correlation coefficient.

To associate a random field with a Finite Element Method (FEM) geometry, the Local Average Subdivision (LAS) method is implemented, as defined by Fenton and Vanmarke [156]. LAS divides global averages into regions which are subdivided such that the local averages preserve the global statistics. The process of LAS leads to a reduction in the variance, as parameter fluctuations tend to cancel each other out when averaging over a spatial domain. Hence, the variance of a soil region is commonly less than the variance of a point field. To remedy this, Vanmarcke [1] suggested a dimensionless variance adjustment function to correct the cell-to-cell variation, preserving the correct variance.

Finite Element Method (FEM) for slope stability

In a landmark paper, the implementation of the Finite Element Method for the purposes of slope stability analysis was comprehensively detailed by Griffiths and Lane [32]. FEM for slope stability provides a powerful alternative to Limit Equilibrium Methods (LEM), requiring fewer a priori assumptions, while allowing slope failure surfaces to develop naturally and without predefined failure locations and shapes. Furthermore, there is no requirement for assumptions related to inter-slice forces, while progressive failure can be analysed up to the overall shear failure event.

Numerous constitutive soil models have been considered with FEM simulation [272]. In this study, we consider slope stability analysis with the linear elastic model combined with the Mohr-Coulomb perfectly plastic failure criterion. Forces due to gravity loading are generated, producing normal and shear stresses, which are compared to the Mohr-Coulomb failure envelope as defined by:

$$F = \frac{\sigma_1 + \sigma_3}{2} \sin \phi - \frac{\sigma_1 - \sigma_3}{2} - c \cos \phi \qquad (7.10)$$

in which σ_1 and σ_3 are the respective major and minor principal stresses.

To provide spatial variability, the FEM geometry is partitioned into mutually exclusive element sets, each allocated with a set of material strength parameters derived from an associated random field. The *Abaqus* element type CPE4P (4-node plane strain quadrilateral, with bilinear displacement, bilinear pore pressure) was used for all finite elements within the model geometry. Due to the complexities associated with the slope geometry, stratigraphy and shear strength variation, a particularly fine mesh of 40,000 elements was constructed for each two-dimensional cross-section (Fig. 7.1).
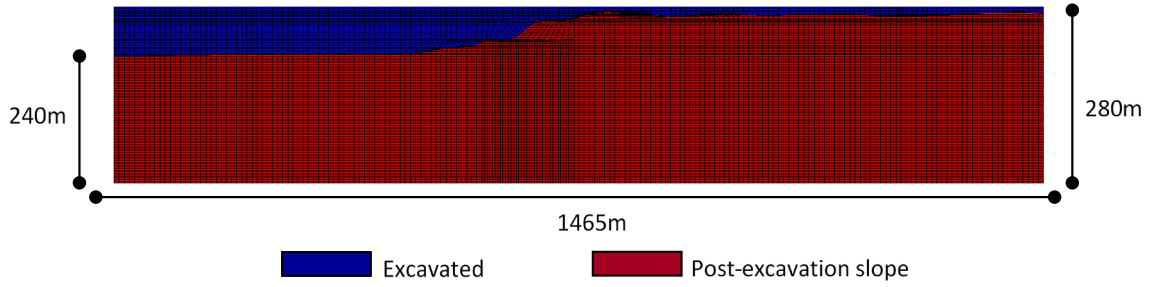
Figure 7.1. Slope geometry mesh distribution

Strength reduction method (SRM)

The Strength Reduction Method (SRM), sometimes referred to as the Shear Strength Reduction Method, is a method commonly applied with FEM slope stability to calculate the slope Factor of Safety. The SRM determines the FoS of a slope, defined as the ratio of the original soil shear strength with respect to shear strength required to achieve the onset of slope failure [75]. Commonly known as c/φ reduction, the method iteratively reduces material cohesion c and the tangent of the angle of internal friction φ by a common Strength Reduction Factor (SRF):

$$c = \frac{c_0}{SRF} \tag{7.11}$$

$$\phi = \tan^{-1}\frac{\tan \phi_0}{SRF} \tag{7.12}$$

in which c_0 and ϕ_0 are the initial cohesion and internal friction angle parameters, respectively; and SRF is the iterative Strength Reduction Factor. Once the shear strength parameters are sufficiently reduced to produce slope failure, the FoS is defined as:

$$FoS = \frac{c_0}{c_f} = \frac{\tan \phi_0}{\tan \phi_f} \tag{7.13}$$

where, c_f and ϕ_f are the shear strength parameters required to bring the slope to the verge of failure. When considering the SRM coupled with the FEM environment, several common attributes are associated with the critical SRF, including:

1.   The development of plasticised shear band along the critical shear surface.

2.   Excessive slope deformation.

3.   Non-convergence of the FEM solution [35].

It is necessary for sufficiently complex FEM models to conduct Strength Reduction with a procedure to optimise the SRF trial reduction factors, such that the number of reduction steps is kept to a minimum, limiting computation time. In this study, the SRM was implemented with an optimised reduction method, as described by Dyson and Tolooiyan [228], developed in the FEM package *Abaqus* [273], which contains no inbuilt predefined SRM.

Random field similarity and clustering

Monte Carlo simulation of spatially variable random fields can be used to both predict and classify slope stability characteristics such as the critical slip surface shape and factor of safety. In particular, random field similarity comparison techniques allow for individual random field realisations to be compared and clustered based on locationally dependent patterns of geotechnical parameters [246]. Random fields of geotechnical shear strength properties can be compared with the Frobenius norm $||\boldsymbol{D}||_F$, defined as:

$$||\boldsymbol{D}||_F = \left(\sum_{i=1}^{m}\sum_{j=1}^{n}|a_{ij} - b_{ij}|^2\right)^{1/2} = \sqrt{trace[(\boldsymbol{A}-\boldsymbol{B})^T(\boldsymbol{A}-\boldsymbol{B})]} \qquad (7.14)$$

where, **A** and **B** are two random field instances considered for comparison; and a_{ij} and b_{ij} are their respective elementwise components. When $||\boldsymbol{D}||_F$ is small, the two random fields instances are similar, yielding similar FoS values. As $||\boldsymbol{D}||_F$ increases, the random fields become dissimilar and random field comparison no-longer produces analogous factors of safety. Random field similarities can be implemented as a predictive measure, avoiding unnecessary RFEM simulation of random field instances. When a random field is deemed sufficiently similar to a previously simulated slope instance, simulation of the random field instance is not required, and the FoS is assumed. Once a set of random field instances is sufficiently large to produce FoS convergence, instances can be

clustered into categories based on spatial variation characteristics, with random field realisations exhibiting similar slope failure surfaces [246].

Dyson and Tolooiyan examined slope failure mechanisms of individual clusters to determine the regions where geotechnical parameter variation produced the greatest impact on observed slope slip surfaces and safety factors [274]. Within-cluster random field instances were compared to determine the total pairwise difference of each realisation, determined at each random field element location, defined by

$$C_k = \sum_{i \neq j \in K} |M_i - M_j| \tag{7.15}$$

where, C_k is the overall similarity matrix C of the cluster K; and M_i and M_j are the ith and j^{th} random fields of the cluster K. Elements within the matrix C_k consisting of near-zero values signify locations with parameters common to all random fields within the cluster. These regions, named Regions of Significance (RoS) are the positions deemed to be significant contributors to the overall failure mechanisms observed within the cluster. This method can be implemented to examine clusters which consist of instances producing similar critical slip surfaces, to determine the regions and mechanisms contributing to the observed slip shape. The process of determining Regions of Significance from a cluster set is detailed in Fig. 7.2.
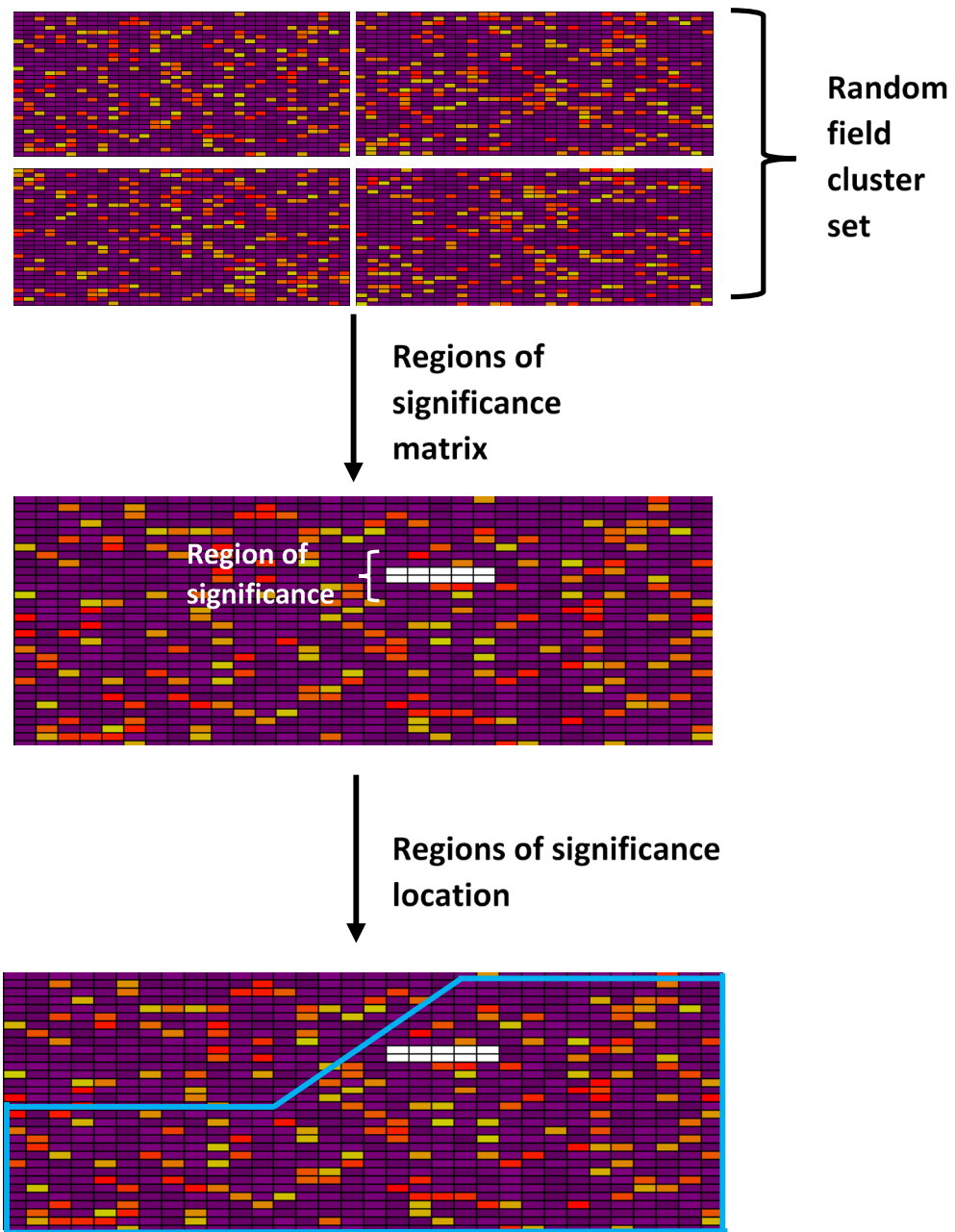
Figure 7.2. Random field cluster regions of significance process.

7.3   Field Conditions

Yallourn open cut coal mine

The Yallourn open-pit brown coal mine, located in the Latrobe Valley region of Victoria, situated

150km east of Melbourne (Fig. 7.3) is the second-largest open-cut mine in Australia [252]. The

lignite deposits of the region contain 23% of the world's reserves of brown coal [275] with some of

the thickest continuous brown coal seam in the world [187]. Recent movements in the mine batters

of the three operating open-cut mines in the region have raised concerns about the understanding of

slope failure mechanics for Victorian Brown Coal (VBC). VBC is classified as low-rank coal,

corresponding to Lignite B in the American Society of Testing and Materials standards [192]. With

a unit weight of 11.5KN/m^3, VBC is a light-weight organic material, with a water content of up to

65% of its volume [193]. The permeability of VBC was observed by Tolooiyan et al. through in-

situ Lugeon testing to be 7.6e-3 m/day [195]. Rosengren noted permeability values as low as 6.64e-

4 m/day (4.22e-9 m/sec), declaring that fractures have a significant influence on permeability, such

that field measurement may be the only reliable testing regime for estimating VBC permeabilities

[196]. Although several large joints are visible within the northern batter of the Yallourn mine, the

brittle nature of VBC commonly exhibits micro-fracture and cracking in addition to large vertical

jointing [252]. Beneath the coal seam at Yallourn is a layer of interseam material consisting of clay

and silt, much weaker in strength than VBC [207]. Due to the difference in strengths of the two

materials, block-sliding along the low frictional interseam is a likely failure mechanism [209].
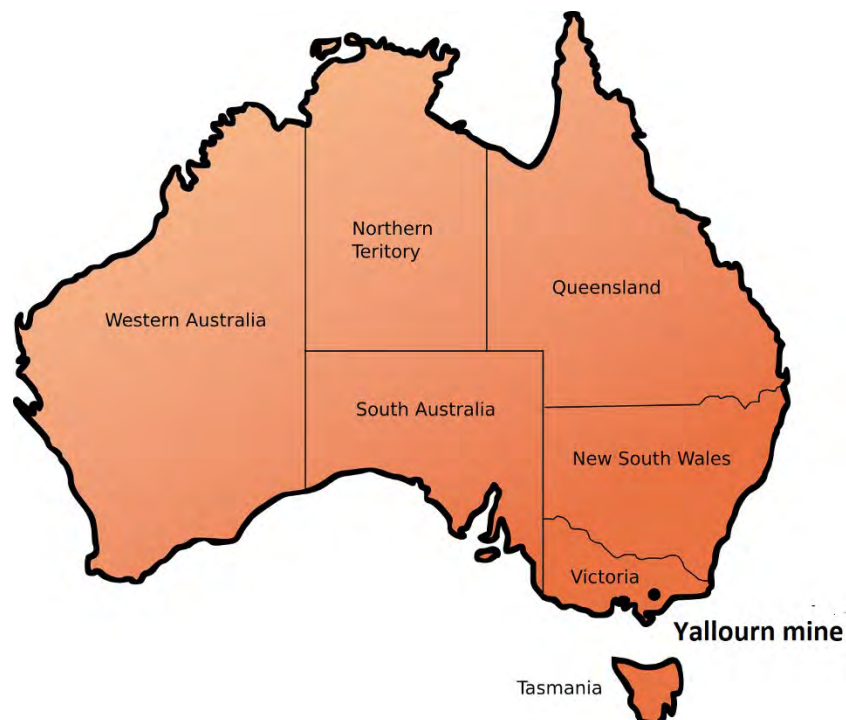
Figure 7.3. Location of the Yallourn Mine

7.3.1   Material Parameters and Statistical Distributions

Commencing in the 1950s, the State Electricity Commission of Victoria (SECV) conducted a comprehensive exploration drilling program, consisting of roughly 15,000 boreholes, with a wide range of geotechnical parameters identified from both laboratory and in-situ tests on material samples. More recently, a considerable number of modern geotechnical laboratory tests on both coal and interseam materials has been conducted at Federation University Australia's Geotechnical and Hydrogeological Research Group (GHERG). Table 7.1 presents geotechnical parameters collected for both VBC and non-coal interseam material, including saturated and unsaturated unit weight γ, Elastic modulus E, Poisson's ratio ν and permeability k. Shear strength distribution statistics, consisting of cohesion and internal friction angle are provided in Table 7.2. Of particular note is the high variation of coal cohesion due to the brittle nature of the material, consisting of many micro-fractures and cracks [251]. The shear strength parameter distributions are considered lognormal, as all data are strictly non-negative. Coal and non-coal spatial auto-correlation structures (Table 7.3) are noticeably anisotropic, with rapid down-the-bore variation compared to reasonably smooth across-the-bore fluctuations. Transverse anisotropy is a common feature in soft rock due to their depositional nature.

The relationship between shear strength parameters has been studied for a range of different soils [149, 150, 253]. In this particular case, the depth-dependent autocorrelations and c/φ cross-correlations for coal and non-coal are presented in Table 7.4. The Pearson correlation coefficient used in both cases is defined by:

$$r_{x,y} = \frac{\sum_{i-1}^{n}(x_i-\bar{x})(y_i-\bar{y})}{\sqrt{\sum_{i-1}^{n}(x_i-\bar{x})^2 \sum_{i-1}^{n}(y_i-\bar{y})^2}} \tag{7.16}$$

in which, *r* is Pearson's correlation coefficient; *n* is the number of samples; x_i and y_i are i[th] variable samples; and $\bar{x}$ and $\bar{y}$ are the variable means.

In both cases, as no significant trends were observed, all variables were considered as uncorrelated.

Page **163**

*Chapter 7. An Investigation of Cross-Sectional Spatial Variation
with Random Finite Element Method Slope Stability Analysis*

Table 7.1. Geotechnical parameters for coal and non-coal materials

Material	γ_{unsat} (kN/m³)	γ_{sat} (kN/m³)	E (MPa)	ν	k (m/day)
Coal	11.4	11.5	40	0.3	7.6e-3
Non-coal	20.15	20.2	52	0.3	4.7e-2

Table 7.2. Shear strength parameter statistics

	Coal		Non-coal	
Parameter	c (kPa)	φ (°)	c (kPa)	φ (°)
Mean (μ)	150.7	27.3	31.8	23.7
Standard Deviation (s)	69.8	4.9	5.0	4.5
COV	0.5s	0.2	0.2	0.2

Table 7.3. Shear strength length scales

	Coal		Non-coal	
Scale of Fluctuation (m)	C	φ	c	φ
θ_x	320.3	772.4	812	627.8
θ_y	23.1	8.7	35	13.1

Table 7.4. Shear strength correlations with depth

	Coal		Non-coal	
	c	φ	c	φ
Correlation	0.129	-0.260	-0.027	-0.060
$r_{c,\varphi}$	0.046		-0.003	

Cross-sections and assumptions

Five cross-sections of Yallourn's North-East mine batter (labelled CS1-5) were selected for two-dimensional plane-strain Finite Element analysis as shown in Fig. 7.4(a) – (b). The 2D segments are located at 150 metre intervals, with each cross-section 1465 metres in length. Undulations in the sloping topography are depicted in Fig. 7.5(a) – (c). To initially determine the effects of cross-sectional variation in slope geometry and strata, without interactions from varying groundwater conditions, the location of the nearby Latrobe river is assumed to run completely East-West, such that each cross-sectional model was given the same initial pore-water pressure conditions. Although this assumption is a minor departure from field conditions, the location of the river is not drastically different for cross-sections CS2-CS5. The Regions of Significance are presented for each cross-section, drawing attention to the mechanisms inducing slope failure across varying

Page **164**

Chapter 7. An Investigation of Cross-Sectional Spatial Variation with Random Finite Element Method Slope Stability Analysis

geometries. To further quantify the Factor of Safety distributions produced by each set of cross-sectional simulations, an analysis of variance (ANOVA) is conducted to determine if significant differences exist between each of the five distributions. Following the initial examination of the five slopes with identical groundwater conditions, cross-sectional analysis with appropriate varying water distributions is taken into account to determine the combined effects of varying slope geometry and groundwater distribution. Fig. 7.6 presents an individual random field realisation, detailing the spatially variable structure of (a) material friction angle, and (b) cohesion. Of particular note are the dissimilarities of coal and non-coal cohesion parameters compared to the friction angle.

Page **165**

*Chapter 7. An Investigation of Cross-Sectional Spatial Variation
with Random Finite Element Method Slope Stability Analysis*
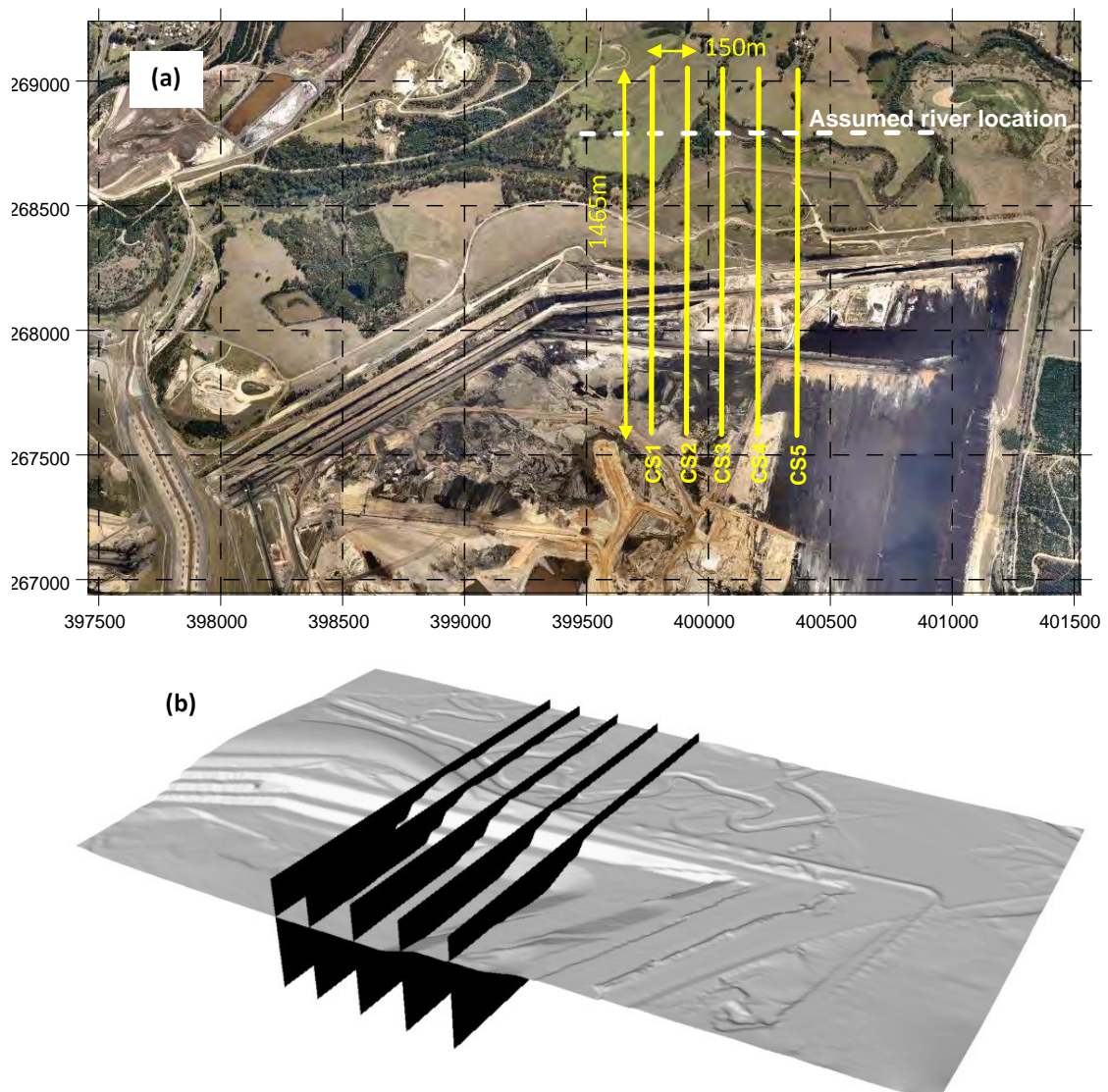
Figure 7.4. (a) Yallourn North-East mine batter cross-section (b) three-dimensional and cross-

sectional topography
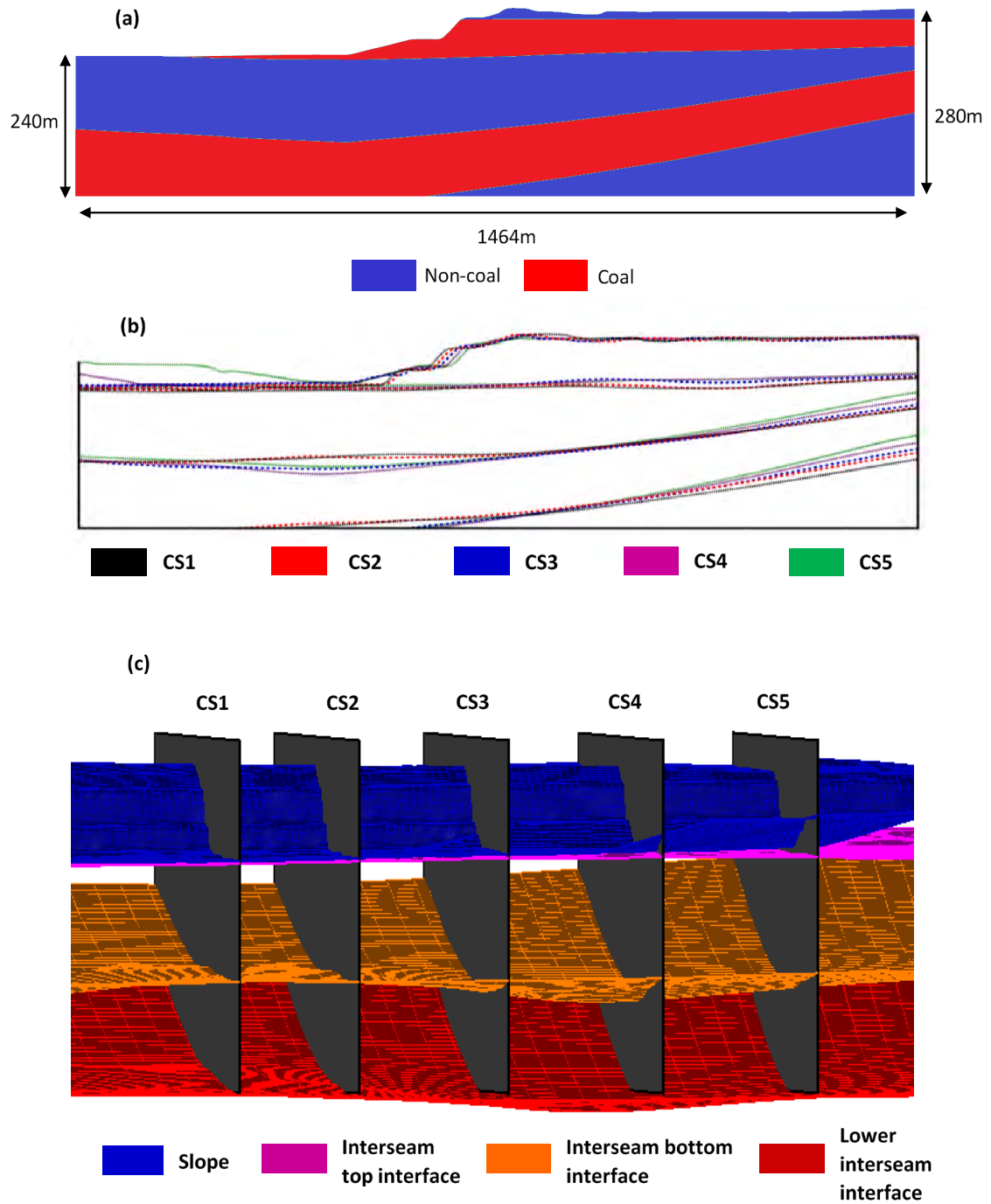
Figure 7.5. (a) CS1 cross-section materials (b) variation of cross-section strata (c) cross-section

interface boundaries

Page **166**

*Chapter 7. An Investigation of Cross-Sectional Spatial Variation
with Random Finite Element Method Slope Stability Analysis*
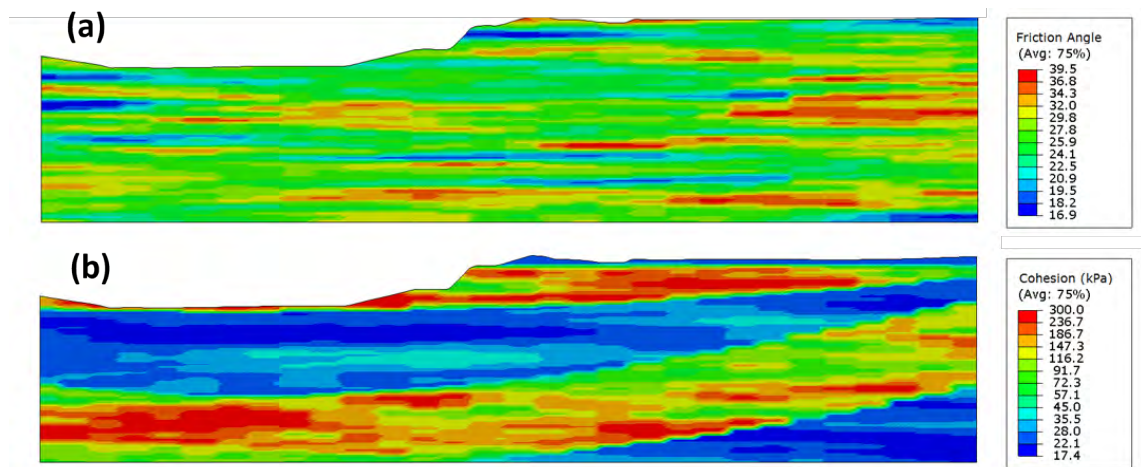
Figure 7.6. Random field realisation of (a) friction angle (degrees) (b) cohesion (kPa)

7.4   Results

RFEM results with constant groundwater conditions

Cross-sections 1 – 5 are first considered with identical initial groundwater boundary conditions, with a constraint on the location of the Latrobe River at a fixed distance from the slope face (Fig. 7.4a). Table 5 portrays the variation of FoS values for both deterministic and spatially variable FEM analysis. When spatial variation of shear strengths are incorporated within the FEM simulations, a significant decline in safety factors is observed. The overall strength of these spatially variable slopes is controlled by elements with weak shear strength parameters. Due to the presence of these weaker elements, probabilistic simulations display noticeably lower factors of safety. Fig. 7.7(a) - (b) depict the FoS distributions for each cross-section. There are no noticeable differences in the FoS distributions, as confirmed by Analysis of Variance (ANOVA) statistical testing. With a null hypothesis (H_0) that no significant difference exists between Cross-Section FoS distributions, an F-statistic of 0.17 provides no strong evidence to discount the null hypothesis.

Table 7.5. Comparison of deterministic and probabilistic Factors of Safety

Cross-Section	Deterministic FoS	Probabilistic mean FoS	Difference in FoS
CS1	2.08	1.54	0.54
CS2	2.06	1.44	0.62
CS3	2.1	1.57	0.53
CS4	2.1	1.55	0.55
CS5	2.14	1.59	0.55

Fig. 7(c) – (d) details the length of slip surfaces, measured along the shear band, from the head to toe (Fig. 8), for each cross-section, with CS1-2 exhibiting slightly shorter slip lengths than CS3-5. This difference is confirmed by ANOVA (F < 0.05). Tukey's Honest Significant Difference Test (Tukey's HSD) confirms the existence of two distinct sets of slip surface length distributions, corresponding to CS1-2 and CS3-5. Fig. 7.9(a) provides an overall FoS distribution, independent of cross-section location, while Fig. 7.9(b) identifies the slip surface length distributions for the aforementioned groups. Although two distinct slip surface distributions are detected, the magnitude of their differences is small. FoS rates of convergence are presented in Fig. 7.10, with convergence attained in less than 100 simulations. An initial set of 50 random field realisations was considered with full RFEM simulation, coupled with the prediction techniques detailed by Dyson and Tolooiyan [246] to calculate FoS results for a further 950 random fields. Although each cross-section was assigned the same set of random fields, slip surfaces of varying lengths were observed, as shown in Fig. 7.11. In this case, the left-most cross-sections CS1 and CS2 produced slightly deeper slip surfaces, due to the variation in slope geometry and stratigraphy. The Regions of Significance which provide the greatest impact on slope failure mechanisms are presented in Fig. 7.12 and 7.13, for the cross-section sets CS1-2 and CS3-5. It is evident that the Regions of Significance (RoS) for the cohesion random fields do not drastically shift in space when examining these two distinct sets. Although random fields in the range of FoS = 1.1 – 1.4 exhibit RoS locations that are slightly deeper and closer to the slope toe for CS1-2 compared to CS3-5, the difference is negligible, as depicted in Fig. 7.12(a) – (b). The cohesion random field RoS locations become increasingly similar to greater FoS values. As the FoS increases, the region directly behind the slope face becomes the main region of influence for all cross-sections, shown in Fig. 7.12(c) – (f).

Similarly, the Regions of Significance for the friction angle random field are presented in Fig. 7.13.

The RoS locations for CS1-2 are located at a slightly lower depth than CS3-5 for each of the three

slip surface depths detailed. Nevertheless, the variation of both friction angle and cohesion RoS

locations provides a strong indication of the similarity of cross-sectional failure mechanisms and

FoS values. As the simulations with fixed groundwater distributions do not produce highly varied

FoS results, the effects of varying slope geometry coupled with spatially variable shear strengths

are considered minimal in this particular case study.
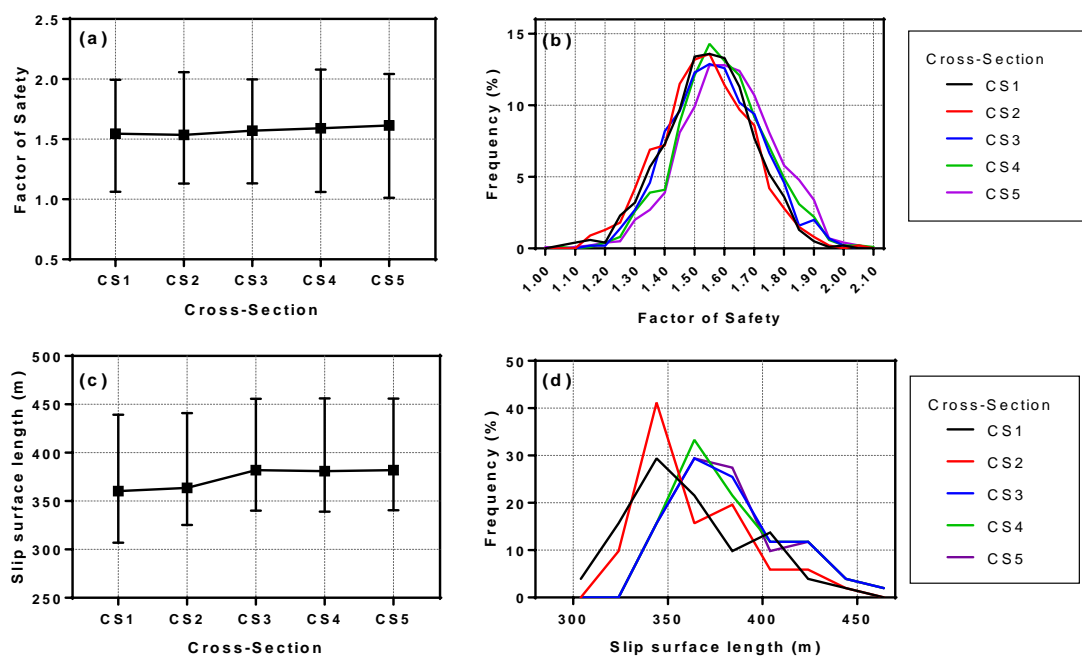
Figure 7.7. (a) Factor of Safety mean and range (b) Factor of Safety probability density function

(c) Cross-sectional slip surface length mean and range (d) Slip surface length probability density

function
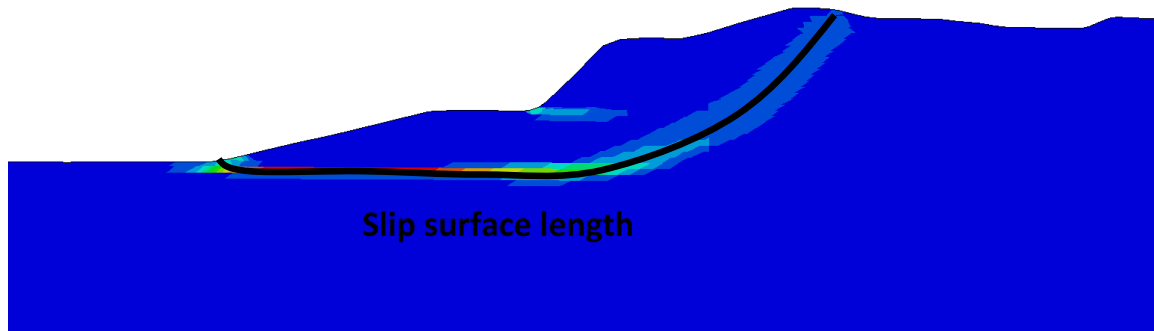
Figure 7.8. Slip surface length.
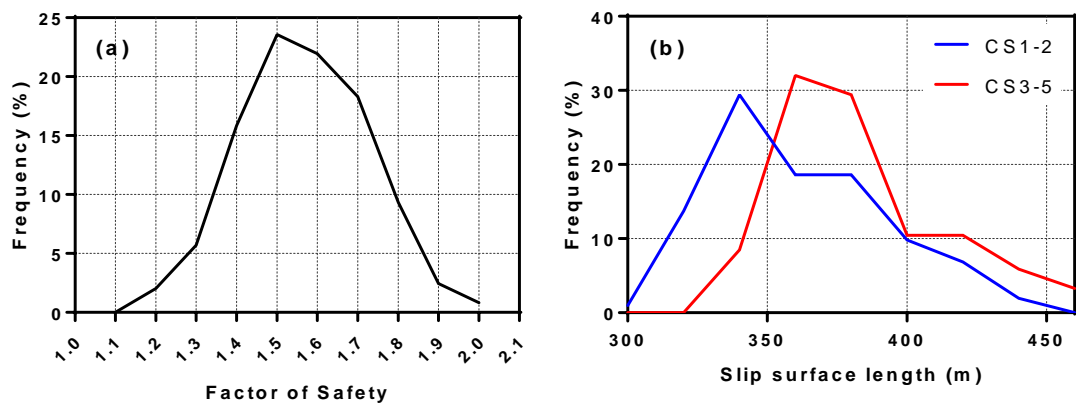
Figure 7.9. (a) Factor of safety independent of cross-section (b) Slip lengths for the cross-sections CS1-2 and CS3-5
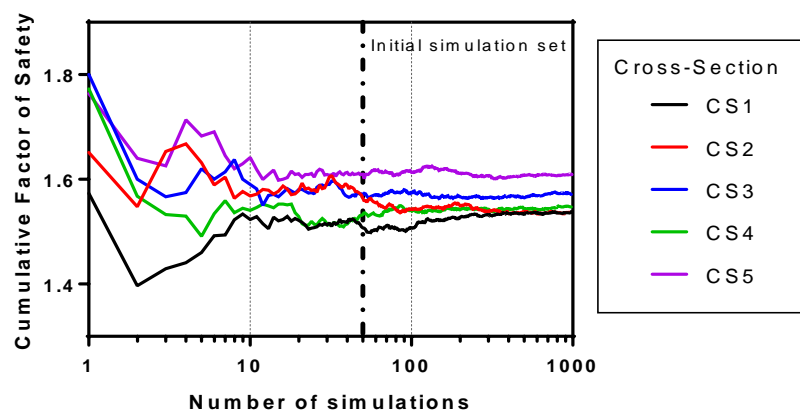
Figure 7.10. Factor of Safety rates of convergence

Page **170**

*Chapter 7. An Investigation of Cross-Sectional Spatial Variation
with Random Finite Element Method Slope Stability Analysis*
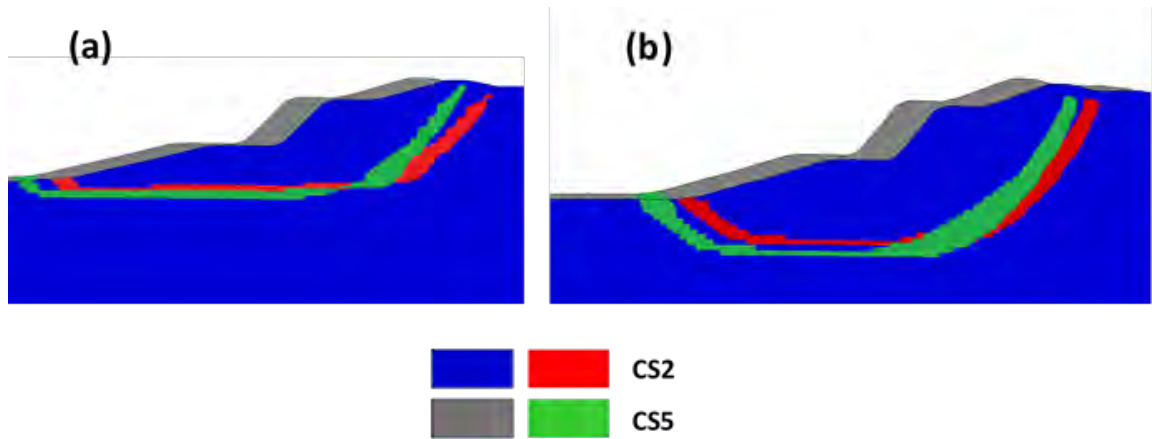
Figure 7.11. Comparison of cross-sectional slip surfaces for CS2 and CS5 (a) Random field

realisation with a shallow failure (b) Random field realisation causing deep failure
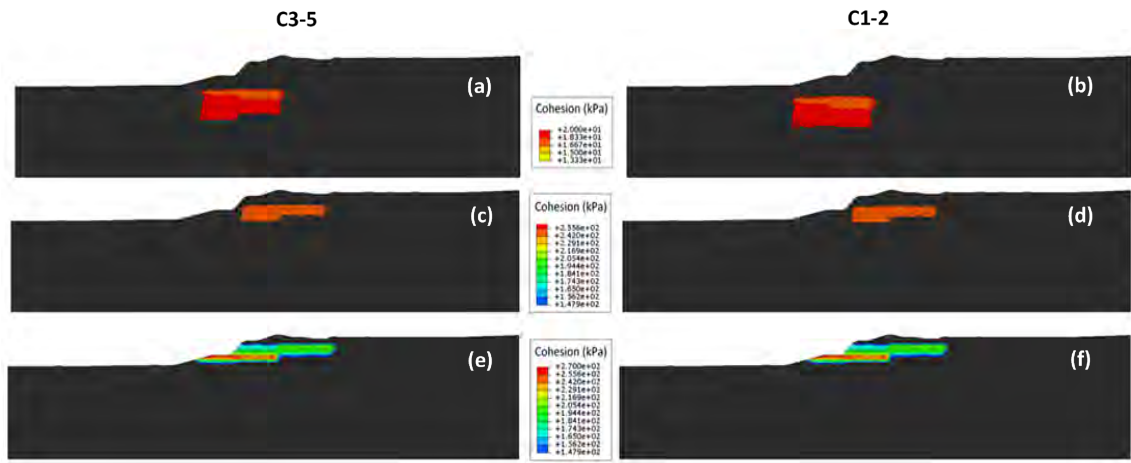
Figure 7.12. Regions of Significance cohesion for FoS values between (a) - (b) 1.1 - 1.4 (c) - (d)

1.6 - 1.8 (e) - (f) 1.8 – 2

C3-5   C1-2
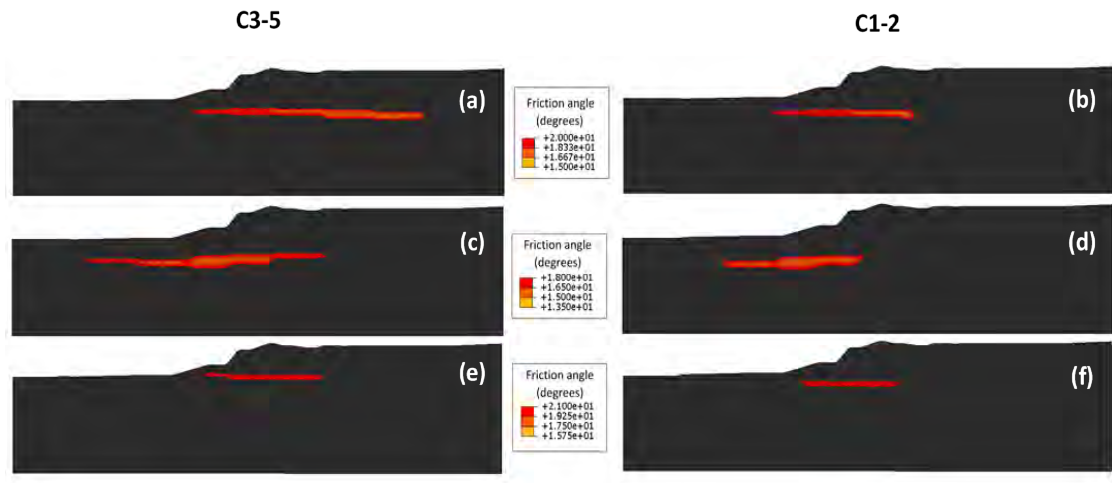
Figure 7.13. Regions of Significance friction angles for slip surfaces at (a) – (b) RL -55 (c) – (d)

RL -75 (e) – (f) RL -45

RFEM results with varying groundwater conditions

Varying groundwater conditions are investigated by removing the prior constraints for the location

of the river. In this section of analysis, the distance of the Latrobe River from the face of each

cross-section is not constrained across CS1-5, although the variation across CS3-5 is minimal (Fig.

7.14). With the varying groundwater conditions, Factor of Safety distributions branch into two

distinct sets, as illustrated in Fig. 7.15(a) – (b). The existence of two distinct sets is confirmed by

ANOVA and Tukey's HSD, as with the previous section of analysis, and presented in Fig. 7.16. A

mean FoS of 1.46 for CS1-2 is observed, compared with 1.57 for CS3-5, with the convergence of

mean parameters in approximately 100 simulations (Fig. 7.17). It is evident that with the

introduction of varying groundwater conditions, that selection of an appropriate cross-section is of

particular importance for 2D plane-strain analysis in this case. As such, cross-sections CS1 and

CS2 provide more conservative Factor of Safety distributions compared with CS3-5 when

conducting stochastic analyses with spatially variable shear strength parameters.
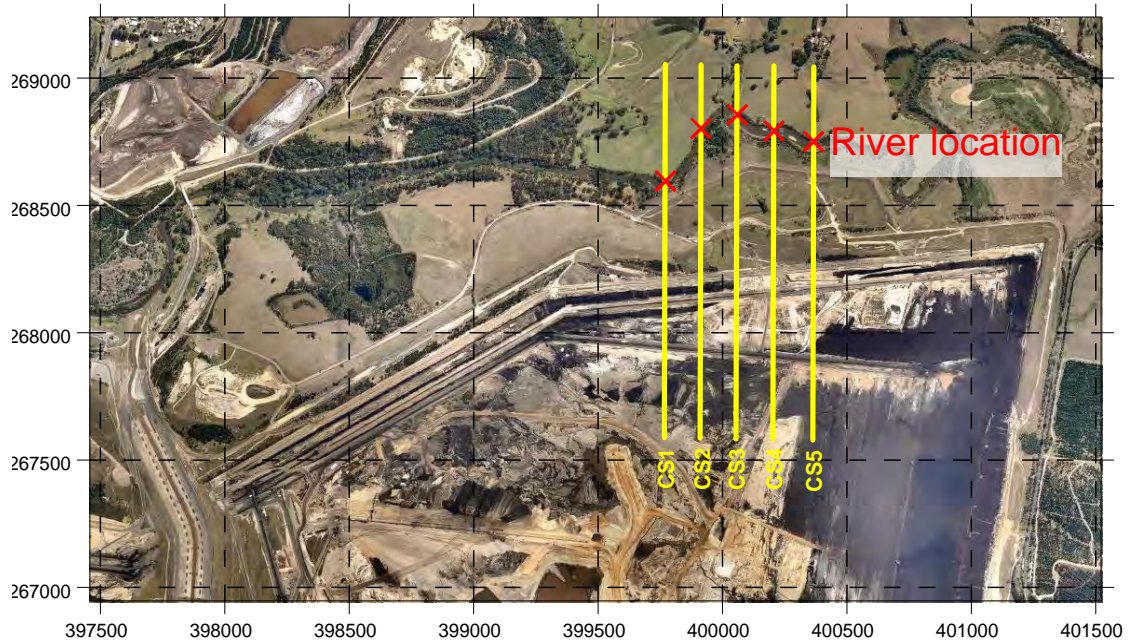
Figure 7.14. River locations for cross-sections CS1-5
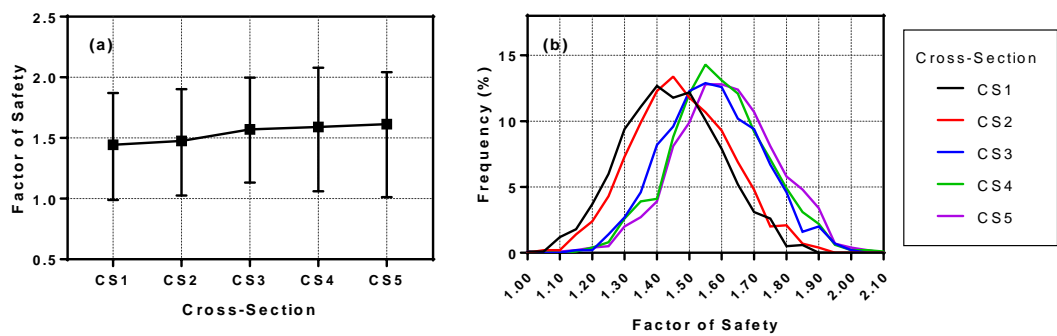
Figure 7.15. (a) Factor of Safety mean and range (b) Factor of Safety probability density function
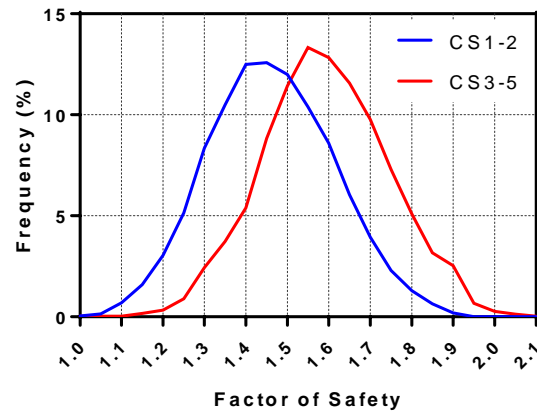
Figure 7.16. Factor of Safety rates of convergence
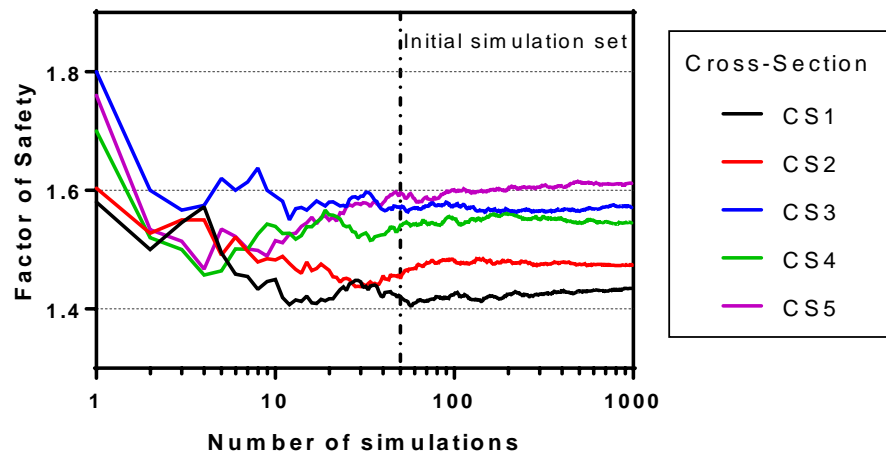
Figure 7.17. Factor of Safety distributions for cross-sections CS1-2 and CS3-5

7.5   Discussion and Conclusion

Two-dimensional plane-strain stability analysis is an especially important technique for complex

spatially variable slopes where three-dimensional finite element analysis is impractical or

unaffordable. The selection of the weakest likely cross-section is necessary to produce appropriate

factor of safety estimates. In this study, the impact of slope geometry and strata is considered by

simulating five cross-sections of a Victorian open-cut mine with identical groundwater conditions

and a fixed set of random field realisations. Although two distinct distributions of slip surfaces

were identified, the impact of varying slope geometry and strata without fluctuating groundwater conditions was considered to have a negligible effect. In particular, the Regions of Significance for producing a range of safety factors and slip surfaces were largely unchanged with cross-sectional selection, although minor differences in the depth of these regions due to the varying cross-sectional layering was noted. In this case, when considering groundwater distributions indicative of field conditions due to varying river geometry, two separate Factor of Safety distributions emerged, suggesting that spatially variable, probabilistic realisations coupled with changing groundwater conditions play a greater role in stability than variation of slope geometry and layering. Hence, a set of cross-sections were identified as appropriate for 2D Monte Carlo slope stability analysis of a large 3D mine cross-section.

Acknowledgments

8   Comparative Approaches to Probabilistic Finite Element Methods for Slope Stability Analysis

The following journal paper explores the Random Finite Element Method for slope stability analysis with several other probabilistic methods to determine the need to perform expensive spatially variable slope stability analysis as opposed to traditional probabilistic slope stability analysis. This journal paper is an accurate representation of the published version, with minor alterations to table and figure numbers for the purposes of continuity.

Abstract

Probabilistic slope stability analyses are often preferable to deterministic methods when soils are inherently heterogeneous or the reliability of geotechnical parameters is largely unknown. These methods are suitable for evaluating the risk of slope failure by producing a range of potential scenarios for the slope factor of safety. Several probabilistic methods can be combined with the Finite Element environment, including the Point Estimate Method, Monte Carlo Method and Random Finite Element Method. In this study, various distributions are considered for three different probabilistic Finite Element Methods to determine Factor of Safety and Probability of Failure distributions, based on the associated method of slope stability analysis. Results are presented for a case study of an Australian open-pit brown coal mine, with a range of shear strength parameter distributions for brown coal and interseam materials considered. Coal and interseam shear strength parameters are varied independently, to determine the effects of each material on slope failure.

Keywords

Random Finite Element Method; Monte Carlo simulation; point estimate method; spatial variation; slope stability analysis.

8.1 Introduction

Probabilistic methods are an important aspect of risk assessment for slope stability of open-cut mines. In many cases, probabilistic methods are able to capture soil variability and uncertainty when a deterministic analogue is deemed inappropriate. Soils often exhibit highly heterogeneous properties which can have a profound impact on the soil mechanical behaviour of large geostructures such as slopes and embankments [140]. Uncertainty and heterogeneity are particularly important in regions displaying appreciable anisotropy or weakened materials [242]. Even when a range of material parameters are available, inaccuracies due to measurement and laboratory conditions compared with in-situ field-scale behaviour can produce significant errors [276]. Hence, probabilistic slope stability methods have become an increasingly prevalent tool for geotechnical analysis [17, 247]. A range of applicable probabilistic methods exist, including First Order Second Moment (FOSM) [277], the Point Estimate Method (PEM) [115], the Modified Point Estimate Method (mPEM) [278], Monte Carlo Simulation (MCM) [16] and the Random Finite Element Method (RFEM) [158]. RFEM differs from FOSM, PEM and MCM by including the effects of spatial variability, incorporating a distance-based correlation length. In certain cases, probabilistic methods may be favourable to deterministic analyses, however, a common drawback is the often excessive computational resources required [279]. Griffiths and Fenton noted that one thousand simulations were necessary to achieve Factor of Safety (FoS) convergence for a 2:1 undrained clay slope [2]. For this reason, prediction and optimisation techniques are sometimes required to investigate large numerical models with high levels of complexity [246, 274]. Two of the most common slope stability analysis methods for incorporating material heterogeneity are Finite Element Method (FEM) and the Limit Equilibrium Method (LEM). The Finite Element

Method can be used in combination with the Point Estimate Method, (known as the Finite Element Method – Point Estimate Method), Monte Carlo simulation, and the Random Finite Element Method (RFEM).

In this study, the MCM, PEM and RFEM methods are compared for a range of distributions to determine slope safety factors, thereby highlighting the robustness of each method for varying distributions. A case study of the Yallourn open-cut brown coal mine in Victoria, Australia is presented, with a focus on determining factors of safety for varying probabilistic methods, when presented with varying distributions of input shear strength parameters. Furthermore, analysis of the variation of each material distribution considered independently, allows for a greater understanding of the impacts of each material layer.

8.2   Probabilistic Finite Element Methods

Point Estimate Method (PEM)

The Point Estimate Method as developed by Rosenblueth [130], is a multivariate technique for estimating the expected value of a performance function (e.g. the Factor of Safety). In the PEM, the continuous Probability Density Functions (PDFs) of input random variables are replaced by sets of discrete points by evaluating PDFs at locations determined by the standard deviation and Pearson's coefficient of skewness of the input parameters. Thus a two-point Probability Mass Function (PMF) is produced. These point values are then weighted to provide an estimate of the first two moments of the performance function. Given a performance function y of n variables (Equation 8.1), each variable is evaluated at two points x_{i+} and x_{i-} (Equation 8.2):

$$y = f(\boldsymbol{x}) = f(x_1, x_2, \ldots, x_n) \tag{8.1}$$

$$x_{i+} = \bar{x}_i + \xi_{xi+} \cdot \sigma_{xi}, \, x_{i-} = \bar{x}_i + \xi_{xi-}\sigma_{xi} \tag{8.2}$$

where $\bar{x}_i$ is the mean of the distribution of x_i; σ_{xi} the standard deviation; and ξ_{xi+} and ξ_{xi-} are so called standard deviation units, derived from the Pearson skewness coefficient ν_{xi}, as shown by

Equation 8.3. In the case where symmetric distributions are considered, both ξ_{xi+} and ξ_{xi-} are equal to unity. When considering a single random variable, the weights (named probability concentrations) are determined for each point estimate (Equation 8.4). For uncorrelated variables the weights i and j, are given by Equation 8.5. When the random variable distribution is symmetric, both weights are equal to 0.5. Finally, the Factor of Safety performance function mean and standard deviation can be evaluated by Equations 8.6 and 8.7, respectively.

$$\xi_{xi+} = \frac{v_{xi}}{2} + \left[1 + \left(\frac{v_{xi}}{2}\right)^2\right]^2, \ \xi_{xi-} = \xi_{xi+} - v_{xi} \tag{8.3}$$

$$P_{x+} = \frac{\xi_{xi-}}{\xi_{xi+}+\xi_{xi-}}, P_{x-} = 1 - P_{x+} \tag{8.4}$$

$$P_{i,j} = P_{xi} \cdot P_{xj} \tag{8.5}$$

where P_{xi} and P_{xj} are evaluated as the weights of a single random variable. For each variable, there are two points evaluated, meaning y is evaluated for a total number of 2^n combinations. Although the PEM is a simple procedure, the number of required computations grows exponentially with the number of input variables, often beyond what is reasonable for practical purposes.

$$FoS_\mu = \sum_{i=1}^{2^n} P_i FoS_i \tag{8.6}$$

$$FoS_\sigma = \sqrt{\sum_{i=1}^{2^n} P_i (FoS_i - FoS_\mu)^2} \tag{8.7}$$

Monte Carlo Method (MCM)

The Monte Carlo Method, when coupled with Finite Element Method simulation, can be a powerful tool for probabilistic slope stability analysis. By sampling a set of material properties from joint PDFs, a Factor of Safety distribution can be determined. The general iterative procedure of a Monte Carlo method for Finite Element Method slope stability is covered in the four steps described below:

1) Estimate the probability distribution for each input parameter for a given soil layer/region;

2) Generate random values for each parameter;

3) Finite Element Method simulation using parameters from (2);

4) Repeat the process N times (N > 100) to determine the converged statistical properties of
   interest.

The Probability of Failure (PoF) for a given slope is given by

$$PoF = \frac{N-M}{N}$$

(8.8)

where M is the number of slope safety factors less than 1.0.

Random Finite Element Method (RFEM)

One of the principal sources of material heterogeneity is the inherent spatial variability of soils
due to their stress history and depositional nature [280]. As such, common statistical parameters
such as the mean and standard deviation do not capture the relationships of material properties
based on their spatial structure [281]. A common method for describing the correlation structure
at given locations is provided by random field theory initially developed by Vanmarcke [282].
An important parameter for describing spatial structure is the autocorrelation function, which
provides a correlation measure as a function of distance. Although many correlation functions
exist, the most common two-dimensional correlation function is the Markovian exponentially
decaying correlation function:

$$\rho(\tau_x, \tau_y) = \exp\left(-\frac{2|\tau_x|}{\theta_x} - \frac{2|\tau_y|}{\theta_y}\right)$$

(8.9)

where ρ is the autocorrelation coefficient, defined at lag distances τ_x and τ_y, in the x and y
directions, respectively. Similarly, θ_x and θ_y are the scales of fluctuation (SoF) for both x and y.
The scale of fluctuation is defined as the measure of distance within which points are significantly
correlated [283]. Li et al. noted that the sensitivity to slope failure was insensitive to the type of
autocorrelation function [271]. Often, variables must be considered simultaneously when variables

are correlated. The covariance function Cov[X,Y] describes the strength of the relationship between

the random variables X and Y as

$$Cov[X, Y] = E[XY] - E[X]E[Y] = E[XY] - \mu_X \mu_Y \qquad (8.10)$$

A range of slope stability parameters may be considered for random field generation, however, the

most frequently implemented soil parameters are material cohesion c, internal friction angle φ,

dilation angle ψ, elastic modulus E, unit weight γ and permeability k. Alonso noted that the

variation of material strength parameters c and φ are a significant contributing factor in the Factor

of Safety distributions compared with the variation of soil unit weight [16]. Furthermore, Griffiths

and Fenton observed that the variation of cohesion, friction angle and unit weight provided the

greatest impact on safety factors when using random finite element methods [2].

In many cases, geotechnical parameters follow lognormal distributions, especially in cases where

parameters require strictly non-negative values, e.g. cohesion, unit weight, etc. The lognormal

random field X is specified by a transformation from a standard Gaussian random field G(x) by

$$X_i = \exp\left[\mu_{lnX} + s_{lnX}G(x_i)\right] \qquad (8.11)$$

where X_i is the lognormal parameter for the ith random field element; x_i is the centre point of the

i^{th} element; and μ_{lnX} and s_{lnX} are the mean and standard deviation of the normal distribution $\ln X$,

respectively. Both mean μ_{lnX} and standard deviation s_{lnX} parameters of the distribution are

determined by the following transforms:

$$\mu_{lnX} = \ln(\mu) - \frac{s_{lnX}^2}{2} \qquad (8.12)$$

$$s_{lnX}^2 = ln(1 + \frac{s^2}{\mu^2}) \qquad (8.13)$$

while the lognormal PDF is defined as:

$$f(X) = \frac{1}{X\,s_{\ln X}\,\sqrt{2\pi}}\,exp\left\{-\frac{1}{2}\left(\frac{\ln X - \mu_{\ln X}}{s_{\ln X}}\right)^2\right\} \qquad (8.14)$$

In many cases, material parameter distributions may be linked or jointly influenced by another parameter. In particular, weak negative cross-correlations between cohesion and the internal friction angle of materials have been observed. Cherubini noted correlations in the range of -0.7 to -0.24 [148] while Yucumen et al. noted values from -0.49 to -0.24 [150].

A common method of random field generation for a Finite Element geometry is the Local Average Subdivision (LAS method) [156]. Global averages are subdivided into local regions with the constraint that the local averages preserve the global statistical properties. LAS leads to a variance reduction, as fluctuations in the parameters tend to cancel each other out when averaged across the spatial region. As such, the variance of a LAS region is commonly less than the variance of a point field and requires a dimensionless variance adjustment to rectify the cell-to-cell variance.

Finite Element Method (FEM) for slope stability

The Finite Element Method has become one of the prevailing tools for numerical analysis of slope stability, requiring few a priori assumptions, especially regarding the slope failure mechanism. FEM slope failure develops "naturally" in zones where the soil shear strength is unable to provide sufficient support to resist the shear stresses [238]. Unlike Limit Equilibrium Methods, FEM does not incorporate the concept of slices and requires no assumptions of inter-slice forces. FEM is capable of progressive failure simulation up to and including overall shear failure, detailing information regarding deformations at working stress levels.

In this study, FEM slope stability analysis is performed with a two-dimensional plane strain, linear elastic model combined with the Mohr-Coulomb (MC) perfectly plastic failure criterion. Due to gravity loading of the slope materials, forces are generated, creating normal and shear stresses. In terms of the principal stresses with the convention of a compression-negative sign, the stresses are compared with the MC criterion can be defined as follows:

$$F = \frac{\sigma_1' + \sigma_3'}{2}\sin\phi' - \frac{\sigma_1' - \sigma_3'}{2} - c'\cos\phi' \qquad (8.15)$$

where σ'_1 and σ'_3 are the major and minor principal effective stresses, respectively; c' and ϕ' are the effective cohesion and internal friction angle parameters, respectively; and F is the failure function which is interpreted as:

F < 0 elastic (stresses inside the failure envelope)

F = 0 yielding (stresses are on the failure envelope)

F > 0 yielding but must be redistributed (stresses outside the failure envelope)

In the case of RFEM, the FEM geometry is partitioned into distinct element sets, where each element is allocated a set to material shear strength parameters (c and ϕ) from an associated random field distribution. The *Abaqus* element type CPEP (4-node plane strain quadrilateral, with bilinear displacement, bilinear pore pressure) was implemented for all finite elements within the slope model geometry. In the case of RFEM modelling, complexities associated with the spatially variable shear strength parameters require a particularly fine mesh distribution (in the case of this research, 40,000 elements) as depicted in Fig. 8.1.
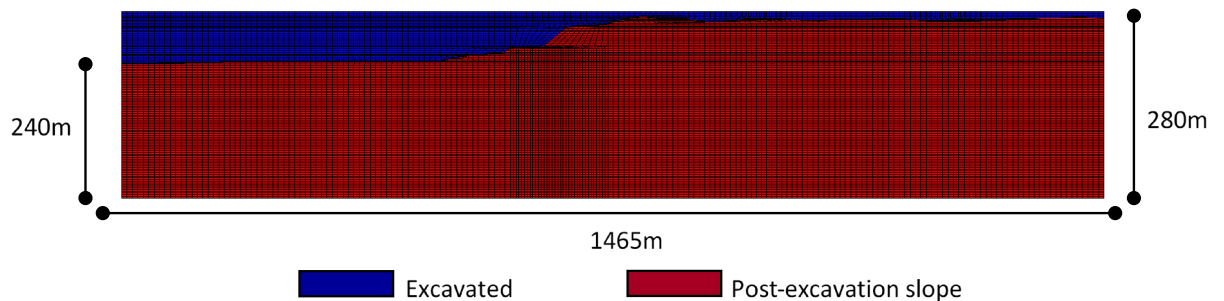
Figure 8.1. Slope geometry dimensions and mesh distribution.

Strength Reduction Method (SRM)

The Factor of Safety (FoS) of a slope is defined as the factor of the original slope shear strength parameters must be reduced by in order to bring the slope to the point of failure. The Strength Reduction Method (SRM), sometimes referred to as the Shear Strength Reduction Method, iteratively reduces shear strength parameters by a Strength Reduction Factor (SRF) until the failure

state is achieved. The method defined by Bishop [8] defines the coupled reduction of cohesion and

friction angles as follows:

$$c = \frac{c_0}{SRF} \tag{8.16}$$

$$\phi = \tan^{-1}\frac{\tan\phi_0}{SRF} \tag{8.17}$$

in which c_0 and ϕ_0 are the initial material cohesion and friction angle parameters, respectively; c

and ϕ are the reduced parameters; and SRF is the iterative Strength Reduction Factor. Once the

shear strength parameters are reduced to precipitate the onset of slope failure, the FoS is defined as

by the ratio of the initial shear strength parameters with respect to the final shear strength parameters

by:

$$FoS = \frac{c_0}{c_f} = \frac{\tan\phi_0}{\tan\phi_f} \tag{8.18}$$

where c_f and ϕ_f are the shear strength parameters required to bring the slope to the verge of failure.

There are several definitions of slope failure as discussed by Zienkiewicz and Taylor [284]

including bulging of the slope line [81] and limiting of the shear stresses on the failure surface

[285]. The most common attributes for determining the critical SRF includes:

1. Development of the shear surface through plasticised elements [30].

2. Large scale slope deformation.

3. Non-convergence within the FEM solver, indicating that no stress distribution can be
   determined that can satisfy both the MC failure criterion and global equilibrium [35]. Non-
   convergence is associated with a rapid increase in nodal displacements.

Although the Strength Reduction Method is the predominant FEM technique for determining slope

safety factors, the Finite Element package *Abaqus* does not implement an inbuilt Strength Reduction

Method. In this research, an optimised SRM was considered by incorporating Fortran and Python

codes in conjunction with *Abaqus* scripts by the procedure detailed by Dyson and Tolooiyan [228].

FEM for MCM and PEM vs. RFEM

The Finite Element Method can be applied to many probabilistic slope stability analysis techniques, including Point Estimate Methods, Monte Carlo Simulation and Random Finite Element Methods. In this research, two categories exist – probabilistic methods whereby shear strength parameters are sampled, then applied as properties for the whole layer, without intra-layer variation (PEM and MCM); and probabilistic spatial variation (RFEM), where numerous values are sampled from shear strength distributions, then applied within each layer with a given parameter correlation length.

The parameter distributions of cohesion and friction angle are identical for both the aforementioned cases and provide two different paradigms for probabilistic analysis – the combination of layers with parameters sampled from a distribution can be thought of as the uncertainty in selecting the "true" parameter value; while spatially varying elements sampled from shear strength distributions can be considered as potential realisations of spatially variable patterns within soils.

As such, the analysis of these two methods for a range of input distributions allows for the comparison of methods in determining Factors of Safety and Probabilities of Failure (PoF), while also considering how robust the results are, given different input distributions. Given random field analysis for slope stability, regions within random fields that provide the greatest impact to slope stability (named Regions of Significance or RoS), can be determined [246, 274]. In the study of RFEM simulation within this research, the impact of varying shear strength distributions on the locations of Regions of Significance is considered. Table 8.1 highlights the importance of the Probability of Failure when considering slope design and assessment. PEM, MCM and RFEM are all amenable to the calculation of such a parameter, given the requirement of numerous probabilistic realisations necessary for each method.

The similarity of random fields may be considered by the element-wise comparison of random field matrices, in conjunction with the Frobenius norm [246, 274]:

$$||\boldsymbol{D}||_F = \left(\sum_{i=1}^m \sum_{j=1}^n |a_{ij} - b_{ij}|^2 \right)^{1/2} \tag{8.19}$$

where A and B are two random field matrix instances of size m x n; and a_{ij} and b_{ij} are their elementwise components, respectively. When the random field similarity $||D||_F$ is small, the two random field instances are considered as similar, and produce comparable Factors of Safety. As $||D||_F$ increases, the random fields become dissimilar, with FoS comparison no longer possible. Random field realisations can be clustered based on their similarity values, depicting the level of association between random fields considered (Fig. 8.2). After the classification of random field instances deemed as similar, comparisons of the element-wise random field characteristics can be used to determine the regions of greatest impact on slope safety factors and slip surface geometries. Comparisons of random field characteristics within cluster groups is determined by the total absolute difference between each realisation within each cluster:

$$C_k = \sum_{i \neq j \in K} |M_i - M_j| \tag{8.20}$$

where, C_k is the overall random field similarity matrix C of the cluster K; and M_i and M_j are the ith and jth random fields of the cluster K. Elements within the matrix C_k with values approaching zero are locations with parameters common to the random fields within the cluster. Once the locations of significance within the cluster are identified, the individual random fields are analysed to determine the values within the region of interest. The clusters deemed of greatest importance are those with safety factors at the extremities of the FoS distribution.

Table 8.1. Comparative Significance of Probability of Failure [286].

Probability of Failure (%)	Design Criteria on Basis of which Probability of Failure is Established			Aspects of Natural Situation in Terms of which Probability of Failure can be Assessed	
	Serviceable Life	**Public Liability**	**Minimum Surveillance Required**	**Frequency of Evident Slope Failures**	**Rate of Evidently Unstable Movements**
50 to 100	Effectively zero	Public access is forbidden	Serves no purpose (excessive probability tantamount to failure)	Slope failures generally evident	Abundant evidence of creeping valley sides
20 to 50	Very short term (temporary open pit mines)	Public access forcibly prevented	Continuous monitoring with intensive sophisticated instruments	A significant number of unstable slope works	Clear evidence of creeping valley sides
10 to 20	Very short term	Public access actively prevented	Continuous monitoring with sophisticated instruments	Somewhat unstable slopes evident	Some evidence of slowly creeping valley sides
5 to 10	Short term	Public access prevented	Conscious superficial monitoring	No read evidence of unstable slopes	Extremely slowly creeping valley sides not readily evident
0.5 to 5	Medium-term (semi-permanent slopes)	Public access allowed	Incidental superficial monitoring	No unstable slopes evident	No unstable movements evident
Less than 0.5	Very long term (permanent)	Public access free	No monitoring required	Stable slopes	No movements
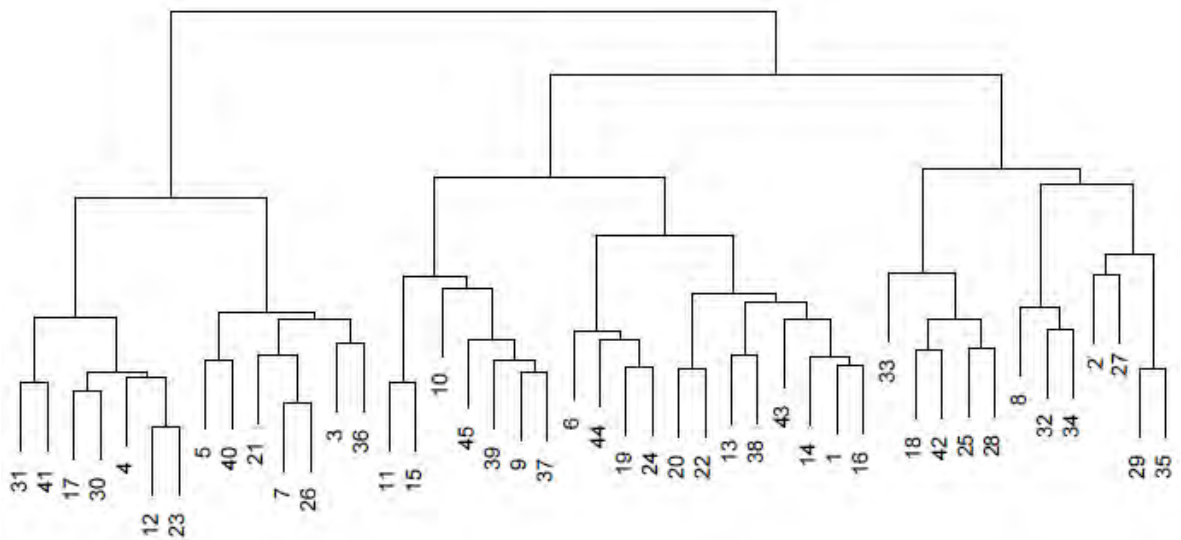
Figure 8.2. A cluster dendrogram of groups of similar random field realisations.
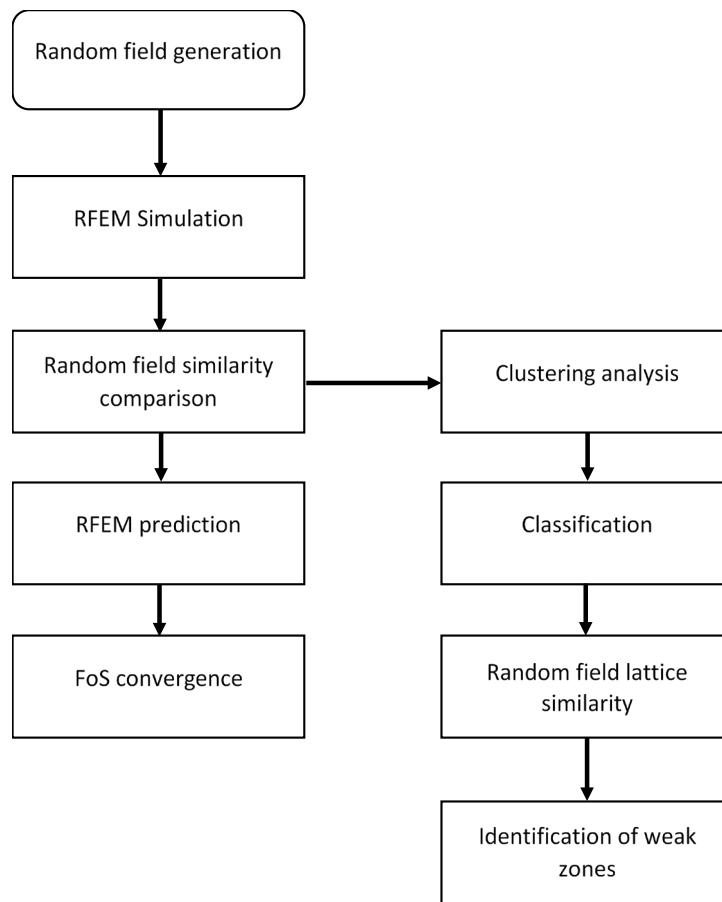
Figure 8.3. RFEM analysis procedure as described by Dyson and Tolooiyan [274].

8.3   Field Conditions

Victorian brown coal and Yallourn open-pit mine site conditions

The Latrobe Valley Depression is an extension of the Gippsland Sedimentary Basin in Victoria,

Australia, and covers an area of 800km^2 [186], containing some of the world's thickest continuous

brown coal seams [287]. The Yallourn open-pit (Fig. 8.4), is one of three large brown coal mines

in the region. Table 8.2 presents Yallourn brown coal properties as detailed by Perera et al. [206].

Beneath the coal seam at Yallourn lies an interseam layer consisting of a clayey material much

weaker in strength [207], with geotechnical parameters of both coal and non-coal interseam

materials shown in Table 8.3. A two-dimensional cross-section (Fig. 8.5) was chosen for Finite

Element Method slope stability analysis of the Yallourn North-Eastern batter, with associated shear

strength parameter distributions necessary for probabilistic analyses given in Table 8.4. A common

parameter for describing the variation of a distribution is the Coefficient of Variation (CoV), defined as the ratio of the distribution standard deviation (s) with respect to the distribution mean (μ). Commonly observed CoVs are detailed in Table 8.5. As a comparison, typical values for the Coefficient of Variation observed by Queiroz et al. [142] are presented in Table 8.6.

Of particular importance for RFEM simulation are parameter Scales of Fluctuation (θ), defining the spatial variability of the random field. Coal and interseam shear strength SoF values in both the x and y directions are shown in Table 5. Of particular note is the anisotropy of both coal and non-coal materials, with rapid variation of shear strengths in the "down the bore" direction, compared with "across-the bore". Victorian Brown Coal exhibits no significant shear strength parameter correlations, no depth dependent trends (Table 8.6). As such, parameter correlation has been neglected in this study.

Figure 8.4. Location of the Yallourn open-cut mine.

Table 8.2. Yallourn brown coal properties [206].

Property	Value
Rank	ASTM lignite B
Moisture content (% wb)	58.0
Ash yield (% db)	1.7
Volatile matter content (% bd)	50.3
Fixed carbon (% db)	48.0
Sulphur content (% db)	0.28
Gross dry specific energy (MJ/kg)	26.1
Net wet specific energy (MJ/kg)	6.9
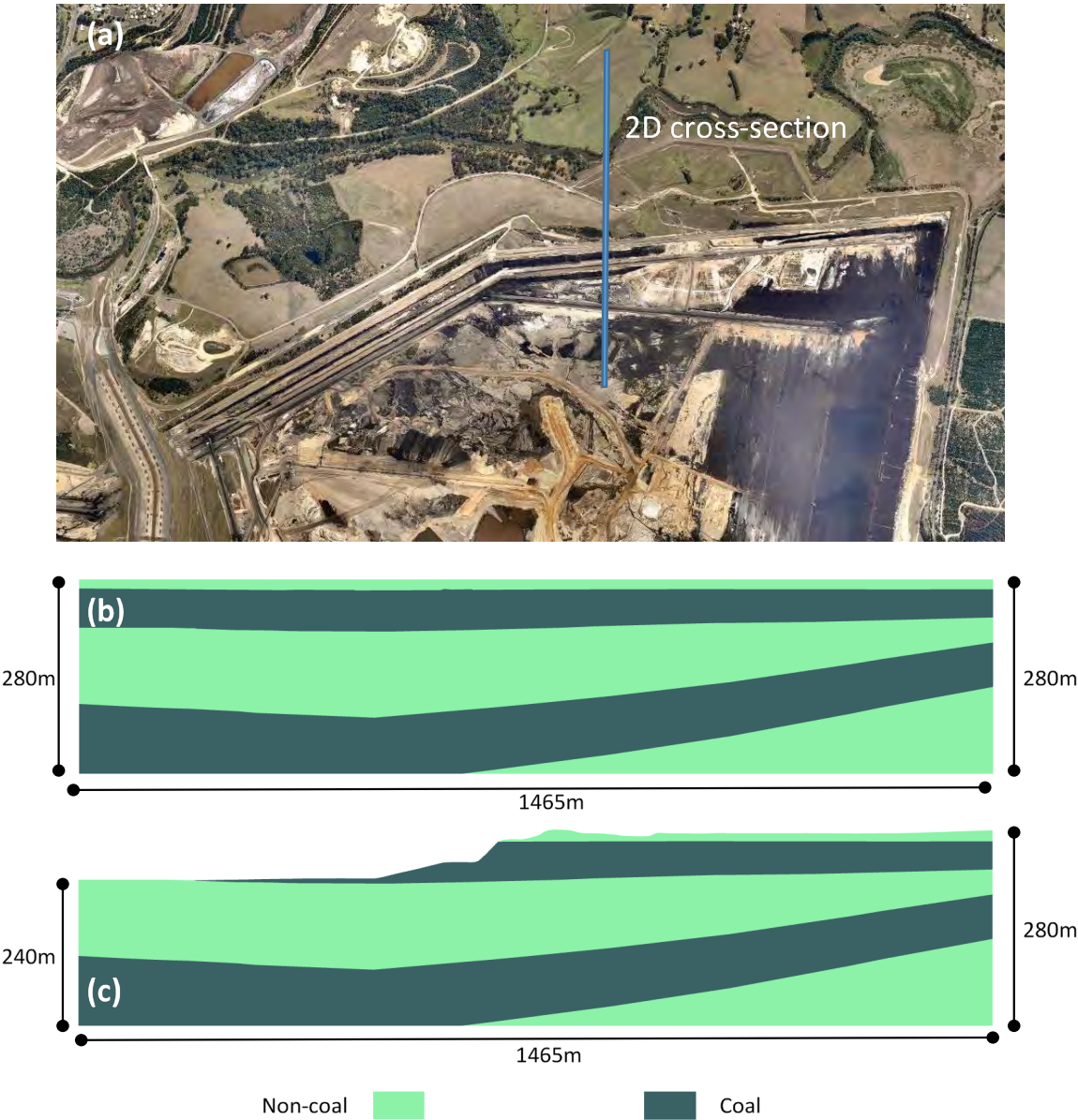
Figure 8.5. (a) Yallourn North-East batter with 2D cross-section location (b) unexcavated cross-section geometry (c) excavated cross-section geometry.

Table 8.3. Geotechnical parameters for coal and non-coal materials.

Material	γ_{unsat} (kN/m^3)	γ_{sat} (kN/m^3)	E (MPa)	ν	k (m/day)
Coal	11.4	11.5	40	0.3	7.6e-3
Non-coal	20.15	20.2	52	0.3	4.7e-2

Table 8.4. Shear strength parameter statistics.

	Coal		Non-coal	
Parameter	c (kPa)	φ (°)	c (kPa)	φ (°)
Mean (μ)	150.7	27.3	31.8	23.7
Standard Deviation (s)	69.8	4.9	5.0	4.5
COV (%)	0.4	0.2	0.2	0.2

Table 8.5. Common Coefficient of Variation shear strengths [142].

Parameter	Coefficient of Variation (%)
Cohesion	20 – 80
Friction angle	4 – 20

Table 8.6. Shear strength length scales.

	Coal		Non-coal	
Scale of Fluctuation (m)	c	φ	c	φ
θ_x	320.3	772.4	812	627.8
θ_y	23.1	8.7	35	13.1

Table 8.7. Shear strength correlations.

	Coal		Non-coal	
	c	φ	C	φ
Correlation with depth	0.129	-0.260	-0.027	-0.060
$r_{c,\varphi}$	0.046		-0.003	

8.4   Probabilistic Simulation Results and Comparison

To compare safety factor results PEM, MCM and RFEM, a range of mean parameters and CoVs
for coal and non-coal cohesion and internal friction angles were considered. The number of
simulation realisations for each test method is shown in Table 8.8. While PEM only requires 2^N
simulations, MCM and RFEM require numerous simulation instances to achieve convergence. In
the case of RFEM simulation, FoS prediction techniques based on the first 50 random field instances
are used to predict all further RFEM realisations, without the need for cumbersome full FEM
simulation [246].   Mean and CoV multipliers were implemented to consider a number of
distributions, altering parameters by a given scalar with respect to the initial mean and standard
deviation parameters. The mean multipliers considered are shown in Table 8.9, while the CoV
multipliers are presented in Table 8.10. Initially, mean and CoV parameters are altered individually
while all other parameters are kept constant to assess the impact of each distribution change on the

FoS. Typical cohesion and friction angle random fields are shown in Fig. 8.6a and b, respectively,

while Fig. 8.6c shows an example of commonly occurring slope failure slip surface.

Table 8.8. Number of realisations required per mean/CoV parameter.

Method	Number of simultions
PEM	16
MCM	100
RFEM	100

Table 8.9. List of distribution mean parameters tested.

Mean value multiplier	Coal		Non-coal interseam	
	Cohesion (kPa)	Friction angle (°)	Cohesion (kPa)	Friction angle (°)
1.2	180.8	32.7	38.1	28.4
1.1	165.7	30.0	34.9	26.0
1	150.7	27.2	31.8	23.6
0.9	135.6	24.5	28.6	21.3
0.8	120.5	21.8	25.4	18.9
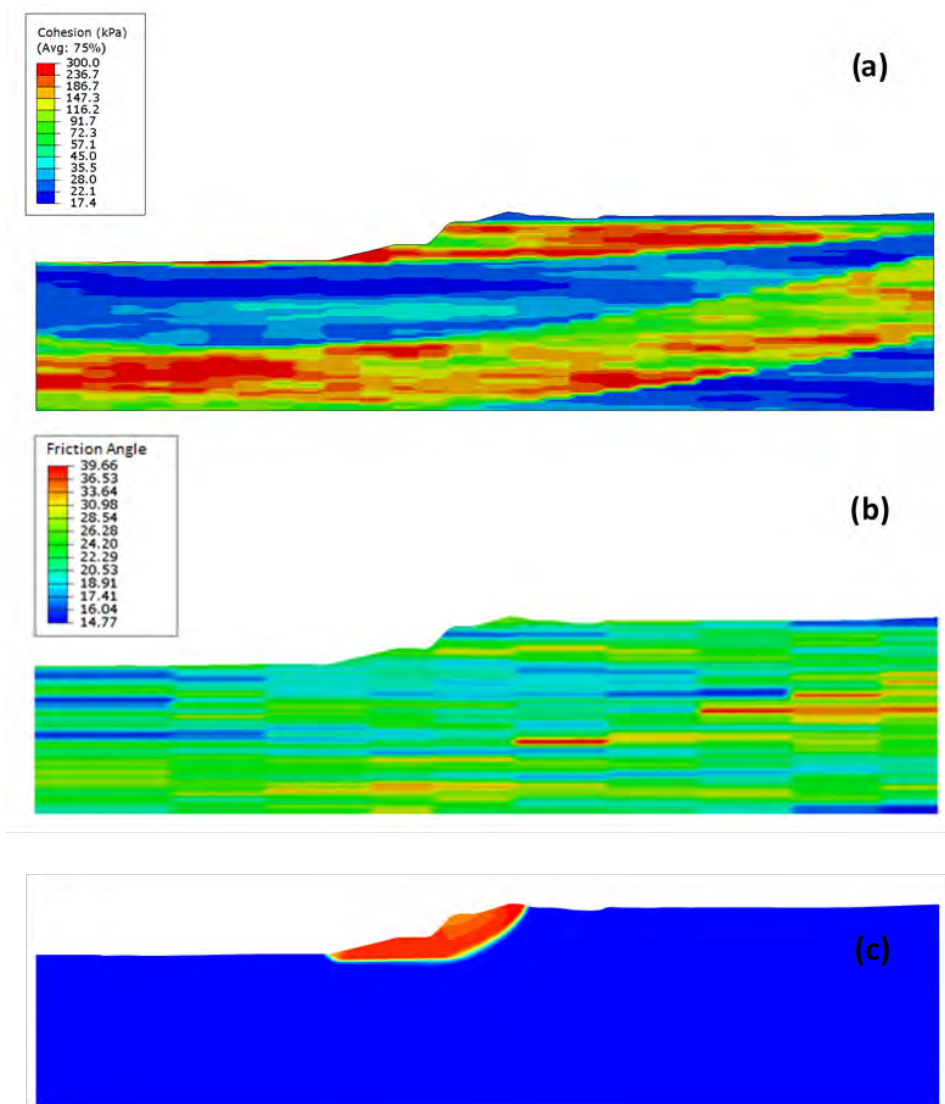
Figure 8.6. Typical random field realisations and slope slip surface (a) cohesion random field

realisation (b) typical friction angle realisation (c) slope slip surface.

Fig. 8.7 shows a range of FoS values, for mean shear strength input parameters. In each case,

RFEM produced the lowest safety factors due to the numerous weak elements in each spatially

varying random field. PEM and MCM provided similar safety factors across both shear strength

parameters and both materials. Due to the computational expense of simulating numerous MCM

realisations, PEM is preferable of the two methods for determining the FoS in this particular

instance. The interseam cohesion and friction angle produced the greatest levels of slope instability,

with the FoS dropping below 1.3 with the variation of both parameters. The variability of FoS

values for a range of mean input parameters is shown in Fig. 8.8. In all cases, PEM overpredicts

the FoS variability, with respect to MCM and RFEM. The convergence of mean safety factors is

sparticularly important to ensure the minimum number of simulation realisations are used (Fig. 8.9).

PEM two-point samples for four variables produces only 16 realisations, while both MCM and

RFEM were implemented with 100 probabilistic instances. In the case of RFEM, only the first 50

realisations were simulated with full FEM, while 100 MCM full FEM simulations were required.
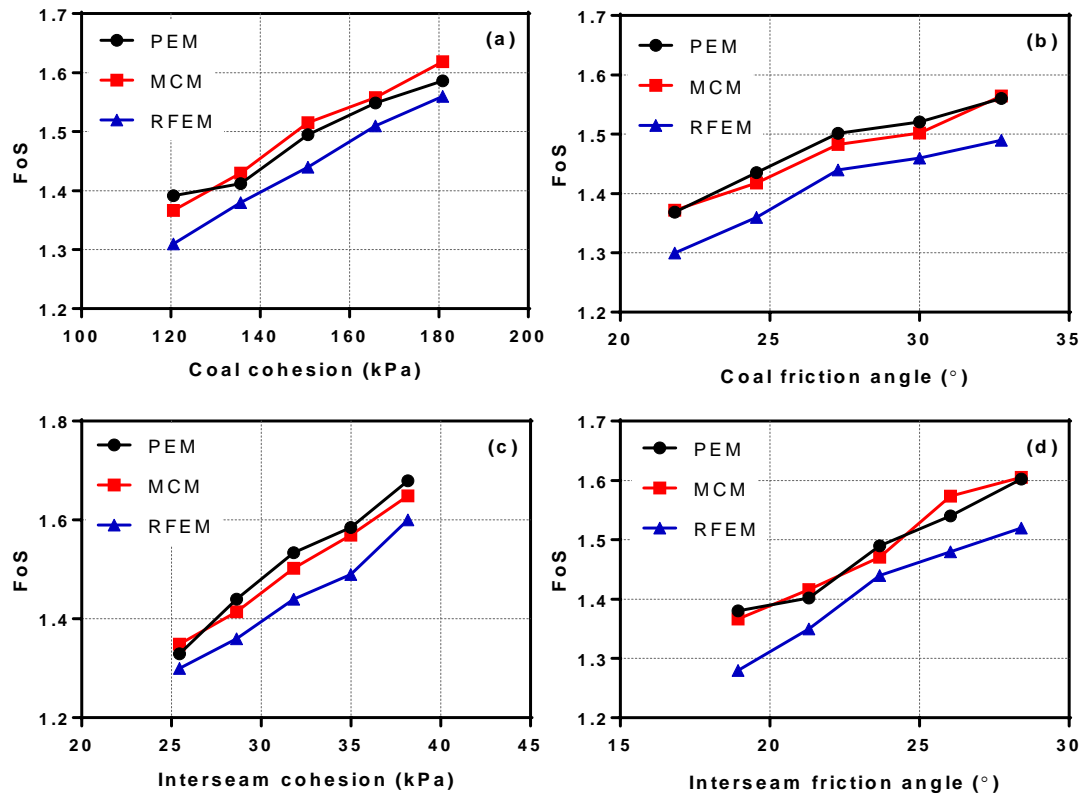
Figure 8.7. Mean safety factors for various mean value input parameters (a) coal cohesion FoS

(b) coal friction angle FoS (c) interseam cohesion FoS (d) interseam friction angle FoS.
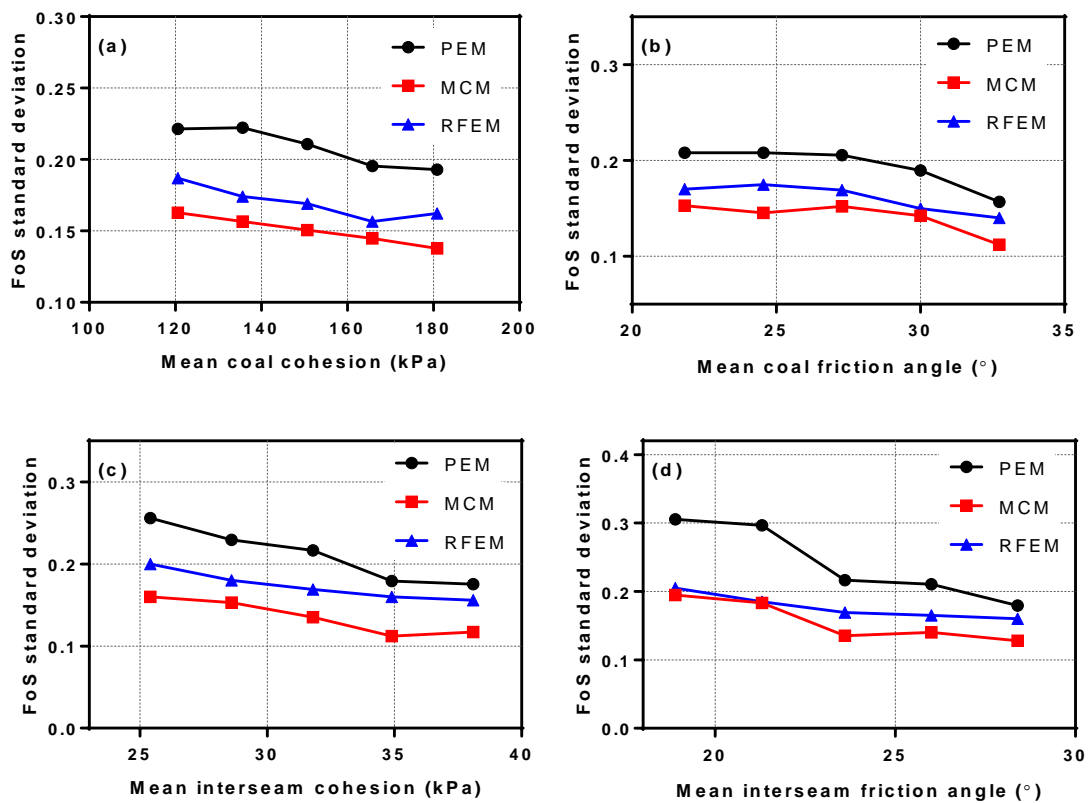
Figure 8.8. Factor of Safety standard deviation for mean value input parameters (a) coal cohesion

(b) coal friction angle (c) interseam cohesion (d) interseam friction angle.
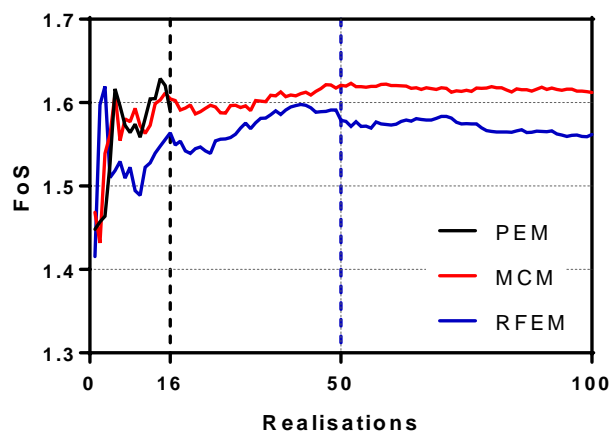
Figure 8.9. Factor of Safety convergence.

Similar to the mean value multipliers of Table 8.9, CoV multipliers are presented in Table 8.10. In

the case of the Coefficient of Variation, the distribution mean remains constant, while the

distribution standard deviation is the unconstrained variable. For all three methods, Factors of

Safety decrease with respect to the Coefficient of Variation (Fig. 8.10). As with Fig. 8.7, the lowest

levels of the slope FoS occurred when the interseam distributions were varied. As the CoV

increases, RFEM FoS values decrease at a greater rate than PEM and MCM. Moreover, the

variability of PEM safety factors is observed to be significantly greater than both RFEM and MCM,

with respect to input shear strength variation (Fig. 8.11). Similarly, the Probability of Failure for

PEM is decidedly higher than RFEM and MCM (Fig. 8.12). As only 16 PEM simulation

realisations are computed, the failure of a slope when considering a combination of slow valued

strengths will produce an overpredicted PoF, suggesting the method has yet to converge. In the

case where CoV multipliers of 1.5 were used, indicating a 50% increase in CoVs compared with

the initial dataset of observed material parameters, PoF values did not exceed 0.05 for MCM and

0.08 for REM. As such, even the most conservative of shear strength parameter distributions

produce Factors of Safety within the categories of Table 8.1 deemed as short and medium-term

semi-permanent slopes. Given these Probabilities of Failure, Kirsten [286] states that these slopes

are likely to exhibit no evidently unstable movements or are likely to be extremely slow creeping.

Table 8.10. List of distribution Coefficient of Variation parameters tested.

CoV multiplier	Coal		Non-coal interseam	
	Cohesion	Friction angle	Cohesion	Friction angle
1.5	0.69	0.27	0.24	0.285
1.25	0.58	0.125	0.20	0.237
1	0.46	0.18	0.16	0.190
0.75	0.35	0.135	0.12	0.142
0.5	0.23	0.09	0.09	0.095
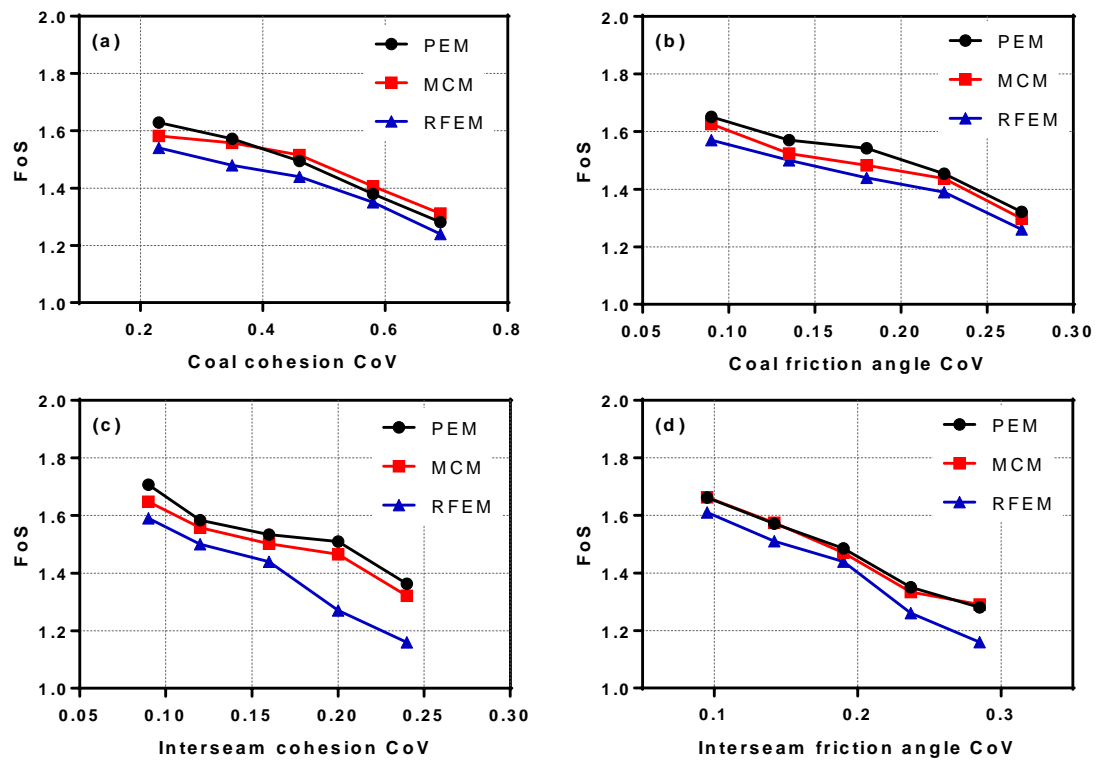
Figure 8.10. Mean safety factors for various CoVs (a) coal cohesion (b) coal friction angle (c)

interseam cohesion (d) interseam friction angle.
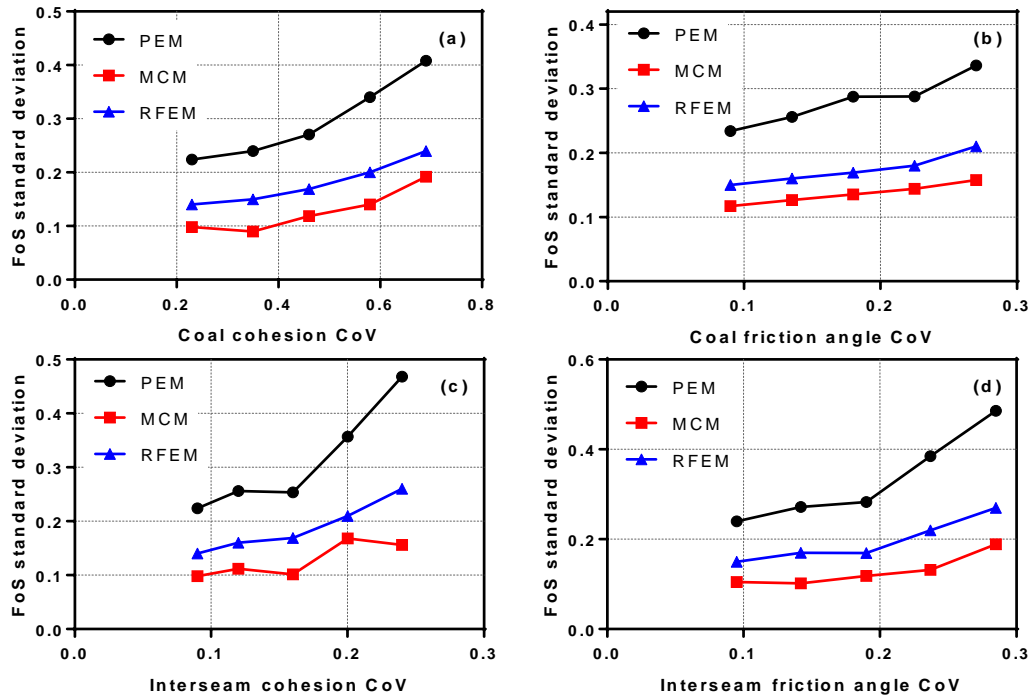
Figure 8.11. FoS standard deviation for various CoVs (a) coal cohesion (b) coal friction angle (c)

interseam cohesion (d) interseam friction angle.
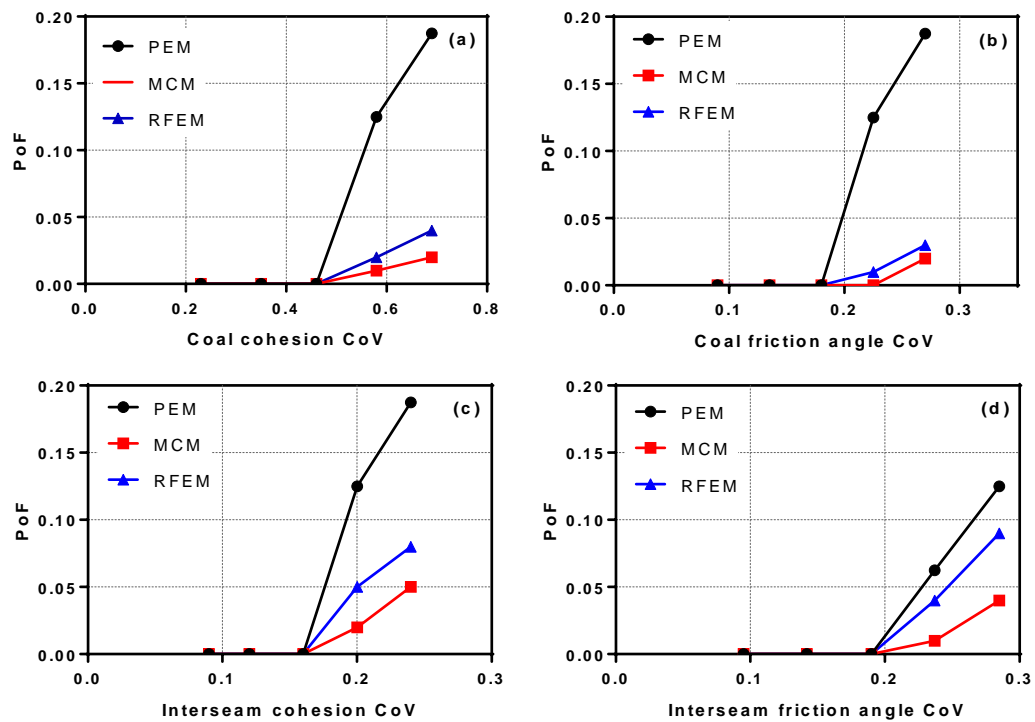
Figure 8.12. Probability of failure for various CoVs (a) coal cohesion (b) coal friction angle (c)

interseam cohesion (d) interseam friction angle.

8.5   Discussion and Conclusion

Probabilistic slope stability analysis methods are often necessary for evaluating soil variability and

uncertainty.   Although a number of numerical methods may be incorporated within the Finite

Element environment, output Factor of Safety and Probability of Failure distributions can be

dissimilar and technique dependent.   In the case of the MCM and RFEM methods, numerous

simulation instances are necessary to attain parameter convergence, requiring a significant

computational capacity.   A case study of the Yallourn open-cut mine in Victoria, Australia, is

presented, with the variability of input shear strength parameter distributions presented for both coal

and interseam materials.   The variation of interseam shear strength parameters produced lower

safety factors compared with the variation of coal parameters, suggesting the interseam materials

are more likely to impact the slope failure mechanism than the coal.   Although the sampling

procedure for each probabilistic method was different, the presented mean Factors of Safety with respect to the input mean shear strength parameters and coefficient of variation distributions were relatively similar for both PEM and MCM. In the case of RFEM, zones containing weakened shear strength parameters allow slopes to fail at lower Factors of Safety, as noted by Griffiths and Fenton [2], where increased Probabilities of Failure were observed for small correlation lengths. As correlations lengths increase, the presence of localsed zones containing materials with weakened shear strengths become less likely. Monte Carlo Simulation represents the case with "infinite" correlation lengths. As a result, the absence of material weak zones present in spatially variable cases inflates the Factor of Safety and reduces the Probability of Failure.

When considering slope Probabilities of Failure, PEM significantly overpredicts failure, due to the relatively few instances simulated for this method as well as the high level of FoS distribution variability. Although RFEM is the most complex method considered, requiring additional knowledge of the spatial variability of cohesion and friction angle parameters, the method produces the most conservative FoS parameters for all materials and input distributions. In cases where the effects of slope failure pose a significant risk to life and economic productivity, the addition of the spatial variability captured in RFEM (resulting in lower safety factors) is a necessary consideration in many cases of slope stability.

9   Conclusions

9.1   Summary

The research of this PhD thesis has examined the effects of spatially variable soils on numerical slope stability analysis by implementation of the Random Finite Element Method. A set of optimised methods for slope stability computation, prediction and analysis were developed for the assessment of slopes exhibiting spatially variable shear strength parameters.

The computational complexity of large Random Finite Element Method slope models provides strong motivation for a procedural step-by-step optimisation and prediction regime defined in this research, allowing the effects of two-dimensional analysis and statistical distributions to be carefully examined. The results of this research detail these methods of analysis, considering the distribution of safety factors for North-East batter of the Yallourn open-pit brown coal mine.

Although discussion summaries are provided at the conclusion of each of the preceding chapters of this thesis, an overview of the results are presented below.

The material of *Chapter 2* provided common methods for slope stability analysis as well as detailing the characteristics of inherent soil variability. The advantages and disadvantages of Finite Element Method analysis were compared and contrasted with the Limit Equilibrium Method. In particular, the Finite Element Method does not require failure mechanisms to be predefined prior to slope analysis. Rather, the slope failure surface emerges as a natural progression of Finite Element Method simulation. As the failure mechanisms of spatially variable soils can be wide ranging, the progression of slope slip surfaces is a desirable feature of FEM slope analysis. For industrial scale projects and slope stability investigation, the effects of spatially variable soils are seldom considered in depth due to the complexity of soil variation and difficulty in modelling parameter variation. Furthermore, currently available commercial software do not readily allow for Random Finite Element Method slope stability analysis. A review of the relevant literature has indicated that RFEM, initially developed by Griffiths and Fenton [2] is a powerful tool for evaluating the effects

of soil variability, using probabilistic Monte Carlo simulation, providing the necessary framework for the large scale spatially variable slope analysis conducted in this research.

The material of *Chapter 3* provided an overview of the Latrobe Valley, with a particular focus on the Yallourn open pit brown coal mine and Victorian Brown Coal. A brief history of the region was presented, with the necessary details of geology, location and geotechnical parameters, providing summary information for the chapters following.

The material of *Chapter 4* presented an optimised Strength Reduction Method for implementation in the Finite Element software *Abaqus*, which does not include in-built Strength Reduction codes. The method provides an alternative Strength Reduction definition, with an optimised treatment for the probabilistic analyses to follow. In particular, the alternative description provided significant computational efficiency for complex 2D and 3D models requiring large computation times. The method produces full slope simulation for each reduction step, rather than solely results for the final reduction stage. The codes provided within this chapter are implemented in the research of the chapters thereafter.

The material of *Chapter 5* presented random field similarity methods for comparison of spatially variable structures prior to full Finite Element Method simulation. The methods were used as a prediction method for slope safety factors, drastically reducing the necessary computation for Monte Carlo simulation. Three examples were presented, highlighting the versatility of the similarity method for a range of slope model conditions. For each case, random field comparison methods identified random field instances sufficiently similar for prediction. Several clustering techniques were explored, based on the Frobenius similarity norm measure. The prediction measure was compared with results of full FEM Monte Carlo simulation, indicating convergence to matching slope safety factors.

The material of *Chapter 6* implemented the random field similarity methods of *Chapter 5* while extending the techniques to compare random field instances and investigate the effect of individual random field spatial structures on slope failure mechanisms, as well as slip surface shapes and

locations. Initially, 40 random field instances were generated for full RFEM simulation, with further random field realisations used for the purposes of prediction, to obtain Factor of Safety and slip surface distribution convergence. RFEM slope stability analysis is presented for the North-East batter of the Yallourn mine, with the regions of significance locations highlighted for cohesion and friction angle parameters and a range of slope safety factors and slip surface depths. It is noted that the results of these analyses provide mechanisms useful for further mine site investigation, allowing for the reduction uncertainty with a posteriori targeted site examination.

The material of *Chapter 7* considered the investigation of two-dimensional cross-sectional slope simulation coupled with spatially variable soils. Plane-strain stability analysis is an important tool for simulation of complex slopes where three-dimensional analysis is heavily restricted by computational resources and time constraints. A set of random field instances were generated for RFEM simulation, and analysed for five cross-sections of the Yallourn mine. Each cross-section was provided an identical collection of random fields to determine the impacts of varying slope geometry and material layering, with the objective of identifying the most conservative cross-section exhibiting the lowest safety factors. Variation in the locations of regions of significance were further investigated for each cross-section, with various groundwater distributions considered. Two distinct cross-sectional distributions were identified (named CS 1-2, and CS 3-5), with CS1-2 producing lower Factors of Safety. The identification of appropriate cross-sectional locations provides not only a method of analysis for exploration of large slopes with spatially variable parameters, but also results necessary for any additional slope stability simulations.

The material of *Chapter 8* considered the effects of several probabilistic FEM techniques (PEM and MCM), compared with RFEM. In the case of both PEM and MCM, do not take material spatial variation into account. Instead, material layer parameters are sampled from material statistical distributions. Factor of Safety distributions and slip surface characteristics are presented for each method, with rates of distribution convergence examined. The aforementioned methods are considered for a range of friction and cohesion Coefficients of Variation to consider the impact of various input statistical distributions on slope stability. RFEM simulation produced lower safety

factor mean values compared to PEM and MCS, as spatially variable materials allow slopes to plasticise in zones containing weaker shear strengths.

9.2   Recommendations for Further Research

The slope stability analysis conducted in this research has assumed a water table based on monitoring data provided by the Yallourn mine. It is well established that pore-water pressures can have a significant effect on the stability of slopes. Furthermore, as with shear strength parameters, pore-water pressures are subject to significant levels of uncertainty. While the spatial variability of material permeabilities and pore-water pressures is not considered in this research, it is a worthwhile aspect of RFEM slope stability analysis for future work. Although spatially variable permeability parameters are not considered in this thesis, horizontal and vertical permeabilities are well suited to random field analysis as they are often considered to be highly variable and spatially dependent.

In this research, probabilistic stability models are developed based on shear strength parameter statistical distributions provided by the State Electricity Commission of Victoria. Griffiths and Fenton [2] noted the effects of material unit weight on safety factors. In the absence of sufficient data regarding the spatial correlation length of material unit weights, variability of this parameter was not considered as part of this research, however, further analysis in this respect is suggested when considering Yallourn and Latrobe Valley mine stability.

Chapter 8 considered the effects of varying statistical parameter distributions. It is accepted that variation of a number of further parameter distributions in this research may be considered for investigation. Given opportunity to consider the impacts of spatially variable soils, further investigation of spatial correlation lengths and their effects on regions of significance is suggested. It is the belief of the author that examination of regions of significance with respect to parameter correlation lengths, while implementing random field similarity comparison methods is an aspect of RFEM slope stability analysis worthy of exploration.

The Strength Reduction Method given in *Chapter 4* provides a method of determining slope safety factors for linear elastic, perfectly plastic soils with the Mohr-Coulomb failure criterion. Although RFEM slope analysis of more complex soil constitutive models is as yet uncommon, a Strength Reduction Method capable of incorporating a range of soil constitutive models is of importance when faced with a diverse set of soils.

The RFEM analysis conducted in this research assumes two-dimensional plane strain conditions. *Chapter 7* provides methods of analysis to study varying slope geometries in a two-dimensional framework. Due to the cumbersome nature of three-dimensional RFEM computation, slope stability analysis of this form was not conducted. It is the author's belief that with the passing of time and the increase of computational capacity, three-dimensional large scale RFEM slope stability analysis will be common practice in the not too distant future.

9.3 Conclusion

From the analyses presented, it is concluded that the effects of spatial variability of shear strength parameters can have significant impacts on the stability of slopes, with FEM playing a critical role in this analysis. The objectives of this thesis have been achieved by development of a cohesive framework for conducting two-dimensional Random Finite Element Method slope stability analysis in an efficient and optimised capacity, with techniques allowing for the prediction, comparison and classification of slope failure mechanisms and safety factors.

References

[1] Vanmarcke EH. Reliability of earth slopes. Journal of the Geotechnical Engineering Division. 1977;103(11):1247-65.

[2] Griffiths DV, Fenton GA. Probabilistic slope stability analysis by finite elements. Journal of Geotechnical and Geoenvironmental Engineering. 2004;130(5):507-18.

[3] Duncan JM, Wright SG, Brandon TL. Soil strength and slope stability: John Wiley & Sons, 2014.

[4] Fellenius W. Calculation of stability of earth dam. Transactions 2nd Congress Large Dams, Washington, DC, 19361936. p. 445-62.

[5] Read J, Stacey P. Guidelines for open pit slope design. 2009.

[6] Duncan JM. Soil slope stability analysis. Landslides: Investigation and Mitigation, Transportation Research Board Special Report 247. 1996:337-71.

[7] Whitman RV, Bailey WA. Use of computers for slope stability analysis. Journal of Soil Mechanics & Foundations Div. 1967.

[8] Bishop AW. The use of the slip circle in the stability analysis of slopes. Geotechnique. 1955;5(1):7-17.

[9] Abramson LW, Lee TS, Sharma S, Boyce GM. Slope stability and stabilization methods: John Wiley & Sons, 2001.

[10] Janbu N. Slope stability computations, soil mechanics and foundation engineering report. Technical University of Norway, Trondheim. 1968.

[11] Janbu N. Slope stability computations. Publication of: Wiley (John) and Sons, Incorporated. 1973.

[12] Nash D. A comparative review of limit equilibrium methods of stability analysis. Slope stability. 1987:11-75.

[13] Fredlund D, Morgenstern NR, Widger R. The shear strength of unsaturated soils. Canadian geotechnical journal. 1978;15(3):313-21.

[14] Fredlund DG, Rahardjo H. Soil mechanics for unsaturated soils: John Wiley & Sons, 1993.

[15] Duncan JM. Factors of safety and reliability in geotechnical engineering. Journal of geotechnical and geoenvironmental engineering. 2000;126(4):307-16.

[16] Alonso EE. Risk analysis of slopes and its application to slopes in Canadian sensitive clays. Geotechnique. 1976;26(3):453-72.

[17] Tang W, Yucemen M, Ang A-S. Probability-based short term design of soil slopes. Canadian Geotechnical Journal. 1976;13(3):201-15.

[18] Wu TH, Kraft LM. Safety analysis of slopes. Journal of Soil Mechanics & Foundations Div. 1970.

[19] Lam L, Fredlund D. A general limit equilibrium model for three-dimensional slope stability analysis. Canadian geotechnical journal. 1993;30(6):905-19.

[20] Duncan JM, Wright SG. Soil strength and slope stability: John Wiley & Sons, 2005.

[21] Taylor DW. Stability of earth slopes. J Boston Soc Civil Engineers. 1937;24(3):197-247.

[22] Haines A, Terbrugge P, Carrieri G. Preliminary estimation of rock slope stability using rock mass classification systems. 7th ISRM Congress: International Society for Rock Mechanics and Rock Engineering, 1991.

[23] Laubscher D, Jakubec J. The MRMR rock mass classification for jointed rock masses. Underground Mining Methods: Engineering Fundamentals and International Case Studies, WA Hustrulid and RL Bullock (eds) Society of Mining Metallurgy and Exploration, SMME. 2001:475-81.

[24] Cousins BF. Stability charts for simple earth slopes. Journal of the Geotechnical Engineering Division. 1978;104(2):267-79.

[25] Morgenstern N, Bishop A. Stability coefficients for earth slopes. 1960.

[26] Spencer E. A method of analysis of the stability of embankments assuming parallel inter-slice forces. Geotechnique. 1967;17(1):11-26.

[27] Taylor DW. Fundamentals of soil mechanics: LWW, 1948.

[28] Courant R. Variational methods for the solution of problems of equilibrium and vibrations: Verlag nicht ermittelbar, 1943.

[29] Bathe K-J, Wilson EL. Numerical methods in finite element analysis. 1976.

[30] Matsui T, San K-C. Finite element slope stability analysis by shear strength reduction technique. Soils and Foundations. 1992;32(1):59-70.

[31] Zienkiewicz OC, Taylor RL, Taylor RL, Taylor RL. The finite element method: solid mechanics: Butterworth-heinemann, 2000.

[32] Griffiths DV, Lane PA. Slope stability analysis by finite elements. Géotechnique. 1999;49(3):387-403.

[33] Hoek E, Brown ET. Underground excavations in rock: CRC Press, 1980.

[34] Smith I, Hobbs R. Finite element analysis of centrifuged and built-up slopes. Geotechnique. 1974;24(4):531-59.

[35] Zienkiewicz OC, Humpheson, C. & Lewis, R. W. Associated and non-associated visco-plasticity and plasticity in soil mechanics. Geotechnique. 1975.

[36] Griffiths DV, Marquez RM. Three-dimensional slope stability analysis by elasto-plastic finite elements. Geotechnique. 2007;57(6):537-46.

[37] Lane PA, Griffiths DV. Assessment of Stability of Slopes under Drawdown Conditions. Journal of Geotechnical & Geoenvironmental Engineering. 2000;126(5):443.

[38] Potts D, Kovacevic N, Vaughan P. Delayed collapse of cut slopes in stiff clay. Selected papers on geotechnical engineering by PR Vaughan: Thomas Telford Publishing, 2009. p. 362-91.

[39] Troncone A. Numerical analysis of a landslide in soils with strain-softening behaviour. Geotechnique. 2005;55(8):585-96.

[40] Chai J, Carter JP. Simulation of the progressive failure of an embankment on soft soil. Computers and Geotechnics. 2009;36(6):1024-38.

[41] Duncan JM. State of the art: limit equilibrium and finite-element analysis of slopes. Journal of Geotechnical engineering. 1996;122(7):577-96.

[42] Hall L. Simulations and analyses of train-induced ground vibrations in finite element models. Soil Dynamics and Earthquake Engineering. 2003;23(5):403-13.

[43] Loukidis D, Bandini P, Salgado R. Stability of seismically loaded slopes using limit analysis. Geotechnique. 2003;53(5):463-80.

[44] Mellah R, Auvinet G, Masrouri F. Stochastic finite element method applied to non-linear analysis of embankments. Probabilistic Engineering Mechanics. 2000;15(3):251-9.

[45] Huang M, Jia C-Q. Strength reduction FEM in stability analysis of soil slopes subjected to transient unsaturated seepage. Computers and Geotechnics. 2009;36(1-2):93-101.

[46] Zhu H, Zhang L, Zhang L, Zhou C. Two-dimensional probabilistic infiltration analysis with a spatially varying permeability function. Computers and Geotechnics. 2013;48(249-59.

[47] Smith IM, Griffiths DV. Programming the finite element method. 2nd ed. ed: Wiley, 1988.

[48] Smith IM, Griffiths DV. Programming the finite element method. 3rd ed. ed: John Wiley & Sons, 1998.

[49] Moregenstern N. Stability charts for earth slopes during rapid drawdown. Geotechnique. 1963;13(2):121-31.

[50] Lechman J, Griffiths D. Analysis of the progression of failure of earth slopes by finite elements. Slope Stability 20002000. p. 250-65.

[51] De Buhan P, Freard J, Garnier D, Maghous S. Failure properties of fractured rock masses as anisotropic homogenized media. Journal of engineering mechanics. 2002;128(8):869-75.

[52] Zienkiewicz O, Cormeau I. Visco-plasticity—plasticity and creep in elastic solids—a unified numerical solution approach. International Journal for Numerical Methods in Engineering. 1974;8(4):821-45.

[53] Sazzad M, Rahman F, Mamun M. Mesh effect on the FEM based stability analysis of slope. International Conference on Recent Innovation in Civil Engineering for Sustainable Development (IICSD-2015)2015. p. 387-91.

[54] Cami B, Javankhoshdel S, Bathurst RJ, Yacoub T. Influence of mesh size, number of slices, and number of simulations in probabilistic analysis of slopes considering 2D spatial variability of soil properties. IFCEE 2018. p. 186-96.

[55] Huang J, Griffiths D. Determining an appropriate finite element size for modelling the strength of undrained random soils. Computers and Geotechnics. 2015;69(506-13.

[56] Chugh AK. On the boundary conditions in slope stability analysis. International journal for numerical and analytical methods in geomechanics. 2003;27(11):905-26.

[57] Ho I-H. Parametric studies of slope stability analyses using three-dimensional finite element technique: Geometric effect. Journal of GeoEngineering. 2014;9(1):33-43.

[58] Li XW, Yuan X, Li XW. Analysis of slope instability based on strength reduction method. Applied Mechanics and Materials: Trans Tech Publ, 2012. p. 1238-42.

[59] Cheng YM, Lau C. Slope stability analysis and stabilization: new methods and insight: CRC Press, 2014.

[60] Troncone A, Conte E, Pugliese L. Analysis of the Slope Response to an Increase in Pore Water Pressure Using the Material Point Method. Water. 2019;11(7):1446.

[61] State Government of Victoria. Mining Warden Yallourn Mine Batter Failure Inquiry. 2008.

[62] Cascini L, Cuomo S, Sorbino G. Flow-like mass movements in pyroclastic soils: remarks on the modelling of triggering mechanisms. Italian Geotechnical Journal. 2005;4(11-31.

[63] Zhang K, Li W, Shi J. FEM stability analysis on soil slope with different constitutive models. Slope Stability and Earth Retaining Walls2011. p. 26-33.

[64] Roscoe KH, Schofield A, Wroth aP. On the yielding of soils. Geotechnique. 1958;8(1):22-53.

[65] Cai M, Horii H. A constitutive model of highly jointed rock masses. Mechanics of Materials. 1992;13(3):217-46.

[66] Bandis S, Lumsden A, Barton N. Fundamentals of rock joint deformation. International Journal of Rock Mechanics and Mining Sciences & Geomechanics Abstracts: Elsevier, 1983. p. 249-68.

[67] Goodman RE, Taylor RL, Brekke TL. A model for the mechanics of jointed rock. Journal of Soil Mechanics & Foundations Div. 1968.

[68] Hicher P-Y, Shao J-F. Constitutive modeling of soils and rocks: Wiley Online Library, 2008.

[69] Sekhavatian A, Choobbasti AJ. Comparison of Constitutive Soil Models in Predicting Movements Caused by an Underground Excavation. International Journal of Soil Science. 2018;13(18-27.

[70] Ti KS, Huat BB, Noorzaei J, Jaafar MS, Sew GS. A review of basic soil constitutive models for geotechnical application. Electronic Journal of Geotechnical Engineering. 2009;14(1-18.

[71] Yan ZX, Duan J, Jiang P, Wang HY. A study on constitutive model and parameters of rock slope stability. Materials Science Forum: Trans Tech Publ, 2008. p. 1210-6.

[72] Zheng H, Liu D, Li C. On the assessment of failure in slope stability analysis by the finite element method. Rock Mechanics and Rock Engineering. 2008;41(4):629.

[73] Swan CC, Seo YK. Limit state analysis of earthen slopes using dual continuum/FEM approaches. International Journal for Numerical and Analytical Methods in Geomechanics. 1999;23(12):1359-71.

[74] Dawson E, Roth W, Drescher A. Slope stability analysis by strength reduction. Geotechnique. 1999;49(6):835-40.

[75] Duncan JM. State of the art: limit equilibrium and finite-element analysis of slopes. Journal of Geotechnical Engineering. 19967):577.

[76] Zheng H, Tham L, Liu D. On two definitions of the factor of safety commonly used in the finite element slope stability analysis. Computers and Geotechnics. 2006;33(3):188-95.

[77] Hammouri NA, Malkawi AIH, Yamin MMA. Stability analysis of slopes using the finite element method and limiting equilibrium approach. Bulletin of Engineering Geology and the Environment. 2008;67(4):471.

[78] Tschuchnigg F, Schweiger HF, Sloan SW. Slope stability analysis by means of finite element limit analysis and finite element strength reduction techniques. Part II: Back analyses of a case history. Computers and Geotechnics. 2015;70(Supplement C):178-89.

[79] Ugai K, Leshchinsky D. Three-dimensional limit equilibrium and finite element analyses: a comparison of results. Soils and foundations. 1995;35(4):1-7.

[80] Wei WB, Cheng YM. Strength reduction analysis for slope reinforced with one row of piles. Computers and Geotechnics. 2009;36(7):1176-85.

[81] Snitbhan N, Chen W. Finite element analysis of large deformation in slopes. Proc 2nd Conf on Num Methods in Geomechanics, ASCE1976. p. 7171.

[82] Crisfield MA. Non-linear finite element analysis of solids and structures: Wiley New York, 1993.

[83] Farias M, Naylor D. Safety analysis using finite elements. Computers and Geotechnics. 1998;22(2):165-81.

[84] Kim J, Kim J, Lee SR. Analysis of soil nailed earth slope by discrete element method. Computers and Geotechnics. 1997;20(1):1-14.

[85] Griffiths D, Kidger D. Enhanced visualization of failure mechanisms by finite elements. Computers & structures. 1995;55(2):265-8.

[86] Zheng H, Liu D, Li C. Slope stability analysis based on elasto-plastic finite element method. International Journal for Numerical Methods in Engineering. 2005;64(14):1871-88.

[87] Conte E, Silvestri F, Troncone A. Stability analysis of slopes in soils with strain-softening behaviour. Computers and Geotechnics. 2010;37(5):710-22.

[88] Manzari MT, Nour MA. Significance of soil dilatancy in slope stability analysis. Journal of Geotechnical and Geoenvironmental Engineering. 2000;126(1):75-80.

[89] Cruden DM, Varnes DJ. Landslides: investigation and mitigation. 1996.

[90] Poisel R, Preh A, Hofmann R. Slope failure process recognition based on mass-movement induced structures. Proceedings, 2nd Conference on Slope Tectonics2011. p. 6-11.

[91] Hoek E, Bray JD. Rock slope engineering: CRC Press, 1981.

[92] Hudson JA, Harrison JP. Engineering rock mechanics: an introduction to the principles: Elsevier, 2000.

[93] Bobet A. Analytical solutions for toppling failure. International Journal of Rock Mechanics and Mining Sciences. 1999;36(7):971-80.

[94] Adhikary D, Dyskin A, Jewell R, Stewart D. A study of the mechanism of flexural toppling failure of rock slopes. Rock Mechanics and Rock Engineering. 1997;30(2):75-93.

[95] Cundall PA, Strack OD. A discrete numerical model for granular assemblies. geotechnique. 1979;29(1):47-65.

[96] Kawamura Y, Kobayashi Y. Basic study on application of discrete element method for slope failure analysis. Proceeding of the 15th world conference on earthquake engineering2012.

[97] Cheng Y, Nakata Y, Bolton M. Discrete element simulation of crushable soil. Geotechnique. 2003;53(7):633-41.

[98] Wang C, Tannant D, Lilly P. Numerical analysis of the stability of heavily jointed rock slopes using PFC2D. International Journal of Rock Mechanics and Mining Sciences. 2003;40(3):415-24.

[99] Guan Y, Liu X, Wang E, Wang S. The stability analysis method of the cohesive granular slope on the basis of graph theory. Materials. 2017;10(3):240.

[100] Xu W, Wang S, Bilal M. LEM-DEM coupling for slope stability analysis. Science China Technological Sciences. 2019:1-12.

[101] Katz O, Morgan JK, Aharonov E, Dugan B. Controls on the size and geometry of landslides: Insights from discrete element numerical simulations. Geomorphology. 2014;220(104-13.

[102] Lu W, Zhou Z, Liu T, Liu YH. Discrete Element Simulation Analysis of Rock Slope Stability Based on UDEC. Advanced Materials Research: Trans Tech Publ, 2012. p. 384-8.

[103] Harlow FH. The particle-in-cell computing method for fluid dynamics. Methods Comput Phys. 1964;3(319-43.

[104] Andersen S, Andersen L. Modelling of landslides with the material-point method. Computational Geosciences. 2010;14(1):137-47.

[105] Dong Y, Wang D, Randolph MF. Investigation of impact forces on pipeline by submarine landslide using material point method. Ocean engineering. 2017;146(21-8.

[106] Liu X, Wang Y, Li D-Q. Investigation of slope failure mode evolution during large deformation in spatially variable soils by random limit equilibrium and material point methods. Computers and Geotechnics. 2019;111(301-12.

[107] Bandara S, Soga K. Coupling of soil deformation and pore fluid flow using material point method. Computers and geotechnics. 2015;63(199-214.

[108] Soga K, Alonso E, Yerro A, Kumar K, Bandara S. Trends in large-deformation analysis of landslide mass movements with particular emphasis on the material point method. Géotechnique. 2015;66(3):248-73.

[109] Wang B, Vardon P, Hicks M. Investigation of retrogressive and progressive slope failure mechanisms using the material point method. Computers and Geotechnics. 2016;78(88-98.

[110] Wang B, Vardon P, Hicks M. Rainfall-induced slope collapse with coupled material point method. Engineering Geology. 2018;239(1-12.

[111] Zabala F, Alonso E. Progressive failure of Aznalcóllar dam using the material point method. Géotechnique. 2011;61(9):795-808.

[112] Vardon PJ, Wang B, Hicks MA. Slope failure simulations with MPM. Journal of Hydrodynamics. 2017;29(3):445-51.

[113] Coelho B, Rohe A, Aboufirass A, Nuttall J, Bolognin M. Assessment of dike safety within the framework of large deformation analysis with the material point method. Prooceedings of NUMGE2018. 2018.

[114] Mostyn G, Li K. Probabilistic slope analysis—state of play. Proceedings, Conference on Probabilistic Methods in Geotechnical Engineering, Canberra, Australia, AA Balkema, Rotterdam1993. p. 89-110.

[115] Wolff TF. Probabilistic slope stability in theory and practice. Uncertainty in the geologic environment: From theory to practice: ASCE, 1996. p. 419-33.

[116] Harr E. Reliability based design in civil engineering: McGraw-Hill, 1987.

[117] Christian JT, Ladd CC, Baecher GB. Reliability applied to slope stability analysis. Journal of Geotechnical Engineering. 1994;120(12):2180-207.

[118] Li K, Lumb P. Probabilistic design of slopes. Canadian Geotechnical Journal. 1987;24(4):520-35.

[119] Mostyn G, Soo S. The effect of autocorrelation on the probability of failure of slopes. 6th Australia, New Zealand Conference on Geomechanics: Geotechnical Risk1992. p. 542-6.

[120] El-Ramly H, Morgenstern N, Cruden D. Probabilistic slope stability analysis for practice. Canadian Geotechnical Journal. 2002;39(3):665-83.

[121] Duzgun H, Bhasin R. Probabilistic stability evaluation of Oppstadhornet rock slope, Norway. Rock Mechanics and Rock Engineering. 2009;42(5):729.

[122] Hassan AM, Wolff TF. Search algorithm for minimum reliability index of earth slopes. Journal of Geotechnical and Geoenvironmental Engineering. 1999;125(4):301-8.

[123] Cornell C. First-order uncertainty analysis of soil deformation and stability. 1972.

[124] Dolinski K. First-order second-moment approximation in reliability of structural systems: critical review and alternative approach. Structural Safety. 1982;1(3):211-31.

[125] Baecher GB, Christian JT. Reliability and statistics in geotechnical engineering: John Wiley & Sons, 2005.

[126] Cho SE. Effects of spatial variability of soil properties on slope stability. Engineering Geology. 2007;92(3-4):97-109.

[127] Chowdhury R, Rao B. Probabilistic stability assessment of slopes using high dimensional model representation. Computers and Geotechnics. 2010;37(7-8):876-84.

[128] Wang Y. Reliability-based economic design optimization of spread foundations. Journal of geotechnical and geoenvironmental engineering. 2009;135(7):954-9.

[129] Low B. Efficient probabilistic algorithm illustrated for a rock slope. Rock Mechanics and Rock Engineering. 2008;41(5):715-34.

[130] Rosenblueth E. Point estimates for probability moments. Proceedings of the National Academy of Sciences. 1975;72(10):3812-4.

[131] Rosenblueth E. Two-point estimates in probabilities. Applied Mathematical Modelling. 1981;5(5):329-35.

[132] Miller SM, Whyatt JK, McHugh EL. Applications of the point estimation method for stochastic rock slope engineering. Gulf Rocks 2004, the 6th North America Rock Mechanics Symposium (NARMS): American Rock Mechanics Association, 2004.

[133] Park H, West T. Development of a probabilistic approach for rock wedge failure. Engineering Geology. 2001;59(3-4):233-51.

[134] Valerio M, Clayton C, D'Ambra S, Yan C. An application of a reliability based method to evaluate open pit slope stability. Slope Stability. 2013.

[135] McGuffey V, Grivas D, Iori J, Kyfor Z. Conventional and probabilistic embankment design. Journal of the Geotechnical Engineering Division. 1982;108(10):1246-54.

[136] Nguyen V, Chowdhury R. Probabilistic study of spoil pile stability in strip coal mines—two techniques compared. International Journal of Rock Mechanics and Mining Sciences & Geomechanics Abstracts: Elsevier, 1984. p. 303-12.

[137] Thornton S. Probability calculation for slope stability. Computer Methods and Advances in Geomechanics. 1994:2505-9.

[138] Chandler DS. Monte Carlo simulation to evaluate slope stability. Uncertainty in the Geologic Environment: From Theory to Practice: ASCE, 1996. p. 474-93.

[139] El-Ramly H, Morgenstern N, Cruden D. Probabilistic stability analysis of a tailings dyke on presheared clay shale. Canadian Geotechnical Journal. 2003;40(1):192-208.

[140] Griffiths DV, Fenton GA. Risk assessment in geotechnical engineering: Hoboken, New Jersey: John Wiley & Sons, Inc, 2008.

[141] Phoon K-K, Kulhawy FH. Characterization of geotechnical variability. Canadian Geotechnical Journal. 1999;36(4):612-24.

[142] Queiroz IM. Comparison between Deterministic and Probabilistic Stability Analysis, Featuring Consequent Risk Assessment. World Academy of Science, Engineering and Technology, International Journal of Environmental, Chemical, Ecological, Geological and Geophysical Engineering. 2016;10(6):636-43.

[143] Lumb P. The variability of natural soils. Canadian Geotechnical Journal. 1966;3(2):74-97.

[144] Hooper J, Butler F. Some numerical results concerning the shear strength of London clay. Geotechnique. 1966;16(4):282-304.

[145] Chiasson P, Lafleur J, Soulié M, Law KT. Characterizing spatial variability of a clay by geostatistics. Canadian Geotechnical Journal. 1995;32(1):1-10.

[146] Brejda JJ, Moorman TB, Smith JL, Karlen DL, Allan DL, Dao TH. Distribution and variability of surface soil properties at a regional scale. Soil Science Society of America Journal. 2000;64(3):974-82.

[147] Fenton GA. Random field modeling of CPT data. Journal of geotechnical and geoenvironmental engineering. 1999;125(6):486-98.

[148] Cherubini C. Data and considerations on the variability of geotechnical properties of soils. Proceedings of the international conference on safety and reliability, ESREL1997. p. 1583-91.

[149] Lumb P. Safety factors and the probability distribution of soil strength. Canadian Geotechnical Journal. 1970;7(3):225-42.

[150] Yucemen MS, Tang WH, Ang A-S. A probabilistic study of safety and design of earth slopes. University of Illinois Engineering Experiment Station. College of Engineering. University of Illinois at Urbana-Champaign., 1973.

[151] Fenton GA. Error evaluation of three random-field generators. Journal of Engineering Mechanics. 1994;120(12):2478-97.

[152] Vanmarcke E. Random fields: analysis and synthesis: World Scientific, 2010.

[153] Hilyati S, Nizam Z, Zurisman M, Hazreek Z, Saiful A. Estimation of the Scale of Fluctuation for Spatial Variables of RC Structures. MATEC Web of Conferences: EDP Sciences, 2017. p. 02026.

[154] Jaksa MB, Fenton GA. Random field modeling of CPT data. Journal of Geotechnical and Geoenvironmental Engineering. 2000;126(12):1212-6.

[155] Lacasse S, Nadim F. Uncertainties in characterising soil properties. Uncertainty in the geologic environment: From theory to practice: ASCE, 1996. p. 49-75.

[156] Fenton GA, Vanmarcke EH. Simulation of random fields via local average subdivision. Journal of Engineering Mechanics. 1990;116(8):1733-49.

[157] Vanmarcke E. Random fields. Random Fields, by Erik Vanmarcke, pp 372 ISBN 0-262-72045-0 Cambridge, Massachusetts, USA: The MIT Press, March 1983(Paper). 1983:372.

[158] Griffiths D, Fenton GA. Influence of soil strength spatial variability on the stability of an undrained clay slope by finite elements. Slope stability 2000, 2000. p. 184-93.

[159] Fenton GA, Griffiths D. Bearing-capacity prediction of spatially random c ϕ soils. Canadian geotechnical journal. 2003;40(1):54-65.

[160] Griffiths DV, Fenton GA. Bearing capacity of spatially random soil: the undrained clay Prandtl problem revisited. Geotechnique. 2001;51(4):351-60.

[161] Fenton GA, Griffiths D. Probabilistic foundation settlement on spatially random soil. Journal of Geotechnical and Geoenvironmental Engineering. 2002;128(5):381-90.

[162] Fenton GA, Griffiths D. Three-dimensional probabilistic foundation settlement. Journal of Geotechnical and Geoenvironmental Engineering. 2005;131(2):232-9.

[163] Paice G, Griffiths D, Fenton GA. Finite element modeling of settlements on spatially random soil. Journal of Geotechnical Engineering. 1996;122(9):777-9.

[164] Fenton GA, Griffiths D, Williams M. Reliability of traditional retaining wall design. Risk and Variability in Geotechnical Engineering: Thomas Telford Publishing, 2007. p. 165-72.

[165] Chen D, Xu D, Ren G, Jiang Q, Liu G, Wan L, Li N. Simulation of cross-correlated non-Gaussian random fields for layered rock mass mechanical parameters. Computers and Geotechnics. 2019;112(104-19.

[166] Gong W, Juang CH, Martin II JR, Tang H, Wang Q, Huang H. Probabilistic analysis of tunnel longitudinal performance based upon conditional random field simulation of soil properties. Tunnelling and Underground Space Technology. 2018;73(1-14.

[167] Griffiths D, Huang J, Fenton GA. Influence of spatial variability on slope reliability using 2-D random fields. Journal of geotechnical and geoenvironmental engineering. 2009;135(10):1367-78.

[168] Zhu D, Griffiths D, Fenton G. Worst-case spatial correlation length in probabilistic slope stability analysis. Géotechnique. 2018;69(1):85-8.

[169] Hicks MA, Nuttall JD, Chen J. Influence of heterogeneity on 3D slope reliability and failure consequence. Computers and Geotechnics. 2014;61(198-208.

[170] Hicks MA, Spencer WA. Influence of heterogeneity on the reliability and failure of a long 3D slope. Computers and Geotechnics. 2010;37(7-8):948-55.

[171] Li Y, Hicks M, Vardon P. Uncertainty reduction and sampling efficiency in slope designs using 3D conditional random fields. Computers and Geotechnics. 2016;79(159-72.

[172] Zhu H, Griffiths D, Fenton G, Zhang L. Undrained failure mechanisms of slopes in random soil. Engineering Geology. 2015;191(31-5.

[173] Yang R, Huang J, Griffiths D, Sheng D. Probabilistic stability analysis of slopes by conditional random fields. Geo-Risk 20172017. p. 450-9.

[174] Chiles J-P, Delfiner P. Geostatistics: modeling spatial uncertainty: John Wiley & Sons, 2009.

[175] Ma JZ, Zhang J, Huang HW, Zhang LL, Huang JS. Identification of representative slip surfaces for reliability analysis of soil slopes based on shear strength reduction. Computers and Geotechnics. 2017;85(199-206.

[176] Ji J, Low BK. Stratified response surfaces for system probabilistic evaluation of slopes. Journal of Geotechnical and Geoenvironmental Engineering. 2012;138(11):1398-406.

[177] Shen H, Abbas SM. Rock slope reliability analysis based on distinct element method and random set theory. International Journal of Rock Mechanics and Mining Sciences. 2013;61(15-22.

[178] Sakellariou M, Ferentinou M. A study of slope stability prediction using neural networks. Geotechnical & Geological Engineering. 2005;23(4):419.

[179] Shahin MA, Jaksa MB, Maier HR. Artificial neural network applications in geotechnical engineering. Australian geomechanics. 2001;36(1):49-62.

[180] Shahin MA, Jaksa MB, Maier HR. State of the art of artificial neural networks in geotechnical engineering. Electronic Journal of Geotechnical Engineering. 2008;8(1):1-26.

[181] Li D-Q, Yang Z-Y, Cao Z-J, Au S-K, Phoon K-K. System reliability analysis of slope stability using generalized subset simulation. Applied Mathematical Modelling. 2017;46(650-64.

[182] Ching J, Phoon K-K, Hu Y-G. Efficient evaluation of reliability for slopes with circular slip surfaces using importance sampling. Journal of Geotechnical and Geoenvironmental Engineering. 2009;135(6):768-77.

[183] Li D-Q, Qi X-H, Cao Z-J, Tang X-S, Phoon K-K, Zhou C-B. Evaluating slope stability uncertainty using coupled Markov chain. Computers and Geotechnics. 2016;73(72-82.

[184] Santoso A, Phoon K, Quek S. Modified Metropolis–Hastings algorithm with reduced chain correlation for efficient subset simulation. Probabilistic Engineering Mechanics. 2011;26(2):331-41.

[185] Tang K, Wang J, Li L. A Prediction Method Based on Monte Carlo Simulations for Finite Element Analysis of Soil Medium considering Spatial Variability in Soil Parameters. Advances in Materials Science and Engineering. 2020;2020(

[186] Gloe C. The Latrobe Valley coal measures. Contribution to Tertiary Section of the Geology of Victoria, Geological Society of Australia. 1974.

[187] Barton CM, Gloe CS, Holdgate GR. Latrobe Valley, Victoria, Australia: A world class brown coal deposit. International Journal of Coal Geology. 1993;23(1):193-213.

[188] Thomas D, Baragwanath W. Geology of the brown coals of Victoria: Department of Mines, 1949.

[189] Gloe C. The geology, discovery, and assessment of the brown coal deposits of Victoria. Victoria's brown coal—a huge fortune in chancery: Australasian Institute of Mining and Metallurgy, Monograph Series. 198411):79-109.

[190] Government VS. Latrobe Valley Coal Data Package Tender T02801 Information Booklet Environment. Department of Natural Resources and Environment State. 2001.

[191] State Electricity Commission of Victoria. Yallourn North Open Cut Seepage Study Report No SO/82/50. SECV, Research and Development, Dec 1983.

[192] ASTM. STANDARD D388-12. Standard Classification of Coals by Rank. American Society for Testing and Materials. 2012.

[193] Tolooiyan A, Mackay R, Xue J. Measurement of the Tensile Strength of Organic Soft Rock BT - Measurement of the Tensile Strength of Organic Soft Rock. ASTM Geotechnical Testing Journal, Volume 37, Issue 6. 2014.

[194] Moein F, Xue J, Dent B, Mackay R. Review of the historical data characterizing Latrobe Valley brown coal consolidation behaviour. In: Eggers MJ, Griffiths JS, Parry S, Culshaw MG, editors. Developments in Engineering Geology: Geological Society of London, 2016.

[195] Tolooiyan A, Dyson A, Karami M, Shaghaghi T, Ghadrdan M. An In-situ Investigation of Permeability Variation in a Soft Rock. Bulletin of Engineering Geology and the Environment. 2020.

[196] Rosengren K. The Structure and Strength of Victorian Brown Coals: University of Melbourne, 1961.

[197] Mackay R, Xue J, Powrie W, Dent BB. A new ring shear apparatus for determination of the residual shear resistance of remoulded brown coal. Australia New Zealand Geomechanics Conference 2012: Australian Geomechanics Society, 2012. p. 902-7.

[198] Trollope D, Rosengren K, Brown E. The mechanics of brown coal. Géotechnique. 1965;15(4):363-86.

[199] Victoria SECo. Three Decades: The Story of the State Electricity Commission of Victoria from Its Inception to December 1948: Hutchinson, 1949.

[200] Golder, Brawner & Associates Ltd., Report to the State Electricity Commission of Victoria, Australia, on Preliminary Evaluation Subsurface Movement (Excerpted). 1970.

[201] Chowdhury R. Yallourn Open Cut, Stability of Permanent Batters, Yallourn Township Area with Emphasis Probabilistic Considerations in Slope Analysis. 1989.

[202] Gloe CS. Land Subsidence Related to Brown Coal Open Cut Operations Latrobe Valley, Victoria, Australia. 1976

[203] Hutchings R, Fajdiga, M. and D. Raisbeck. The Effects of Large Ground Movements Resulting from Brown Coal Open Cut Excavations in the Latrobe Valley, Victoria. 1977

[204] Sun H. Yallourn's awesome power play. 2007.

[205] Flatley A, Rutherfurd I, Hardie R. River Channel Relocation: Problems and Prospects. Water. 2018;10(10):1360.

[206] Perera M, Ranjith P, Peter M. Effects of saturation medium and pressure on strength parameters of Latrobe Valley brown coal: carbon dioxide, water and nitrogen saturations. Energy. 2011;36(12):6941-7.

[207] Xue J, Tolooiyan A. Reliability analysis of block sliding in large brown coal open cuts. The 2012 World Congress on Advances in Civil, Environmental, and Materials Research (ACEM'12)2012. p. 1578-87.

[208] Soliman AW, Bill; Hibberd, Doug;. Brown coal open pit, Yallourn Eastfield, Victoria, FLAC modelling: Morwell River diversion channel-southern batters buffer width. Australian Geomechanics Journal, Volume 42, Number 2. 2007.

[209] Rosengren K, Krehula F. Earth Movements and Batter Stability in the Latrobe Valley Open Cuts. Proc 8th Commonwealth Min Met Congress Aust & New Zealand1965. p. 573-85.

[210] Tolooiyan A, Dyson AP, Karami M, Shaghaghi T, Ghadrdan M. Investigation of an Australian soft rock permeability variation. Bulletin of Engineering Geology and the Environment. 2020:1-18.

[211] Karami M, Tolooiyan A. Investigating the elastoplasticity of an Australian soft rock based on laboratory test results. Engineering Geology. 2020;276(105762.

[212] Bishop AW. The use of the slip circle in the stability analysis of slopes. The Essence of Geotechnical Engineering: 60 years of Géotechnique: Thomas Telford Publishing, 2008. p. 223-33.

[213] Li XW, Yuan X, Li XW. Analysis of Slope Instability Based on Strength Reduction Method. Applied Mechanics and Materials. 2012;170(1238-42.

[214] Su K, Li Y. Discussion of SRFEM with Mohr-Coulomb Plasticity Model in Slope Stability Analysis. 2012 Asia-Pacific Power and Energy Engineering Conference2012. p. 1-4.

[215] Zheng H, Tham LG, Liu D. On two definitions of the factor of safety commonly used in the finite element slope stability analysis. Computers and Geotechnics. 2006;33(3):188-95.

[216] Cheng Y, Lansivaara T, Wei W. Two-dimensional slope stability analysis by limit equilibrium and strength reduction methods. Computers and Geotechnics. 2007;34(3):137-50.

[217] Zheng Y, Tang X, Zhao S, Deng C, Lei W. Strength reduction and step-loading finite element approaches in geotechnical engineering. Journal of Rock Mechanics and Geotechnical Engineering. 2009;1(1):21-30.

[218] Krahn J. The 2001 R.M. Hardy Lecture: The limits of limit equilibrium analyses. Canadian Geotechnical Journal. 2003;40(3):643-60.

[219] Schneider-Muntau B, Medicus G, Fellin W. Strength reduction method in Barodesy. Computers and Geotechnics. 2017.

[220] Xue H, Dang F, Yin X, Ding W, Yang C. Nonproportional Correlative Reduction Finite Element Method for Slope Strength Parameters. Mathematical Problems in Engineering. 2016;2016(

[221] Zheng H, Sun G, Liu D. A practical procedure for searching critical slip surfaces of slopes based on the strength reduction technique. Computers and Geotechnics. 2009;36(1):1-5.

[222] Waterman RBJBaWBaD. Plaxis 2D: Plaxis B.V, Netherlands: Delft University, 2016.

[223] Smith M. ABAQUS/Standard User's Manual, Version 7.5: Simulia, 2017.

[224] Allan F, Yacoub T, Curran J. On using spatial methods for heterogeneous slope stability analysis. 46th US Rock Mechanics/Geomechanics Symposium: American Rock Mechanics Association, 2012.

[225] Liu L-L, Cheng Y-M, Wang X-M, Zhang S-H, Wu Z-H. System reliability analysis and risk assessment of a layered slope in spatially variable soils considering stratigraphic boundary uncertainty. Computers and Geotechnics. 2017;89(213-25.

[226] Ahmed AA. Stochastic analysis of seepage under hydraulic structures resting on anisotropic heterogeneous soils. Journal of Geotechnical and Geoenvironmental Engineering. 2012;139(6):1001-4.

[227] Chok Y, Jaksa M, Griffths D, Fenton G, Kaggwa W. Probabilistic Analysis of a Spatially Variable C'-Phi' Slope. Australian Geomechanics Journal. 2015;50(2):17-27.

[228] Dyson AP, Tolooiyan A. Optimisation of strength reduction finite element method codes for slope stability analysis. Innovative Infrastructure Solutions. 2018;3(1):38.

[229] Dyson AP, Tolooiyan A, Mackay R. Advanced Strength Reduction Search Strategies Applied to Finite Element Analysis of Slope Stability. Slope Stability 20182018.

[230] Der Kiureghian A, Ke J-B. The stochastic finite element method in structural reliability. Stochastic Structural Mechanics: Springer, 1987. p. 84-109.

[231] Cho SE. Probabilistic assessment of slope stability that considers the spatial variability of soil properties. Journal of geotechnical and geoenvironmental engineering. 2009;136(7):975-84.

[232] Samy K. Stochastic analysis with finite elements in geotechnical engineering: University of Manchester, 2003.

[233] Zhu H, Zhang LM. Characterizing geotechnical anisotropic spatial variations using random field theory. Canadian Geotechnical Journal. 2013;50(7):723-34.

[234] Li L, Chu X. Multiple response surfaces for slope reliability analysis. International Journal for Numerical and Analytical Methods in Geomechanics. 2015;39(2):175-92.

[235] Cheng H, Chen J, Chen R, Chen G, Zhong Y. Risk assessment of slope failure considering the variability in soil properties. Computers and Geotechnics. 2018;103(61-72.

[236] Green DK, Douglas K, Mostyn G. The simulation and discretisation of random fields for probabilistic finite element analysis of soils using meshes of arbitrary triangular elements. Computers and Geotechnics. 2015;68(91-108.

[237] Li D-Q, Xiao T, Cao Z-J, Zhou C-B, Zhang L-M. Enhancement of random finite element method in reliability analysis and risk assessment of soil slopes using Subset Simulation. Landslides. 2016;13(2):293-303.

[238] Griffiths D, Lane P. Slope stability analysis by finite elements. Geotechnique. 1999;49(3):387-403.

[239] Everitt B. Cluster analysis: Chichester, West Sussex : Wiley, 2011.

5th ed., 2011.

[240] Johnson SC. Hierarchical clustering schemes. Psychometrika. 1967;32(3):241-54.

[241] MacQueen J. Some methods for classification and analysis of multivariate observations. Proceedings of the fifth Berkeley symposium on mathematical statistics and probability: Oakland, CA, USA, 1967. p. 281-97.

[242] Mouyeaux A, Carvajal C, Bressolette P, Peyras L, Breul P, Bacconnet C. Probabilistic stability analysis of an earth dam by Stochastic Finite Element Method based on field data. Computers and Geotechnics. 2018;101(34-47.

[243] Christakos G. Modern statistical analysis and optimal estimation of geotechnical data. Engineering Geology. 1985;22(2):175-200.

[244] van den Eijnden A, Hicks M. Probability-dependent failure modes of slopes and cuts in heterogeneous cohesive soils. Géotechnique Letters. 2018:1-5.

[245] Griffiths DV. Stability analysis of slopes in variable soils by finite elements. University of Minnesota 58th Annual Geotechnical Engineering Conference: University of Minnesota Press, 2010.

[246] Dyson AP, Tolooiyan A. Prediction and classification for finite element slope stability analysis by random field comparison. Computers and Geotechnics. 2019;109(117-29.

[247] Vanmarcke EH. Probabilistic modeling of soil profiles. Journal of the geotechnical engineering division. 1977;103(11):1227-46.

[248] Smith IM, Griffiths DV, Margetts L. Programming the finite element method: John Wiley & Sons, 2013.

[249] Hahn GJ, Shapiro SS. Statistical models in engineering. 1967.

[250] Mantel N. The detection of disease clustering and a generalized regression approach. Cancer research. 1967;27(2 Part 1):209-20.

[251] Dyson AP, Tang Z, Tolooiyan A. Use of stochastic XFEM in the investigation of heterogeneity effects on the tensile strength of intermediate geotechnical materials. Finite Elements in Analysis and Design. 2018;145(1-9.

[252] Tolooiyan A, Dyson A, Karami M, Shaghaghi T, Ghadrdan M. Application of Ground Penetrating Radar (GPR) to Detect Joints in Organic Soft Rock. Geotechnical Testing Journal. 2019.

[253] Wolff TF. Analysis and design of embankment dam slopes: a probabilistic approach: Purdue University, 1985.

[254] Leong EC, Rahardjo H. Two and three-dimensional slope stability reanalyses of Bukit Batok slope. Computers and geotechnics. 2012;42(81-8.

[255] Shen J, Karakus M. Three-dimensional numerical analysis for rock slope stability using shear strength reduction method. Canadian Geotechnical Journal. 2013;51(2):164-72.

[256] Cavoundis S. On the ratio of factors of safety in slope stability analyses. Geotechnique. 1987;37(2).

[257] Leshchinsky D, Baker R. Three-dimensional slope stability: end effects. Soils and Foundations. 1986;26(4):98-110.

[258] Wei W, Cheng Y, Li L. Three-dimensional slope failure analysis by the strength reduction and limit equilibrium methods. Computers and geotechnics. 2009;36(1-2):70-80.

[259] Arellano D, Stark TD. Importance of three-dimensional slope stability analyses in practice. Slope Stability 20002000. p. 18-32.

[260] Anagnosti P. Three-dimensional stability of fill dams. Proceeding of 7th International Conference on Soil Mechanics and Foundation Engineering, Mexico1969. p. 275-80.

[261] Bromhead EN, Martin PL. Three-dimensional limit equilibrium analysis of the Taren landslide. Advances in geotechnical engineering: The Skempton conference: Proceedings of a three day conference on advances in geotechnical engineering, organised by the Institution of Civil Engineers and held at the Royal Geographical Society, London, UK, on 29–31 March 2004: Thomas Telford Publishing, 2004. p. 789-802.

[262] Chen R, Chameau J-L. Three-dimensional limit equilibrium analysis of slopes. Geotechnique. 1983;33(1):31-40.

[263] Saeed MS, Maarefvand P, Yaaghubi E. Two and three-dimensional slope stability analyses of final wall for Miduk mine. International Journal of Geo-Engineering. 2015;6(1):9.

[264] Sainak A. Application of three-dimensional finite element method in parametric and geometric studies of slope stability analysis. Advances in geotechnical engineering: The Skempton conference: Proceedings of a three day conference on advances in geotechnical engineering, organised by the Institution of Civil Engineers and held at the Royal Geographical Society, London, UK, on 29–31 March 2004: Thomas Telford Publishing, 2004. p. 933-42.

[265] Seed RB, Mitchell JK, Seed HB. Kettleman hills waste landfill slope failure. II: stability analyses. Journal of Geotechnical Engineering. 1990;116(4):669-90.

[266] Wines D. A comparison of slope stability analyses in two and three dimensions. Journal of the Southern African Institute of Mining and Metallurgy. 2016;116(5):399-406.

[267] Hoek E, Bray JD. Rock slope engineering: CRC Press, 2014.

[268] Chen R-HJ. Three-dimensional slope stability analysis. 1981.

[269] Jenike AW, Yen BC. Slope stability in axial symmetry: Salt Lake City Press, 1962.

[270] Abdulai M, Sharifzadeh M. Uncertainty and Reliability Analysis of Open Pit Rock Slopes: A Critical Review of Methods of Analysis. Geotechnical and Geological Engineering. 2018:1-25.

[271] Li D-Q, Jiang S-H, Cao Z-J, Zhou W, Zhou C-B, Zhang L-M. A multiple response-surface method for slope reliability analysis considering spatial variability of soil properties. Engineering Geology. 2015;187(60-72.

[272] Lade PV. Overview of constitutive models for soils. Soil constitutive models: Evaluation, selection, and calibration2005. p. 1-34.

[273] Simulia DS. Abaqus FEA. 2018 ed: Dassault Systèmes Simulia Corp., 2018.

[274] Dyson AP, Tolooiyan A. Probabilistic investigation of RFEM topologies for slope stability analysis. Computers and Geotechnics. 2019;114(103129.

[275] Trollope D, Rosengren K, Brown E. The mechanics of brown coal. Geotechnique. 1965;15(4):363-86.

[276] Sekhavatian A, Choobbasti AJ. Comparison of Point Estimate and Monte Carlo probabilistic methods in stability analysis of a deep excavation. International Journal of Geo-Engineering. 2018;9(1):20.

[277] Liang R, Nusier b, OK, Malkawi A. A reliability based approach for evaluating the slope stability of embankment dams. Engineering geology. 1999;54(3-4):271-85.

[278] Harr ME. Probabilistic estimates for multivariate analyses. Applied Mathematical Modelling. 1989;13(5):313-8.

[279] Gibson W. Probabilistic methods for slope analysis and design. Australian Geomechanics. 2011;46(3):29.

[280] Elkateb T, Chalaturnyk R, Robertson PK. An overview of soil heterogeneity: quantification and implications on geotechnical field problems. Canadian Geotechnical Journal. 2003;40(1):1-15.

[281] Emery X. Properties and limitations of sequential indicator simulation. Stochastic Environmental Research & Risk Assessment. 2004;18(6):414-24.

[282] Vanmarcke EH. Random fields : analysis and synthesis: MIT Press, 1983.

[283] Lloret-Cabot M, Fenton GA, Hicks MA. On the estimation of scale of fluctuation in geostatistics. Georisk: Assessment and Management of Risk for Engineered Systems and Geohazards. 2014;8(2):129-40.

[284] Zienkiewicz O, Taylor R. The finite element method, 4th edn., vol. 1. Basic Formulation and Linear. 1989.

[285] Duncan JM, Dunlop P. Slopes in stiff-fissured clays and shales. University of California Berkeley, 1968.

[286] Kirsten H. Significance of the probability of failure in slope engineering. Civil Engineering= Siviele Ingenieurswese. 1983;1983(v25i1):17-29.

[287] Barton C, Gloe C, Holdgate G. Latrobe Valley, Victoria, Australia: a world class brown coal deposit. International journal of coal geology. 1993;23(1-4):193-213.

Ali Tolooiyan,[1] Ashley P. Dyson,[2] Mojtaba Karami,[2] Tahereh Shaghaghi,[2] and Mohsen Ghadrdan[2]

Application of Ground Penetrating Radar (GPR) to Detect Joints in Organic Soft Rock

ABSTRACT

The detection of joints and discontinuities is of particular importance to the stability of a broad range of geostructures, including slopes and underground and open-pit mines. As a common example, the mechanical response of soft rocks observed within open-pit mines is significantly influenced by the existence of joint networks, resulting in a complex stress distribution that governs the stability factor of safety as well as the failure mechanism. In this article, surface geophysics scanning by ground penetrating radar (GPR) is presented for the detection of vertical joints at one of the largest open-pit coal mines in Australia. The optimum soil velocity, point interval, and antenna frequency for joint detection in Victorian Brown Coal (VBC) are presented in comparison with electromagnetic properties of known organic soils. Furthermore, the performance of an assorted set of post-processing signal filtering techniques to successfully identify the underground coal fractures are detailed, along with obstructions affecting the feasibility of GPR vertical joint discovery in this light organic soft rock.

Keywords

joint detection, ground penetrating radar, intermediate geotechnical material, Victorian brown coal

Introduction

The Latrobe Valley brown coal fields, excavated using present day open-cut technology, represent about 25 % of Australia's total fossil energy reserves and are one of Australia's major national sources of energy supply (Guy and Perry 1992). They are situated around 150 km east of Melbourne in the State of Victoria. Traralgon, Morwell, and Yallourn formations contain the three main brown coal seam groups, which form some of the thickest continuous coal successions in the world (Barton, Gloe, and Holdgate 1993). As the second largest open-cut mine in Australia, Yallourn mine is one of the three open-cut brown coal mines in Latrobe Valley and fuels Yallourn Power Station with the capacity of 1,480 megawatts. Yallourn Power Station supplies 22 % of state's and 8 % of Australia's electricity needs.

Since the start of coal mining at Yallourn open-cut in 1924, a considerable amount of expertise has been employed by geotechnical engineers and hydrogeologists to ensure the stability of mining batters. For about 100 years, engineers have worked on several factors that affect the stability of the batters, such as mining slope, geotechnical properties of Victorian brown coal (VBC), hydrogeology of the coal and interseam layers, and orientation of joints and discontinuities. However, in late 2007, an 80-m-high batter collapsed and slid about 250 m across the Yallourn open-cut floor, taking with it 6,000,000 m^3 of coal and clay, and a mine road. Through post-failure investigations and reviewing the historical data in 2008, it was presumed that the rise in water pressures in a joint along the rear of the failure has increased the horizontal stress as the acting stress and shifted the batter in block sliding mode.

Since then, joint mapping and monitoring at VBC mines have been performed more rigorously, and extensive dynamic digital database systems have been developed during the last ten years to monitor the behavior of joints and displacement of the batters by the aid of global positioning system (GPS) and regular site inspections.

Although regular site inspection and spatial analysis of GPS and pin data are widely applied nowadays as effective joint management practices, the application of geophysical methods in detecting subsurface discontinuities is growing rapidly in this area. Electrical resistivity methods are used for mapping fractured rocks filled with some representative minerals (Orellana 1972). Vertical anisotropy profiles of apparent electrical resistivity can be considered as a valuable tool for monitoring crack patterns at depth (Daniels 1996). In some rocks, variation in the velocity of seismic waves can be used for mapping rock discontinuities. Ground penetrating radar (GPR) based on electromagnetic radiation is also used for detecting subsurface objects, cavities, and geological discontinuities (Butnor et al. 2012; Zajc, Pogačnik, and Gosar 2014; Di Prinzio et al. 2010; Sagnard and Tebchrany 2015; Barr 1993; Conyers 1995).

VBC is a very light, organic, and brittle non-textbook geotechnical material with the saturated unit weight of 12.5 kN/m^3. Because of the very high energy release rate of VBC and decades of mining and stress relaxation in Yallourn open-cut, existing joints have propagated well across the thickness of coal seam. This fact eases the joint mapping practice in the areas where coal surface is uncovered. However, this practice can be extremely challenging where the coal surface is laid under a layer of sandy/gravelly overburden material, or the coal surface is face-trimmed by dozers as a routine mining method in the Yallourn mine (Fig. 1).

In this article, researchers at the Geotechnical and Hydrogeological Engineering Research Group, Federation University Australia, investigated the application of GPR with

FIG. 1 Map of Australia showing the location of the Yallourn mine.

different wave frequencies in detecting vertical subsurface joints in VBC covered by silt and gravel.

Background

In general, GPR utilizes electromagnetic waves to provide useful resolution and nondestructive measurements of dielectric contrasts in geological materials and formations (Daniels 2004). Similar to most of the geophysical methods, this method can be classified as a nondestructive geophysical method, in which electromagnetic waves are sent into the ground with the ability to gather data from underground soil without drilling and mechanical sampling. These electromagnetic waves are reflected back when they reach an underground object or a boundary between two different materials. In the end, the GPR system detects the reflected wave and calculates the location of targets based on its time–distance algorithm (Hassan and Toll 2014).

The history of using GPR dates back to 1904, when this method was used to detect remote terrestrial metal objects (Greve, Acworth, and Kelly 2010). After that, application of GPR continued for estimating the thickness of ice, fresh water, salt deposition, pavement, rock, and coal (Greve, Acworth, and Kelly 2010; Hassan and Toll 2014; Al-Qadi and Lahouar 2005). In 1989, the Norwegian Geotechnical Institute used georadar systems for

applications in environmental purposes, which have been tested in over 60 projects and found to yield satisfactory results (Cheng, Tang, and Chan 2013). The GPR scanning technique was also used to investigate backfilling of a retaining wall to find the location of bedrock when it was not possible to conduct traditional geotechnical field investigations (Beben, Anigacz, and Ukleja 2013).

GPR is also applicable in finding discontinuities in rocks. The reflection of electromagnetic waves happens at the interface between two media having different propagation velocities, like the interface of a crack and the surrounding rock (Daniels 2004). This concept has been successfully examined for detecting fractures and structural features in different rocks such as marble, granite and gneiss (Toshioka, Tsuchida, and Sasahara 1995; Porsani, Sauck, and Júnior 2006; Kong and By 1995; Cheng, Tang, and Chan 2013; Arosio 2016). This method has been also used by (Orlando 2003) to evaluate rock quality based on the concept that in good quality rock, most of the energy is transmitted, while in low quality rock, the energy is backscattered from fractures. The GPR scanning method has also been applied in airport road maintenance by identifying the location of subsurface cracks. This method has allowed the engineers to propose a repair program for the worse affected areas rather than a full-scale reconstruction, resulting in a significant saving in road maintenance cost (Grandjean and Gourry 1996). The effectiveness of the GPR method has been examined by (Di Prinzio et al. 2010) to detect the presence of voids and discontinuities within levees and river embankments.

In mining engineering, in addition to batter stability investigations and the mapping of fractures and unloaded joints by nondestructive geophysical methods such as GPR, scanning helps the development of the quarry in a rational and profitable manner. This information is fundamental for guiding the development of new benches by avoiding areas with close-spaced fractures, thus optimizing the extraction process and increasing benefits (Daniels 2004). Also, GPR has been found as a successful crack detecting tool for the monitoring of historical buildings (Stevens et al. 1995). In general, GPR scanning has been found to be an effective method in capturing discontinuities and external objects within materials with low attenuation such as ice, sand, crude oil, rock, and fresh water, and less effective in high attenuation media such as clay and salt water (Cheng, Tang, and Chan 2013).

Through the review of literature, it has been noted that although a number of studies have been conducted for the purposes of using GPR to detect discontinuities in different quarries, there is still a lack of research in the application of GPRs in finding cracks and joints in open-cut coal mines. Because of the low unit weight of VBC, pre-existing joints in VBC mines have a tendency to open and extend because of earthworks or excessive pore water pressure, explaining that joints in VBC mines can be considered as ongoing threats to the stability of batters. Hence, GPR scanning might be regarded as a useful field investigation method in VBC open-cut mining, as well as a key component towards successful mine rehabilitation after closure, if it can be used for mapping of subsurface joints in a practical way.

Testing Program

The GPR system used in this research project consists of a control unit, an antenna (transmitter and receiver), and survey wheels (see Fig. 2). The control unit triggers the antenna to send radar waves into the ground and also receive the reflected waves. As a standard

FIG. 2

Overview of the employed GPR system.

practice, survey wheels equipped with an odometer have been used to facilitate fieldwork and record reference points during surveying (Greve, Acworth, and Kelly 2010; Hassan and Toll 2014).

The velocity of the propagated GPR waves (radio signals) through subsurface is related to the electrical property of the underground materials and the materials' dielectric permittivity. When the radio signals reach the interface of two materials with different dielectric properties, a portion of the signal is returned back to the antenna on the ground surface. The control unit on the GPR system measures the amount of time taken for the radio signal to traverse to and from the target (two-way travel time), which indicates its depth and location of the target (Eq 1) (ASTM D7128-05, *Standard Guide for Using the Seismic-Reflection Method for Shallow Subsurface Investigation*, 2010).

$$D = \frac{tV}{2}$$

(1)

where V is the velocity of the electromagnetic wave in a material, D is the one-way distance to the object, and t is the two-way travel time to the object.

In the ground, the velocity of electromagnetic waves (V) changes depending on the relative dielectric permittivity (Eqs 2 and 3) (ASTM D7128-05 2010). The higher the dielectric constant, the lower the electromagnetic waves passing through the materials

TABLE 1

Approximate electromagnetic properties of some materials (ASTM D7128-05 2010).

Material	Dielectric Constant (K)	Pulse Velocities (m/ns)
Air	1	0.3
Fresh water[f,t]	81	0.033
Sea water[f,t,s]	70	0.033
Sand (dry)[d]	4–6	0.15–0.12
Sand (saturated)[d,w,f]	25	0.055
Silt (saturated)[d,w,f]	10	0.095
Clay (saturated)[d,w,f]	8–12	0.106–0.087
Dry sandy coastal land[d]	10	0.095
Fresh water ice[f,t]	4	0.15
Permafrost[f,t,p]	4–8	0.15–0.106
Granite (dry)	5	0.134
Limestone (dry)	7–9	0.113–0.1
Dolomite	6–8	0.122–0.106
Quartz	4	0.15
Coal[d,w,f,ash content]	4–5	0.15–0.134
Concrete[w,f,age]	5–10	0.134–0.095
Asphalt	3–5	0.173–0.134
Sea ice[s,f,t]	4–12	0.15–0.087
PVC, epoxy, polyesters vinyls, rubber[f,t]	3	0.173

Note: d: function of density; w: function of porosity and water content; f: function of frequency; t: function of temperature; s: function of salinity; p: function of pressure.

(Hassan and Toll 2014; Kadioglu 2008). **Table 1** gives the electromagnetic characteristics of different materials.

$$V = \frac{C}{\sqrt{K}} \qquad (2)$$

$$K = \frac{\varepsilon}{\varepsilon_0} \qquad (3)$$

where C is the velocity of light (0.2997 m ns^{-1}), K is dielectric constant, ε is permittivity of the target, and ε_0 is permittivity of free space (8.854 × 10^{-12} Fm^{-1}).

Choosing the right antenna is the key part of GPR testing program. In general, the frequency of antennas available in the market varies from 10 MHz to 1.6 GHz. The frequency of GPR antenna is chosen according to the aims of the survey (see **Table 2**). In

TABLE 2

Examples of scanning capability with different frequencies (Hassan and Toll 2014) and (ASTM D7128-05 2010).

| Frequency	Typical application	Maximum depth (m)
1.6 GHz	Structural concrete, roadways, bridge decks	0.5
900 MHz	Concrete, shallow soils, archaeology	1
400 MHz	Shallow geology, utility, environmental, archaeology	3
200 MHZ	Geology, environmental	8
100 MHz	Geology, environmental	20

general, the deeper the penetration, the lower the antenna frequency and the lesser the resolution, and vice versa.

As explained before, there is a direct relation between the antenna's frequency and the resolution and an inverse relation between the antenna's frequency and the penetration depth. Hence, because of the fact that joints in VBC formations commence from shallow depths (from the coal surface just underneath the overburden material) and are relatively closed, medium range frequency was considered to be suitable for this investigation. The equipment used in this survey is MALÅ Ground Explorer HDR, manufactured by Malå GeoScience Förvaltnings AB (Sweden) (GuidelineGeo, 2016), which consists of two antennae, one 450 MHz and the other one 750 MHz. According to Table 1, the velocity of electromagnetic waves in coal ranges between 0.134–0.15 m/ns. Thus, the velocities of 0.1, 0.13, and 0.15 m/ns are set on the control unit, which runs a basic real-time processing during the test. This allows the user to find the possible location of the joints while the test is being conducted. The same range of velocities are used later during the data post-processing by a third-party processing software package.

The two joints cutting through VBC formation at the northern batter of Yallourn mine (Fig. 3) are visible from the side and invisible at the ground surface and are considered as benchmark joints for GPR scanning (Figs. 4 and 5). On the batter and access road, both joints are covered with silty overburden material (0.5-m to 1-m thick) and compacted gravel and silt (0.2-m to 0.4-m thick), respectively, while they are exposed at the batter face. Because the location of the covered joints under the overburden layer and access road pavement are seen from the side view, this spot provides a good location for investigating the capabilities of GPR in this joint mapping exercise. As shown in Fig. 5, two tracks perpendicular to the joints are defined as survey lines, one 21-m long on the batter (Survey Line 1) and the other one 56-m long on the access road (Survey Line 2).
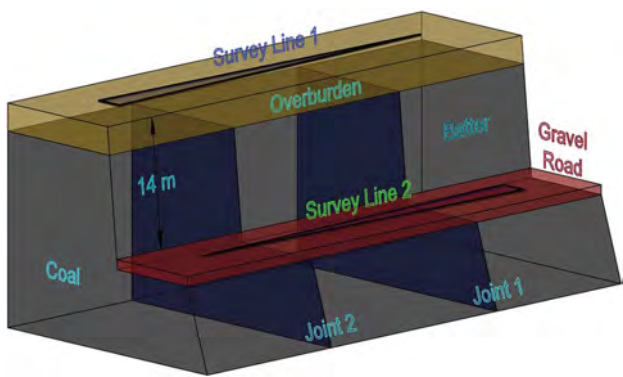
A total of twenty scan runs were conducted, eight along the Survey Line 1 and twelve along the Survey Line 2 (Fig. 6), with a range of varying parameters as shown in Table 3. These parameters were altered on a "one factor at a time" basis to determine the best framework for joint detection.
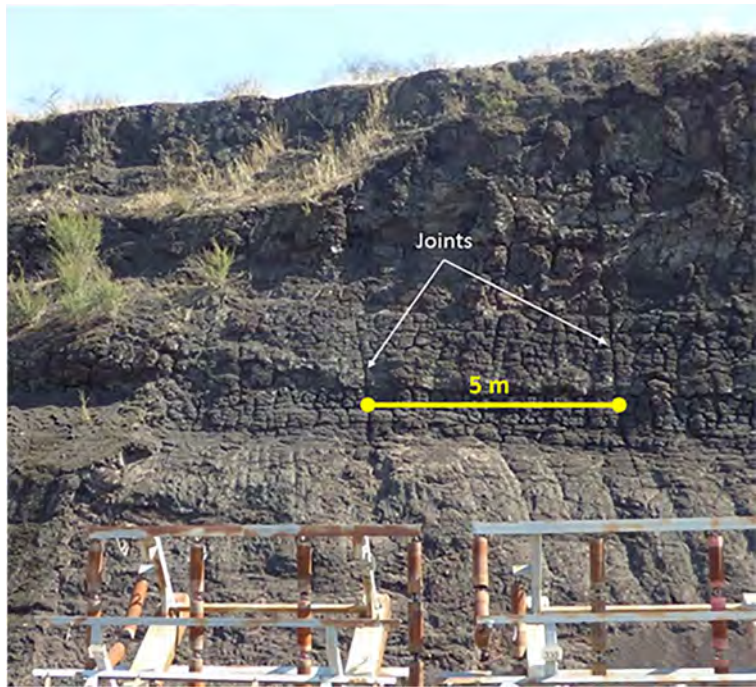
FIG. 3 Location of survey.
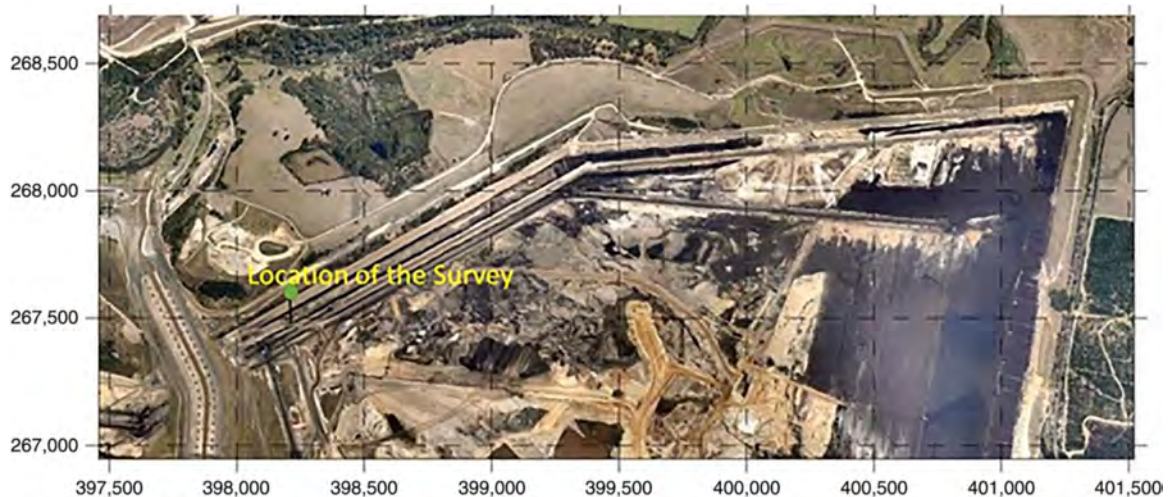
FIG. 4

Schematic diagram of the survey lines.

FIG. 5

Side view of the joints at the VBC batter.

Data Processing

Once testing was completed, the data was uploaded from the GPR unit memory and analyzed with the R software package R GPR (Developer: Sadeghi, A). GPR images viewed in their initial unfiltered state proved ineffective in identifying the positions of joints (**Fig. 7**). Furthermore, virtually no discernible details were able to be identified, suggesting the suitability of filtering techniques to enhance image quality.

FIG. 6

Scanning on Survey Line 2.

TABLE 3

Test parameters.

Test number	Location	Antenna frequency (MHz)	Soil velocity (m/ns)	Point interval (cm)
1	Survey line 1	450	0.130	1
2	Survey line 1	450	0.130	1
3	Survey line 1	450	0.130	1
4	Survey line 1	450	0.100	1
5	Survey line 1	450	0.100	1
6	Survey line 1	450	0.150	1
7	Survey line 1	450	0.150	1
8	Survey line 1	450	0.150	1
9	Survey line 2	750	0.130	1
10	Survey line 2	750	0.130	0.5
11	Survey line 2	750	0.100	0.5
12	Survey line 2	750	0.150	0.5
13	Survey line 2	750	0.100	1
14	Survey line 2	750	0.150	1
15	Survey line 2	450	0.130	1
16	Survey line 2	450	0.100	1
17	Survey line 2	450	0.150	1
18	Survey line 2	450	0.130	0.5
19	Survey line 2	450	0.100	0.5
20	Survey line 2	450	0.150	0.5

FIG. 7

GPR image of Test 11 before post processing.
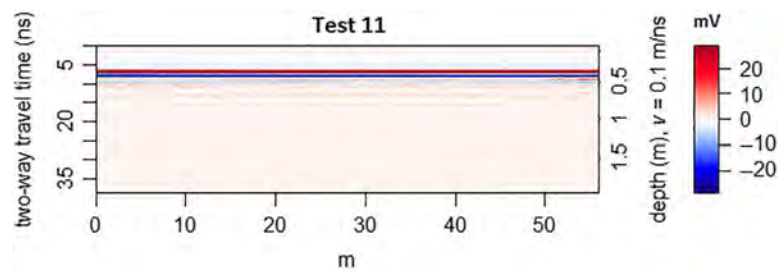
To produce images of high detail, a procedure utilizing a range of filtering techniques (Fig. 8) was devised with the objective of improved visualization of joint features:

DC SHIFT REMOVAL

Because of the energy input from the air and ground waves, the GPR receiver signal becomes saturated, introducing low frequency components known as "wow." A bulk DC shift in amplitude towards zero is applied as a correction.

BANDPASS FILTERING

A bandpass filter is an algorithm that permits frequencies of a given range while rejecting all frequencies outside the range. In this case, higher frequencies were filtered out, effectively removing signal noise, allowing key joint characteristics to be identified without the interference of small and desiccation cracks. Davis and Annan (1989) stated that "GPR systems are designed to achieve bandwidths that are about equal to the center frequency." Hence, the bandpass filter ranges implemented were 225–675 MHz and 375–1125 MHz for the 450 and 750 MHz antennae, respectively.

GAIN RECOVERY

Time–gain recovery was applied to account for the effects of signal attenuation. The exponential gain function applied is given in Eq 4:

$$A_{gain}(t) = A(t) \exp(\alpha t)$$

(4)

where $A(t)$ is the initial signal, α is the exponential gain constant, and t is the sample trace (ns). The exponential gain constant α of 0.5 was determined to give the best visualizations for the test instances considered in this article (Cassidy 2009).

INVERSE NORMAL TRANSFORMATION

A histogram of frequencies (Fig. 9) indicates a narrow band of values about zero. To broaden the spectrum, a rank-based inverse normal transform is implemented, producing a wider spectrum (Fig. 10).

MEDIAN TRACE FILTER

A median trace filter (or alpha–mean trim) is applied to vertically along each trace, removing high frequency noise spikes (Cassidy 2009).

FIG. 8

Flowchart of data
post-processing and
joint identification.
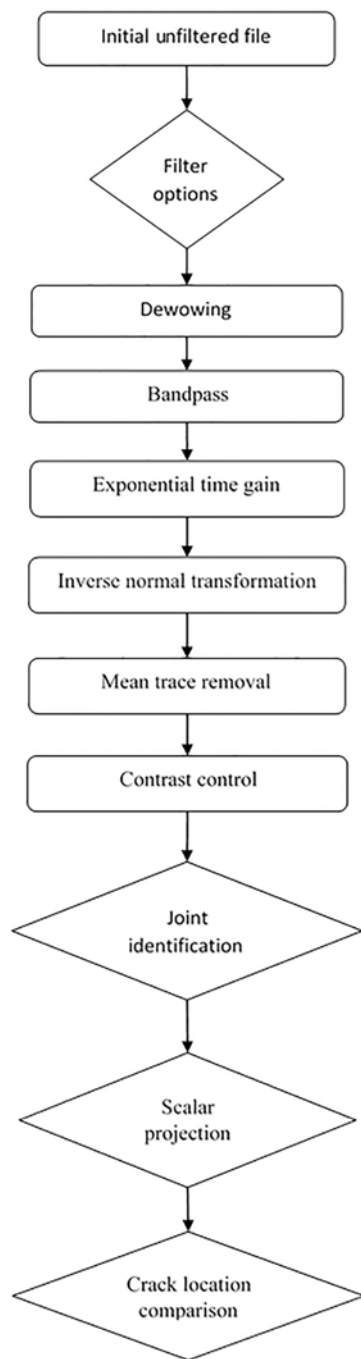
CONTRAST CONTROL

The image color contrast is maximized to highlight potential joint locations.

When analyzing the GPS coordinates taken along Survey Lines 1 and 2, it was noted that the two lines were not completely parallel. To remedy this, a scalar projection of

FIG. 9

Histogram of frequencies,
indicating a narrow peak, Test 9.
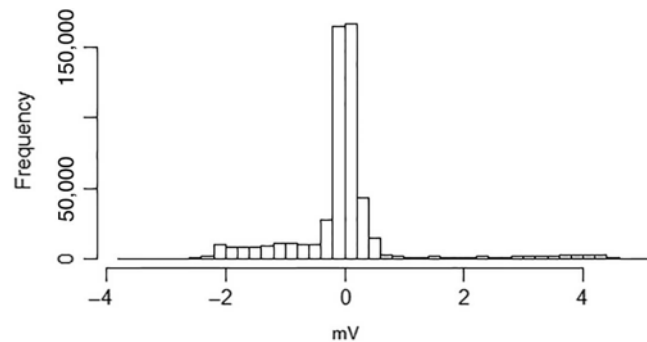
FIG. 10

Histogram of frequencies,
indicating a broadened peak
after Inverse Normal
Transformation, Test 9.
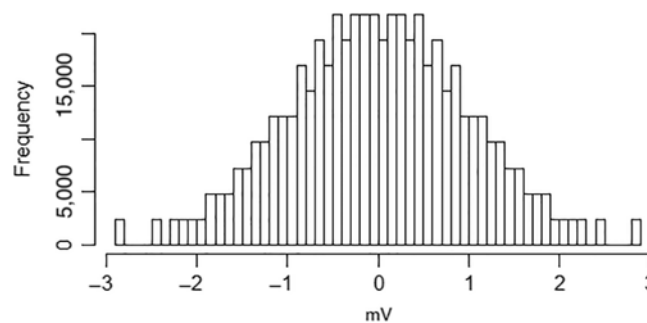
Survey Line 1 coordinates was projected onto Survey Line 2, suggesting that Joints 1 and 2 should be located at 29 and 36 m along Survey Line 2, respectively.

A time–zero correction is commonly used in GPR studies to designate the starting point of the received wave form. A correction is often applied to rescale depths, such that the ground surface occurs at 0 m. Because of the vertical nature of the joints of interest in this study, it was deemed unnecessary to perform a time–zero correction, as the detection of the below-the-surface joint locations was the prime objective. As the rescaling of vertical depths by less than 0.5 m provides no further information for the purposes of this study, no zero–time correction was performed.

Results and Discussion

Tests with a point interval parameter value of 0.5 cm (Tests 10–12, 18–20) proved too grainy for further analysis (Fig. 11). For this reason, only point intervals of 1 cm were considered for additional investigation.

The impact of the variation of soil velocity and antenna frequencies on joint visualization is clearly visible in Fig. 12 for the 750 MHz antenna, conducted along the base of the batter, with vertical joints discernible at 29 and 36 m. In Test 14, joints 1 and 2 are located at 31 and 38 m, respectively, because of a difference in the test starting position. The two joints are best visible in Test 12, with a soil velocity of 0.15 m/ns, whereas the lower soil velocities of 0.1 and 0.13 m/ns were unable to easily locate both joints together
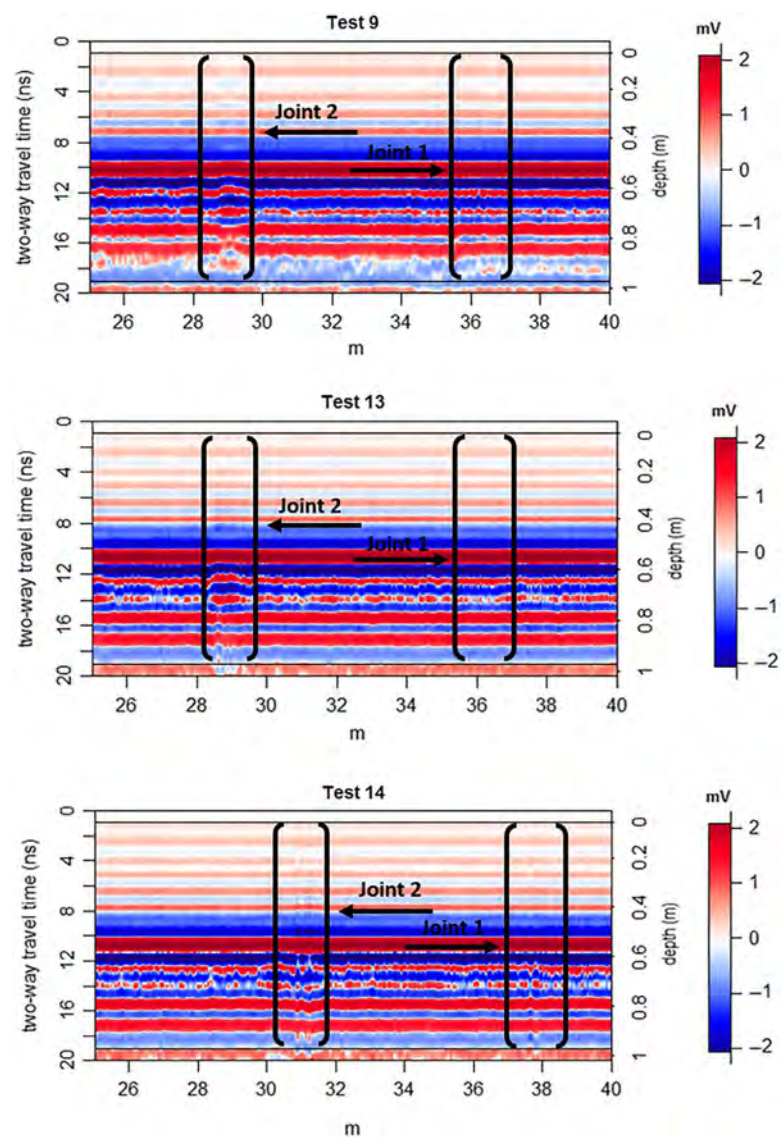
FIG. 11

Test 11 results. Point interval: 0.5 cm.
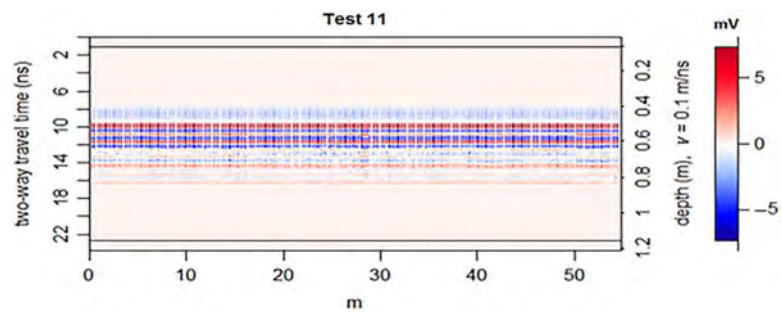
FIG. 12

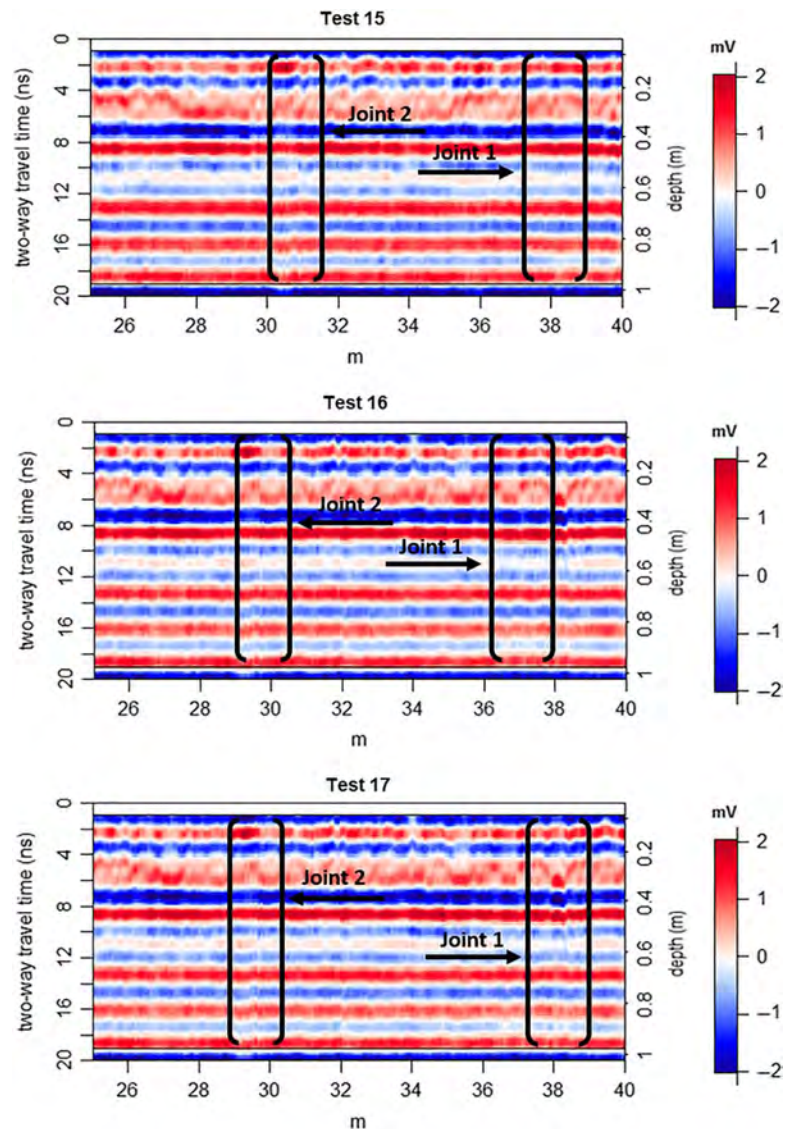Varying joint resolution for the 750 MHz antenna (Survey Line 2).

(Tests 9 and 13). In both tests, Joint 1 was easily located, however, Joint 2 appears only as a small anomaly. Tests 15, 16, and 17 were performed with a 450 MHz antenna (Fig. 13). Although Joints 1 and 2 are visible in Tests 16 and 17, the quality of the joint visualization was considerably lower than with the 750 MHZ antenna, suggesting that 450 MHz is an unsuitable frequency for detection of coal joints of this type. Fig. 13 indicates that there are potentially numerous desiccation cracks running through the VBC batter. However, two prominent joints are visible at 29 m and 36 m, being the two joints detailed in Fig. 5. In addition to the observed joints, a number of surface cracks are visible in Fig. 13 that do not appear to propagate vertically through large depths of the coal.

The location of Joints 1 and 2 are visible along Survey Line 1 at 15 and 10 m, respectively (Fig. 14). It is noted that the two main joints identified along Survey Line 1 align
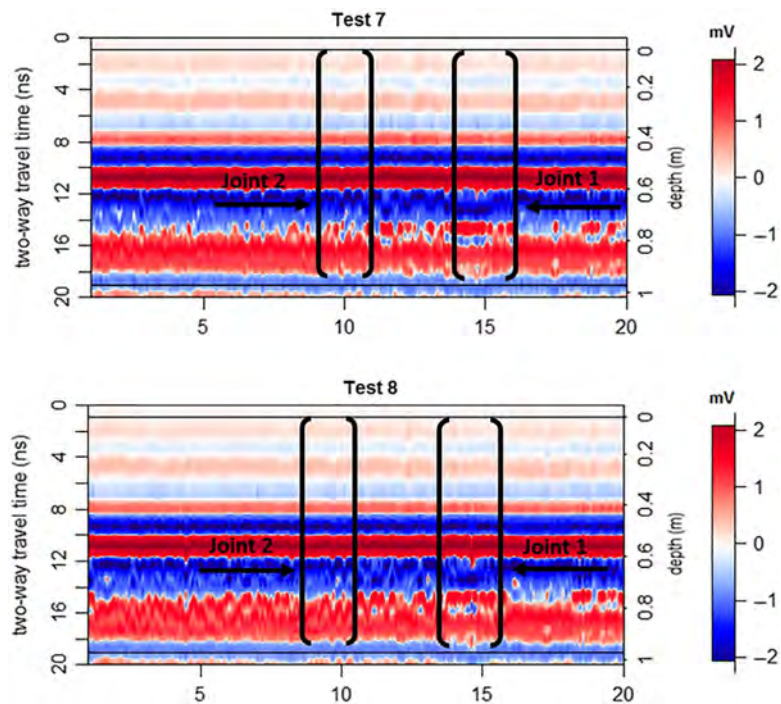
FIG. 13

Varying joint resolution for the 450 MHz antenna (Survey Line 2).

Varying joint resolution for the 450 MHz antenna (Survey Line 1).

with those of Survey Line 2, within acceptable experimental error due to variation in the initial start position along the survey lines. The joints along Survey Line 1 are best visualized in Test 7 and 8 (Fig. 14) with a soil velocity of 0.15 m/ns. It is notable that the batter contains numerous fractures, with two further large joints visible at 5 m and 18 m. Although joints along Survey Line 2 were best observed with an antenna frequency of 750 MHz, the main joints along Survey Line 1 are not easily distinguished at this frequency because of the numerous other fractures. Hence, heavily jointed coal was considered with the 450 MHz antenna.

In both cases, the highest soil velocity (0.15 m/ns) provided the best joint resolution, however, the considerable number of joints along the batter provides a considerably challenging environment for locating specific joints. Nevertheless, the most apparent of the joints can be differentiated from smaller fractures. It is suggested that the joints were difficult to locate because of their vertical nature and could have been identified if their angle with the ground surface was smaller.

Conclusion

GPR can be considered as a useful tool for a broad range of geotechnical investigation purposes. In this study, GPR was adopted as a technique for the identification of preexisting vertical joints in VBC because of the method's non-destructive qualities. Two survey tracks were constructed to identify known batter joints, visible to the naked eye from the side view and fully covered at the ground surface.

With the variation of a range of parameters including soil velocity, point interval distance, and antenna frequency, these known joints were detected. Although this method was theoretically feasible, joint detection requires numerous parameter variations and significant post-processing using software tools. Furthermore, the joints identified were visible within the coal batter. Hence, the process of verifying their locations on GPR images was straightforward. It is suggested that determining the locations of unexposed joints may prove exceedingly more complicated, especially when considering surveying on the magnitude of large sections of mine slopes.

To determine joints within VBC, a 1-cm point interval resolution, with a 450 MHz antenna for heavily jointed environments and 750 MHz for infrequently jointed conditions, is recommended. The joints were best observed at a soil velocity of 0.15 m/ns.

To view these fractures, considerable data processing was required, with a number of filters implemented, including DC shift, bandpass, median trace, and gain filters.

For the reasons detailed above, it is suggested that GPR detection of brown coal joints is a theoretically valid method. However, the technique is impractical in reality because of poor resolution and the need for excessive filtering of results.

References

Al-Qadi, I. L. and Lahouar, S., 2005, "Measuring Layer Thicknesses with GPR–Theory to Practice," *Constr. Build. Mater.*, Vol. 19, No. 10, pp. 763–772, https://doi.org/10.1016/j. conbuildmat.2005.06.005

Arosio, D., 2016, "Rock Fracture Characterization with GPR by Means of Deterministic Deconvolution," *J. Appl. Geophys.*, Vol. 126, pp. 27–34, https://doi.org/10.1016/j. jappgeo.2016.01.006

ASTM D7128-05, 2010, *Standard Guide for Using the Seismic-Reflection Method for Shallow Subsurface Investigation*, ASTM International, West Conshohocken, PA.

Barr, G. L., 1993, "Application of Ground-Penetrating Radar Methods in Determining Hydrogeologic Conditions in a Karst Area, West-Central Florida," *Water-Resources Investigations Report 92-4141*, US Geological Survey, Tallahassee, FL, 26p.

Barton, C. M., Gloe, C. S., and Holdgate, G. R., 1993, "Latrobe Valley, Victoria, Australia: A World Class Brown Coal Deposit," *Int. J. Coal Geol.*, Vol. 23, Nos. 1–4, pp. 193–213, https://doi.org/10.1016/0166-5162(93)90048-F

Beben, D., Anigacz, W., and Ukleja, J., 2013, "Diagnosis of Bedrock Course and Retaining Wall Using GPR," *NDT and E Int.*, Vol. 59, pp. 77–85, https://doi.org/10.1016/j.ndteint. 2013.05.006

Butnor, J. R., Barton, C., Day, F. P., Johnsen, K. H., Mucciardi, A. N., Schroeder, R., and Stover, D. B., 2012, "Using Ground-Penetrating Radar to Detect Tree Roots and Estimate Biomass," *Measuring Roots: An Updated Approach*, S. Mancuso, Ed., Springer Berlin Heidelberg, Berlin, Germany, pp. 213–245.

Cassidy, N. J., 2009, "Ground Penetrating Radar Data Processing, Modelling and Analysis," *Ground Penetrating Radar: Theory and Applications*, Elsevier, Amsterdam, the Netherlands, pp. 141–176.

Cheng, N.-F., Tang, H.-W. C., and Chan, C.-T., 2013, "Identification and Positioning of Underground Utilities Using Ground Penetrating Radar (GPR)," *Sustain. Environ. Res.*, Vol. 23, No. 2, pp. 141–152.

Conyers, L. B., 1995, "The Use of Ground-Penetrating Radar to Map the Buried Structures and Landscape of the Ceren Site, El Salvador," *Geoarchaeology*, Vol. 10, No. 4, pp. 275–299, https://doi.org/10.1002/gea.3340100404

Daniels, D. J., 1996, *Surface Penetrating Radar*, Institution of Electrical Engineers, London, UK, 300p.

Daniels, D. J., 2004, *Ground Penetrating Radar*, Institution of Electrical Engineers, London, UK, 726p.

Davis, J. L. and Annan, A. P., 1989, "Ground-Penetrating Radar for High-Resolution Mapping of Soil and Rock Stratigraphy," *Geophys. Prospect.*, Vol. 37, No. 5, pp. 531–551, https://doi.org/10.1111/j.1365-2478.1989.tb02221.x

Di Prinzio, M., Bittelli, M., Castellarin, A., and Pisa, P. R., 2010, "Application of GPR to the Monitoring of River Embankments," *J. Appl. Geophys.*, Vol. 71, Nos. 2–3, pp. 53–61, https://doi.org/10.1016/j.jappgeo.2010.04.002

Grandjean, G. and Gourry, J. C., 1996, "GPR Data Processing for 3D Fracture Mapping in a Marble Quarry (Thassos, Greece)," *J. Appl. Geophys.*, Vol. 36, No. 1, pp. 19–30, https://doi.org/10.1016/S0926-9851(96)00029-8

Greve, A. K., Acworth, R. I., and Kelly, B. F., 2010, "Detection of Subsurface Soil Cracks by Vertical Anisotropy Profiles of Apparent Electrical Resistivity," *Geophysics*, Vol. 75, No. 4, pp. WA85–WA93, https://doi.org/10.1190/1.3474590

Guidelinegeo, 2016, "Guideline Geo Products Archive," *Guideline Geo AB*, http://web.archive.org/web/20180612084352/https://www.guidelinegeo.com/ (accessed 12 June 2018).

Guy, P. J. and Perry, G. J., 1992, "Victorian Brown Coal as a Source of Industrial Carbons: A Review," *Fuel*, Vol. 71, No. 10, pp. 1083–1086, https://doi.org/10.1016/0016-2361(92)90088-6

Hassan, A. A. and Toll, D. G., 2014, "Investigation of the Directional Dependence of Soil Resistivity in Cracking Clays," presented at the *Sixth International Conference on Unsaturated Soils (UNSAT2014)*, Sydney, Australia, CRC Press/Balkema, Leiden, the Netherlands, pp. 137–142.

Kadioglu, S., 2008, "Photographing Layer Thicknesses and Discontinuities in a Marble Quarry with 3D GPR Visualisation," *J. Appl. Geophys.*, Vol. 64, Nos. 3–4, pp. 109–114, https://doi.org/10.1016/j.jappgeo.2008.01.001

Kong, F.-N. and By, T. L., 1995, "Performance of a GPR System which Uses Step Frequency Signals," *J. Appl. Geophys.*, Vol. 33, Nos. 1–3, pp. 15–26, https://doi.org/10.1016/0926-9851(95)90026-8

Orellana, E., 1972, *Prospección Geoeléctrica en Corriente Continua* (in Spanish), Paraninfo, Madrid, Spain, 523p.

Orlando, L., 2003, "Semiquantitative Evaluation of Massive Rock Quality Using Ground Penetrating Radar," *J. Appl. Geophys.*, Vol. 52, No. 1, pp. 1–9, https://doi.org/10.1016/S0926-9851(02)00229-X

Porsani, J. L., Sauck, W. A., and Júnior, A. O. S., 2006, "GPR for Mapping Fractures and as a Guide for the Extraction of Ornamental Granite from a Quarry: A Case Study from Southern Brazil," *J. Appl. Geophys.*, Vol. 58, No. 3, pp. 177–187, https://doi.org/10.1016/j.jappgeo.2005.05.010

Sagnard, F. and Tebchrany, E., 2015, "Using Polarization Diversity in the Detection of Small Discontinuities by an Ultra-Wide Band Ground-Penetrating Radar," *Measurement*, Vol. 61, pp. 129–141, https://doi.org/10.1016/j.measurement.2014.10.035

Stevens, K. M., Lodha, G. S., Holloway, A. L., and Soonawala, N. M., 1995, "The Application of Ground Penetrating Radar for Mapping Fractures in Plutonic Rocks within the Whiteshell Research Area, Pinawa, Manitoba, Canada," *J. Appl. Geophys.*, Vol. 33, Nos. 1–3, pp. 125–141, https://doi.org/10.1016/0926-9851(95)90036-5

Toshioka, T., Tsuchida, T., and Sasahara, K., 1995, "Application of GPR to Detecting and Mapping Cracks in Rock Slopes," *J. Appl. Geophys.*, Vol. 33, Nos. 1–3, pp. 119–124, https://doi.org/10.1016/0926-9851(95)90035-7

Zajc, M., Pogačnik, Ž., and Gosar, A., 2014, "Ground Penetrating Radar and Structural Geological Mapping Investigation of Karst and Tectonic Features in Flyschoid Rocks as Geological Hazard for Exploitation," *Int. J. Rock Mech. Min. Sci.*, Vol. 67, pp. 78–87.

Investigation of an Australian soft rock permeability variation

Ali Tolooiyan[1] · Ashley P. Dyson[2] · Mojtaba Karami[2] · Tahereh Shaghaghi[2] · Mohsen Ghadrdan[2]

Abstract

In this study, permeabilities of Victorian Brown Coal (VBC) as an Australian soft rock are determined for a range of depths of a continuous coal seam located at the batter crest of the Yallourn brown coal open-cut mine in Victoria, Australia, by implementing a Lugeon packer testing procedure. Permeability values are determined both analytically and by numerical simulation and are compared with laboratory test results. Field testing resulted in permeabilities several orders of magnitude higher than laboratory testing, suggesting the existence of fractures common to lignite structures on a greater scale than can be observed in the laboratory. The variation of depth-based field and laboratory permeabilities is discussed, as well as the necessary conditions required for the numerical modelling of packer testing within VBC.

Keywords Intermediate geotechnical material · Victorian brown coal · Permeability · Hydraulic conductivity · Packer test

Introduction

The estimation of hydraulic conductivity parameters is necessary for widely varying applications including tunnelling, underground storage and mine design. Hydraulic conductivity can be determined either by field tests (such as pumping and water pressure experiments) or laboratory permeability tests (such as falling and constant head tests), while permeability values can vary considerably due to the presence of fracture zones and material heterogeneity (Sahimi and Pop 1996). The Lugeon test, also known as the packer test, is commonly used to determine field-scale permeability in geotechnical and hydrological engineering settings, where a borehole section is isolated between two inflatable packers (Lugeon 1933). Measurements of the relationship between groundwater head and flow for a segment of the bore can then be considered. Field tests are often considered advantageous compared to laboratory investigation, as field-scale results in many cases may represent in situ conditions on a scale above the representative elementary volume (REV) required to describe macroscale systems. However, permeability field testing procedures often produce their own set of obstacles due to the complexities inherent in large-scale geological systems. Conversely, laboratory testing is often conducted on idealized intact samples, where the effects of spatial variability may be greater in the smaller-scale laboratory environment than in the field (Hamm et al. 2007).

Flow patterns may be further considered by core logging, geophysical surveying and pumping tests. However, core sampling does not consider material fissures and solution channels, while geophysical tests yield potential flow mechanisms without exact quantitative information (Bliss and Rushton 1984).

Previous studies have detailed the applicability of in situ testing procedures with their advantages and disadvantages outlined by Becker (2001) and Yihdego (2017). One of the fundamental goals of geotechnical assessment is the site characterization of ground conditions and parameters, where natural materials may be subject to high levels of heterogeneity or uncertainty.

✉ Ali Tolooiyan
ali.tolooiyan@utas.edu.au; tolooiyan@gmail.com

Ashley P. Dyson
a.dyson@federation.edu.au

Mojtaba Karami
m.karami@federation.edu.au

Tahereh Shaghaghi
t.shaghaghi@federation.edu.au

Mohsen Ghadrdan
m.ghadrdan@federation.edu.au

Extended author information available on the last page of the article

Fig. 1 Yallourn open-cut mine location

These uncertainties in geotechnical engineering methods must be carefully considered to achieve requisite safety levels in design while managing the limitations of the geotechnical equipment to detect material variation (Becker et al. 2010; Levy et al. 1993).

The objectives of this study are (1) to compare field-scale permeability test results of VBC with those from laboratory scale permeability testing, (2) to examine the effects of repeated water injection on packer test results by comparative numerical finite element method (FEM)

Fig. 2 Stratigraphy of the Latrobe Valley depression (Holdgate et al. 2002)
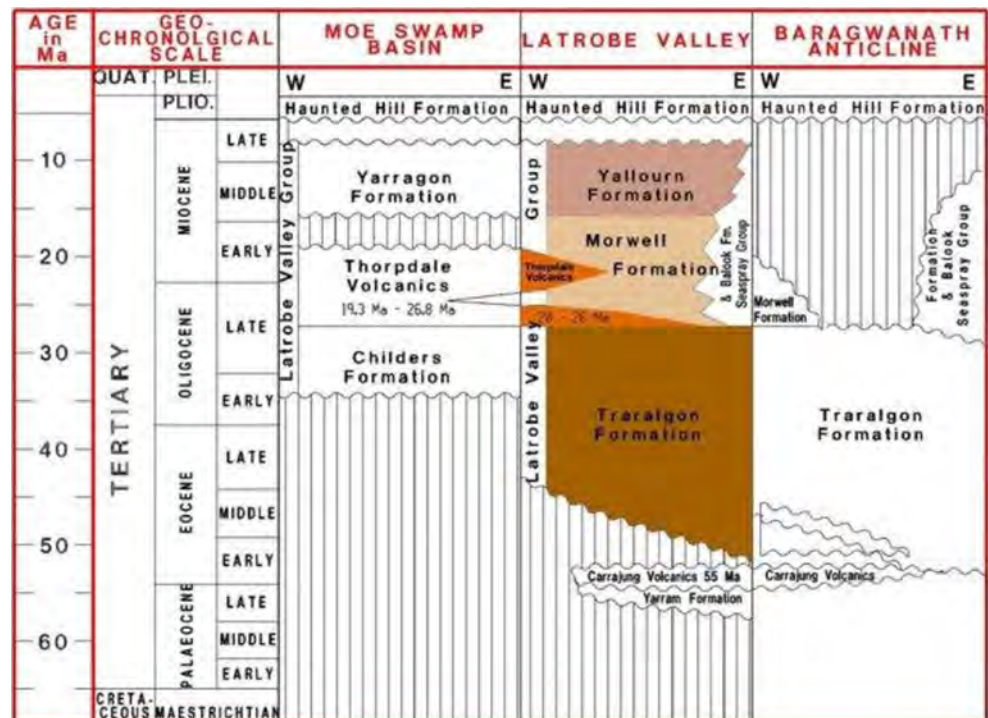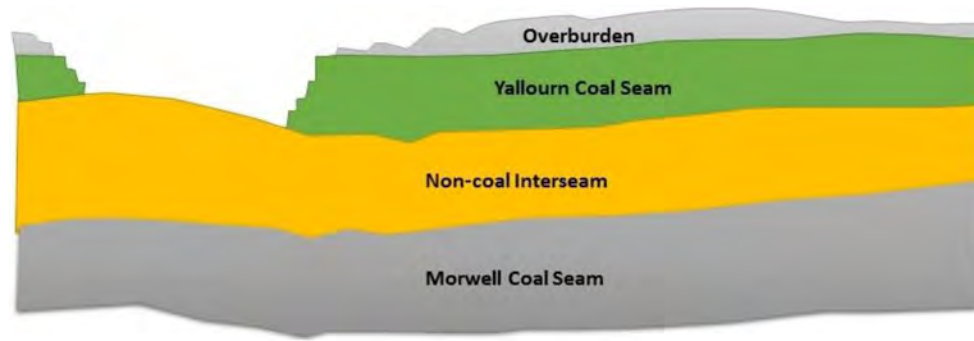
Fig. 3 Yallourn north-east batter stratigraphy, initially detailed in (Soliman et al. 2007)

modelling, (3) to compare closed-form analytic solutions for packer test permeability with FEM based groundwater flow simulation and (4) to investigate vertical spatial permeability trends in VBC seams.

Test material and location

Australia's second-largest open pit, the Yallourn brown coal mine, is located in the Latrobe Valley, in the state of Victoria, Australia, approximately 150 km east of the capital city Melbourne (Energy Australia 2018) (Fig. 1). Greater than 80% of Victoria's brown coal resources are located within the Gippsland Basin, specifically in the Latrobe Valley, with seams containing an estimated 65 billion tonnes of coal (Barton et al. 1993). The Yallourn mine is one of the three large lignite mines in the region supplying the two power stations responsible for the majority of Victoria's electricity production.

Victorian brown coal is a low-rank coal and can be considered as lignite B, as classified by the American Society for Testing and Materials (ASTM 2012). The coals of the Latrobe Valley region were deposited the Eocene to late Miocene period (Fig. 2). Three main formations exist, the Traralgon, Morwell and Yallourn formations, in ascending sequence. Figure 3 shows a typical stratigraphic cross-section of the Yallourn north-east batter. VBC is relatively soft and light with a specific gravity around 1.1 g/cm (Tolooiyan et al.

2014) and a water content above 60% by volume (Moein et al. 2016).

Previous State Electricity Commission of Victoria (SECV) studies have recorded Yallourn seam permeability values ranging from 7×10^{-7} m/s to 3.8×10^{-6} m/s with constant head permeability testing methods and laboratory permeability tests estimated coal permeabilities of 8.2×10^{-9} m/s (State Electricity Commission of Victoria 1983). Rosengren noted that the permeability of VBC is low (estimated at 4.23×10^{-9} m/s) but stated that cracks in the coal have an unknown influence and that field measurements are the only reliable method for estimating the pore water pressures in the coal (Rosengren 1963).

Due to the brittle characteristics of VBC, cracking and jointing are common features at the Yallourn mine (State Government of Victoria 2008). A range of major joint characteristics within the Yallourn East Field (YEF) and north-east batter have been detected through joint surveys conducted in the 1990s and 2000s, as shown in Tables 1, 2 and Fig. 4. Although a range of joints are identified, not all joints are readily detectable, as many are not unable to be observed as surface levels. Figure 5 shows a range of joints mapped to the north-east batter, after a large batter failure occurred in 2007. Due to the presence of large in situ jointing, permeability values can exhibit distinct differences when considered in the laboratory compared with in situ environments.

Table 1 Characteristics of joints in YEF, 1997 (Geo Eng 1996)

Joint set	Dip (degrees)		Dip direction (degrees)		Comments
	Mean	Standard deviation	Mean	Standard deviation	
J1	86	8	209		Dominant, subvertical set occurring throughout East Field
J2	88	9	243		Dominant, subvertical set occurring throughout East Field
J3	83	7	338		Uncommon subvertical set
J4	48	11	239		Critically dipping joint set
J5	12	4	240		Bedding parallel joints

Table 2 Characteristics of joints in YEF, 1999 (Geo Eng 1997)

Joint set	Dip (degrees)		Dip direction (degrees)		Comments
	Mean	Standard deviation	Mean	Standard deviation	
J1	85	3		180	Dominant, subvertical set
J2	85	3		225	Dominant, subvertical set
J3	47	2		229	Critically dipping joint set
J4	25	12		211	Uncommon joint

Permeability test background and design

Groundwater flow and governing equations

The flow of water in a saturated soil is often described using Darcy's law (Darcy 1856) where the water flow rate is proportional to the hydraulic gradient. Groundwater flow equilibrium is defined by

$$\nabla p_w = p_w \underline{g} + \underline{\varphi} = 0 \tag{1}$$

where $\underline{g} = (0, -g, 0)^T$ is the gravitational acceleration vector; $\underline{\varphi}$ is the friction force vector, per unit volume, between the flowing fluid and the soil skeleton; and p_w is the pore water pressure. The coefficient of permeability k_{sat} defined by

$$k_{sat} = p_w g \frac{\kappa}{\mu} \tag{2}$$

where κ is the intrinsic permeability of the porous medium and μ is the dynamic viscosity of the fluid. In an unsaturated state, the coefficient of permeability depends on the degree of saturation. The relative permeability k_{rel} is defined as the ratio of permeability at a given saturation k with respect to the permeability of the fully saturated state:

$$k = k_{rel} k_{sat} \tag{3}$$

Darcy's law, describing the fluid flow through a porous medium is defined as follows:

$$\underline{q} = \frac{k_{rel}}{p_w g} k_{sat} (\nabla p_w + p_w \underline{g}) \tag{4}$$

where $\underline{q}$ is specific discharge or fluid velocity. The above equation is a governing equation for single-phase fluid flow within an isotropic porous medium.

Given transient state analysis of groundwater flow, the hydraulic head can vary with respect to time. Neglecting the displacement of solid particles, the flow of groundwater can be considered with the following transient saturated/unsaturated groundwater flow model – a form of the Richards equation (Brinkgreve et al. 2010):

$$-n\left(\frac{S}{K_x} - \frac{\partial S}{\partial p_w}\right)\frac{\partial p_w}{\partial t} + \nabla^T \left[\frac{k_{rel}}{p_w g} \underline{k_{sat}} \left(\nabla p_w + p_w \underline{g}\right)\right] = 0 \tag{5}$$

where n is the ratio of the void volume with respect to the total volume, K_x is the horizontal permeability coefficient and S is the ratio of the free water with respect to the void volume, known as the degree of saturation.

Packer testing background

Packer testing is implemented by isolating bore sections between two expandable packers or between a solitary packer and the bottom of a bore. Seals are created by packer rubbers that are pressurized, with the rubber expanding against the borehole sidewalls. Packers are commonly inflated with a pressurized gas. Water is then injected into the section between the packers, and the water pressure decline during the test is measured over time.

Several factors are of particular importance to the test results: the presence of fractured material zones, the length of the packer testing region and interaction effects with the water table such as rivers and lakes. For the testing procedure to function properly, no leakage from the packers to the surrounding material is permitted. Furthermore, the bore must not be unsuitably flushed, and hydraulic fracturing must not be allowed to occur (Mollah and Sayed 1995). The data from the packer is then interpreted to determine the vertical flow variation for a set of depths of the surrounding borehole (Price et al. 1977).

A number of methods exist for the analysis of steady-state and transient water pressures. Doe and Geier sectioned the flow dimension into linear, cylindrical and spherical, conditioned by the shape of flow areas (Doe and Geier 1990). Leveinen devised a model for the fractional flow dimension with two composite zones, an inner zone of the section surrounding the well and an outer zone of the aquifer (Leveinen 2000). Permeability is determined for steady-state laminar flow in an isotropic, homogeneous material. Sections with insignificant fractures often reach a steady state within minutes. However, major fracture zones with lower permeability
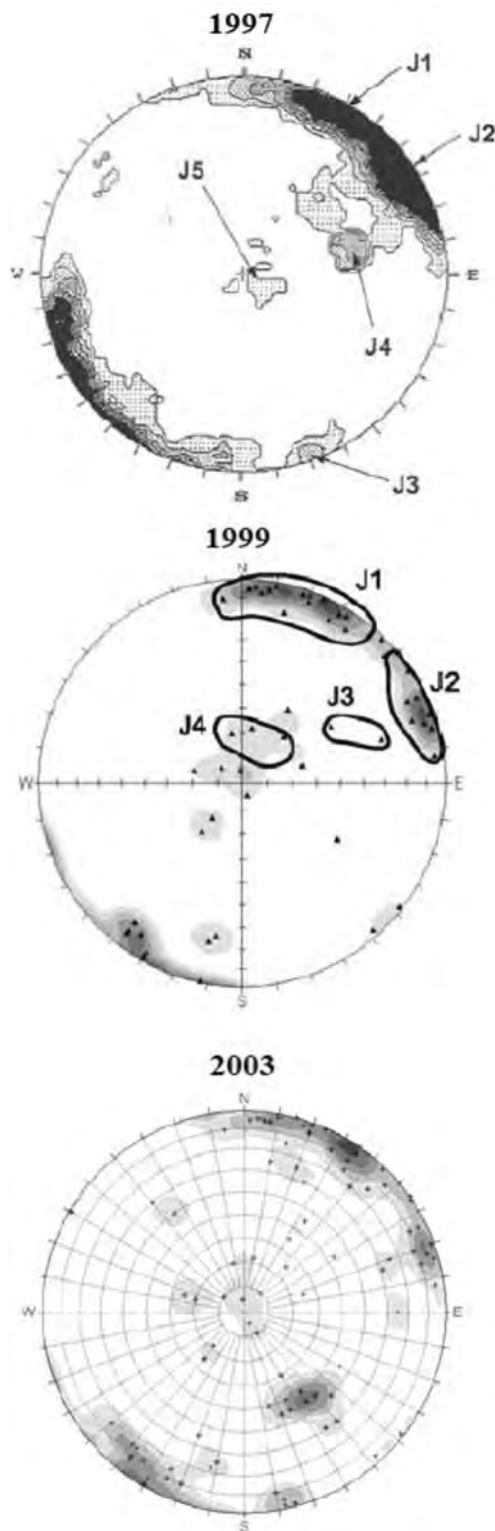
1997

1999

2003

Fig. 4 Contoured stereographic plots of Yallourn Joint Data from 1997, 1999 and 2003. Reproduced from State Government of Victoria 2008

values can take longer to reach equilibrium (Bliss and Rushton 1984). A common method for determining permeability is the Hvorslev equation, which considers inflow and outflow only through the borehole section between the packers (Hvorslev 1951):

$$k = \frac{Q}{2\pi L H_0} \ln\left[\frac{L}{2r_w} + \sqrt{1 + \left(\frac{L}{2r_w}\right)^2}\right] \tag{6}$$

where k is the hydraulic conductivity (L/t), Q is the flow rate (L^3/t), r_w is the bore radius (L), L is the length of the packer section (L) and H_0 is the water head introduced into the system. H_0 is determined by:

$$H_0 = H_w + H_p - H_L \tag{7}$$

where H_w (L) is the distance from the pressure monitor to the phreatic level, H_p (L) is the increase in pressure due to water injection and H_L (L) is the loss in pressure over the duration of the test. When an anisotropy between vertical and horizontal permeability occurs, Eq. (6) is adjusted to the form:

$$k = \frac{Q}{2\pi L H_0} \ln\left[\frac{mL}{2r_w} + \sqrt{1 + \left(\frac{L}{2r_w}\right)^2}\right] \tag{8}$$

where the ratio $m = \sqrt{\frac{K_r}{K_z}}$ describes the horizontal permeability K_r with respect to the vertical permeability K_z. Eq. (8) condenses to:

$$k = \frac{Q}{2\pi L H_0} \ln \frac{mL}{r_w} \tag{9}$$

when $mL > 20\ r_w$. As Eq. (6) is formulated based on the symmetric ellipsoidal flow around the packer region's axis, Moye's cylindrical symmetrical flow (Moye 1967) is commonly used:

$$K = \frac{Q}{2\pi L H_0}\left[1 + \ln\frac{L}{2r_w}\right] \tag{10}$$

While there are a number of closed-form equations to determine the permeability soil, the calculation of in situ permeability values in this research is determined through numerical simulation, based on the transient groundwater flow detailed in Eq. 5.

A schematic of the packer design for a PQ bore (122.6 mm diameter) is given in Fig. 6, indicating the gas line required to inflate the packers, the location and dimension of the packers and the location of pressure logger pockets. Thirty uniformly spaced holes (6 mm in diameter) are placed along the drill pipe to allow water seepage between the two packers.

Laboratory permeability testing procedure

In general, there are six different methods for measuring the hydraulic conductivity (coefficient of permeability) in the laboratory:
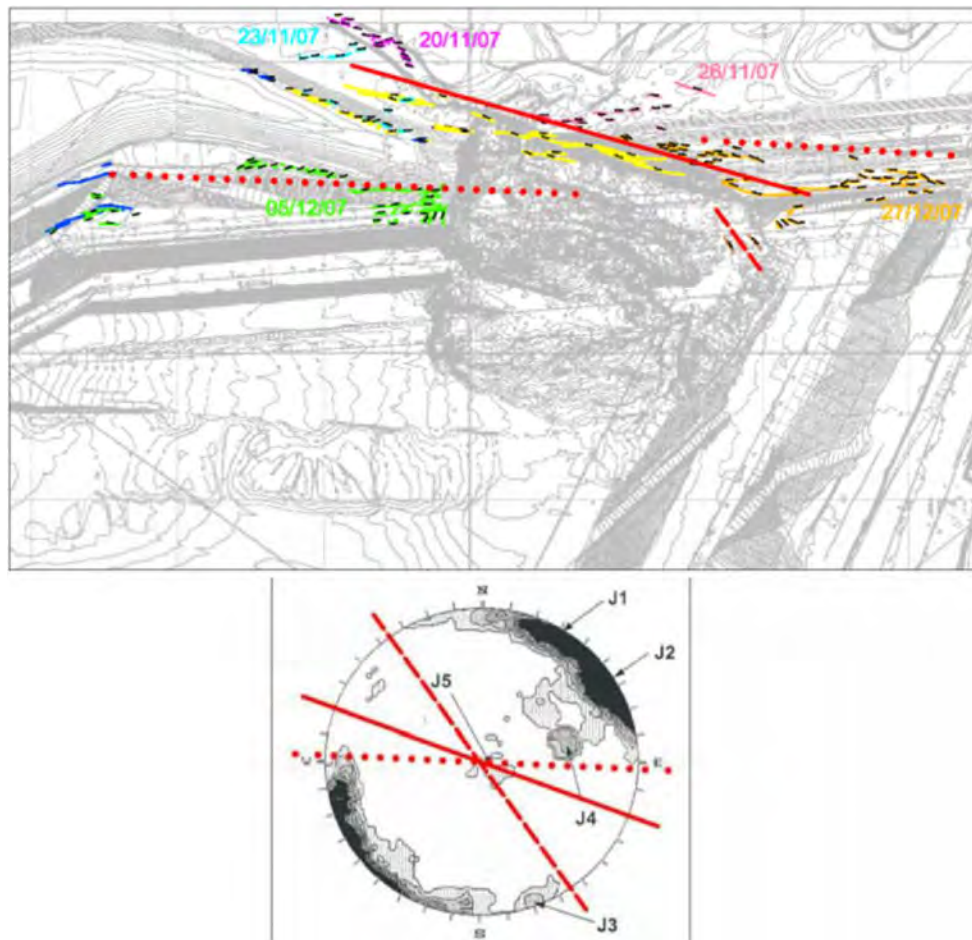
Fig. 5 Yallourn cracks mapped after 2007 failure. Colour coded with dates shown. Reproduced from State Government of Victoria 2008

(1) constant head, (2) falling head with constant tailwater elevation, (3) falling head with rising tailwater elevation, (4) constant rate of flow, (5) constant volume-constant head and (6) constant volume-falling head (ASTM D5084-16a 2010). In this study, in addition to the field tests, a series of constant head tests were conducted for determining the hydraulic conductivity of VBC. This test was conducted on 25 intact samples collected from Boreholes BH1 and BH2 at depths ranging from 30 m to 89 m below the ground surface (Fig. 9) laboratory conditions based on the standard code 243 ASTM D 5084 (ASTM D5084-16a 2010).

In the constant head test, water flows through a column of cylindrical material under the constant pressure difference, and the volume of flowing water through the column is measured in given time intervals (ASTM 2006). The concept of this test is based on Eq. 11.

$$k = \frac{QL}{A.\Delta h.\Delta t} \tag{11}$$

where k is coefficient of permeability, Q is the volume of discharged water, A is the cross-sectional area of the sample, Δh is the constant pressure difference across the sample

length and Δt is time interval of discharge.

The diameter of the samples was 50 mm with a ratio of the height to diameter equal to one. The surface of the samples was coated by a thin layer of latex to make the surface smoother, improving the contact with the membrane. Once the samples were placed in the permeameter cells, a confining pressure of 39.4 kPa was applied for 20 min to confirm that the membrane completely attached to the sample, with no space between for the flow of fluid. The constant head permeability test method was then conducted by applying a constant water pressure of 35.4 kPa (back pressure) at the bottom of the samples, while the pressure at the top of the samples, where the flow rate is measured, was zero. The volume of water exiting the sample was regularly measured until the flow rate reached a steady state (Figs. 7, 8).

Field testing regime

Two borehole locations at the crest of the Yallourn north-east batter were selected as packer test sites (BH1 and BH2) at a distance of 360 m apart (Fig. 9).
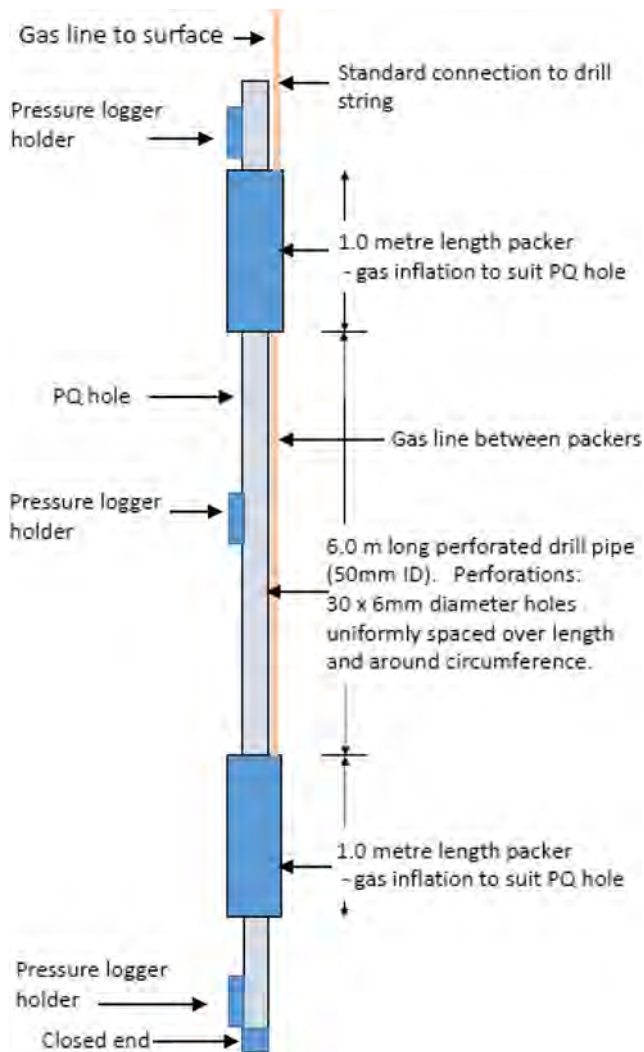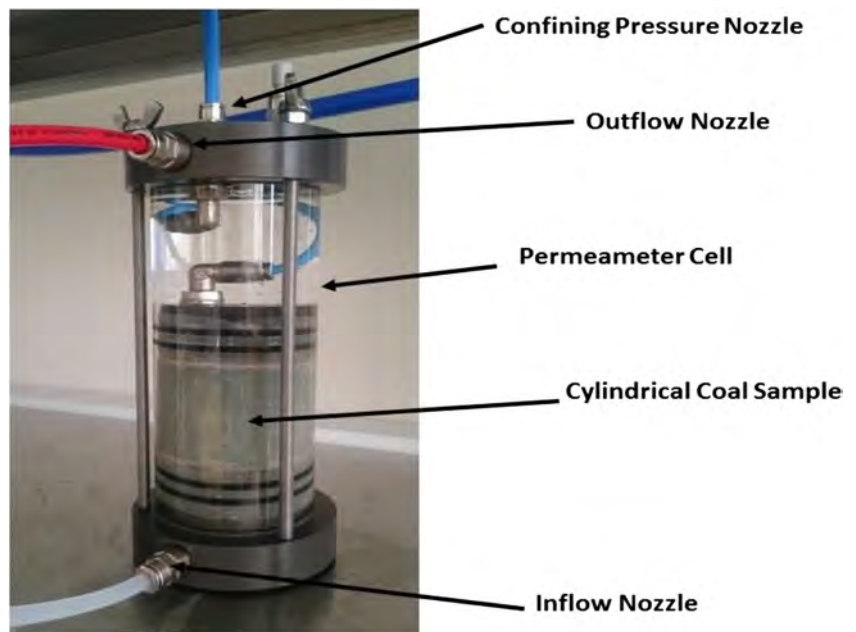
Fig. 6 Packer array schematic

Fig. 7 Equipped constant head permeability cell

Both 200 mm diameter bores were drilled to a depth of 150 m below the ground level (BGL). Material samples were extracted throughout the drilling process for lithological logging and further laboratory testing. Thereafter, borehole geophysical examination provided additional details of the bore structure by gamma and density profile analysis. Interval depths between 55 and 80 m bgl were selected for packer array coal permeability testing due to the extended continuous coal seam found at this declination (Fig. 10). A testing regime was then created, allowing the whole packer array to be elevated in 3-m intervals followed by 3-m downward displacements of the packer array, again in 3-m steps, however creating intervals that are overlapping the initial test intervals by 1.5-m increments. Packer depths, given as the depth of the base of the packer below ground level, are given in Table 3. The measurement of overlap intervals in the downward direction after the initial elevated intervals provides added resolution to the vertical spatial permeability analysis, without interaction effects due to the saturation of overlapping intervals. A thin gravel layer was detected in BH1 at a depth of approximately 65 m BGL; thus testing intervals were selected to exclude the thin gravel band. A total of 7 intervals were selected for each of the BH1 and BH2 bores.

At each packer array testing depth, the following procedure was implemented:

1. Pressure transducers activated with 10-s interval recording and placed within the packer array transducer pouches. Initial air pressures set to zero kPa.

Fig. 8 Constant head permeability apparatus
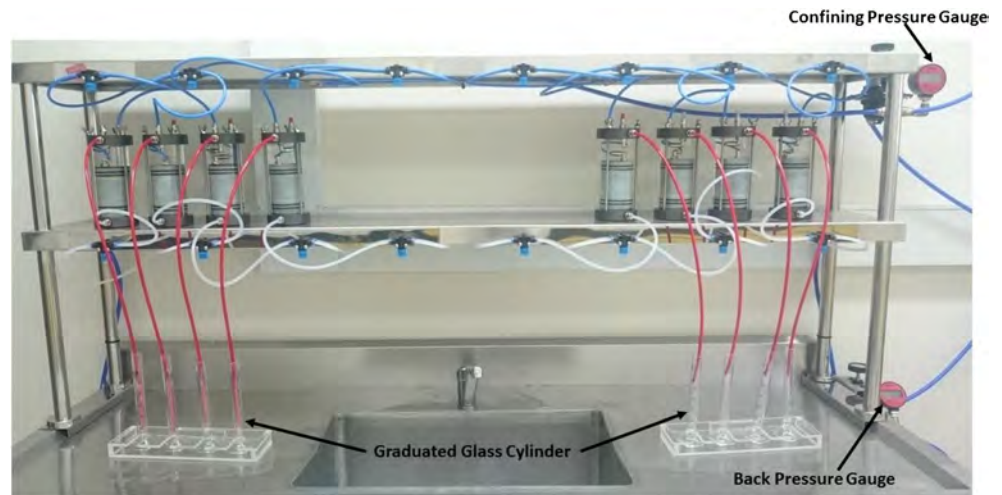
2. A computer configured to monitor the pressures at the middle of the packer array using the vibrating wire pressure transducer.
3. The bottom end cap of packer array closed so water could not flow into the drill string from below the packers.
4. Packer array installed to the initial testing depth (77.6 m and 79 m for BH1 and BH2, respectively).
5. Pressure monitored for 5 min and recorded using the vibrating wire pressure transducer.
6. Packers are inflated to 1100 kPa.
7. Pressure monitored using the vibrating wire pressure transducer until the pressure stabilizes.
8. Sixty litres of water added to raise the water level 30 m within the drill string.
9. The decline of the pressure curve monitored for 30 min.
10. Packers deflated.
11. The packer array shifted to the next testing depth.
12. Steps (5)–(11) repeated for all testing depths.
13. Data downloaded from the pressure transducer data loggers to the computer.

Numerical simulation of field permeability results

Numerical groundwater flow models created in the *Plaxis 2D* axisymmetric FEM software package were deemed suitable due to the rotational symmetry of the packer and bore conditions observed in the field. The objective of these simulations was the generation of pressure-time series curves obtained from the hydraulic packer pressure transducers by providing a permeability value for the VBC material surrounding the bore. When the numerical and field pressure curves match, the permeability of the field tests is assumed to be equal to the numerical permeability result.

Finite element method (FEM) simulations were developed to model a drill string 0.025 m in radius within a bore 0.1 m in diameter, atop a packer 6 m in length and 0.1 m in radius (Fig. 11). The division between the drill string and bore wall above the packer was modelled using a nonporous barrier, allowing no water to flow through the bore wall above the packer array. Interface elements were placed at the top and bottom of the packers, initially closed to fluid flow across the boundaries, allowing no water to flow from the drill string
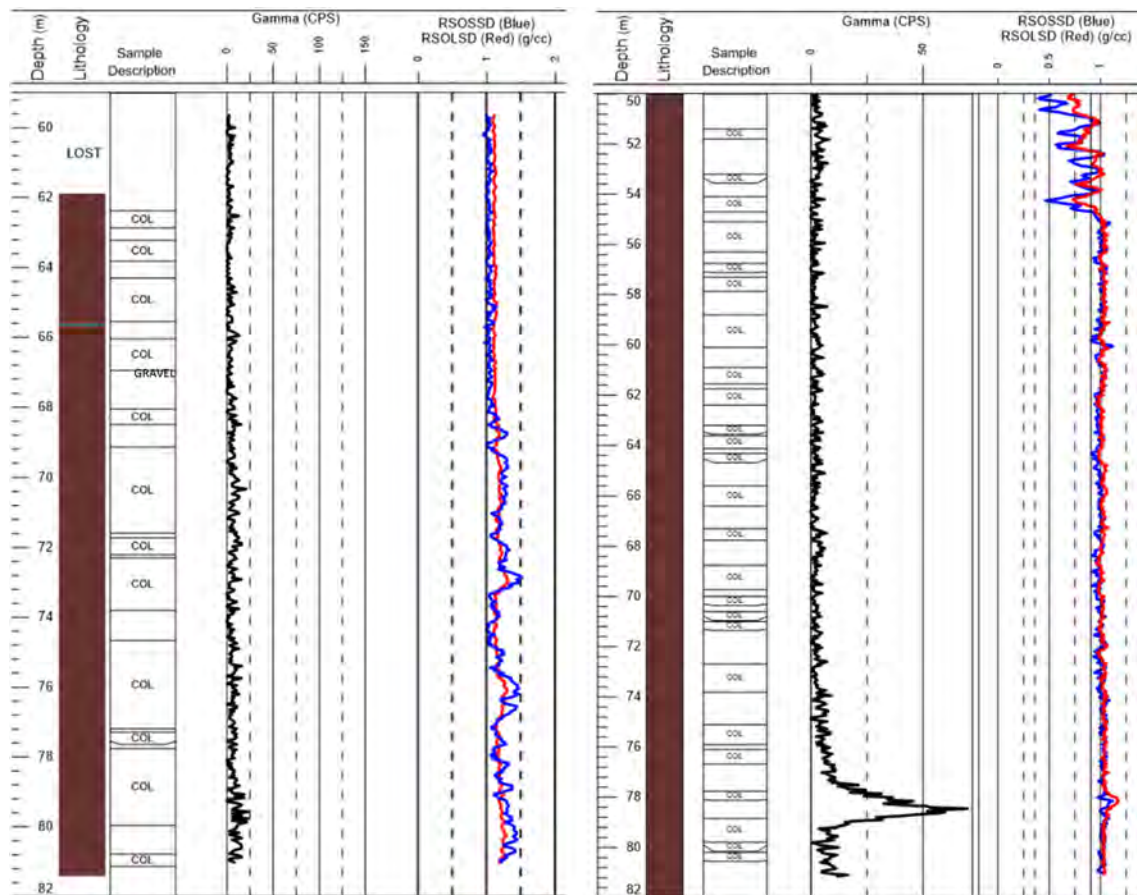
Fig. 9 Borehole locations

Fig. 10 BH1/BH2 lithological and geophysical properties

to the packer and from the packer to the coal. Interface elements in Plaxis are used to simulate impermeable internal structural elements, with zero Darcy flux over internal boundaries. The global phreatic level was set to 52 m below ground level, as observed in-field testing. Modelling consisted of two stages (an initial steady-state phase, followed by a transient groundwater flow phase). In the initial equilibrium stage, the bore contained no added water head. In the following transient stage, a water head (with a volume of approximately 0.06m^3) is applied to the system, and the interface boundaries are

Table 3   Packer array test regime

Packer test order	BH1 packer depth (m)	BH2 packer depth (m)
1	77.6	79
2	74.6	76
3	71.6	73
4	68.6	70
5	70.6	71.5
6	73.6	74.5
7	76.6	77.5

opened, allowing water to flow freely. These boundaries remain open for 30 min, in accordance with the field test regime. As the objective of this analysis is the determination of permeability values, the Plaxis flow-only calculations were performed, rather than fully coupled flow and deformation analysis. The dimensions of the FEM model geometry are determined by the parameter R (the ratio of the coal thickness to the 0.1 m packer radius) as shown in Fig. 11. Furthermore, the length of the drill string D was dependent on the boundary sensitivity analysis conducted in Section 3.4.1 to determine the minimum required dimensions of the coal geometry in relation to the packer array.

The drill string permeability was assigned an arbitrarily large value of 100 m/min to ensure water immediately flows from the drill string to the packer array during the transient analysis phase. Time series pressures were then observed at a location of 2.6 m above the bottom packer, selected to simulate the middle packer pressure curve location and then compared with the middle packer pressure transducer results. To ensure FEM mesh quality was sufficient to allow for the narrow geometry of the packer drill string with respect to the remaining model, a fine mesh consisting of 5998 15-noded elements was generated.
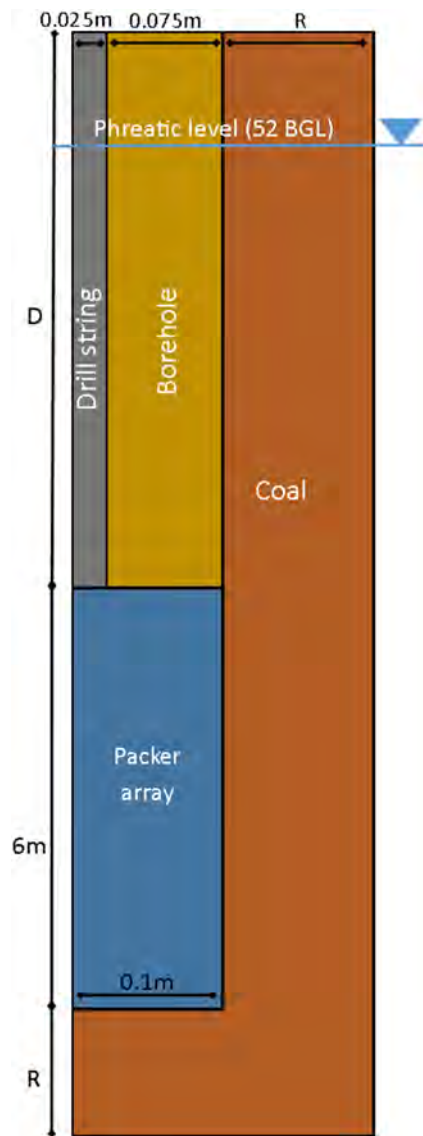
Fig. 11 Model geometry

Boundary sensitivity analysis

As a result of the repeated numerical simulations at a range of testing depths, a boundary sensitivity analysis was conducted to minimize unnecessary calculation due to superfluous geometry dimensions. Initially, the model was tested with the conditions of the BH2 bore at a depth of 79 m BGL, with the model boundaries located 200 m away from the packer array (defined as the parameter length R), deemed sufficiently far from the packer array to prevent unwanted boundary effects. The permeability was then adjusted until the pressure curves obtained numerical analysis aligned with field results. The boundary distance from the packer (R) was thereafter dramatically reduced, and the absolute pressure difference after 30 min (P_{30}) was determined.

Effects of hydraulic head discharge on the testing regime

As the procedure of repetitive water discharge into the bore and surrounding material may have a significant effect to the water table and saturation of the VBC, a set of four consecutive packer tests were conducted in the field at a depth of 79 m BGL in bore BH2. These results were then compared against the numerical modelling results where the permeability and water table were kept constant for all four packer experiments to test the assumption that continued packer testing with half-hour intervals does not drastically affect the phreatic line depth.

Results

Laboratory results and prior in situ test results

The values of permeability of 9 laboratory tested core samples from BH1 are presented in Table 4, with 16 samples from BH2 presented in Table 5. The values range from 6×10^{-11} m/s to 3×10^{-9} m/s with an average of 1.3×10^{-9} m/s. Although the changes in permeability are high, with the

Table 4   Constant head permeability test results for 9 brown coal samples of BH1

Sample number	Density (g/cm³)	Diameter (mm)	Height (mm)	Permeability (m/s)
1	1.10	51.1	55.7	3×10^{-10}
2	1.07	49.6	62.6	3×10^{-9}
3	1.07	50.9	72.1	4×10^{-10}
4	1.03	50.5	58.2	2×10^{-10}
5	1.10	50.7	51.7	1×10^{-10}
6	1.08	50.9	52.5	2×10^{-10}
7	1.07	50.5	55.5	9×10^{-10}
8	1.08	50.9	62.6	1×10^{-10}
9	1.10	50.3	55.7	9×10^{-11}

Table 5 Constant head permeability test results for 16 brown coal samples of BH2

Sample number	Density (g/cm^3)	Diameter (mm)	Height (mm)	Permeability (m/s)
1	1.11	49.2	50.6	3×10^{-9}
2	1.12	49.3	54	3×10^{-9}
3	1.11	49.4	54.8	4×10^{-9}
4	1.12	46.9	50	9×10^{-10}
5	1.1	49.7	50.4	1×10^{-10}
6	1.11	49.6	50.4	9×10^{-11}
7	1.1	49.5	51.2	2×10^{-9}
8	1.1	49.6	51.9	1×10^{-9}
9	1.1	49.7	50.5	9×10^{-10}
10	1.08	49.8	49.5	2×10^{-10}
11	1.12	49.6	50.8	7×10^{-11}
12	1.12	49.6	49.7	6×10^{-11}
13	1.10	63.8	70.9	5×10^{-10}
14	1.11	63.8	60.9	5×10^{-10}
15	1.08	50.1	51.3	2×10^{-10}
16	1.09	50.7	49.6	2×10^{-10}

standard deviation permeability three times the mean, the values themselves are very low, suggesting that intact VBC is quite impermeable.

Tables 6 and 7 detail the comparison of permeabilities determined through laboratory testing and from historical surveys, respectively. The reported laboratory results from previous SECV tests (Table 7) are observed to be within the range of permeabilities of laboratory results from bores BH1 and BH2 (Table 6). The prior SECV results from constant head permeability in situ borehole tests within the field are several orders of magnitude higher than the permeability values observed within the laboratory.

Packer array test results

Figures 12 and 13 show the results of packer test pressures from bores BH1 and BH2, respectively. Three sets of pressure profiles are shown from pressure transducers located at the top, middle and bottom of the packer array. From the bottom packer curve of BH2 testing depths of 70 m and 71.5 m, it is noted that the base packer seal did not make full contact with the bore wall, meaning the pressures observed below the

packer equalized with the testing region of interest. For this reason, the results from these two tests are considered with caution. In both Figs. 9 and 10, a set of jagged steps can be observed in pressures at the commencement and conclusion of the test regime, due to the insertion/removal of drilling rods attached to the packer array. As the addition or removal of a drilling rod takes several minutes to attach or detach, the pressure curves for each logger exhibit behaviour similar to a step function. This behaviour is evident during the initial insertion of the packer array and after the completion of the final test when the packer array is removed from the bore. Due to the length of available drilling rods (3 m in length), packer tests were initially conducted with an upward traversal of the bore at 3 m increments, followed by a downward traversal of the 1.5 m gaps in the initial upward traversal. Although this procedure produced results that are not ordered based on depth, the decision was based on the logistics of the drilling rig, coupled with further time constraints. An upward spike in pressures can be observed at 2:30 h, in Fig. 12, between tests at 77.6 m and 74.6 m. At this time, an aborted test commenced, however, is not considered in this research, due to the test not meeting the constraints of the test procedure. At the BH2 test depth of 76 m (Fig. 13), an initial decrease in pressure is observed, prior to the peak pressure. This property

Table 6 Laboratory permeability K (m/s) summary

	BH1	BH2
Number of core samples	9	16
Minimum	9×10^{-11}	9×10^{-11}
Maximum	3×10^{-9}	4×10^{-9}
Mean	6×10^{-10}	8×10^{-10}
Standard deviation	9×10^{-10}	1×10^{-9}

Table 7 Prior SECV Yallourn coal seam permeability results (Crouch and Esposito 1982)

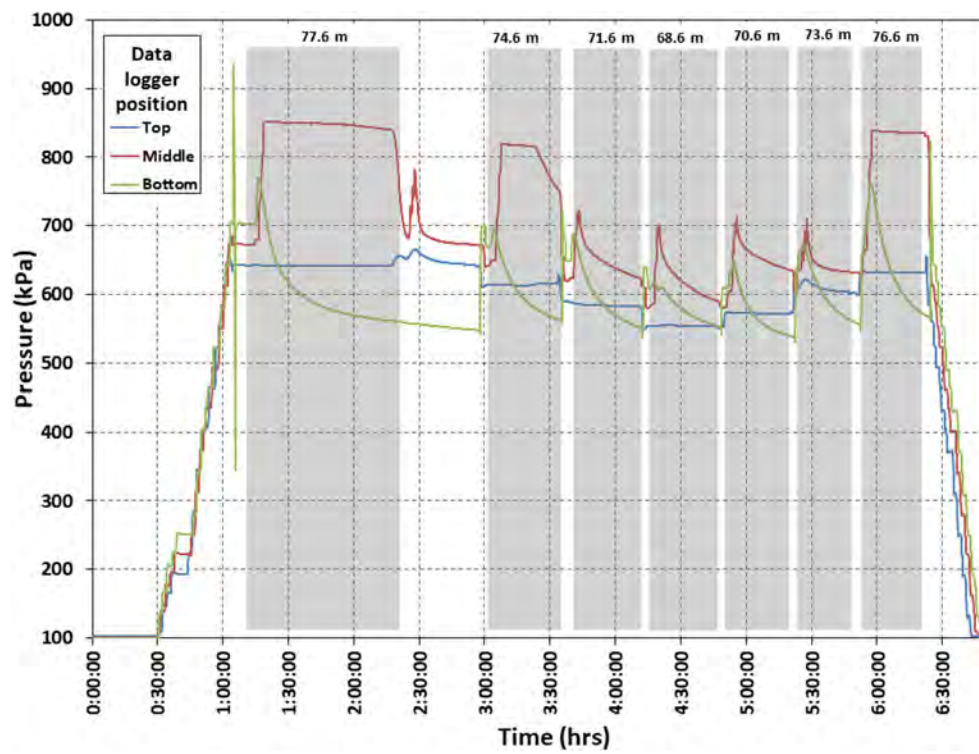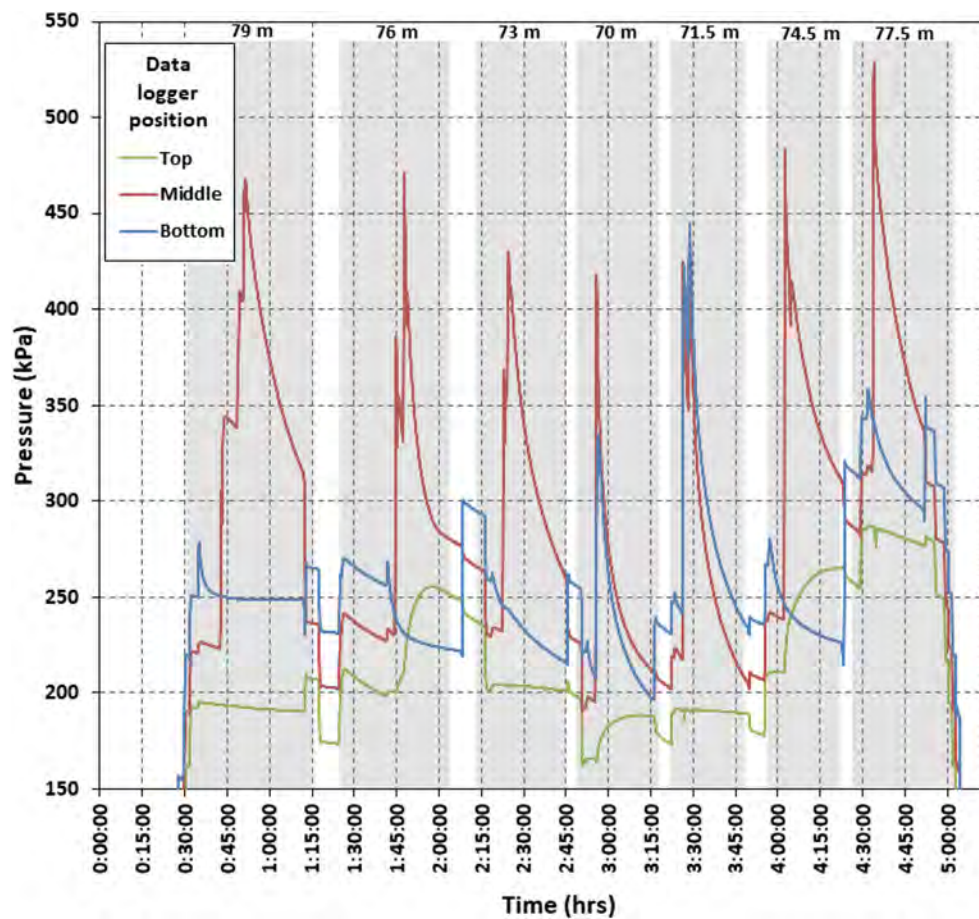| SECV testing procedure	K (m/s)	K (m/s)
Constant head	7×10^{-7}	7×10^{-7}
Laboratory permeameter	8×10^{-9}	8×10^{-9}

Fig. 12 BH1 pressure curves
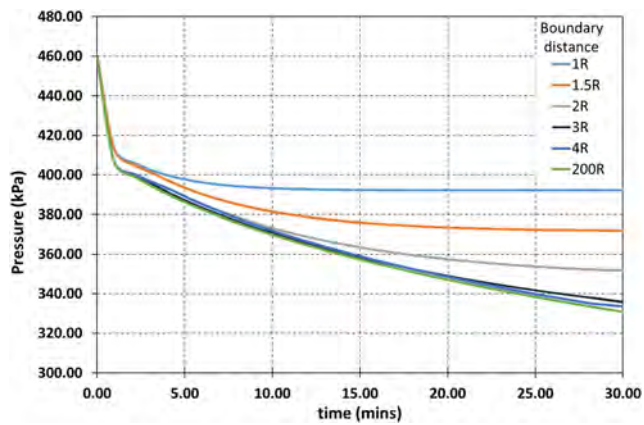

Fig. 13 BH2 pressure curves

Fig. 14 Variation of pressure curves for coal geometry parameter (R) values
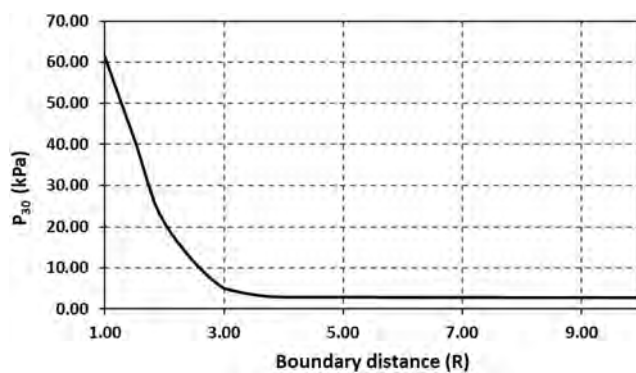

Fig. 15 P_{30} boundary effect

is most likely due to a pocket of pressurized air created during the test. Although the flow of water into the packer was limited to reduce the formation of air pockets, it is suggested that a minor pocket of pressurized air was formed during the commencement of this test.

Boundary sensitivity analysis results

Due to issues related to the flush drilling process, results from bore BH1 were deemed ineffective for this research. Hence, results solely from BH2 are considered herein.

The parameter R (m), defining the distance of the model boundaries from the packer array, was initially set to 200 m and then reduced to 4, 3, 2, 1.5 and 1 for the modelling of BH2 at a packer array depth of 79 m. A geometry parameter of R = 3 or greater produces a sufficient model size to disregard the effects of boundary conditions on the region surrounding the packer (Fig. 14). The parameter P_{30} indicates the difference in pressure (in kPa) after 30 min, for R dimensions with respect to R = 200. Figure 14 indicates P_{30} drops below a 5 kPa difference with R = 200 after the 30-min interval when the R parameter exceeds 3. With this in mind, geometry dimensions for further numerical simulations were set to R = 4, equivalent to 0.4 m. The resulting permeability of 3.33×10^{-7} m/s was calculated for the 79 m packer depth. Figure 15 highlights the groundwater flow with dimension R = 1, once the hydraulic packers are released, and water is permitted to flow from the drill string to the packer array and the surrounding coal (Fig. 16).
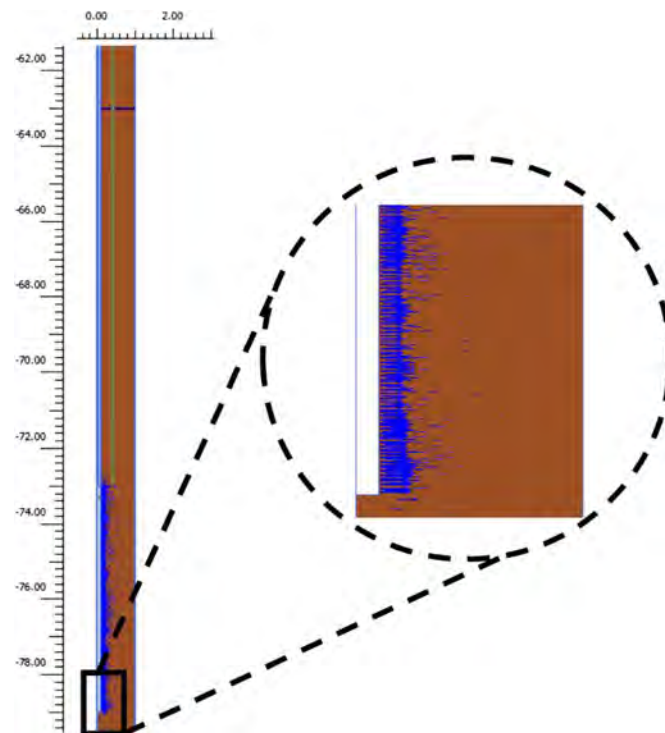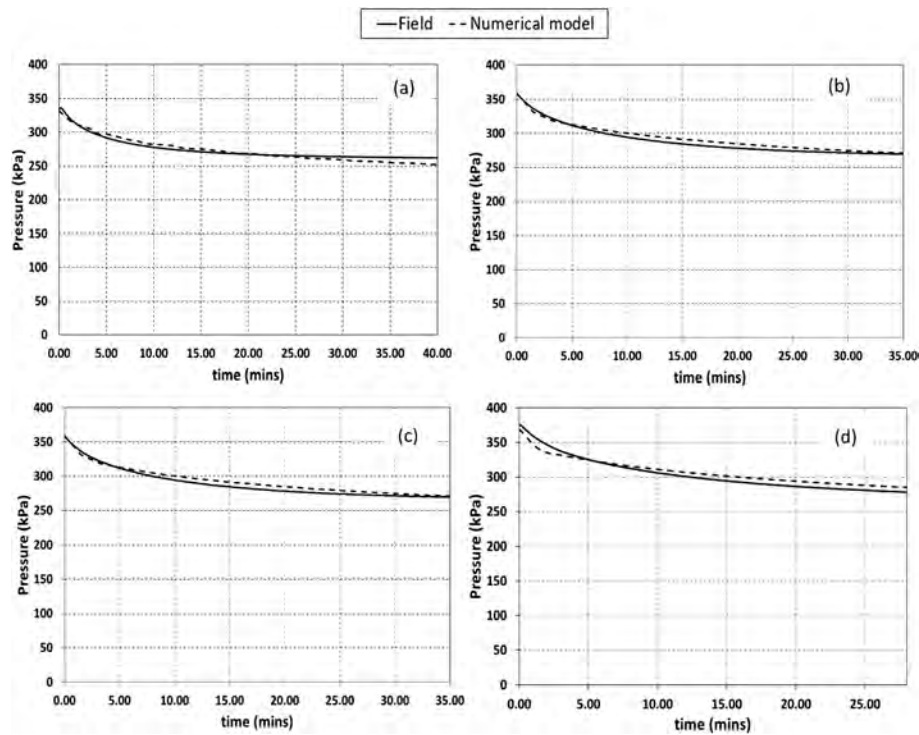

Fig. 16 Numerical model of groundwater flow

Fig. 17 (a)–(d) Pressure curves for repeated numerical/field tests at 79 m BGL

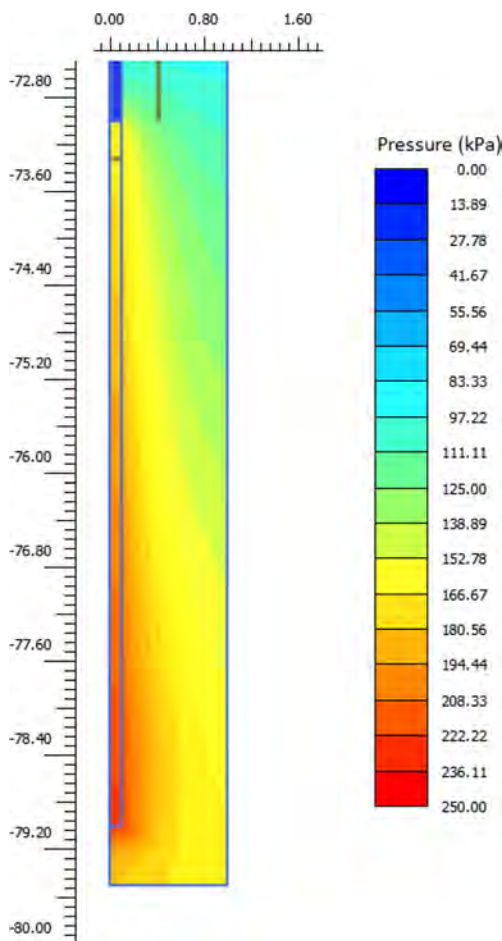
Fig. 18 Packer active pore water pressures after 30 mins discharge

Results of hydraulic head discharge effects on testing regime

Four repeated hydraulic packer tests were conducted for BH2 at a depth of 79 m BGL. Numerical simulations with the final model geometry of Section 4.3 were implemented to model the repeated tests with a constant permeability of 3.33×10^{-7} m/s. Figure 17 shows comparative results between field data and numerical simulation pressures for each of the four replicates, indicating that individual tests are not considerably affected by the repeated hydraulic head discharge. Furthermore, it is noted that all pressures have stabilized after the 30-min interval, suggesting the field testing interval is ample time to observe the characteristics of the pressure curves. Figure 18 illustrates the active pore water pressures surrounding the packer at the conclusion of the 30-min interval.

Comparison of field and laboratory permeabilities

Numerical simulation of BH2 packer tests produced comparable pressure curves to those observed in field experiments (Fig. 19). Fluctuations in the field results of Fig. 19 (b) and (f) observed between the 1–2 min mark are believed to have occurred in the presence of pressurized air pockets caused by the rapid influx of water into the drill string, generating water discharges back up the drill string to the surface. During testing, water was observed erupting from the drill string at the corresponding time intervals. For all depth intervals after a
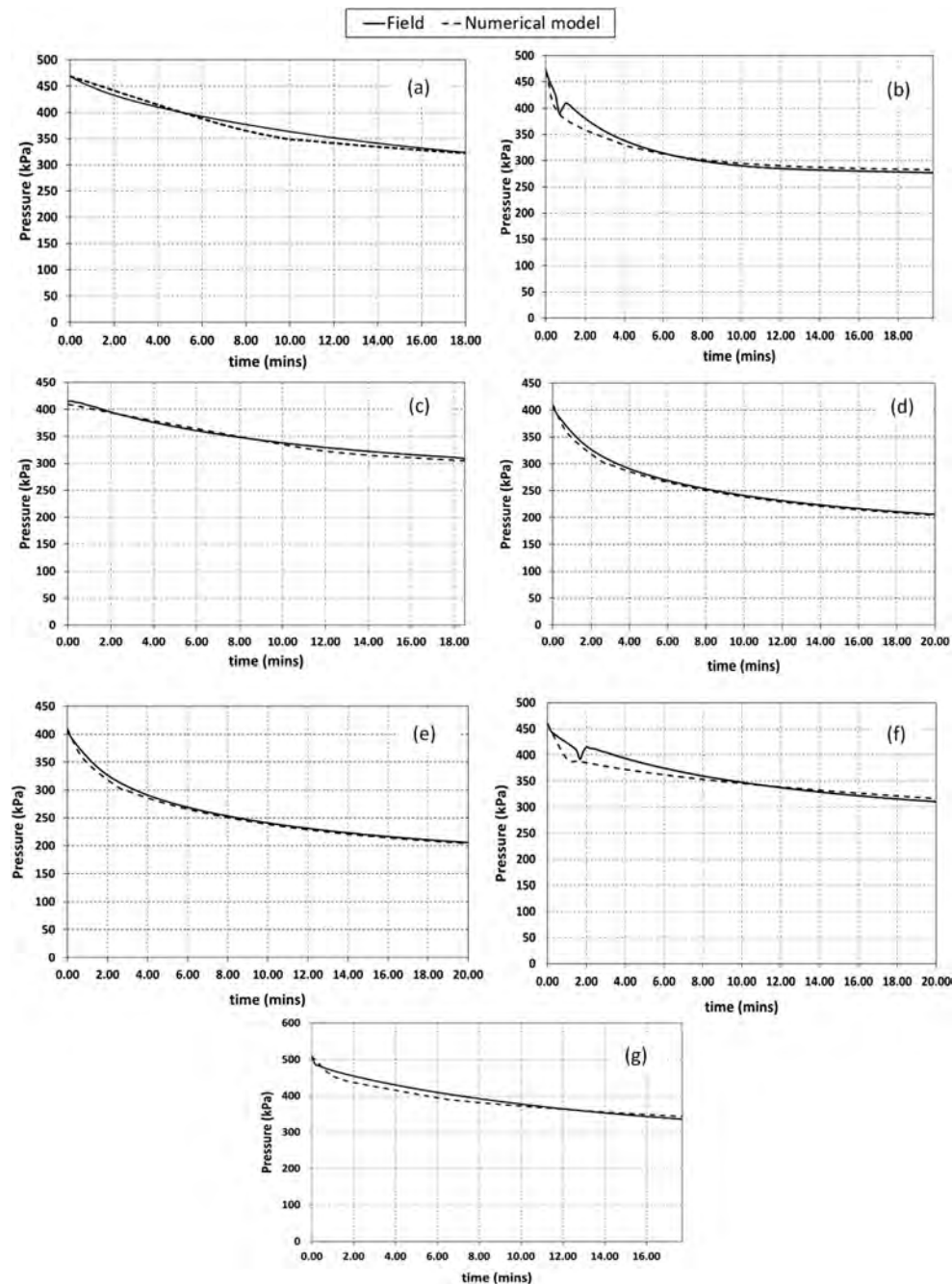
Fig. 19 BH2 pressure curves. (**a**) 79 m, (**b**) 76 m, (**c**) 73 m, (**d**) 70 m, (**e**) 71.5 m, (**f**) 74.5 m, (**g**) 77.5 m

period of 20 min, each of the pressures approached equilibrium. Table 8 details permeabilities ranging from 1.633×10^{-7} to 2×10^{-7} m/s, with the largest permeabilities (77.5 and 79 m) occurring at the coincident location of an artefact observed within the gamma log of Fig. 10, suggesting a change in the material at this depth, potentially due to fracture. Permeability values were not back-calculated from BH1, due to the aforementioned flush drilling complications. As such, permeability values from BH1 are not detailed in Table 8, as their results are deemed as erroneous as a result of issues in the drilling process. The permeabilities obtained from field testing
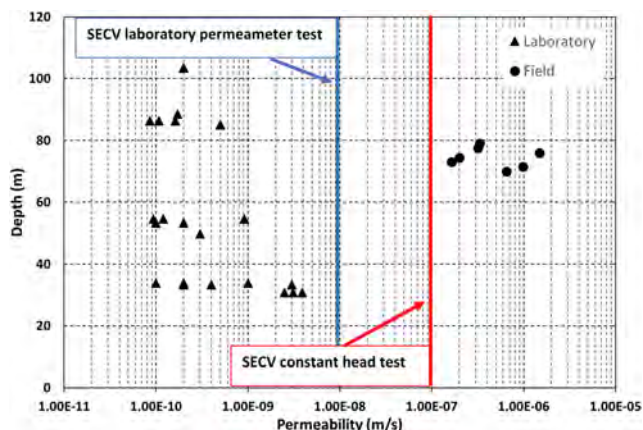
are orders of magnitude greater than those determined from laboratory tests (Tables 4, 5 and Fig. 20), while the results of numerical modelling were in agreeance with analytical results calculated by Eq. (5). The in situ field results back-calculated with the aforementioned numerical analyses produced slightly higher permeability values than the in situ constant head tests previously conducted by the SECV. Conversely, laboratory tests of BH1 and BH2 samples produced lower permeability values compared to SECV laboratory permeameter tests of Victorian brown coal. A distinct difference in laboratory vs in situ results is evident, with a sizeable variation of in situ

Table 8 BH2 packer test permeabilities

Depth (m)	Permeability (m/s)
70.0	6.500×10^{-7}
71.5	1.000×10^{-6}
73.0	1.633×10^{-7}
74.5	2.000×10^{-7}
76.0	1.450×10^{-6}
77.5	3.167×10^{-7}
79.0	3.330×10^{-7}

parameters of particular note, ranging from 1×10^{-10} to 1×10^{-8}. When considering the full range of values for all tests, considerable variation of permeability values is observed (1×10^{-10} to 5.9×10^{-5}). Given the significant dispersion within observed permeability parameters, selection of appropriate values is vital to the modelling the behaviour of Victorian brown coal.

As the field tests were conducted over an interval of 6 m compared to 4 to 7 cm of idealized samples in the laboratory, it is suggested that water dissipates through highly permeable fractured VBC zones in field-scale sized tests, providing substantially higher permeability values. Vertical brown coal joints spanning tens of metres are known to occur within the batters of the Yallourn open pit mine (Tolooiyan et al. 2019), as well as many smaller desiccation cracks. Core sampling of bore BH2 (Fig. 21) indicates considerable variability in structure, from intact regions containing minimal visible cracks to fully fractured regions. Although the tensile strength of VBC has been considered in a number of studies (Dyson et al. 2018; Tang et al. 2017; Tolooiyan et al. 2014), VBC horizontal fracture characteristics over large length scales remain an area of active research. From the results of Fig. 20 and Table 8, no spatial trends are observed. However, it is believed that further packer testing over a greater range of depths is necessary to strengthen this belief. Numerous studies have demonstrated that permeability distributions within homogeneous media
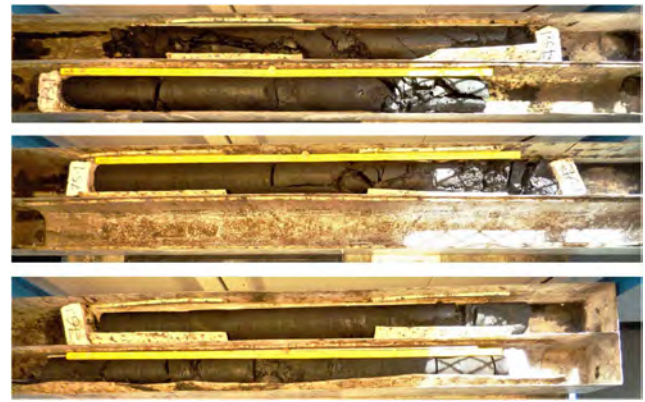
Fig. 21 Coal core samples from 70 to 80 m BGL

obey log-normal trends (Dagan 1979, 1981, 1982; Freeze 1975). Initial results from packer testing suggest that log-normal distributions apply to VBC permeabilities. A log-normal pdf for the permeabilities of bore BH2 is given in Fig. 21, with parameters mean $\mu = -10.537$ and standard deviation $\sigma = 0.821$.

Discussion and conclusion

The permeability values presented in this research have highlighted large variation in laboratory, field-scale and analytically determined values. Although laboratory-based permeability tests are the most common and cost-effective method of hydraulic conductivity testing, it is important to consider the potential effects of in situ material attributes such as fractures that may be neglected in small-scale intact samples within the laboratory environment. Results from prior SECV permeability tests provided field results of comparable scales to those determined from back analysis of in situ Lugeon testing. Similarly, SECV constant head results were of similar (however slightly higher) magnitudes to laboratory test results from boreholes BH1 and BH2. The results of packer testing within this study, coupled with historical field test results of Victorian brown coal suggest that laboratory scale samples may be below the representative elementary volume required to model

Fig. 20 Comparison of field and laboratory permeabilities
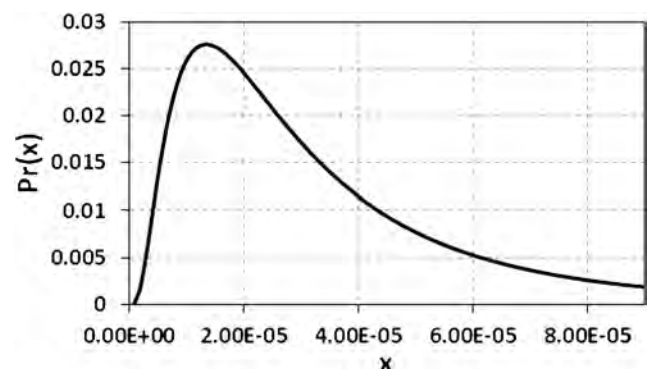
Fig. 22 Log-normal probability density function of bore BH2 results

the effects of large-scale permeability modelling. Numerical results from repeated water injection packer simulations confirm that the presence of additional water from previous tests has negligible effects on further testing regimes, suggesting closed-form analytical solutions are applicable in this setting. Although further packer tests at additional depths are necessary to refine VBC permeability spatial distributions, a log-normal probability density function displaying the range of expected permeabilities is presented (Fig. 22). As the permeability of VBC is a vital component to assess the stability of the open-cut mines of the Latrobe Valley, accurate parameters can be crucial to ongoing geotechnical assessment. Factors related to the length scale of permeability testing, coupled with a variety of analytical and numerical methods, provide additional information for applications requiring accurate permeability parameters.

References

ASTM Standard D2434-68 (2006) Specification for Concrete Aggregates. American Society for Testing and Materials, ASTM International, West Conshohocken, PA, 2003, https://doi.org/10.1520/D2434-68R06. www.astm.org

ASTM D5084-16a (2010) A., Standard test methods for measurement of hydrau618 lic conductivity of saturated porous materials using a flexible wall 619 permeameter. ASTM International, West Conshohocken, PA

ASTM STANDARD D388–12 (2012) Standard Classification of Coals by Rank. American Society for Testing and Materials, ASTM International, West Conshohocken, PA, 2003, https://doi.org/10.1520/D0388-12. www.astm.org

Barton C, Gloe C, Holdgate G (1993) Latrobe Valley, Victoria, Australia: a world class brown coal deposit. Int J Coal Geol 23:193–213

Becker D (2001) Site Characterization. In: Rowe K (ed) Geotechnical and Geoenvironmental Engineering Handbook. Springer, Boston, pp 69–105. https://doi.org/10.1007/978-1-4615-1729-0_4

Becker DE, Eng P, Principal F, Engineer SG (2010) Testing in geotechnical design. Geotech Eng 41:17

Bliss JC, Rushton K (1984) The reliability of packer tests for estimating the hydraulic conductivity of aquifers. Q J Eng Geol Hydrogeol 17: 81–91

Brinkgreve R, Swolfs W, Engin E, Waterman D, Chesaru A, Bonnier P, Galavi V (2010) PLAXIS 2D User Manual. CRC Press I, PLAXIS BV, Delft, Netherlands ISBN: 978-90-76016-10-8

Crouch B, Esposito I 1982 Yallourn open cut east field project diversion of the Morwell River geotechnical investigation report no. ID5, SECV, Research and Development

Dagan G (1979) Models of groundwater flow in statistically homogeneous porous formations. Water Resour Res 15:47–63

Dagan G (1981) Analysis of flow through heterogeneous random aquifers by the method of embedding matrix: 1. Steady flow. Water Resour Res 17:107–121

Dagan G (1982) Analysis of flow through heterogeneous random aquifers: 2. Unsteady flow in confined formations. Water Resour Res 18: 1571–1585

Darcy H (1856) Les Fontaines Publiques de la Ville de Dijon (The Public Fountains of the City of Dijon). Victor Dalmont, Paris, France, 647 pp

Doe TW, Geier JE (1990) Interpretation of fracture system geometry using well test data. Swedish Nuclear Fuel and Waste Management Company (Report ID: STRIPA-TR–91-03), Stockholm, Sweden, 241pp

Dyson AP, Tang Z, Tolooiyan A (2018) Use of stochastic XFEM in the investigation of heterogeneity effects on the tensile strength of intermediate geotechnical materials. Finite Elem Anal Des 145:1–9

Energy Australia 2018 Yallourn Power Station | EnergyAustralia, https://www.energyaustralia.com.au/about-us/energy-generation/yallourn-power-station. Accessed 20 Jan

Freeze RA (1975) A stochastic-conceptual analysis of one-dimensional groundwater flow in nonuniform homogeneous media. Water Resour Res 11:725–741

Geo Eng (1996) Eastfield Geotechnical Assessment (Geotechnical report ID: 1150/5089/01, November 1996)

Geo Eng (1997) Yallourn Eastfield Coal Face Mapping and Operating Face Stability (Geotechnical report ID: 1150/5032/1, March 1997)

Hamm S-Y, Kim M, Cheong J-Y, Kim J-Y, Son M, Kim T-W (2007) Relationship between hydraulic conductivity and fracture properties estimated from packer tests and borehole data in a fractured granite. Eng Geol 92:73–87

Holdgate GR, Smith TAG, Gallagher SJ, Wallace MW (2001) Geology of coal bearing Palaeogene sediments, onshore Torquay Basin. Victoria Australian Journal of Earth Sciences 48(5):657–679. https://doi.org/10.1046/j.1440-0952.2001.485888.x

Hvorslev MJ (1951) Time lag and soil permeability in ground-water observations, Waterways Experiment Station, Corps of Engineers. US Army. Bulletin 36:49

Leveinen J (2000) Composite model with fractional flow dimensions for well test analysis in fractured rocks. J Hydrol 234:116–141

Levy BS, Pannell LJ, Dadoly JP (1993) A pressure-packer system for conducting rising head tests in water table wells. J Hydrol 148:189–202

Lugeon M (1933) Barrages et géologie: méthodes de recherches, terrassement et imperméabilisation. libr. de l'Université, Lausanne, Rouge, France

Moein F, Xue, J, Dent B, Mackay R (2016) Review of the historical data characterizing Latrobe Valley brown coal consolidation behaviour. Geological Society, London, Engineering Geology Special Publications 27(1) 217-226

Mollah MA, Sayed SA (1995) Assessment of in situ permeability with emphasis on packer testing in Kuwait. Eng Geol 39:217–231

Moye D (1967) Diamond drilling for foundation exploration. Inst Engrs Civil Eng Trans, Australia

Price M, Robertson A, Foster S (1977) Chalk permeability-study of vertical variation using water injection tests and borehole logging. 81: Water services, 603

Rosengren KJ (1963) Consolidation of some Victorian brown coals. In Proceedings of the Australasian Institute of Mining and Metallurgy 208 157-193

Sahimi M, Pop M (1996) Flow and transport in porous media and fractured rock. Z Angew Math Mech 76:230–230

Soliman A, Wood B, Hibberd D (2007) Victoria Flac modelling: Morwell River diversion channel-southern batters buffer width. Aust Geomech 42

State Electricity Commission of Victoria (1983) Yallourn north open cut seepage study report (Geotechnical report ID: SO/82/50). State

Electricity Commission of Victoria, Research and Development: SECV

State Government of Victoria (2008) Mining Warden Yallourn mine batter failure inquiry. Parliamentary paper (Victoria. Parliament), session 2006-2008, no. 156. Melbourne, Government Printer

Tang Z, Tolooiyan A, Mackay R (2017) Unconfined expansion test (UET) for measuring the tensile strength of organic soft rock. Comput Geotech 82:54–66

Tolooiyan A, Mackay R, Xue J (2014) Measurement of the tensile strength of organic soft rock. Geotech Test J 37(6). https://doi.org/10.1520/GTJ20140028

Tolooiyan A, Dyson AP, Karami M, Shaghaghi T, Ghadrdan M (2019) Application of ground penetrating radar (GPR) to detect joints in organic soft rock. Geotech Test J 42(2):257–274. https://doi.org/10.1520/GTJ20170279

Yihdego Y (2017) Hydraulic in situ testing for mining and engineering design: packer test procedure, preparation, analysis and interpretation. Geotech Geol Eng 35:29–44

Affiliations

Ali Tolooiyan[1] [ID] · **Ashley P. Dyson**[2] · **Mojtaba Karami**[2] · **Tahereh Shaghaghi**[2] · **Mohsen Ghadrdan**[2]

[1]   Geotechnical Engineering, School of Engineering, University of Tasmania, Hobart, TAS 7001, Australia

[2]   Geotechnical and Hydrogeological Engineering Research Group (GHERG), Federation University Australia, Churchill, Australia

Use of stochastic XFEM in the investigation of heterogeneity effects on the tensile strength of intermediate geotechnical materials

Ashley P. Dyson [a], Zhan Tang [b], Ali Tolooiyan [a,*]

[a] *Geotechnical and Hydrogeological Engineering Research Group (GHERG), Federation University Australia, Gippsland Campus, Victoria, Australia*
[b] *Faculty of Science, Monash University, Australia*

ARTICLE INFO

ABSTRACT

The numerical simulation of an Unconfined Expansion Test (UET) is presented with tensile strength fracture criteria assigned by stochastic methods to take into account material heterogeneity. Tests are performed by producing radial cavity expansion models of thinly sliced cylindrical specimens. The introduction of element-wise allocation of fracture parameters generates instances of specimen failure without the requirement of predefined fracture zones, permitting discontinuities to form naturally within zones containing weak strength parameters. The parallel application of an in-house Python scripts and eXtended Finite Element Method (XFEM) facilitates the investigation of heterogeneity effects on the tensile strength of intermediate geotechnical materials.

1. Introduction and background

Conventional numerical modelling methods such as the Finite Element Method (FEM) often perform poorly in approximation of solutions with non-smooth characteristics in the modelling domain, for example near discontinuities, crack initiation/propagation, and singularities. The eXtend Finite Element Method (XFEM) developed by Belytschko and Black [1] is an effective method to simulate discontinuities and crack opening by enabling a local enrichment of approximation spaces. With the additional degrees of freedom from special enrichment functions, once the failure criteria are fulfilled, cracks are allowed to initiate in local enrichment regions and to propagate based on the energy release criteria without the need for conventional re-meshing. Due to the absence of remeshing requirements, XFEM has become one of the choice methods for modelling fracture of cohesive materials [2–5].

Theoretically, the simplest laboratory testing method for the measurement of tensile strength is the Direct Tension Test (DTT). The method has been extensively implemented in the investigation of the tensile strength of over-consolidated clays, unsaturated soils, and cemented sands. However, the complicated process of specimen preparation is a significant obstacle [6,7]. Coupled with potential bias when compared with the Brazilian Testing method [8], Tang et al. [9] developed an XFEM model using Abaqus code [10] to simulate crack opening and tension failure in Unconfined Expansion Testing (UET) in order to analyse both

the stress distribution of the test and to examine fracture parameters. UET (as seen in Fig. 1) is a newly designed test that aims at measuring the tensile strength of intermediate geotechnical materials (IGM) such as soft rocks. A cylindrical cavity is drilled along the axis of a cylindrical specimen, then, based on Timoshenko's thick wall cylinder expansion theory [11] the UET method is able to create circumferential, uniformly-distributed tensile stresses around the sample cavity by the inflation of an expandable probe. Therefore, an arbitrary crack path is created when natural weaknesses of the sample approach the material's tensile strength. XFEM simulation results confirm an agreement with theoretical assumptions in both pre-failure stress distribution and tensile strength [9]. As stresses evenly develop inside the geometry, a radial XFEM region must be predefined within the geometry to overcome the computational ambiguity of crack opening when XFEM is specified over the full domain.

Of particular interest in the study of UETs is the impact of material heterogeneity. This can be achieved by interpolating XFEM with material variability and performing probabilistic analyses. Probabilistic analysis of heterogeneous brittle materials has continued to gain significant attention [2,12,13]. Understanding of the relationship between heterogeneity and UET test results has two benefits. For materials with known heterogeneity, the method can be applied to determine the test quality and possible error. For unknown heterogeneous materials, engineers can back-estimate the material's heterogeneity by performing a large number

---

* Corresponding author.
E-mail addresses: a.dyson@federation.edu.au (A.P. Dyson), zhan.tang@monash.edu (Z. Tang), ali.tolooiyan@federation.edu.au (A. Tolooiyan).
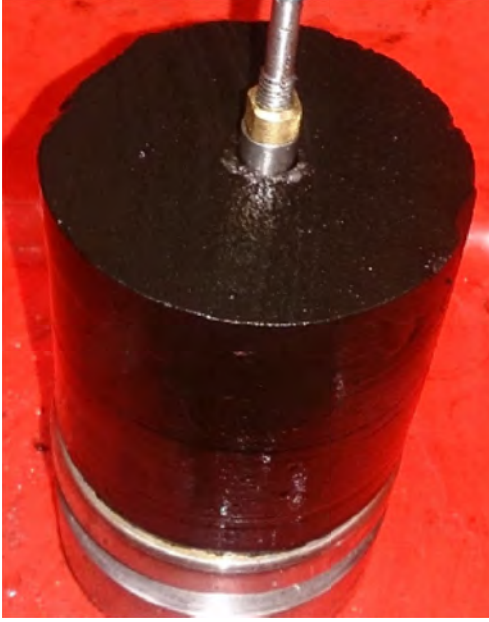
Fig. 1. UET probe placed within a brown coal specimen, Tang et al. [9].

of tests.

This paper introduces the existing uniform XFEM simulation of UET but without a predefined fracture zone. Commencing with the theory of discontinuity simulation by XFEM for implementation of UET modelling, comparisons of scenarios with and without the predefined XFEM region are produced. The process of random variable parameter assignment is detailed, followed by XFEM simulation results. With the aforementioned approach, the goal of this research is to allow fracture to form naturally without predefined XFEM zones, by the process of random variable assignment of element parameters. Furthermore, this paper presents the effects of this process on material strength, such that stochastic models incorporating variation of material characteristics can be calibrated to align with observed laboratory UET results, while also producing numerical results to develop conclusions about empirical UET parameter variability.

2. The extended finite element method overview

The extended finite element method is an indispensable tool for modern numerical simulation of crack initiation, propagation, and coalescence. Initially developed by Belytschko and Black [1,15], XFEM supplements the classic finite element method with local enrichment functions applied to finite element approximation spaces. Alternative existing techniques for fracture simulation include boundary element methods [16,17], continual re-meshing FEM [18], and mesh-free methods [14,19]. However, XFEM exhibits a wide range of beneficial attributes; without the enrichment properties of the extended method, conventional FEM requires appreciable mesh refinement in the neighbourhood of discontinuity tips. Discrete crack propagation phenomena are often modelled efficiently with XFEM without the constraint of extensive re-meshing, a crucial property for computationally expensive non-linear systems. XFEM incorporates the added benefit of integrating readily available codes to existing finite element algorithms and framework.

2.1. Theory

In the extended finite element method, the span of functions for the element-free Galerkin method of Fleming, Chu [19] is implemented utilising Partition of Unity (PU) theory developed by Melenk and

Babuška [20], and Duarte and Oden [21]. The PU method provides analysis of material behaviour characteristics throughout element geometries, rather than exclusively at element nodes. Consequently, mesh and discontinuity alignments are nonessential. Additional degrees of freedom produce near crack tip nodes by enrichment functions. The displacement approximation u, with the partition of unity enrichment is expressed in Equation (1) [10].

$$\boldsymbol{u}^h = \sum_{i \in I} \boldsymbol{u}_i \phi_i + \sum_{j \in J} \boldsymbol{b}_j \phi_j H(x) + \sum_{k \in K} \phi_k \left(\sum_{l=1}^{4} \boldsymbol{c}_k^l F_l(\boldsymbol{x}) \right) \quad (1)$$

where the first contributing part $\mathbf{u}_i$ corresponds to the classical FEM approximation of the displacement field, φ_j is the shape function for the jth node whose support is cut by the crack face (but not the crack tip), $\mathbf{b}_j$ is the crack face jth nodal displacement vector; $H(x)$ is the modified Heaviside function (Equation (2)), $F_l(x)$ are the elastic asymptotic crack tip functions (Equations (3)–(6)); $\mathbf{c}_k^l$ is kth nodal enriched degree of freedom vector of the asymptotic crack tip and φ_k is the shape function for the kth node whose support is cut by the crack tip. The nodal displacement term $\mathbf{u}_i$ applies to all nodes, while the Heaviside term contributes only to nodes whose support is cut by the crack interior. The final term of Equation (1) is applied only to the nodes whose support is cut by the crack tip.

$$H(\boldsymbol{x}) = \begin{cases} 1 & \text{if } (\boldsymbol{x} - \boldsymbol{x}^*) \cdot \boldsymbol{m} \geq 0, \\ -1 & \text{otherwise} \end{cases} \quad (2)$$

where, $\boldsymbol{x}$ is a Gauss point, $\boldsymbol{x}^*$ is the projection of $\boldsymbol{x}$ onto the crack line, and $\boldsymbol{m}$ is the unit outward normal to the crack at position $\boldsymbol{x}^*$.

$$F_{l=1}(x) = \sqrt{r} \sin\frac{\theta}{2} \quad (3)$$

$$F_{l=2}(x) = \sqrt{r} \cos\frac{\theta}{2} \quad (4)$$

$$F_{l=3}(x) = \sqrt{r} \sin\frac{\theta}{2} \sin\theta \quad (5)$$

$$F_{l=4}(x) = \sqrt{r} \cos\frac{\theta}{2} \sin\theta \quad (6)$$

Where, (r, θ) form the polar coordinate system with the crack tip at the origin.

2.2. Extended finite element simulations with predefined enrichment zones

The numerical fracture simulations of Tang et al. [9] provides an innovative technique for the modelling of the tensile strength of organic soft rock cored specimens. Utilising the XFEM in Abaqus 6.14 FEM code, Tang et al. [9] produced a quarter annulus shaped membrane (Fig. 2) with spatially homogeneous material properties shown in Table 1. As shown in Fig. 2, a predefined thin enrichment XFEM region is extending radially from a centre cavity. Due to the expectation of stress developing uniformly through the model geometry, crack initiation and propagation are exclusively allowed to develop within the desired XFEM region.

To trigger the crack initiation, the failure criterion was defined by a Maximum Principal Stress Failure Criteria (MPSFC) of 130 kPa, suitably modelling failure under tension. Conversely, the deviatoric stress criterion modelled failure in compression, as expected in elements close to the annulus cavity wall, where aperture expansion may cause excessive compression.

In preference to implementing a computationally expensive full three-dimensional model, a thin layer consisting of 3842 eight-node linear brick reduced integration elements (ABAQUS type C3D8R) was deemed a suitable specimen geometry for initial analysis. A thin 3D layer was chosen in preference to a 2D plane-strain model, due to the contact

formulation of the inner cavity. Abaqus 3D shell elements (S4R 4-node reduced integration) were chosen due to the number of contact elements, in comparison with the Abaqus beam elements (B31) of 2D plane-strain simulation.

Boundary conditions illustrate side 1 as fixed in the Y direction, side 2 fixed in the X direction, and sides 3 and 4 fixed in the Z direction (Fig. 2). Isotropic cylindrical pressure applied to side 5 simulated the expansion of the internal cavity, providing conditions to trigger fracture initiation. The full dimensions of the UET sample and the quarter annulus considered for modelling are given in Fig. 3.

2.3. Heterogeneous XFEM model without predefined enrichment zone

The model described above constitutes a powerful technique for the simulation of cracked specimens mimicking unconfined expansion tests. However, the prescription of a defined failure region (XFEM region in Fig. 2) represents an unrealistic system. In the paper presented, methods permit solution dependent fracture paths to develop, without the need to predefine the failure region.

In the absence of heterogeneous material characteristics in numerical simulation of isotropic loading scenarios such as UET, homogeneous parameters of elastic modulus and maximum tensile strength are allocated to all specimen elements. Hence, fractures are unable to differentiate strong and weak zones and propagate uniformly, making numerous fractures developing radially from the inner cavity (Side 5). This method of homogenous crack initiation and propagation is not only unrealistic but also causes the solution to fail after a few unconverged iteration (see Fig. 4). To solve this limitation, material variability should be introduced in numerical modelling. The maximum principal stress crack initiation criteria which is available in Abaqus enhanced with the addition of heterogeneous strength parameters allows cracks to initiate naturally, meaning no initial fractures were designed within the Finite Element geometry. Instead, cracks form without predefined orientations, locations and dimensions, with crack characteristics determined by the cavity expansion applied to the unique instance of the of material's maximum principal stresses. Due to the energy release rate and the material strength values, cracks propagate orthogonal to the orientation of the internal cavity.

3. Assign material variation into XFEM

3.1. Definition of model variability

It is widely accepted that computational methods aid the construction

Table 1
Input parameters of initial quarter annulus model.

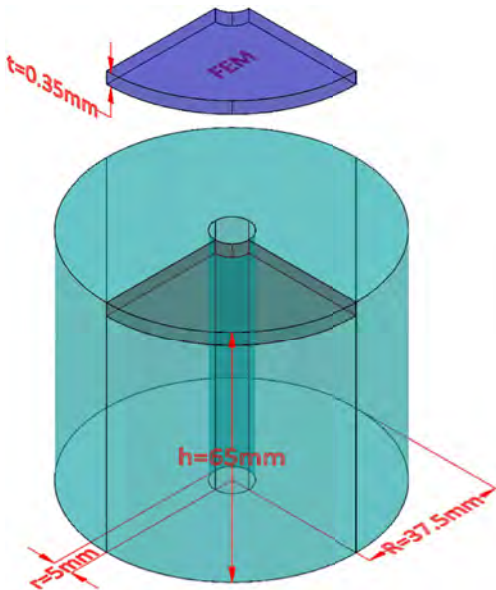| Tensile strength (kPa)	Poisson's ratio	Critical energy release rate (Pa m)	Elastic modulus (MPa)	Friction angle (degrees)	Cohesion (kPa)
130	0.22	2.357	19	20	150

Fig. 3. Quarter annulus of UET sample used for FEM modelling.

and analysis of engineering systems ranging from the nano-scale to the macro-scale. Inherent material uncertainties and their influence on system behaviour have led to an increase in stochastic methods applied to geotechnical problems of high complexity. Numerical simulations containing stochastic and heterogeneous soil models are gaining attention in broad range of geotechnical engineering fields, from slope stability analysis [22,23] to discrete fracture networks [24]. Heterogeneous characteristics may be applied to include Poisson's ratio, elastic modulus, yield stress, methods of loading, etc. Heterogeneities are often generated by means of statistics and probability theory, with resulting behaviour
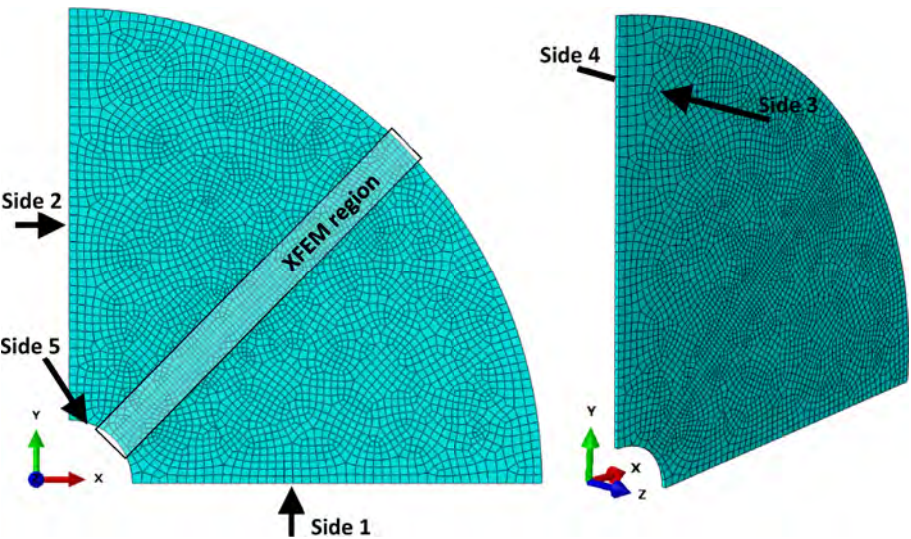

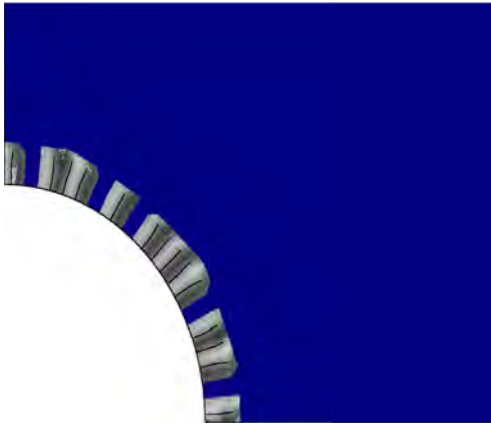**Fig. 2.** XFEM geometry of Tang et al. [9].

Fig. 4. Multiple cavity fractures caused by material homogeneity.

that cannot be achieved by classical deterministic approaches.

3.2. Numerical definition of material variation

Due to the Central Limit Theorem (CLT), sufficiently large random samples of a population of finite variance, produce sample means approximately equal to the mean of the population. Furthermore, sample means will follow an approximately Gaussian distribution, with sample variances mirroring the population variance. Although uncertainties in soil mechanics may follow non-Gaussian distributions, stationary Gaussian random fields are routinely assumed for the sake of simplicity and due to a lack of knowledge regarding experimental data. This paper concentrates exclusively on the normal (Gaussian) distribution for the variation of element maximum principal stress failure criteria and element elastic modulus. The fluctuations in these properties suggest an approach for the production of spatial variation in crack initiation and propagation. As the objective of this research is to naturally produce fracture by material strength parameter variation, the analysis of non-Gaussian distributions is deemed beyond the scope of this paper. Spatially random variables without a spatial correlation length have been implemented in this research, as spatial correlation parameters are not required to produce the goal of fracture initiation.

Material properties are varied as a percentage of their mean value (Fig. 5). As maximum principal stress and elastic modulus variables permit only non-zero values, random variables outside the range of [0, 2μ] were rejected and given random normal values within the

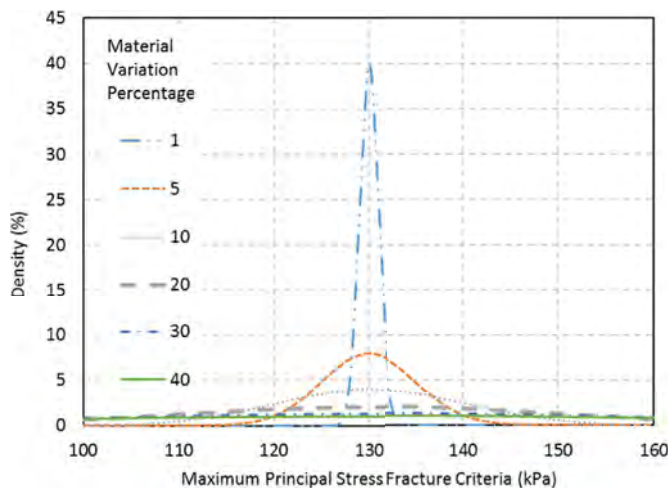permissible domain. This process produced a truncated Gaussian distribution free from skew.

3.3. Simulation methodology

The proposed method is specified by the following procedure and in Fig. 6.

(1) Meshing the domain with Abaqus CAE to create an input (inp) file. A fine mesh is required to ensure crack paths are modelled with satisfactory resolution;
(2) Generating normally distributed tensile strength and elastic modulus parameters for each finite element using in-house Python scripts;
(3) Assigning material element properties to finite elements, indexed within input files generated by Abaqus;
(4) Implementing Abaqus standard solver, running cavity expansion simulation (UET) and producing pressure-volume curves and Abaqus ODB files;
(5) Exporting pressure-volume data to a spreadsheet;
(6) Repeating steps (2–5) for a sufficient number of random initial configurations, as required by the Monte Carlo simulation method. This process is automated by the creation of a batch file;
(7) Determining cavity strength parameters immediately prior to specimen failure;
(8) Conducting statistical analysis using the statistical package R [27].

This procedure is implemented to produce spatially dependent crack initiation and propagation, unachievable in spatially uniform and homogenous materials.

To determine the impact of fluctuating tensile strength and elastic modulus, a one-factor-at-a-time sensitivity analysis was conducted consisting of the variation of four parameters:

1) Impact of mean tensile strength fracture initiation criteria
   Element Maximum Principal Stress Failure Criteria (MPSFC) values
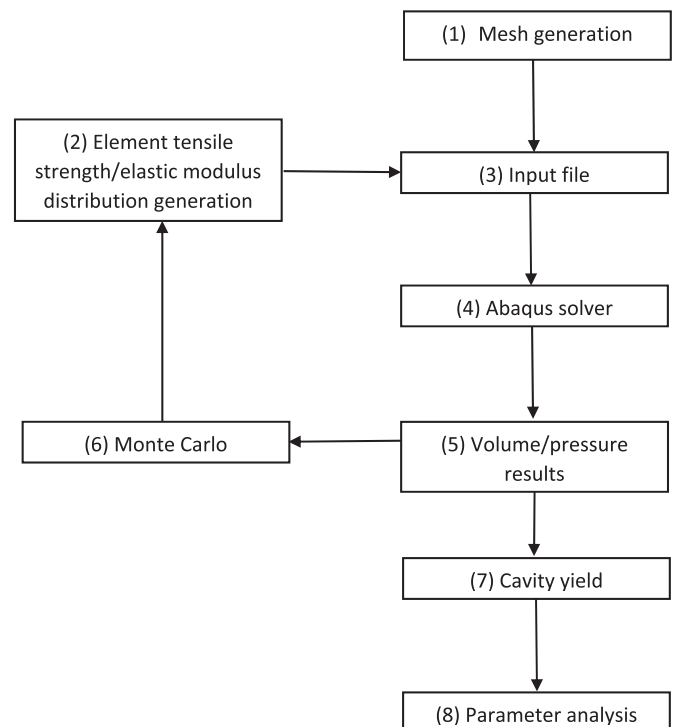

Fig. 5. Distribution of maximum allowable principal stress in tension (fracture initiation criteria).

Fig. 6. Analysis procedure flowchart.

for XFEM crack initiation were generated with distribution means of 104, 117 and 130 kPa, each with a spread of 20% of the mean strength value. The spread is expressed such that three standard deviations each side of the mean contains stress values within 20% of the mean principal stress. The variation of cavity pressure at initial fracture is then determined in terms of mean and percentage spread of yield pressure mean.

2) Impact of tensile strength fracture initiation criteria spread

Element MPSFC values are generated with a mean of 130 kPa and a spread of 1, 5, 10, 20, 25, 30 and 40% of the MPSFC mean. Similarly, cavity yield pressure mean and percentage spreads are determined.

3) Impact of elastic modulus distribution mean

Elemental elastic modulus values are generated with a mean of 15.2, 19 and 22.8 MPa and 20% mean elastic modulus variation. From the cavity pressure-strain curve, the elastic modulus can be determined from the linear component of the pressure versus change volumetric strain, as shown by Wood [25] (Equation (7)). This is then used to calculate a mean output elastic modulus for the model from Hooke's law (Equation (8)). Output elastic modulus mean and percentage material spreads are then determined.

$$G = V_0 \frac{dp}{dV} \tag{7}$$

$$E = 2G(1 + \nu) \tag{8}$$

where, G is shear modulus, V_0 is initial volume of the cavity, E is elastic modulus, and ν is Poisson's ratio of the UET sample.

4) Impact of elastic modulus distribution spread

Elemental elastic modulus values are generated with a mean of 1.9 MPa and spreads of 1, 10, 20 and 30%. The yield elastic modulus mean and percentage material spreads are then determined using the same method as in procedure (3) detailed above.

4. Results

Examples of element variation are shown in Fig. 7. Four instances of crack propagation of the elemental MPSFC with Gaussian distribution ($\mu = 130000$, $\sigma = 4333.33$) are presented in Fig. 8 with contour fields signifying displacement magnitude. As expected, element heterogeneity

of fracture criteria allows crack paths to develop nonuniformly, radially extending from the interior cavity. Although the samples in 7(a) and (c) produced a solitary fracture, 7(b) and (d) indicate that multiple fractures are capable of forming.

As the goal of producing spatially nonuniform cracks has been achieved, analysis of the strength properties of heterogeneously distributed element characteristics is investigated using the methods detailed above.

4.1. Impact of mean tensile strength fracture initiation criteria

When assessing the impact of tensile strength initiation criteria variation (Table 2, Figs. 9 and 10), suggests Gaussian MPSFC distributions with 20% spread have the impact of producing a material that will fail at a cavity pressure (primary failure) slightly lower than the mean MPSFC (between 2% and 3% lower). This is to be expected as crack paths will propagate through weak zones while avoiding regions of high tensile strength. Thus cavity pressures less than the mean MPSFC cause the sample to fracture.

Similarly, yield cavity pressures spreads are smaller than the MPSFC variation of 20% for each of the mean MPSFC values tested. While the percentage differences between mean MPSFC and cavity yield pressure seem mostly unaffected by MPSFC means, the percentage change in spread parameters is more varied. Of particular interest is the narrowing of the distribution of yield cavity pressures, compared with MPFSC variation. This suggests that widely varying MPSFC elements produce a much narrower band of yield pressures (observed between 38% and 47% less). As the initial difference of 30 μm between the cavity and probe radius observed in laboratory testing was not considered for this simulation, the XFEM results are plotted from $dv/dv_0 = 0.013$ (Fig. 9). The whisker plot of Fig. 10 details similar variation for each distribution of MPSFC with increasing mean strength.

4.2. Impact of tensile strength fracture initiation criteria spread

The impact of the distribution spread for a fixed mean MPSFC of 130 kPa is detailed in Table 3. As expected, increased MPSFC element variation produces a wider range of cavity yield pressures, as shown in Fig. 11. It is immediately obvious that variation of input MPSFC parameters does not produce equal yield cavity pressure spreads. For low
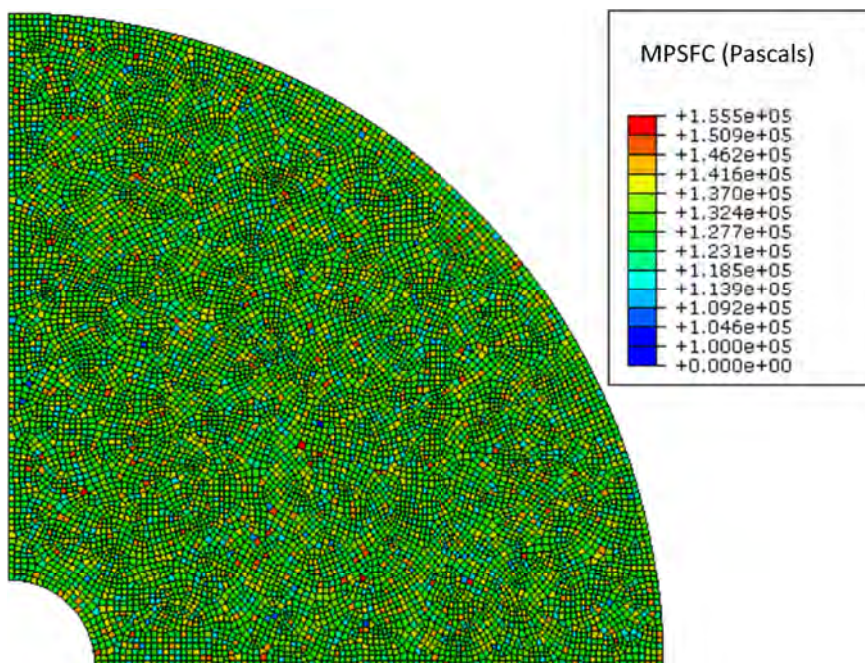

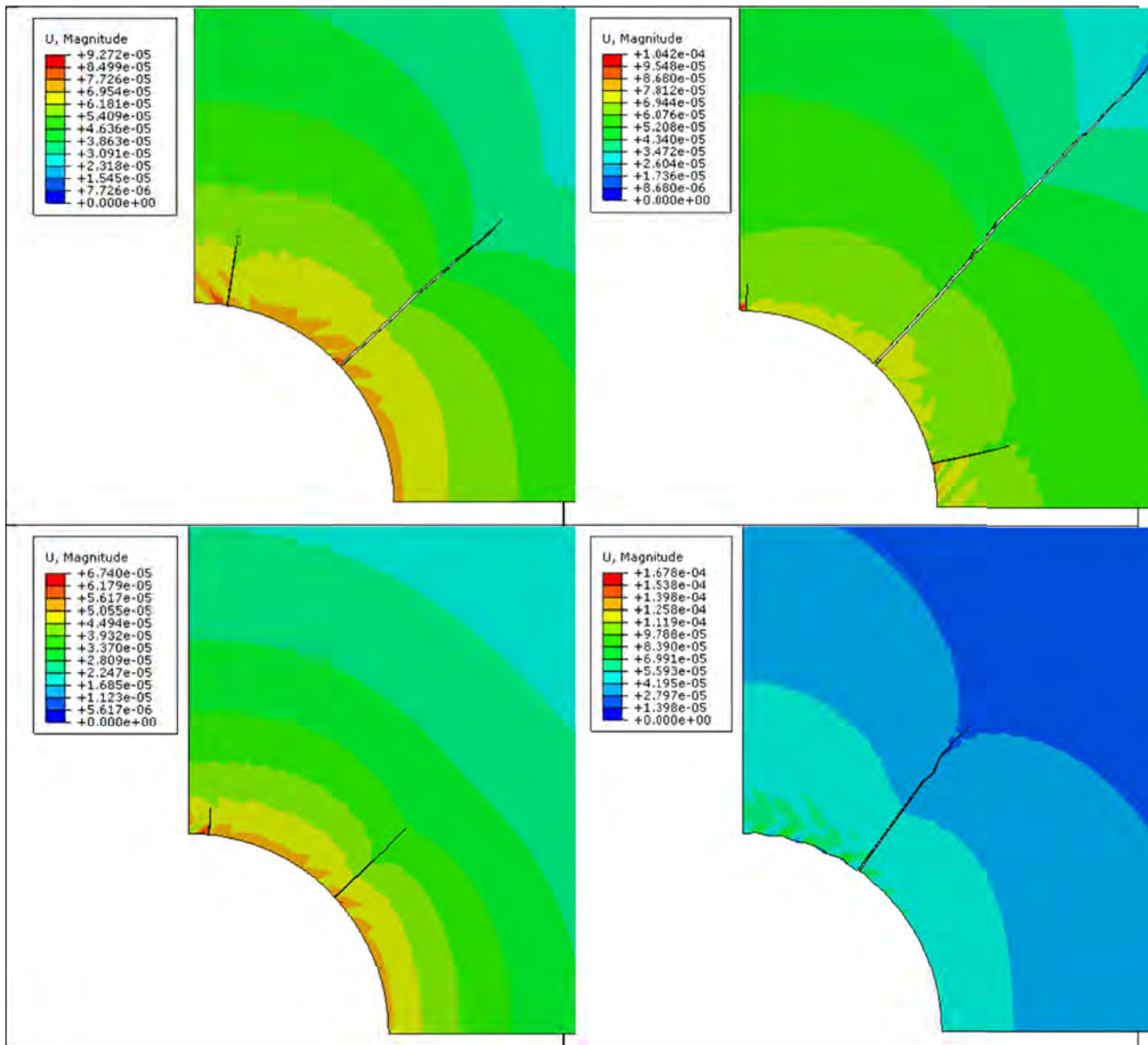**Fig. 7.** Specimens with heterogeneous maximum principal strength fracture initiation criteria.

Fig. 8. Four crack propagation instances (μ = 130000, σ = 4333.33).

Table 2
Variation of mean tensile strength fracture initiation criteria.

Mean elemental MPSFC (kPa)	Mean cavity yield pressure (kPa)	Percentage change in mean parameters	MPSFC variation (%)	Yield cavity pressure variation (%)	Percentage change in spread parameters
104	100.8	−3.07692	20	11.56	−42.2
117	113.1	−3.33333	20	12.38	−38.1
130	127.2	−2.15385	20	10.51	−47.45

MPSFC spreads, the material requires cavity pressures above the MPSFC mean to initiate fracture. Further increasing the spread weakens the material such that cavity pressures well below the mean tensile strength initiation criteria produce cracks.

It is noted MPSFC spread variation has a much greater impact on cavity yield pressure spread than mean cavity yield pressure, especially for small spread values. For small input spreads, the cavity pressure spread increases above the input spread, before drastically narrowing.

Several outliers are observed however, their removal impact is deemed minimal.

To produce models for tensile strength of Loy Yang brown coal between 110 kPa and 130 kPa as reported by Tolooiyan, Mackay [26], a MPSFC mean of 130 kPa with a spread of 40% (Table 3) are proposed. These parameters produce a material with a tensile strength of 119.3 kPa and spread between 110.64 kPa and 127.96 kPa. This range lies within the primary failure zone detailed by Tang et al. [9] for Yallourn brown coal.

4.3. Impact of elastic modulus distribution mean

Investigation of varying element mean elastic modulus values (Fig. 12 and Table 4) indicate that the element mean elastic modulus does not substantially impact the output elastic modulus variation. It is noted in the whisker plot of Fig. 12 that the mean output elastic modulus is minutely diminished compared to the elemental elastic modulus mean. Despite a variation of 20% on the element elastic modulus spread, the output elastic modulus spread is particularly narrow (less than 1.5%)
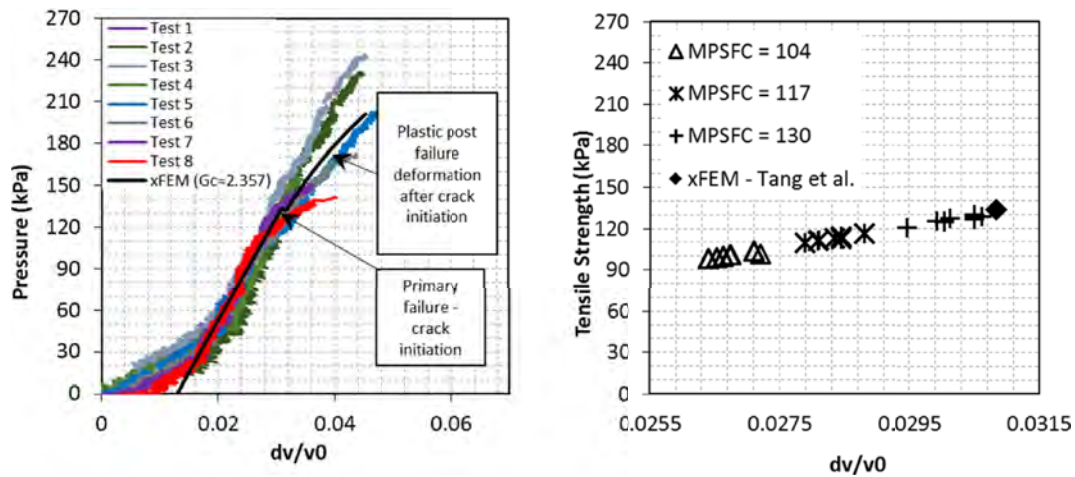
Fig. 9. Variation of yield pressures (primary failure) compared with experimental results produced by Tang et al. [9].
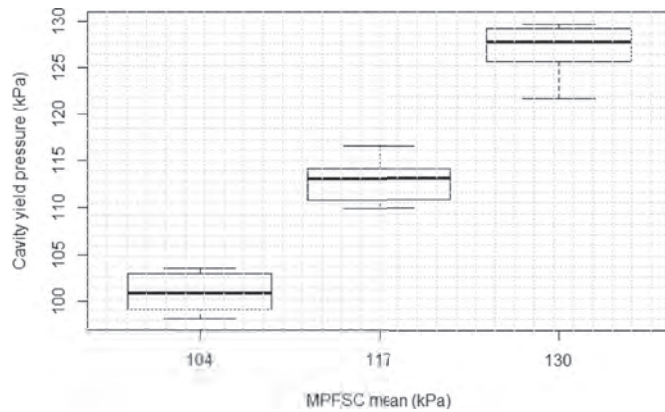

Fig. 10. Whisker plots of mean tensile strength fracture initiation criteria.
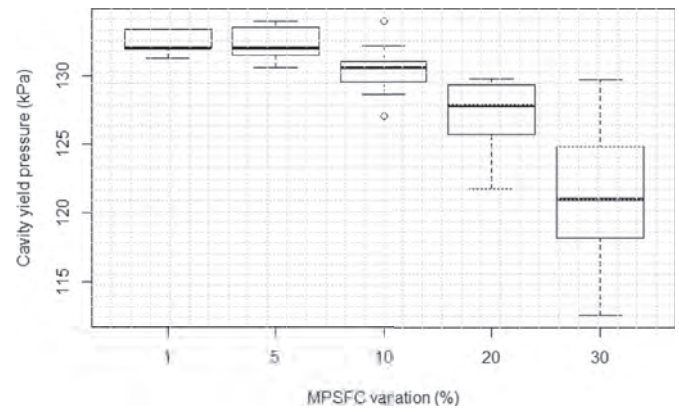

Fig. 11. Whisker plots of tensile strength fracture initiaion criteria spread.

Table 3
Tensile strength fracture initiaion criteria spread.

Mean elemental MPSFC (kPa)	Mean yield cavity pressure (kPa)	Percentage change in mean parameters	MPSFC spread (%)	Cavity yield pressure spread (%)	Percentage change in spread parameters
130	132.5	1.92	1	3.44	244
130	132.2	1.69	5	5.25	5
130	130.4	0.31	10	7.42	−25.8
130	127.2	−2.15	20	10.51	−47.5
130	123.0	−5.38	25	17.74	−29.0
130	121.4	−6.62	30	21.09	−29.7
130	119.3	−8.23	40	17.32	−56.7

compared with MPSFC variation (Table 2). It is noteworthy that the effects of element elastic modulus variation related to output elastic modulus mean and deviation are considered negligible.

4.4. Impact of elastic modulus distribution spread

Variation of element elastic modulus spread (Table 5 and Fig. 13) shows little impact on mean output elastic modulus values while output elastic modulus spreads remain close to constant. This suggests that probabilistic variation of elastic modulus values is an unnecessary parameter for the variation of output elastic modulus.

5. Discussion and conclusion

The simulations described were designed to mimic the uncertainty and variation of strength inherent in specimens of Victorian brown coal as a non-textbook geotechnical material, by the assignment of Gaussian random variables to individual finite elements. Four sets of experiments were performed to determine the sensitivity of heterogeneous XFEM fracture to the distributed parameters of maximum principal stress failure criteria and elastic modulus. Of particular interest was the negligible impact of elastic modulus variation played on failure characteristics. Parameters were determined to accurately simulate brown coal specimen characteristics in alignment with previous test results.

The approach of varying element properties by random variable sampling for extended finite elements lends itself to expanded analysis of full three-dimensional models given sufficient computational resources. The technique accommodates the future study of a wider range of varied model parameters and random variable distributions commonly used in soil mechanics. The addition of spatial correlation length scales provide a supplementary layer of complexity for future implementation.

The results presented in this paper propose that probabilistic distributions of fracture initiation criteria can be applied to XFEM elements to allow fracture initiation and propagation with comparable behaviour to UET testing of laboratory specimens, without the requirement of pre-defined failure zones. The simulations have demonstrated the impact of heterogeneity in maximum principal stress failure criteria and elastic modulus for the understanding of fracture mechanics in brown coal and intermediate geotechnical material.
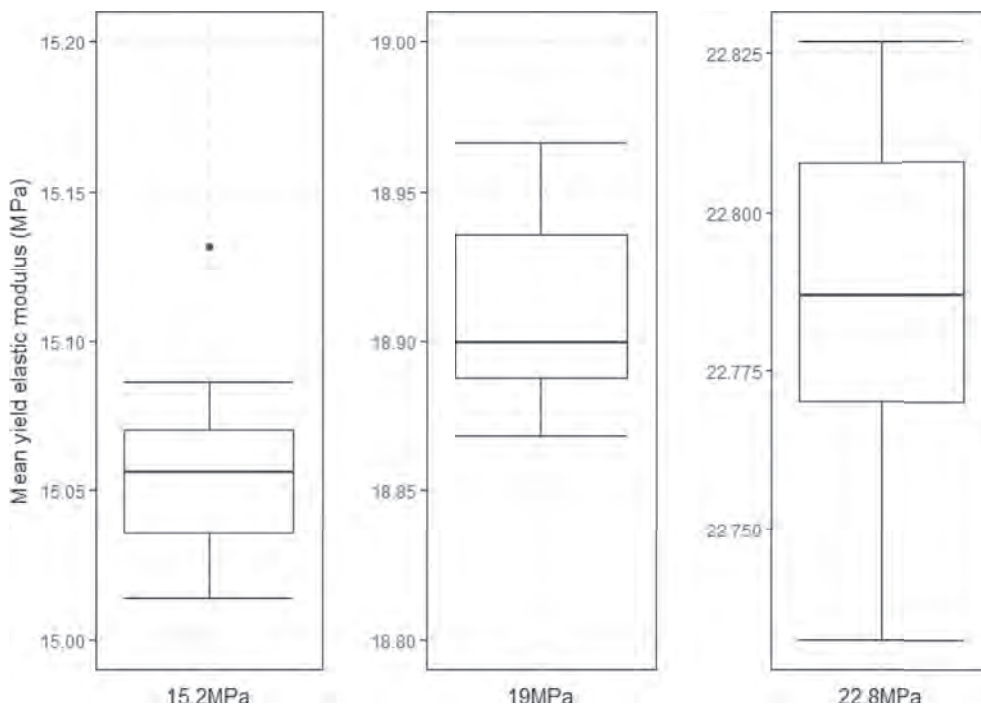
Fig. 12. Whisker plots of elastic modulus distribution mean values.

Table 4
Elastic modulus distribution mean values.

Mean elemental elastic modulus (MPa)	Mean output elastic modulus (MPa)	Percentage change in mean elastic modulus	Elastic modulus spread (%)	Elastic modulus spread (%)	Percentage change in elastic modulus spread
15.2	15.06	−0.95	20	1.21	−93.95
19	18.91	−0.47	20	0.95	−95.25
22.8	22.78	−0.07	20	0.71	−96.45

Table 5
Impact of elastic modulus distribution spread.

Mean elemental elastic modulus (MPa)	Mean output elastic modulus (MPa)	Percentage change in mean elastic modulus	Element elastic modulus spread (%)	Output elastic modulus spread (%)	Percentage change in elastic modulus spread
19	18.91	−0.47	1	0.063026	−93.70
19	18.91	−0.47	10	0.58813	−94.12
19	18.91	−0.47	20	1.050684	−94.75
19	18.89	−0.58	30	0.957721	−96.81

Fig. 13. Primary failure locations.

References

[1] T. Belytschko, T. Black, Elastic crack growth in finite elements with minimal remeshing, Int. J. Numer. Meth. Eng. 45 (5) (1999) 601–620.
[2] H. Liu, F. Alonso-Marroquin, D. Williams, Three-dimensional modelling of the rock breakage process, in: ISRM Regional Symposium-EUROCK 2009, International Society for Rock Mechanics, 2009.
[3] S. Salimzadeh, N. Khalili, A three-phase XFEM model for hydraulic fracturing with cohesive crack propagation, Comput. Geotech. 69 (2015) 82–92.
[4] Y. Xie, P. Cao, J. Liu, L. Dong, Influence of crack surface friction on crack initiation and propagation: a numerical investigation based on extended finite element method, Comput. Geotech. 74 (2016) 1–14.
[5] J. Pogacnik, D. Elsworth, M. O'Sullivan, J. O'Sullivan, A damage mechanics approach to the simulation of hydraulic fracturing/shearing around a geothermal injection well, Comput. Geotech. 71 (2016) 338–351.
[6] A. Ajaz, R.H.G. Parry, Unconfined direct tension test for compacted clays, J. Test. Eval. 2 (3) (1974) 163–172.
[7] N. Lu, B. Wu, P. Tan Chee, Tensile strength characteristics of unsaturated sands, J. Geotech. Geoenviron. Eng. 133 (2) (2007) 144–154.
[8] D. Li, L.N.Y. Wong, The Brazilian disc test for rock mechanics applications: review and new insights, Rock Mech. Rock Eng. 46 (2) (2013) 269–287.
[9] Z. Tang, A. Tolooiyan, R. Mackay, Unconfined Expansion Test (UET) for measuring the tensile strength of organic soft rock, Comput. Geotech. 82 (2017) 54–66.
[10] D. Systèmes, Dassault Systèmes, Abaqus, 6.14 ed., 2014. Providence (RI, USA).
[11] S. Timoshenko, S. Woinowsky-Krieger, Theory of Plates and Shells, McGraw-Hill, New York, 1959, 1959.
[12] I. Kolo, R.K. Abu Al-Rub, R.L. Sousa, Computational modelling of fracture propagation in rocks using a coupled elastic-plasticity-damage model, Math. Probl Eng. 2016 (2016) 15.
[13] X.T. Su, Z.J. Yang, G.H. Liu, Monte Carlo simulation of complex cohesive fracture in random heterogeneous quasi-brittle materials: a 3D study, Int. J. Solid Struct. 47 (17) (2010) 2336–2345.
[14] T. Belytschko, Y. Krongauz, D. Organ, M. Fleming, P. Krysl, Meshless methods: an overview and recent developments, Comput. Meth. Appl. Mech. Eng. 139 (1–4) (1996) 3–47.

[15] N. Moes, J. Dolbow, T. Belytschko, A finite element method for crack growth without remeshing, Int. J. Numer. Meth. Eng. 46 (1) (1999) 131–150.

[16] A.L. Saleh, M.H. Aliabadi, Crack growth analysis in concrete using boundary element method, Eng. Fract. Mech. 51 (4) (1995) 533–545.

[17] W. Wendland, T.A. Cruse, Boundary element analysis in computational fracture mechanics, Math. Comput. 55 (192) (1990) 870.

[18] D.V. Swenson, A.R. Ingraffea, Modeling mixed-mode dynamic crack propagation using finite elements: theory and applications, Comput. Mech. 3 (6) (1988) 381–397.

[19] M. Fleming, Y.A. Chu, B. Moran, T. Belytschko, Enriched element-free Galerkin methods for singular fields, Int. J. Numer. Meth. Eng. 40 (8) (1997) 1483–1504.

[20] J.M. Melenk, I. Babuška, The partition of unity finite element method: basic theory and applications, Comput. Meth. Appl. Mech. Eng. 139 (1–4) (1996) 289–314.

[21] C.A. Duarte, J.T. Oden, Hp clouds-an hp meshless method, Numer. Meth. Part. Differ. Equ. 12 (6) (1996) 673–706.

[22] D. Griffiths, G.A. Fenton, Probabilistic slope stability analysis by finite elements, J. Geotech. Geoenviron. Eng. 130 (5) (2004) 507–518.

[23] S.E. Cho, Probabilistic assessment of slope stability that considers the spatial variability of soil properties, J. Geotech. Geoenviron. Eng. 136 (7) (2009) 975–984.

[24] Q. Lei, J.-P. Latham, C.-F. Tsang, The use of discrete fracture networks for modelling coupled geomechanical and hydrological behaviour of fractured rocks, Comput. Geotech. 85 (2017) 151–176.

[25] R.J.M.D.M. Wood, R.J. Mair, D.M. Wood, Pressuremeter Testing: Methods and Interpretation, first ed. ed. London: CIRIA.

[26] A. Tolooiyan, R. Mackay, J. Xue, Measurement of the tensile strength of organic soft rock BT - measurement of the tensile strength of organic soft rock, ASTM Geotech. Test. J. 37 (6) (2014).

[27] Release 3.4.3, R: A Language and Environment for Statistical Computing, 2017, http://www.R-project.org/.